

Winter 2012

Large-Eddy Simulation of Axially-Rotating, Turbulent Pipe and Particle-laden Swirling Jet Flows

Nicolas D. Castro
Old Dominion University

Follow this and additional works at: https://digitalcommons.odu.edu/mae_etds

 Part of the [Aerospace Engineering Commons](#), and the [Mechanical Engineering Commons](#)

Recommended Citation

Castro, Nicolas D.. "Large-Eddy Simulation of Axially-Rotating, Turbulent Pipe and Particle-laden Swirling Jet Flows" (2012). Doctor of Philosophy (PhD), dissertation, Mechanical Engineering, Old Dominion University, DOI: 10.25777/mpdk-zd57
https://digitalcommons.odu.edu/mae_etds/127

This Dissertation is brought to you for free and open access by the Mechanical & Aerospace Engineering at ODU Digital Commons. It has been accepted for inclusion in Mechanical & Aerospace Engineering Theses & Dissertations by an authorized administrator of ODU Digital Commons. For more information, please contact digitalcommons@odu.edu.

**LARGE-EDDY SIMULATION OF AXIALLY-ROTATING,
TURBULENT PIPE AND PARTICLE-LADEN SWIRLING JET FLOWS**


by

Nicolas D. Castro
B.A. December 2002, Virginia Commonwealth University
M.A. August 2005, Virginia Commonwealth University


A Dissertation Submitted to the Faculty of Old Dominion University
in Partial Fulfillment of the Requirements for the Degree of

DOCTOR OF PHILOSOPHY
MECHANICAL ENGINEERING

OLD DOMINION UNIVERSITY
December 2012

Approved by: 

Ayodeji Demuren (Director)

Chester Grosch (Member) 

 Gregory Selby (Member) 

ABSTRACT

LARGE-EDDY SIMULATION OF AXIALLY-ROTATING, TURBULENT PIPE AND PARTICLE-LADEN SWIRLING JET FLOWS

Nicolas D. Castro
Old Dominion University, 2012
Director: Dr. Ayodeji Demuren

The flows of fully-developed turbulent rotating pipe and particle-laden swirling jet emitted from the pipe into open quiescent atmosphere are investigated numerically using Large-Eddy Simulation (LES). Simulations are performed at various rotation rates and Reynolds numbers, based on bulk velocity and pipe diameter, of 5.3×10^3 , 12×10^3 , and 24×10^3 , respectively. Time-averaged LES results are compared with experimental and simulation data from previous studies. Pipe flow results confirm observations in previous studies, such as the deformation of the turbulent mean axial velocity profile towards the laminar Poiseuille-profile, with increased rotation. The Reynolds stress anisotropy tensor shows a redistribution due to pipe rotation. The axial component near the wall is suppressed, whereas the tangential component is amplified, as rotation is increased. The anisotropy invariant map also shows a movement away from the one-component limit in the viscous sublayer, with increased rotation. Exit conditions for the pipe flow simulation are utilized as inlet conditions for the jet flow simulation. Jet flow without swirl and at a swirl rate of $S=0.5$ is investigated. Swirl is observed to change the characteristics of the jet flow field, leading to an increase in jet spread and velocity decay and a corresponding decrease in the jet potential core. Lagrangian tracking with one way coupling is used to analyze particle dispersion in the jet flow. Three particle diameter sizes are investigated: 10, 100, and 500 μm , which correspond to Stokes numbers of 0.06, 6, and 150, respectively. Particles are injected with an initial velocity set equal to the instantaneous fluid phase flow velocities at the jet inlet. The results show that, in the absence of swirl, particle dispersion is inversely proportional to particle size. With the addition of swirl, particle evolution is much more complicated. Largely unaffected by turbulent structures, the largest particles maintain their initial radial trajectory and disperse radially outward significantly more with the addition of swirl. The smaller

particles, much more susceptible to turbulent structures, are shown to quickly diffuse within the jet, and their dispersion is unaffected by swirl. With the addition of swirl, dispersion of the midsize particles is shown to increase initially from the jet inlet up to a distance of approximately three diameter lengths downstream. Particle tracking and particle concentration analysis shows that the increase in particle dispersion of the midsize particles upstream is due to an initial outward migration of particles that are injected near the edge of the jet inlet.

I dedicate this dissertation to my querida familia: my carnales chingones: Oscar, Alfredo and Arturo, my sweet loving carnalas; Aurora, Leticia and especially mi queridísima carnala Josefina, the most headstrong, courageous, hardest working, beautiful sister in the world! Gracias carnala por todo lo que has hecho por tu burrito! Te prometo que pronto te dare todo lo que te mereces! To my jefe "Don Nico", estemos donde estemos hare todo para que su leyenda siempre viva en mi nombre. Dedicated to my mother Agripina, who has looked over me from heaven since 1987, espero estes bien orgullosa de mi mama...porfavor sigueme cuidando y bendiciendo. To all my nephews and nieces. Los quiero con todo mi corazon! I also dedicate this dissertation to my mentor, friend and great man, Mr. Clifford Scott Hardison, without your belief in me, guidance and all your support I would not be here. I thank you from the bottom of my heart. As my sister puts it, you sir "shall walk into heaven without taking your shoes off!"

ACKNOWLEDGEMENTS

I'd like to sincerely thank my PhD director, Dr. Demuren, for everything he has shared and taught me over the years. My deepest gratitude for his dedication and vision to see me through to the end. It was truly a privilege to work under his guidance. I'd also like to thank my committee members Dr. Selby and Dr. Grosch for their valuable feedback to help me finalize my dissertation. I extend my gratitude to the entire faculty in the Department of Mechanical Engineering for all their support throughout my education at Old Dominion University.

NOMENCLATURE

II, III	Second and third Reynolds stress anisotropic invariants
b_{ij}	Reynolds stress anisotropic tensor
C_p	Pressure loss coefficient; Particle concentration (Chapter 8.2)
C_s	Smagorinsky constant
D	Pipe/Jet diameter; Fluid domain (Chapter 3.2)
D_p	Particle diameter
$D_r^T(x)$	Global particle dispersion in the streamwise direction
H	Shape factor
i,j,k	Components (1,2, or 3)
L	Pipe/Jet domain length
L_s	Smagorinsky SGS length scale
\dot{m}	Mass flow rate
m_p	Mass of particles
m_f	Mass of fluid
N_p	Particle count
P	Pressure
\dot{Q}	Volumetric flow rate
q^2	turbulent kinetic energy
\bar{r}_p	Mean particle radial distance
R	Pipe/Jet Radius
Re	Reynolds number
Re_p	Particle Reynolds number
S	Swirl/Rotation Rate
\hat{S}_{ij}	Rate of strain tensor
S_c	Critical swirl number for vortex breakdown
St	Stokes number. Strouhal number (Chapter 2.2.1)
t	Time
t^*	Characteristic time scale

t_η	Kolmogorov time scale
t_p	Particle response time
$\overline{t_{p(x)}}$	Mean particle residence time
U	Mean axial velocity
U^+	Mean axial velocity in wall units
U_τ	Friction velocity
U_b	Mean bulk velocity
U_c, U_{cl}	Mean axial centerline velocity
U_i	Mean velocity component
U_f	Mean fluid axial velocity
U_p	Mean particle axial velocity
\vec{u}	Velocity vector
\hat{u}_i	Filtered velocity component
u_i	Fluctuating velocity component
u	Streamwise fluctuating velocity component
v	Tangential fluctuating velocity component
w	Radial fluctuating velocity component
u_{rms}	Streamwise root mean square fluctuating velocity
u_{rms}^+	Streamwise root mean square fluctuating velocity in wall units
\overline{uv}	Reynolds Stress (axial-tangential)
\overline{uw}	Reynolds Stress (axial-radial)
\overline{vw}	Reynolds Stress (radial-tangential)
v_{rms}	Tangential root mean square fluctuating velocity
v_{rms}^+	Tangential root mean square fluctuating velocity in wall units
V	Mean Tangential Velocity, Computational volume (Chapter 3.2)
V_w	Pipe Wall tangential Velocity
V_p	Mean Particle tangential velocity; Particle volume (Chapter 2.3)
V_f	Mean fluid tangential velocity; Fluid volume (Chapter 2.3)
w_{rms}	Radial root mean square fluctuating velocity

w_{rms}^+	Tangential root mean square fluctuating velocity in wall units
W	Mean radial velocity
$\frac{\partial}{\partial t}$	Time partial derivative
$\frac{\partial}{\partial x_i}$	Spatial partial derivative
δ_{ij}	Kronecker delta
Δt	Time step
ε	Dissipation
λ	Step length factor
η	Kolmogorov length scale
κ	Von Karman constant
μ	Dynamic viscosity
ν	Kinematic viscosity
μ_τ	Subgrid-scale turbulence viscosity
ρ, ρ_f	Fluid density
ρ_p	Particle density
τ	Stress tensor
τ_w	Wall shear stress
τ_{ij}^a	Anisotropic stress tensor
τ_{ij}^o	Isotropic stress tensor
$\hat{\phi}$	Generic filtered scalar
ϕ_m	Particle mass loading ratio
ϕ_V	Particle volume loading ratio

TABLE OF CONTENTS

	Page
NOMENCLATURE	vi
LIST OF TABLES	xi
LIST OF FIGURES	xii
Chapter	
1 INTRODUCTION AND MOTIVATION	1
2 LITERATURE REVIEW	4
2.1 ROTATING PIPE FLOW	4
2.1.1 EXPERIMENTAL STUDIES	4
2.1.2 NUMERICAL STUDIES	6
2.2 AXISYMMETRIC JET FLOW	9
2.2.1 NON-SWIRLING JET.....	9
2.2.2 SWIRLING JET.....	14
2.3 PARTICLE-LADEN TURBULENT FLOWS.....	17
2.3.1 PARTICLE-LADEN SWIRLING JET FLOW	20
3 NUMERICAL COMPUTATIONS OF TURBULENT FLOWS	23
3.1 DIRECT NUMERICAL SIMUALTION AND REYNOLDS AVERAGED NAVIER STOKES	23
3.2 LARGE-EDDY SIMULATION	26
4 PIPE FLOW MESH SENSITIVITY TESTS.....	30
4.1 PIPE FLOW MESH AND SIMULATION PARAMETERS	30
4.2 PIPE FLOW: $RE=5.3 \times 10^3$; $S=0$	35
4.3 PIPE FLOW: $RE=5.3 \times 10^3$; $S=0.5, 1, 2$	42
4.4 PIPE FLOW: $RE=12 \times 10^3, 24 \times 10^3$; $S=0, 0.5$	45
5 JET FLOW MESH SENSITIVITY TESTS	55
5.1 JET FLOW MESH AND SIMULATION PARAMETERS	55
5.2 JET FLOW: $RE=12 \times 10^3, 24 \times 10^3$; $S=0, 0.5$	61
6 PIPE FLOW VALIDATION	69
6.1 PIPE FLOW: $RE=5.3 \times 10^3$; $S=0$	71
6.2 NON-ROTATING PIPE FLOW: $RE=12 \times 10^3, 24 \times 10^3$; $S=0$	76
6.3 ROTATING PIPE FLOW: $RE=5.3 \times 10^3$; $S=0.5, 1, 2$	81
6.4 ROTATING PIPE FLOW: $RE=12 \times 10^3, 24 \times 10^3$; $S=0.5$	89
6.5 PIPE FLOW: REYNOLDS STRESS ANISOTROPY	92
7 JET FLOW VALIDATION.....	98
7.1 JET FLOW: $RE=12 \times 10^3, 24 \times 10^3$; $S=0, 0.5$	98
7.2 JET FLOW: REYNOLDS STRESS ANISOTROPY	115

	Page
8 PARTICLE-LADEN JET	119
8.1 PARTICLE-LADEN JET SETUP AND PARAMETERS	119
8.2 PARTICLE-LADEN JET RESULTS	122
9 SUMMARY AND CONCLUSIONS	138
REFERENCES	141
VITA	145

LIST OF TABLES

Table	Page
1. Pipe meshes geometry and grid points summary.....	32
2. Mesh comparison of distance in wall units ($Re=5 \times 10^3$, $S=0$) of the first 20 grid points from the pipe wall	33
3. Prescribed Pressure gradient and flow characteristics.....	33
4. Friction velocity, characteristic timescale, and Kolmogorov timescale.	35
5. Pipe Flow: $Re=5.3 \times 10^3$, $S=0$. Average bulk velocity/wall shear grid comparison.	38
6. Centerline Velocity normalized with bulk velocity ($Re=5.3 \times 10^3$). Orlandi and Fatica (1997, $Re=5.0^3$) (OF) and Reich and Beer (1989) (RB).....	42
7. Pipe Flow: $Re=5.3 \times 10^3$, $S=(0.5,1,2)$ shape factor Coefficient in the present simulations and in Orlandi and Fatica (1997) (OF) and Murakami and Kikuyama (1987) (MK).....	43
8. Pipe flow results and grid comparison with available validation data. ($Re=5.3 \times 10^3$, $S=0$, $*Re=5.6 \times 10^3$, $**Re=4.9 \times 10^3$).....	72
9. Distance in wall units, for first 20 points from pipe wall at $Re=5.3 \times 10^3$, $S=0$. $*NASA (Re=5.6 \times 10^3)$, $**Stanford (Re=4.9 \times 10^3)$	73
10. Particle response time and Stokes number. Bulk velocity estimate of $U_b=5.8\text{m/s}$, correspond to non-rotating ($S=0$) jet flow at $Re=24 \times 10^3$	120
11. Particle Volume/Mass fraction.	120

LIST OF FIGURES

Figure	Page
1. Axisymmetric Jet (Contours of mean velocity shown).....	10
2. Pipe mesh cross sections: a. M100L, M200L, M256L b. M256L-SF.	31
3. Pipe mesh cross sections: a. P130C b. P200C.....	31
4. Pipe flow simulation data collection locations, 10 total. (5 axial distances in both Y and Z directions).	36
5. Mean axial velocity average at each measured location (temporal) and overall average for all locations (Mesh P130C).....	37
6. Average bulk velocity mesh comparison. $Re=5.3 \times 10^3$; $S=0$	37
7. Average pipe wall shear stress. $Re=5.3 \times 10^3$; $S=0$	38
8. Average mean axial velocity normalized with bulk velocity U_b (top) and in wall units (bottom). $Re=5.3 \times 10^3$; $S=0$. ($\kappa = 0.41, \beta = 0.59$)	39
9. RMS turbulence intensities in wall units. $Re=5.3 \times 10^3$; $S=0$	40
10. Reynolds shear stress (axial-radial) normalized with friction velocity. $Re=5.3 \times 10^3$; $S=0$	40
11. Mean Pressure normalized with friction velocity. $Re=5.3 \times 10^3$; $S=0$	41
12. RMS Pressure normalized with friction velocity. $Re=5.3 \times 10^3$; $S=0$	41
13. Mean axial velocity normalized with bulk velocity U_b . $Re=5.3 \times 10^3$; $S=0.5, 1, 2$	43
14. Mean axial velocity normalized with centerline velocity U_c , $Re=5.3 \times 10^3$; $S=0.5, 1, 2$	44
15. Mean tangential velocity normalized with bulk velocity U_b . $Re=5.3 \times 10^3$; $S=0.5$, 1, 2.....	44
16. Mean tangential velocity ratio normalized with pipe wall velocity V_w , $Re=5.3 \times 10^3$; $S=0.5, 1, 2$	45
17. Average bulk velocity (1,000 time step samples). $Re=12 \times 10^3, 24 \times 10^3$; $S=0, 0.5$	46
18. Pressure loss coefficient. $Re=5.3 \times 10^3, 12 \times 10^3, 24 \times 10^3$: Effect due to pipe rotation	47
19. Average wall shear (1,000 time step samples). $Re=12 \times 10^3, 24 \times 10^3$; $S=0, 0.5$	48
20. Mean axial velocity normalized with bulk velocity, $Re=12 \times 10^3, 24 \times 10^3$; $S=0, 0.5$	49

Figure	Page
21. Mean axial velocity in wall units. $Re=12 \times 10^3, 24 \times 10^3$; $S=0$	49
22. Mean tangential velocity normalized with bulk velocity. $Re=12 \times 10^3, 24 \times 10^3$; $S=0.5$	50
23. RMS velocities normalized with bulk velocity. $Re=12 \times 10^3$; $S=0, 0.5$	51
24. RMS velocities normalized with bulk velocity. $Re=24 \times 10^3$; $S=0, 0.5$	52
25. Reynolds shear stress (axial-radial) normalized with bulk velocity. $Re=12 \times 10^3$; $S=0, 0.5$	52
26. Reynolds shear stress (axial-radial) normalized with bulk velocity. $Re=24 \times 10^3$; $S=0, 0.5$	53
27. Mean Pressure. $Re=12 \times 10^3, 24 \times 10^3$; $S=0, 0.5$	54
28. RMS Pressure. $Re=12 \times 10^3, 24 \times 10^3$; $S=0, 0.5$	54
29. Jet mesh domain dimensions and boundary conditions.....	55
30. Jet meshes tested.....	57
31. Jet mesh cross sectional views at Jet inlet (blue), $x=0D$	58
32. Jet meshes cross sectional views at $x=5D$	59
33. Jet mesh cross sectional views at $x=10D$	60
34. Jet Centerline Axial velocity. $Re=12 \times 10^3, 24 \times 10^3$; $S=0, 0.5$	62
35. Jet mean axial velocity. $Re=12 \times 10^3$; $S=0$	63
36. Jet mean axial velocity. $Re=12 \times 10^3$; $S=0.5$	63
37. Jet mean tangential velocity at $x=(0, 2, 4, 6, 8, 10)D$. $Re=12 \times 10^3$; $S=0.5$	64
38. Jet mean tangential velocity at $x=(0, 2, 4, 6, 8, 10)D$. $Re=24 \times 10^3$; $S=0.5$	64
39. Jet Centerline RMS Axial velocity. $Re=12 \times 10^3, 24 \times 10^3$; $S=0, 0.5$	65
40. Jet Centerline RMS Radial velocity. $Re=12 \times 10^3, 24 \times 10^3$; $S=0, 0.5$	65
41. Jet Centerline RMS Tangential velocity. $Re=12 \times 10^3, 24 \times 10^3$; $S=0, 0.5$	66
42. Jet centerline Reynolds shear stress (axial-radial). $Re=12 \times 10^3, 24 \times 10^3$; $S=0, 0.5$	67
43. Jet centerline Reynolds shear stress (axial-tangential) . $Re=12 \times 10^3, 24 \times 10^3$; $S=0, 0.5$	67
44. Jet centerline Reynolds shear stress (radial-tangential). $Re=12 \times 10^3, 24 \times 10^3$; $S=0, 0.5$	68

Figure	Page
45. Instantaneous axial velocity. $Re=5.3 \times 10^3, 12 \times 10^3, 24 \times 10^3$; $S=0$	69
46. FFT power decay. Pipe flow $Re=5.3 \times 10^3$ $S=0$	70
47. FFT power decay. Pipe flow $Re=24 \times 10^3$ $S=0$	71
48. Mean axial velocity, normalized with bulk velocity (top), in wall units (bottom) $Re=5.3 \times 10^3$; $S=0$	74
49. Turbulence intensities, $Re=5.3 \times 10^3$; $S=0$	75
50. Reynolds shear stress (axial-radial) normalized with friction velocity, $Re=5.3 \times 10^3$ $S=0$	75
51. Mean axial velocity, normalized with centerline velocity (left) and with bulk velocity(right). $Re=12 \times 10^3, 24 \times 10^3$; $S=0$	76
52. RMS velocities normalized with bulk velocity. $Re=12 \times 10^3, 24 \times 10^3$; $S=0$	78
53. RMS axial velocity in wall units. $Re=12 \times 10^3, 24 \times 10^3$; $S=0$	78
54. RMS radial velocity. $Re=12 \times 10^3, 24 \times 10^3$; $S=0$	79
55. RMS tangential velocity. $Re=12 \times 10^3, 24 \times 10^3$; $S=0$	79
56. Reynolds shear stress (axial-radial) $Re=12 \times 10^3, 24 \times 10^3$; $S=0$	80
57. Mean axial velocity normalized with bulk velocity. $Re=5.3 \times 10^3$; $S=0.5, 1, 2$	82
58. Mean axial velocity normalized with centerline velocity. $Re=5.3 \times 10^3$; $S=0.5, 1,$ 2.....	82
59. Mean axial velocity in wall units. $Re=5.3 \times 10^3$; $S=0.5, 1, 2$. Rotation effects on log- layer.....	83
60. Mean tangential velocity normalized with bulk velocity, $Re=5.3 \times 10^3$; $S=0.5, 1, 2$... 84	84
61. Mean tangential velocity normalized with V_w , $Re=5.3 \times 10^3$; $S=0.5, 1, 2$	84
62. RMS Axial velocity in wall units. $Re=5.3 \times 10^3$; $S=0.5, 1, 2$	85
63. RMS radial velocity normalized with bulk velocity. $Re=5.3 \times 10^3$; $S=0.5, 1, 2$	86
64. RMS tangential velocity normalized with bulk velocity. $Re=5.3 \times 10^3$; $S=0.5, 1, 2$	86
65. Reynolds shear stress (axial-radial) normalized with friction velocity. $Re=5.3 \times 10^3$; $S=0.5, 1, 2$	87
66. Reynolds shear stress (axial-tangential) normalized with friction velocity. $Re=5.3 \times 10^3$; $S=0.5, 1, 2$	88

Figure	Page
67. Reynolds shear stress (radial-tangential) normalized with friction velocity. Re=5.3x10 ³ ; S=0.5, 1, 2.....	88
68. Mean axial velocity, normalized with centerline velocity (left) and bulk velocity (right) Re=12x10 ³ , 24x10 ³ ; S=0.5	89
69. Mean tangential velocity normalized with U _b . Re=12x10 ³ , 24x10 ³ ; S=0.5.	90
70. RMS axial velocity normalized with centerline velocity (left) and bulk velocity (right). Re=12x10 ³ , 24x10 ³ ; S=0.5	91
71. RMS radial velocity normalized with centerline velocity (left) and bulk velocity (right). Re=12x10 ³ , 24x10 ³ ; S=0.5	91
72. RMS tangential velocity normalized with centerline velocity (left) and bulk velocity (right). Re=12x10 ³ , 24x10 ³ ; S=0. 5.	92
73. Reynolds stress anisotropy invariant map showing limiting boundaries.	94
74. Reynolds stress anisotropy tensor components for pipe flow at Re=5.3x10 ³ and S=0,0.5,1,2: Effect of rotation rate.	95
75. Reynolds stress anisotropy invariant map of pipe flow Re=5.3x10 ³ and S=0, 0.5,1,2: Effect of rotation rate.	96
76. Reynolds stress anisotropy tensor components for pipe flow at Re=5.3x10 ³ , 12x10 ³ , 24x10 ³ ; S=0: Effect of Reynolds number.....	97
77. Reynolds stress anisotropy invariant map for pipe flow at Re=5.3x10 ³ , 12x10 ³ , 24x10 ³ ; S=0: Effect of Reynolds number.	97
78. Jet Centerline Axial velocity normalized with U _b	99
79. Jet profiles of axial velocity normalized with U _b . Re=24x10 ³ ; S=0.....	99
80. Jet Centerline Axial velocity normalized with U _c	101
81. Jet profiles of axial velocity normalized with U _c . Re=12x10 ³ ; S=0.	102
82. Jet profiles of axial velocity normalized with U _c . Re=24x10 ³ ; S=0.	102
83. Jet profiles of axial velocity normalized with U _b . Re=12x10 ³ ; S=0.5.....	104
84. Jet profiles of axial velocity normalized with U _b (top) and U _c (bottom). Re=24x10 ³ ; S=0.5.....	104
85. Jet half width. Re=12x10 ³ , 24x10 ³ ; S=0,0.5.....	105

Figure	Page
86. Jet profiles of mean tangential velocity normalized with V_w . $Re=12 \times 10^3$; $S=0.5$	106
87. Jet profiles of mean tangential velocity normalized with V_w . $Re=24 \times 10^3$; $S=0.5$	106
88. Axial component of turbulent intensity along the centerline.....	108
89. Profiles of axial component of turbulent intensity $Re=24 \times 10^3$; $S=0$	109
90. Profiles of axial component of turbulent intensity $Re=24 \times 10^3$; $S=0, 0.5$	109
91. Radial (w_{rms}) and tangential(v_{rms}) components of turbulent intensity along the centerline.....	111
92. Profiles of tangential component of turbulent intensity $Re=24 \times 10^3$; $S=0$	112
93. Profiles of radial (w_{rms}) and tangential (v_{rms}) turbulent intensity $Re=24 \times 10^3$; $S=0.5$	112
94. Jet Reynolds shear stress profiles (axial-tangential). $Re=24 \times 10^3$; $S=0$	114
95. Jet Reynolds shear stress profiles top-(axial-tangential), bottom-(radial- tangential), $Re=24 \times 10^3$ $S=0.5$	114
96. Anisotropy tensor components for Jet flow at $Re=12 \times 10^3, 24 \times 10^3$; $S=0,$ 0.5 at $x/D=6$	115
97. Jet flow anisotropy invariant map at $x/D=6$ for $Re=12 \times 10^3, 24 \times 10^3$; $S=0$	116
98. Jet flow anisotropy invariant map at $Re= 12 \times 10^3$; $S=0, 0.5$	117
99. Jet flow anisotropy invariant map at $Re= 24 \times 10^3$, $S=0, 0.5$	118
100. Jet inlet depicting particle injection locations. (Particles colored by particle ID)..	119
101. Global particle count within domain.....	123
102. Midplane ($z=0$) view of particles distribution at $t=2$ sec. $Re= 24 \times 10^3$; $S=0, 0.5$..	124
103. Midplane ($z=0$) contours of instantaneous axial velocity (m/s) and particles distribution at $t=2$ sec. $Re= 24 \times 10^3$; $S=0, 0.5$	125
104. Contours of instantaneous axial velocity (m/s) and particle distribution at $x/D=1,$ $t=2$ sec. $Re= 24 \times 10^3$; $S=0, 0.5$	125
105. Contours of instantaneous axial velocity (m/s) and particle distribution at $x/D=5, t=2$ sec. $Re= 24 \times 10^3$; $S=0, 0.5$	126
106. Midplane ($z=0$) contours of instantaneous spanwise vorticity (1/s) and particle distribution. $Re= 24 \times 10^3$; $S=0, 0.5$	127

Figure	Page
107. Contours of instantaneous axial vorticity (1/s) and particle distribution at $x/D=1$, $t=2\text{sec}$. $Re= 24 \times 10^3$; $S=0, 0.5$	127
108. Contours of instantaneous axial vorticity (1/s) and particle distribution at $x/D=5$, $t=2\text{sec}$. $Re= 24 \times 10^3$; $S=0, 0.5$	128
109. Average particle axial (U_p), tangential (V_p) and radial (W_p) velocities (m/s) at various downstream axial locations. $Re= 24 \times 10^3$; $S=0, 0.5$	129
110. Particle count fraction, average residence time and average radial distance at various downstream axial locations. $Re= 24 \times 10^3$; $S=0, 0.5$	130
111. Depiction of particle concentration radial count sampling interval.....	131
112. Particle concentration at $x/D=(1,2,3)$	132
113. Particle concentration at $x/D=(5,7,10)$	132
114. Average axial particle velocity, $Re=24 \times 10^3$; $S=0.5$	134
115. Average axial particle velocity, $Re=24 \times 10^3$; $S=0.5$	134
116. Average tangential velocity, $Re=24 \times 10^3$; $S=0.5$	135
117. Particle Dispersion.....	136
118. Particle trajectories.....	137

1 INTRODUCTION AND MOTIVATION

In the consideration of fluid flowing through a pipe, addition of rotation applied to the pipe about its central axis creates a tangential friction force between the inner wall surface of the rotating pipe and the flowing fluid that is in direct contact. The friction force gives the fluid flowing inside the pipe a tangential velocity component that causes the fluid to rotate along with the pipe. The magnitude of the friction force is dependent on the pipe's rotation speed, wall surface roughness, flow conditions and fluid properties. Experimental studies of axially rotating pipe flow have shown that addition of pipe rotation can have either a stabilization or destabilization effect on the flow, depending on the flow's initial conditions. If the pipe flow is initially laminar, addition of pipe rotation tends to destabilize the flow with the creation of spiral waves that allow for transition to turbulence at lower Reynolds numbers (Itoh, et al. 1992,1996). However, if the pipe flow is initially turbulent, axial rotation of the pipe tends to have a stabilizing effect that as rotation is increased, gradually transforms the mean axial turbulent velocity profile into a shape similar to the mean laminar velocity profile. This phenomena is known as 're-laminarization' or simply 'laminarization'. Experiments have also shown that addition of rotation leads to a reduction in hydraulic loss in pipe flow.

Applications that may be optimized through proper implementation of rotating-pipe-flow characteristics includes but is not limited to: fluid transport systems, turbomachinery, irrigation systems, agricultural spraying machines, heat exchangers, engines, combustion chambers, nuclear reactors and multiphase mixing systems. The inclusion of particles in rotating pipe flow is of particular interest in the use of rotational phase separators which are used to separate solid particles or liquid droplets from the fluid via centrifugal force produced by the pipe's rotation. In the oil and gas industry, rotational phase separators are important for the separation of oil/water or liquid/gas mixtures.

Fluid flow forced under pressure that is ejected out of a nozzle into surrounding fluid, otherwise known as jet flow, is present in numerous applications such as jet propulsion, fuel injection, chemical reactors, mixing devices, fountains and cooling systems. Swirling-jet flows, having a tangential velocity distribution superimposed on the

axial velocity, are found to occur in both reacting and non-reacting flows such as flow over delta wings, combustion flames, turbines and other vortex devices. When compared to non-swirling jets, experimental studies have revealed key features that distinguish swirling-jets which include: increased spread rate, enhanced fluid entrainment, and enhanced convective cooling. Swirling-jets are also known to be capable of exhibiting an interesting phenomenon known as 'vortex breakdown', which occurs at a given swirl intensity threshold. Swirl intensity is typically defined as the ratio of azimuthal to axial momentum of the swirling-jet. Although there are various definitions of what constitutes vortex breakdown, it is typically characterized by a transition of a jet-like axial velocity profile to a wake-like profile. In combustion, vortex breakdown is essential and is usually employed for the purpose of flame stabilization and improved combustion efficiency. For swirling-jets emanating from fully-developed turbulent flows in rotating pipes, Facciolo (2006) observed that with the addition of moderate swirl, a counter-rotating core about the jet's central axis develops at an approximate axial distance of six diameters from the pipe exit.

Examples of particle-laden, turbulent flows important to engineering applications include rocket plumes, propulsion devices, aerosol sprays, fluid catalytic cracking in petroleum refineries, pharmaceutical crystallizers, and particle transport systems such as pneumatic conveying systems. A crucial parameter in combustion/fuel injection is the degree of interphase mixing and particle dispersion downstream. In recent years and in the wake of post-2001 anthrax attacks, the threat of particle dispersion, as it relates to chemical and biological warfare attacks, has also raised significant interest. Both experimental and numerical research efforts have been aimed at ultimately having the ability to predict particle dispersion to have the ability to quickly and effectively capture and contain targeted particles to safely decontaminate an affected building or area. Turbulence-particle interaction as it pertains to particle dispersion is thus an important aspect in regards to particle-laden turbulent flows. In particular, the addition of particles in a turbulent, swirling jet has been found to either attenuate or enhance the fluid phase turbulence intensity with respect to its particle-free single-fluid-phase value.

Despite continuous advances in experimental techniques and computational capacity, turbulent, particle-laden, swirling jet flows still present a formidable challenge

for both experimental and numerical studies. The obvious practical relevance to investigation of turbulent rotating-pipe and particle-laden, turbulent jet flows discussed above has attracted the attention of many scholars and has fostered numerous studies. Balachandra and Eaton (2010) presented a review of particle-laden jet flows and how they could be characterized based on loading, particle sizes, Reynolds numbers, etc. However, results of studies with matching geometric boundaries, initial flow conditions and flow parameters over a wide range of Reynolds numbers and swirl rates are still limited. The scientific challenge to understanding the physical phenomenological curiosity of the aforementioned effects of adding rotation/particles to turbulent pipe/jet flows, along with their importance in practical industrial applications, provide great incentive to continue to investigate particle-laden, turbulent rotating-pipe and swirling-jet flows. The objective of this current numerical research is to examine the current viability of accurate implementation of the large-eddy simulation (LES) technique in regards to modeling turbulent, particle-laden swirling-jet flows. The present investigation has considered a swirling-jet emanating from a rotating pipe. Subsequently, particles are introduced into the swirling jet to examine the consequent particle-laden swirling-jet flows. This investigation seeks to contribute to the available database of results currently available by validating results of past studies found in the literature and providing new results based on flow parameters not yet investigated.

2 LITERATURE REVIEW

2.1 ROTATING PIPE FLOW

2.1.1 EXPERIMENTAL STUDIES

The earliest experimental study of axially-rotating, turbulent pipe flow found in the literature is that of White (1964), in which the basic characteristics and behavior of rotating pipe flow were first established. In White (1964), it was found that with addition of rotation, the pressure loss of initially turbulent pipe flow decreased significantly, as much as 40%, when compared to flow through a non-rotating pipe. White (1964) noted that a gradual deformation of the turbulent mean velocity profile into a parabolic shape similar to laminar flow occurred with the addition of rotation. Flow visualization showed that the addition of rotation to pipe flow has one of two effects: destabilization or stabilization, depending on the initial state of the flow. White (1964) and subsequent experimental studies [Kikuyama, et al. (1983), Itoh, et al. (1996)] have shown that if the pipe flow is initially laminar, rotation addition tends to have a destabilizing effect due to the large shear produced by the rotating wall in contact with the flow. If the flow is initially turbulent, however, the addition of rotation tends to have a stabilizing effect due to suppression of turbulent fluctuating components.

Kikuyama and Murakami (1980) confirmed the decrease in hydraulic loss of a rotating turbulent pipe versus a stationary one for a Reynolds number, Re , range of $10^4 < Re < 2 \times 10^5$. Using a three-hole Pitot tube, they found that after a pipe length of approximately 100 diameters downstream, the pressure loss coefficient ratio between a rotating pipe and a stationary one is governed solely by the rate of rotation. Defining the rotation rate or swirl number, S , as the ratio of the rotating wall velocity V_w , to the average bulk velocity U_b ($S = V_w / U_b$), Kikuyama and Murakami (1980) found that beyond a swirl number of $S = 1.2$, the suppression of turbulence was saturated and the decrease in loss coefficients remained unaltered. Kikuyama, et al. (1983) used hot-wire probes to examine the destabilization and stabilization effects of adding rotation to initially non-rotating pipe flows. Their experimental setup consisted of a stationary pipe section upstream followed by a rotating pipe section downstream. They studied the effects of pipe rotation on both initially laminar and fully turbulent pipe flow. Kikuyama, et al.

(1983) showed that for initially laminar flow entering the rotating pipe, the laminar boundary layer was destabilized due to the large shear caused by the rotating pipe section near the inlet region, resulting in spiral vortices that at sufficient rotation brought about bursts of turbulence that shifted the transition point from laminar to turbulent further upstream. Further downstream from the inlet region, however, Kikuyama, et al. (1983) observed that the stabilizing effect due to the centrifugal force of the tangential velocity component of the rotating pipe flow became dominant and turbulence suppression was observed. A step-ring placed prior to the inlet of the rotating pipe to trip the flow showed that rotation of the pipe suppressed the intensity of turbulence in the boundary layer. Kikuyama, et al. (1983), also showed that far downstream of the rotating pipe, the mean axial velocity turbulent profile that entered the rotating pipe gradually deformed into a parabolic profile as the rotation rate was increased, so as to resemble a laminar profile (demonstrating the phenomena known as ‘laminarization’). A follow-up study by Kikuyama, et al. (1987) showed that the reduction in turbulence level reduces the gradient of the axial velocity component at the wall, that in turn reduces the wall shear stress and increases the centerline velocity. According to their experiments, complete laminarization occurred at a swirl number of $S \sim 3.5$. Kikuyama, et al. (1987) took measurements both far downstream and throughout the rotating pipe to examine the flow profile development. For a distance downstream greater than 120 diameters from the inlet, the velocity profiles were found to be independent of axial distance. Kikuyama, et al. (1987) observed that the tangential velocity of the flow does not approach a solid-body rotation profile but instead approaches the parabolic profile $V/V_w = (r/R)^2$.

The aforementioned observations made by Kikuyama, et al. (1980, 1983, 1987) were confirmed by the associated experimental study of Reich and Beer (1989) for Reynolds numbers of $5 \times 10^4 < Re < 5 \times 10^5$. In addition to velocity profiles, Reich and Beer (1989) examined temperature distribution profiles and found that heat transfer was reduced considerably with pipe rotation, due to radially growing centrifugal forces that suppress radial turbulent migration of fluid particles. Itoh, et al. (1996) measured fully-developed turbulent flow associated with a rotating pipe at a Reynolds number of 20,000 and swirl rates ranging from $0 < S < 1$. Itoh, et al. (1996) measured mean velocity profiles, the distribution of five of the Reynolds shear stresses, and velocity fluctuations along

with their power spectra. Their results showed that turbulence intensity decreased with increasing rotation. Results showed that the Reynolds shear stresses decreased more markedly than the turbulent intensity. Itoh, et al. (1996) also verified the relation of mixing length in swirling flows and Richardson number first proposed by Bradshaw (1969).

More recently, Durst, et al. (2006) used a swirl generator made up of a 50mm diameter rotating housing and 0.5m long honeycomb formed with 4mm outer-diameter tubes. The swirl generator was positioned upstream of a stationary pipe section with a matching diameter of 50mm and length of 7m. Using laser doppler anemometry (LDA) they measured the swirl decay characteristics of the mean flow and turbulence stresses exiting the swirl generator. For the measurements in the region of $L/D=3$ and $L/D=17.3$, the mean tangential velocity in the vortex core showed a linear variation versus radial distance from the pipe centerline. Durst, et al. (2006) showed that pipe rotation significantly modifies the anisotropy of turbulence, and their measurements also verified previous DNS findings showing turbulence tends towards the isotropic two-component limit as pipe rotation increases.

2.1.2 NUMERICAL STUDIES

Although experimental studies of turbulent rotating pipe flow date back to the 1960's, numerical studies of turbulent rotating pipe and its effect on turbulent flow statistics have only been reported within the last two decades. The limited number of numerical studies is in part due to the fact that conventional two equation $k-\varepsilon$ and $k-\omega$ models that have generally been considered the working horse of CFD analysis and that have been applied with success to many practical flow applications, are not readily reliable for rotating pipe flow. It has been well known for some time that the performance of two equation models while robust and computationally efficient, offer poor results when they are used to evaluate swirling flows [Nallasamy M., (1987)]. Hirai, et al. (1988) showed that the conventional $k-\varepsilon$ model produced unrealistic results for rotating pipe flow, predicting a solid body rotation profile for the mean tangential velocity that experimental studies show should instead resemble a parabolic distribution as rotation is increased. The deviation of tangential velocity from solid body rotation in

rotating pipe flow is due to an intricate influence and interaction between the Reynolds stress components, a phenomena that standard $k-\varepsilon$ and $k-\omega$ two equation models are essentially unresponsive to and are therefore unable to predict. Hirai, et al. (1988) also showed that the standard $k-\varepsilon$ model was also incapable of predicting the correct mean axial velocity profile that results when rotation is applied. Although there have been several studies that have been devoted specifically to developing and assessing modified $k-\varepsilon$ and $k-\omega$ models to accommodate and account for rotational effects, most are typically limited to specific range of flow and boundary conditions and require input based on known flow profile characteristics that somewhat defeats the prediction purpose of a numerical model.

Thanks to the advent of computational processing capabilities in recent years, direct numerical simulation (DNS) and Large-Eddy simulation (LES) models, capable of capturing the complexities of rotating flow and Reynolds stress component interactions that were previously beyond computational limits are now computationally feasible and are steadily becoming a more prevalent tool being applied to practical engineering problems.

The first DNS and LES study of fully-developed rotating turbulent pipe flow found in the literature seems to be that of the doctoral thesis of Eggels (1994) conducted at a Reynolds number of $Re=5.3 \times 10^3$ and swirl number of $S=0.5$. Eggels (1994) investigated the influence of pipe rotation on mean flow properties and Reynolds stress components. Eggels (1994) simulation results for both DNS and LES rotating turbulent pipe flow compared well with experimental results predicting a near parabolic profile of the mean azimuthal velocity, a smaller friction coefficient (i.e. decreased hydraulic loss), an increase in mean axial velocity in the center of the pipe and a decrease in axial velocity near the wall (i.e. laminarization). In a follow up study Eggels (1994) also investigated the energy budgets of the Reynolds stresses and showed that pipe rotation leads to a decrease in turbulence intensity close to the pipe mostly attributed to a significant decrease of the streamwise turbulent component.

The DNS investigations of Orlandi and Fatica (1997) at $Re=5 \times 10^3$, considered higher rotation numbers ($S=1,2$), were not considered by Eggels (1994). The study presented instantaneous flow field data, mean velocity profiles and Reynolds stress

components. A key finding in their investigation was that changes in turbulent statistics due to rotation are due to tilting of the near wall streamwise vortical structures in the direction of applied rotation. A follow up study by Orlandi and Ebstein (2000) extended the rotation rates up to $S=10$ and presented turbulent budgets for various rotation rates. Orlandi and Fatica(1997) and Orlandi and Ebstein (2000) showed that the friction factor decreases approximately 15% when rotation increases from $S=0$ to $S=2$ but actually starts to increase upon reaching a rotation rate of $S\sim 5$ and beyond. At $S=10$ it was shown that the predicted friction factor was actually higher than the non-rotation case, $S=0$. Maintaining a constant Reynolds number as swirl number was varied, they showed that if the mean axial velocity profile is normalized with the bulk velocity U/U_b , all profiles collapse at the value of $U/U_b\sim 1.14$ at $r/R\sim 0.6$, which agrees well with experimental results. It was found that the change in the normal Reynolds stress components due to rotation are markedly reduced for the streamwise component with only a slight increase in the radial and azimuthal components. They also noted that the axial-radial (\overline{uw}) shear stress (only stress found in non-rotating pipe) decreased with rotation while the other two shear stresses, axial-tangential (\overline{uv}) and radial-tangential (\overline{vw}) increased. Orlandi and Fatica(1997) observed that beyond a swirl number of $S\sim 1$, oscillations along the pipe radius develop for the mean axial-tangential (\overline{uv}) distribution. They go on to explain that the observed oscillation behavior is due to the presence of large scale structures in the central region of the pipe found at higher rotation rates that makes it necessary to increase averaging time to obtain stable distributions.

Satake and Kunugi (2002) performed DNS simulations at similar Reynolds and swirl numbers as Orlandi and Fatica (1997) for a rotating pipe flow with uniform heat flux at the wall. Temperature distributions were calculated, and data showed a steady decrease in friction factor for increasing swirl. Similar to Orlandi and Fatica(2000), Satake and Kunugi (2002) also presented detailed turbulent budgets as well as temperature fluctuations. Their results also noted an oscillating behavior for the axial-tangential (\overline{uv}) shear stress data for high swirl number ($S>1$). Feiz, et al. (2002) and Yang (2000) conducted LES investigations at higher Reynolds numbers comparing the

dynamic and Smagorinsky subgrid scale LES models. Their results generally agreed well with previous DNS and experimental simulations.

2.2 AXISYMMETRIC JET FLOW

Because of their fundamental significance as a basic flow in the fluid mechanics scientific research community and their numerous practical and industrial applications, many experimental/numerical investigations have been devoted to the study of turbulent axisymmetric swirling jet flows. A brief review of the characteristics of a non-swirling axisymmetric jet is included first to help in assessing and distinguishing features and effects of swirl addition.

2.2.1 NON-SWIRLING JET

An axisymmetric non-swirling jet results when fluid under pressure is ejected from a circular pipe/nozzle into ambient fluid, ambient fluid considered in this study is assumed to be quiescent and of the same fluid type as the emerging jet. Upon exiting the nozzle/pipe, a thin axisymmetric circular shear layer is formed around the jet perimeter as the higher speed jet fluid attempts to slide past the lower speed ambient fluid. Due to the Kelvin-Helmholtz process (i.e. velocity difference/shear across continuous fluid), vortical structures are formed at the shear layer interface of the discharging jet. The vortical structures at the shear layer wrap ambient fluid about itself carrying turbulent jet fluid into the irrotational ambient fluid and also entrain irrotational fluid into the jet core in the process. The ring shear layer initially formed at the jet's boundary perimeter is unstable and grows rapidly with complete breakdown of initially orderly vortex motion typically occurring just a few diameters downstream. As seen in Figure 1, jet flow is typically characterized by three distinct flow regions: near, intermediate and far field.

The near field region is considered to be confined to a range of approximately $0 < x/D < 6$. Within the near field a "potential core" characterized by unchanged axial velocity and flow characteristics matching those at the nozzle/pipe exists initially very near the jet exit. The potential core begins to diminish within a diameter of the exit as the shear layer spreads outward and inward toward the centerline. Upon reaching the end of the potential core the appropriate length scale is considered to be the jet diameter, and the

frequency of the large-scale structures is referred to as the jet column mode or preferred mode. The nondimensional frequency Strouhal number, $St = fD/\bar{U}$, is used to describe the jet column mode where f is the frequency, D is the jet diameter and \bar{U} is the mean jet exit velocity. A broad range of Strouhal numbers for axisymmetric jets ($0.25 < St < 0.85$) has been reported in various studies. The intermediate field or transition region following the near field of the jet is characterized by eddy structures of various scales that interact in a non-linear fashion to entrain fluid from the ambient fluid. The eddy structures observed in the intermediate region eventually collapse leaving the jet flow fully turbulent showing as it begins to exhibit self-preserving flow characteristics in the far field.

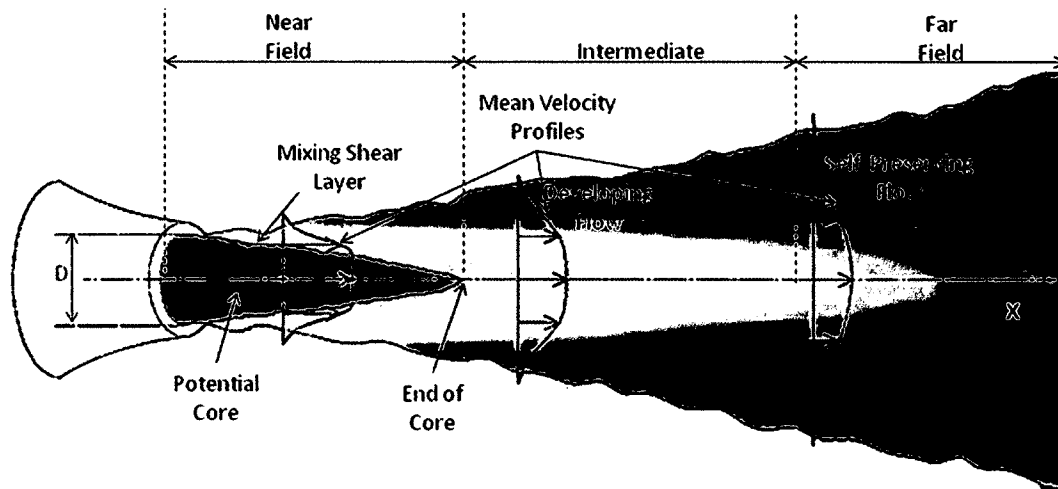


Figure 1: Axisymmetric Jet (Contours of mean velocity shown).

The far field region, characterized by 'self-preserving' or 'self-similar' flow behavior is considered to begin at an axial distance far enough downstream where initial and transient flow conditions cease to influence the jet's flow development. Self similar behavior or 'similarity' in the far field region refers to flow properties becoming invariant with axial distance when expressed in terms of local scales, typically the jet half-width. The far field region of axisymmetric jets is typically considered to begin at approximately $x \sim 20D$, the point at which the mean axial centerline velocity decay becomes inversely proportional to the axial distance as shown in Eqn. 2-1.

$$\frac{U}{U_{\max}} \approx f\left(\frac{y}{b}\right) \text{ or } f\left(\frac{r}{b}\right) \text{ where } b=(\text{const})x \quad \text{Eqn. 2-1}$$

Self-similar behavior for Reynolds stresses and higher order turbulence statistics however are generally exhibited much further downstream, with studies giving estimates of approximately $x \sim 50-70D$ diameters from the nozzle/pipe exit. The greater downstream length necessary for fluctuating components to exhibit similarity is thought to be due to the fact that energy transferred to these components is from the pressure-strain components only, unlike the axial velocity fluctuations which have transferred energy directly from the mean flow.

Experimental axisymmetric jet flow studies have typically used one of two types of boundary conditions: jet flow exiting a smooth contraction nozzle or jet flow exiting a long pipe, with the majority using the former. For a contraction nozzle, the velocity profile produced is a nearly uniform 'top hat' velocity profile whereas the velocity profile is that of a fully-developed turbulent pipe flow profile for a jet emerging from a long pipe without contraction. Several studies have shown that the near field dynamics and time-mean structure evolution of the jet is markedly different for a jet emerging from a fully-developed pipe without contraction than from a contraction nozzle [Bradshaw (1969), Hussain and Zaman (1981)]. Xu and Antonia (2002) showed that a contraction nozzle jet flow developed and reached self preservation much faster than the pipe jet. Mi, et al. (2001) experimentally studied the differences between jet flow emerging from a contraction nozzle and a long straight pipe at a Reynolds number of 16,000. Mi, et al. (2001) took scalar field measurements from 0 to 70 diameter lengths from the jet outlet. The differences observed between the two jets were attributed to the larger pipe shear layer thickness of the pipe jet and differences in turbulence structure in both the near and far fields of the two jet configurations.

Regardless of the outlet type, the near field dynamics of an axisymmetric jet are dominated by the inflectional instability mechanism in the shear layer that amplifies upstream disturbances to generate large-scale structures with shape and characteristics dependent on the Reynolds number and the type of disturbances. In the near field region

the disturbances are amplified to give rise to quasi-periodic axisymmetric rings of concentrated vorticity. The mean velocity profile and the thickness of the boundary layer at the jet exit are factors that determine the rate of amplification. As the structures move downstream they start to merge and interact to create even larger structures. This is the main mechanism by which the 'memory' of the initial stability is gradually lost. Most researchers conclude that lack of agreement observed among studies stems from the jet's instability sensitivity to upstream conditions of the experimental setup which typically varies from study to study.

Crow and Champagne (1971) were among the first investigators to recognize and study axisymmetric shear layer instabilities and their direct relation to large coherent structures. Their study showed the existence of preferred frequency modes at which an axisymmetric disturbance exhibits maximum amplification. In their study the Strouhal number measured was approximately $St=0.3$. They also noted that as the Reynolds number was increased, the observed coherent structure of the jet evolved from a sinusoid, to a helix and finally to a train of axisymmetric waves. Hussain and Zaman (1981) went on to distinguish two types of jet instabilities: the shear layer mode and the preferred mode. The shear layer mode was found to arise from the instability of the initial shear layer where the unstable frequency scales with the shear layer thickness, whereas the preferred mode is a global instability of the entire jet column where the unstable frequency scales with the jet diameter.

Ferdman, et al. (2000) investigated a jet issuing from a straight pipe as well as one with a bend at a Reynolds number of 24,000 to investigate the effects of an uniform and non-uniform initial velocity profile. In their study it was found that the initial growth of turbulence intensities was higher for uniform initial-velocity profiles. The Rayleigh light scattering (RLS) experiments of Papadopoulos and Pitts (1998,1999) studied the jets issuing from a pipe and recognized the initial turbulence intensity per unit area as the controlling parameter for the centerline mixing behavior in the near-field of constant and variable density jets.

Similar to Crow and Champagne (1971), Lai (1991) also investigated the preferred mode of a jet emerging from a fully-developed laminar and turbulent pipe for Reynolds numbers ranging from $200 < Re < 20,000$ and three pipe length/diameter ratios of

$L/D=576, 1152, \text{ and } 2304$. In this study it was found that for fully-developed laminar exit condition the Strouhal number increased with Reynolds number and approaches an asymptotic value of $St=0.5$. For fully-developed turbulent exit conditions it was found that the Strouhal number was independent of Reynolds number with a value of approximately $St=0.4$.

The effects of Reynolds number on turbulent round jets has also been a key parameter that has been experimentally investigated extensively especially for top-hat velocity profiles of jets issued from a contraction nozzle. The flow visualizations of Dimotakis, et al. (1983) showed that near a critical Reynolds number of 10^3 to 20×10^3 the mixing transition and characteristics changed dramatically for jets issued from a nozzle. The experimental PIV study of Weisgraber and Liepman(1998) at a Reynolds number of 5.5×10^3 and 16×10^3 showed that in the transitional region $15 < x/D < 30$ the development of turbulence, vorticity, flow structure, and rate of jet development was heavily influenced by the Reynolds number. At a Reynolds number of 19×10^3 , Ganapathisubramani's, et al. (2002) PIV experimental study focused on the identification and comparison of four vortex identification schemes. Ganapathisubramani, et al. (2002) showed that vortex cores formed as early as $x/D \sim 0.5$ and showed their evolution downstream led to vortex pairing up and the creation of larger-scale structures. Felluoah, et al. (2009) also investigated the effect of Reynolds number on the mixing transition of a free round jet with a top-hat velocity profile. The transition Reynolds number was found to be above 20×10^3 . Shinneeb, et al. (2008) used particle image velocimetry (PIV) and proper orthogonal decomposition (POD) to investigate large-scale structures in the near-field ($0 < x/D < 2.2$) of a jet with top-hat velocity profile and Reynolds number 21,900. At higher Reynolds numbers of 78,400, 117,600 and 156,800, the hot-wire measurements in the near field ($2 < x/D < 6$) of Jung, et al. (2004) revealed the evolution of 'volcano-type' eruptions and 'propeller-like' blade patterns near $x/D \sim 2-3$ where the number of blades diminished with downstream distance. Ball and Pollard (2008) give a complete review of these and other experimental and numerical studies performed to date on a round jet including an appendix with a tabulated list and brief description of every study.

2.2.2 SWIRLING JET

For a non-swirling jet, the near field flow is driven mainly by shear layer instabilities and turbulent mixing with pressure effects playing only a minor role in the jet's development. Swirling jet flows on the other hand are subjected to combined interactions of shear layer and centrifugal instabilities. The addition of tangential velocity superimposed on the axial velocity of an axisymmetric swirling jet generates both radial and axial pressure gradients that can significantly influence the flow evolution and interaction between vortical structures [Farokhi, et al. (1989)]. It is well known that addition of moderate swirl to a free turbulent axisymmetric jet increases jet spreading, jet width, jet decay, jet entrainment and mixing with the surrounding fluid [Chigier and Chervinsky (1967), Lilley (1977), Gupta, et al. (1984), Park and Shin (1993), Panda, et al. (1994) Liang and Maxworthy (2005), Ivanic, et al. (2003)]. Gilchrist and Naughton's (2005) study of the near field of a swirling jet showed that enhanced growth persisted up to 20 diameters downstream of the jet exit even after swirl had decayed to where it was nearly undetectable.

Most experimental swirling jet flow studies have used unique experimental setups and varying methods to generate swirl. These include rotating pipe, a rotating honeycomb, tangential injection slots, deflecting vanes, and coil inserts. The difference in geometry and swirl generation technique used for each particular experimental study is such that the initial velocity profile and other flow conditions at the jet outlet can vary considerably among experiments and can therefore significantly affect the jet development making it difficult to quantify, compare, and validate independent results. The swirl intensity is quantified by the swirl number, S , whose definition also varies from study to study. Depending on the study, swirl numbers have been defined on the basis of: geometric parameters, ratio of tangential velocity versus axial velocity, ratio of angular flux to the flux of linear momentum, Reynolds stress components, and/or various variations thereof. The swirl number, S , is defined in this current study as the ratio of the tangential velocity at the pipe wall and the mean bulk axial velocity, $S=V_w/U_b$.

The flow of swirling jets is typically characterized based on the swirl intensity. At low swirl numbers, the jet behaves similar to the non-swirling jet with only slight modifications in the mean and fluctuating velocity components as well as the spread rate

and jet width. At moderate swirl numbers, the distinguishing swirling jet characteristics such as considerable increases in jet spreading, jet width, jet decay, jet entrainment and mixing are clearly apparent. At even higher swirl numbers, an adverse axial pressure can develop and cause what is known as 'vortex breakdown', an interesting and important phenomena. Extensive experimental investigations have been carried out in regards to understanding vortex breakdown, but it still remains a phenomena without a clear unambiguous definitive explanation. Lucca-Negro and Coherty (2001) offer an extensive review of numerous vortex breakdown experimental and theoretical studies undertaken in the past 50 years. They note that prior to the 1980's experimental studies of swirling jet flow focused primarily on the measurement of the mean flow fields and turbulent stresses. During this time the main characteristics of swirling jet flow such as the displacement of the location of the maximum axial velocity from the axis, the existence of a strong reverse flow near the centerline of the jet (i.e. vortex breakdown), change in velocity components with increasing swirling jet velocity and high spreading rate were all well documented.

The first experimental investigation of turbulent swirling jets issuing from a fully-developed turbulent pipe is that of Rose (1962) in which hot-wire anemometry was used to determine radial profiles and mean velocity components as well as turbulence intensities from the pipe outlet up to approximately 15 diameters downstream. In addition Rose (1962) also measured the centerline decay of the streamwise mean velocity as well as the turbulence intensity up to 70 diameters downstream. For the flow in the rotating pipe, even after 100 pipe diameters it was noted that the mean azimuthal velocity deviated from solid body rotation which Rose(1962) figured would occur with a sufficiently longer pipe. Follow up studies such as those by Kikuyama, et al. (1983) and Itoh, et al. (1996) showed that the fully-developed rotating pipe flow exhibits a parabolic profile regardless of the pipe length.

Chigier and Chervinsky (1967) also measured mean velocity components and static pressure distribution for a wide range of swirl numbers from weak to strong swirl that included vortex breakdown. Their results showed that after about 10 diameters downstream of the jet exit the swirling motion had nearly completely vanished. Similar to Chigier and Chervinsky (1967), Pratte and Keffer (1972) measured the streamwise decay

and showed that the maximum axial and swirling velocity components varied asymptotically as x^{-1} and x^{-2} in the region beyond the initial formation region. At high swirl numbers, Chigier and Chervinsky (1967) observed that the maximum mean axial velocity shifted from the centerline outwards (vortex breakdown). After 10 diameters, however, the peak mean axial velocity value shifted back to the centerline.

In recent studies researchers have continued to study vortex breakdown and have paid particular attention to the dominant role of vortical flow structure interaction and dynamical evolution [Panda, et al.(1994), Billant, et al. (1998), Loiseleux and Chomaz (2003), Liang and Maxworthy (2005)]. The critical swirl number value, S_c , for which vortex breakdown occurs in swirling jet flow can vary significantly from study to study due to the initial conditions that depend on the type of swirl generation technique employed, variations in nozzle geometry and the definition of swirl number among studies. Studies such as Farokhi, et al. (1989) showed that the flow characteristics of a swirling jet are not only dependent on the swirl number but also depend on the initial flow velocity distribution. In their study, Farokhi, et al. (1989) observed vortex breakdown at a critical swirl number of $S_c=0.48$ for a swirling jet that had an azimuthal velocity profile in the form of a free vortex which is similar to the reported critical swirl number of $S_c=0.45$ found by Panda, et al. (1994) but is lower than the higher value of $S_c=0.6$ found by Chigier and Chervinsky (1967). In the same study, Farokhi, et al. (1989) also showed that at the same swirl number of $S=0.48$, no vortex breakdown occurred for a swirling jet with solid body rotation swirl distribution.

Billiant, et al. (1998) used a rotating honeycomb to generate a high degree of swirl with a contraction nozzle at the outlet and studied a swirling water jet at various swirl numbers and Reynolds numbers ($300 < Re < 1200$). The rotating honeycomb created an azimuthal velocity profile with solid body rotation from $r/R < 0.5$ and decreased from $0.5 < r/R < 1$. Due to the contraction used in Billiant, et al. (1998), the axial velocity was distorted with an increase near the centerline axis. Billiant, et al. (1998) found that vortex breakdown reached a well defined threshold of $S_c \sim 1.3$ to 1.4 which was found to be independent of Reynolds number and nozzle diameter used. Billiant, et al. (1998) discussed different forms of vortex breakdown that can arise with swirl. Four unique forms of vortex breakdown were identified: namely, the bubble state, an open conical

sheet state and two associated asymmetric states of these two. The latter two vortex breakdown configurations differ from the former by the presence of a stagnation point around the jet central axis in a co-rotating direction with respect to the upstream flow. Although several forms of vortex breakdown have been identified in various studies and a clear definition of what it entails is not yet established, most researchers seem to agree on the general characteristic of vortex breakdown that results in an abrupt flow transition with a free stagnation point on the axis that is followed by a reverse flow and a fully turbulent region.

Liang and Maxworthy (2005) also used a rotating honeycomb to generate high swirl but did not include a contraction nozzle at the outlet as in Billiant, et al. (1998). Liang and Maxworthy (2005) studied swirling jet flow at a Reynolds number of $Re=1000$ for swirling numbers ranging from 0 to 1.1. In their study, Liang and Maxworthy (2005) were able to classify the jet flow into four regimes: non-swirling ($S=0$), weakly swirling $0 < S < S_{c1}$ ($S_{c1}=0.6$), strongly swirling before vortex breakdown $0.6 < S < S_{c2}$ ($S_{c2}=0.88$), and stable vortex breakdown $S_c > S_{c2}$.

Among the experimental swirling jet flow studies found in the literature, Rose (1962), Pratte & Keffer (1972) Liang & Maxworthy (2005) and Facciolo (2006) are the only experimental studies found that have used a rotating pipe to generate swirl. Rose (1962) used a pipe with a length to diameter ratio $L/D=100$. Pratte and Keffer (1972) used a shorter pipe with a flow divider at the inlet to generate an azimuthal component to the flow. More recently Facciolo (2006) and Facciolo, et al. (2008) have presented experimental LES and DNS data for rotating pipe flow as well as the swirling jet at low rotation rates. An interesting observation by Facciolo (2006) was the formation of a counter rotating core that appears in the near field of the swirling jet at an axial distance of 5 to 6 diameters from the jet exit. Facciolo (2006) also observed that double mass entrainment occurs at 6D for a non-swirling jet whereas it occurs at around 4D for the swirling jet (i.e. enhanced entrainment).

2.3 PARTICLE-LADEN TURBULENT FLOWS

In the field of fluid mechanics, the study of turbulence and particle-laden/multiphase flows pose a great challenge for both experimental and numerical

investigations on their own. When the two are combined the challenge of capturing the inherently stochastic nature of the carrier fluid as well as capturing the distribution and dispersion of the particles becomes much more formidable with complex fluid-particle interactions between the fluid carrier phase and particles. Two key parameters that determine the degree of fluid-particle interactions and coupling in particle-laden flows are the ratio of the particle to fluid mass and volume, respectively defined as mass loading ($\phi_m = m_p/m_f$) and volume fraction ($\phi_v = V_p/V_f$). The simplest type of interaction is known as "one-way" coupling and is considered for very dilute particle-laden flow (i.e. low ϕ_m and ϕ_v), where the dominant effect is that of the carrier flow on the particle dynamics with the presence of the particles having little or no effect on the carrier fluid motion. In the case of one-way coupling, studies have shown that the passive particle dispersion of particles can be modeled using a simplified form of the particle equations of motion. As the particle volume fraction and mass loading increases however, the effects of the presence of particles on the fluid phase are no longer negligible, and "two-way" coupling is necessary to account for modifications in the carrier phase mean flow and turbulence characteristics. In two-way coupling the fluid phase and particle equations are thus coupled by source terms representing the inter-phase exchange of mass, momentum and energy. Turbulence modulation in this case can be attributed to two main mechanisms, gas-particle interaction and inter-particle collision that gives a redistribution of the particle fluctuating velocity that in turn imparts velocity fluctuations in the gas phase due to modification in the gas-phase Reynolds stress that controls the rate of turbulence production and dissipation. At even higher particle volume fraction, interactions between particles (particle collision, agglomeration and break up) also become important; this is typically described as "four-way" coupling [Elgobashi (1991, 1994)]. For the extreme limit of very large particle concentration the flow regime is known as "granular" in which interparticle collision is the dominant mechanism and the effect of the fluid phase becomes less important. Elgobashi and Truesdell (1992) also studied both one way and two-way coupling in a DNS study of solid particles dispersed in a homogeneous turbulent shear flow.

Most experimental research on particle-laden turbulent flows has focused mainly on measuring mean velocity and Reynolds stresses of the carrier phase as well as the

particle concentration and mean/rms velocities of the particles. Several experimental studies have investigated higher-order quantities such as the carrier-fluid turbulent dissipation rate, Lagrangian particle velocity correlations, and particle-particle and particle-fluid velocity correlations. Prior to the standard laser-Doppler anemometer (LDA) it was difficult to measure the carrier phase due to particle interference with tracer particles. With the advent of LDA, however, in which small tracer particles are used to follow the fluid motion it became a more straightforward task to distinguish the signal obtained from the movement of the larger particles in the dispersed particle phase from that of the smaller tracer particles used to measure the carrier fluid. In gas flows, tracer diameters are typically around $1\ \mu m$ whereas dispersed-phase particle diameters are typically of the order of $(10-1000)\ \mu m$.

In regards to computational investigations, two numerical approaches to calculating particle-laden turbulent flows are typically employed and are known as the Euler-Lagrange and the Euler-Euler approach. In both approaches the multiphase flow is computed at a macroscale only with the details and effects of the flow at the microscale (order of the particle diameter) incorporated through models. The Euler-Lagrange approach used in this study requires the fundamental assumption that the particles occupy a low volume fraction. In the Euler-Lagrange approach the fluid phase is treated as a continuum while the dispersed phase is solved by tracking each particle through the flow field. The effects of the fluid velocity on the surface of each particle in a large scale simulation is not currently a practical approach to resolving particle motion. Instead, a simple point particle-tracking approach is usually applied to compute the particle path from the fluid velocity field. Balachandar and Eaton (2010) provide a review of some of the latest state-of-the art experimental and computational techniques for studying turbulent dispersed multiphase flows. Balachandar and Eaton (2010) also review three important aspects of turbulent multiphase flow which include preferential concentration of particles, coupling effects of turbulence between dispersed and carrier phases, and turbulence modulation on the carrier fluid due to the presence of particles.

2.3.1 PARTICLE-LADEN SWIRLING JET FLOW

A key feature observed and studied in particle-laden turbulent flows is that of particle distribution and preferential accumulation. It is now well accepted that particle distribution is non-uniform even in isotropic turbulence. Studies have shown that heavier than fluid particles tend to avoid regions of intense vorticity, accumulating in regions of high strain rate, whereas lighter than fluid particles tend to congregate in highly vortical regions. Accurate modeling of particle dispersion in a turbulent jet is critical to industrial applications that require effective and controlled particle dispersion such as fuel combustion. The presence of particles in a turbulent jet has been found to either attenuate or enhance the fluid phase turbulence intensity with respect to its particle free single fluid phase value. Gore and Crowe (1989) and Hestroni (1989) reviewed data available in the literature for both liquid-particle and gas-particle pipe/jet flows for particles of various size, density and concentration. Gore and Crowe (1989) and Hestroni (1989) summarized turbulence modulation trends using the particle Reynolds number, Re_p defined as $Re_p = \rho_f D_p |\bar{U}_f - \bar{U}_p| / \mu_f$ where D_p , ρ_f , and μ_f are particle diameter, fluid density, and viscosity, respectively, whereas \bar{U}_f and \bar{U}_p are the streamwise mean (i.e. time-averaged) velocities of the fluid and particle, respectively. In the case of pipe flow it was concluded that turbulence intensity was attenuated in the pipe core for small particles (low Re_p) due to viscous drag force exerted on the small particles traveling with the turbulent eddies. For large particles (large Re_p), on the other hand, it was found that enhancement of turbulence was due to vortex shedding in the wake region of the larger particles which enhanced the gas-phase velocity fluctuation. Gore and Crowe (1989) went on to propose that the particle diameter to the turbulence length scale could be used as an indicator to predict either the attenuation or enhancement of turbulence.

Crowe, et al. (1989) reviewed several experimental studies of particle dispersion in free jets and mixing layers and discussed various mechanisms and models for particle dispersion in homogeneous, isotropic turbulence available in the literature. The compiled data reviewed included both liquid particle and gas-particle shear flows at a wide range of particle size, density and concentration. They were the first to propose the use of the Stokes number which is the ratio of the particle aerodynamic response time to the large-

scale vortex structure time scale of free shear flows. They point out that whereas gradient diffusion and stochastic models that are reasonably adequate for modeling particle dispersion in homogeneous turbulence, these are not applicable to particle dispersion of non-homogeneous, anisotropic flows structures found in free shear layers which must take into account fluid dynamic behavior of large-scale structures that dominate the flow. Crowe, et al. (1989) concluded that the mixing and dispersion of particles in free shear layers are dominated by the motion of large-scale structures. For a given Stokes range particles can become entrained in the rotating large-scale structures or centrifuged to the outer edges of the structures that can cause a lateral dispersion exceeding that of the fluid particle.

Longmire and Eaton's (1992) experimental investigation of lightly-loaded non-evaporating droplets dispersion in a round jet clearly showed 'preferential accumulation' for particles at a Stokes number near unity where particles concentrate largely in the high-strain -rate and low vorticity regions. Uthuppan's, et al. (1994) numerical study used various flow visualization and analysis to show the influence of large-scale vortical structures on particle dispersion. By examining particle trajectories at various injection locations as well as performing a dispersion analysis, their study showed good qualitative and quantitative description of the role of large vortex structures on particle dispersion. Three dispersion mechanisms were identified and termed that include the vortex, centrifugal and inertial mechanisms. The vortex mechanism in which particles are trapped by the vortical structures was found to be dominant of small particles with $St \leq 0.02$ which follow the behavior of tracer particles. The centrifugal mechanism identified by particle confinement towards the periphery of the vortex structure due to centrifugal action of vortex rotation that causes the particles to be flung was found to be mostly responsible for the dispersion of intermediate particles $0.02 < St < 4$. The inertial mechanism which applies to large particles in the shear region and small particles injected in the core region which are not subjected to the centrifugal motion but rather by the flow induced by the vortex motion.

Michioka and Kurose (2008) used LES to study the effects of particle size and jet swirl on particle dispersion at a Reynolds number of $Re=40 \times 10^3$ based on jet diameter and bulk velocity. Three particle sizes of 10, 100, and 500 μm with Stokes number of

$St=(2.31 \times 10^3, 0.231, 5.78)$ and Swirl rates of $S=(0, 0.29, 0.5)$ were studied. In their study it was observed that with addition of swirl, particle number density was located on the central axis for small size particles. Small size particles were observed to diffuse almost uniformly in the radial direction upon exiting the jet inlet. For larger particles, however, addition of swirl tended to shift particle outward in the upstream region due to increasing centrifugal force with increasing particle size. In the downstream region larger particles gradually migrate inward. Particle migration behavior was explained in terms of the turbulent motions where in the downstream region, turbulent motions near the central axis cause all particles inward whereas particle motions near the edges of the swirling jet inversely shift the particles outward.

Luo, et al. (2006) studied the effects of particle dispersion by turbulence transition in a three-dimensional plane jet using DNS. Their study verified dispersion characteristics of previous studies [Longmire and Eaton (1992), Uthupan, et al. (1994)] when large-scale vortex structures are dominant such as uniform dispersion for particles with small Stokes number ($St=0.01$) that closely follow the vortex motion as well as strong particle preferential concentration in the outer boundaries of the large-scale structures for particles with Stokes number of $St=1$. For larger particle sizes with Stokes number of $St=10$ and above their study showed that particles moved downstream through the vortex structure with little lateral dispersion. Luo, et al. (2008) concluded that transition of large scale vortex to small-scale turbulence causes a transition in particle dispersion not only in time but also in space. Particles with Stokes number of $St=1$ and 10 transition showed particle dispersion to go from non-uniform to uniform pattern; the changes were attributed to the characteristic time scale of vortex structures found in the flow.

3 NUMERICAL COMPUTATIONS OF TURBULENT FLOWS

Prior to advances in computational power capable of efficiently processing a large number of numerical calculations beginning in the 1980s, analysis of turbulence was limited to physical experimental measurements only. This chapter provides a brief overview of some of the typical CFD numerical techniques that, thanks to advances in computational capabilities, have now been widely used to model turbulence; namely, Direct Numerical Simulation (DNS), Reynolds Average Navier Stokes Equations (RANS), and the Large-Eddy Simulation (LES) methods are discussed. A brief discussion of their advantages and disadvantages along with a brief mathematical overview pertinent to each technique are discussed.

3.1 DIRECT NUMERICAL SIMULATION AND REYNOLDS AVERAGED NAVIER STOKES

Turbulence is usually regarded as the time-dependent chaotic behavior observed in many fluid flows. Although turbulent flows appear to be random, it is generally considered that all flows, laminar or turbulent, evolve in a deterministic manner according to the physical laws of conservation of mass, conservation of momentum and conservation of energy. Five basic variables as functions of space and time are typically necessary to determine the flow field evolution of a fluid which includes three velocity components and any two thermodynamic properties such as temperature, pressure, density, enthalpy, entropy, etc, which, once known, suffice to determine the state and hence all other properties of the fluid. Five independent equations are therefore needed. These usually include the three components of the equation of motion (conservation of momentum), the continuity equation (conservation of mass) and the energy equation. For an incompressible and temperature independent fluid the energy equation is not needed since density is taken as a known and only conservation of mass and conservation of momentum to determine the pressure along with the velocity components are needed to completely describe the fluid flow. The conservation of mass and momentum are the well known Navier-Stokes equations (NSE) which many textbooks cover in great detail and

are therefore not derived in detail here, Rather, they are only presented in their general form as given in the Fluent (2006) user manual.

Conservation of Mass:

$$\frac{\partial \rho}{\partial t} + \nabla \cdot (\rho \bar{u}) = S_m \quad \text{Eqn. 3-1}$$

Conservation of Momentum:

$$\frac{\partial}{\partial t} (\rho \bar{u}) + \nabla \cdot (\rho \bar{u} \bar{u}) = -\nabla p + \nabla \cdot (\bar{\tau}) + \rho \bar{g} + \bar{F} \quad \text{Eqn. 3-2}$$

where S_m is a source term representing mass added to the continuous phase from the dispersed second phase plus any user-defined sources, p is the static pressure, $\bar{\tau}$ is the stress tensor, $\rho \bar{g}$ is a body force due to gravity and \bar{F} is any additional external body force. The stress tensor $\bar{\tau}$ is defined as

$$\bar{\tau} = \mu \left[(\nabla \bar{u} + \nabla \bar{u}^T) - \frac{2}{3} \nabla \cdot \bar{u} I \right] \quad \text{Eqn. 3-3}$$

where I is the unit tensor and μ is the molecular velocity.

For steady laminar flows the conservation of mass and momentum equations presented above and initial boundary conditions typically suffice to resolve flow characteristics. Most flows in nature however are turbulent and are characterized by having a wide range of dynamically significant scales of motion. In theory it is possible to resolve the entire spectrum of turbulent scales by spatially and temporally discretizing the Navier-Stokes equations so as to account for even the smallest eddy scales of motion, an approach known as direct numerical simulation (DNS) in which no modeling is required. The possibility that turbulence may occur is generally measured by the flow Reynolds number, $Re = \rho LU / \mu$, which is a measure of the relative importance of fluid inertia to viscous forces. Even with the most sophisticated super-computers of today however, full resolution using the DNS approach is still not practical for most

applications at high Reynolds numbers since the cost required to resolve the entire range of scales is found to be proportional to R^3 which quickly reaches unfeasible computational limits at a large Reynolds number. A great incentive, therefore, has existed for developing turbulent models and techniques to efficiently and accurately model the effects of turbulence.

One typical approach has been to apply a process known as Reynolds averaging or the Reynolds-averaged Navier-Stokes (RANS) equation in which the idea is to attempt to obtain solutions for the average quantities instead of the instantaneous flow quantities. As the name implies, in this method the solution variables in the instantaneous Navier-Stokes equations are substituted by the averaged and fluctuating components. For the instantaneous velocity components: $\bar{u}_i = U_i + u_i$ where U_i and u_i are the mean and fluctuating velocity components ($i=1,2,3$) respectively. Assuming incompressibility and omitting gravitational and body forces, Eqn. 3-1 and Eqn. 3-2 gives:

RANS Conservation of Mass:

$$\frac{\partial \rho}{\partial t} + \frac{\partial(\rho U)}{\partial x_i} = 0 \quad \text{Eqn. 3-4}$$

RANS Conservation of Momentum:

$$\frac{\partial(\rho U_i)}{\partial t} + U_j \frac{\partial(\rho U_i)}{\partial x_j} = -\frac{\partial(P)}{\partial x_i} + \mu \nabla^2 U_i - \frac{\partial(\overline{\rho u_i u_j})}{\partial x_j} \quad \text{Eqn. 3-5}$$

In this approach the averaging process introduces unknown terms, $\overline{u_i u_j}$ known as Reynolds stresses which require an additional relation to close the system which in turn introduce even more unknowns in an unending process known as the closure problem. Various RANS models exist to resolve the Reynolds stresses and can typically be divided into two approaches: the Boussinesq hypothesis and the Reynolds stress model (RSM). In the Boussinesq hypothesis the concept of an eddy viscosity is introduced, and the process involves the use of an algebraic equation for the Reynolds stresses and requires determining the turbulent viscosity, and sometimes depending on the level of model sophistication also requires solving transport equations for determining the turbulent

kinetic energy and dissipation. The mixing length model, Spalart-Allmaras, $\kappa-\varepsilon$ (k-epsilon) and $\kappa-\omega$ (k-omega) model are typical models associated with the Boussinesq hypothesis approach. The pros of the Boussinesq hypothesis models are their relatively simplicity and robustness, but they have the drawback of not being adaptable to different flows with the same set of constants (universality) and tend to be overly diffusive. The Reynolds stress models attempt to model directly the Reynolds stresses that appear in the RANS equations and are typically mathematically more expensive with 6 additional equations. There are a lot of variants of the Boussinesq hypothesis and Reynolds Stress models that have been developed and tweaked over the years to attempt to overcome some of their apparent disadvantages. The biggest drawback to these RANS approaches seems to be the difficulty of attempting to establish an accurate relationship between transport correlations such as the Reynolds stresses and the complex flow physics that might cause them. The alternative to not having a priori averaging of the Navier-Stokes equations and keeping the equations in the form of DNS, however, is not usually a practical task. The Large-Eddy Simulation (LES) approach which can be considered to be somewhere between RANS and DNS has received much attention in recent years and has come to the forefront of turbulence flow computations.

3.2 LARGE-EDDY SIMULATION

Like DNS, LES is a method that also solves directly for instantaneous velocities. The difference, however, is that DNS resolves all length scales of turbulence and thus requires a computational domain with sufficient resolution to capture even the smallest turbulent scales. Alternatively, LES directly resolves only the larger turbulent scales (i.e. low frequency, high energy eddies) while modeling the subgrid scales (i.e. high frequency, low energy motions) is responsible for the dissipation of turbulent kinetic energy. LES seeks to take advantage of the fact that the geometry and boundary-condition-dependent larger eddies are mostly responsible for transport of momentum, energy and scalars. Small eddies tend to be more isotropic and less flow dependent which makes modeling of their independent behavior easier. In LESs, only the larger energy-carrying eddies are directly computed while the smaller eddies are modeled.

Resolving only the large energy eddies allows for the use of a much coarser mesh and larger time step size than DNS. When compared to RANS calculations however, LES still requires a substantially finer mesh and typically requires a longer flow-time to obtain stable statistics of the flow which means that the computational cost of LES is still several orders of magnitude more than RANS calculations and, thus, typically requires the use of high-performance computing and higher memory and CPU time.

The main principle of LES is the application of a low-pass filtering of the time dependent Navier-Stokes equations in either Fourier (wave-number) space or physical space to reduce the range of length scales of the solution which are directly resolved.

Eqn. 3-6 through Eqn. 3-10 are taken from the Fluent (2006) user manual. Flow structures that are smaller than the mesh size or subgrid scales that are not resolved (filtered out) are modeled, and the equivalent stress is added to the equations of motion. A filtered variable, $\hat{\phi}$, is represented by an over-carrot and is determined according to

$$\hat{\phi}(x) = \int_V \phi(x') G(x, x') dx' \quad . \quad \text{Eqn. 3-6}$$

In Fluent, the filtered scalars in the fluid domain, D , are reduced to a function that is based on the computational cell volume, V , such that

$$\hat{\phi}(x) = \frac{1}{V} \int_V \phi(x') dx', \quad x' \in v \quad , \quad \text{Eqn. 3-7}$$

and the filtered function $G(x, x')$ is given by a "tophat" filter:

$$G(x, x') \begin{cases} 1/V, & x' \in v \\ 0, & x' \text{ otherwise} \end{cases} \quad : \quad \text{Eqn. 3-8}$$

Applying the filter to the Navier-Stokes equations:

LES Conservation of Mass:

$$\frac{\partial \rho}{\partial t} + \frac{\partial(\rho \hat{u})}{\partial x_i} = 0 \quad \text{Eqn. 3-9}$$

LES Conservation of Momentum:

$$\frac{\partial(\rho \hat{u}_i)}{\partial t} + \frac{\partial(\rho \hat{u}_i \hat{u}_j)}{\partial x_j} = \frac{\partial}{\partial x_j} \left(\mu \frac{\partial \sigma_{ij}}{\partial x_j} \right) - \frac{\partial(\hat{p})}{\partial x_i} - \frac{\partial(\tau_{ij})}{\partial x_j} \quad \text{Eqn. 3-10}$$

where σ_{ij} is the stress tensor due to molecular viscosity and τ_{ij} is the subgrid-scale stress defined as:

$$\tau_{ij} \equiv \overline{\rho \hat{u}_i \hat{u}_j} - \rho \hat{u}_i \hat{u}_j \quad \text{Eqn. 3-11}$$

Similar to the Reynolds shear stresses $\overline{u_i u_j}$ that result from averaging of the Navier-Stokes equations in RANS, the subgrid-scale stresses resulting from the filtering operations in the LES model are also unknown and require modeling. Also like the RANS models, the subgrid-scale turbulence models for LES in Fluent use the Boussinesq hypothesis. The subgrid-scale model is a function of the Rate of Strain Tensor, \hat{S}_{ij} , and subgrid-scale turbulence viscosity μ_τ .

$$\tau_{ij} - \frac{1}{3} \tau_{kk} \delta_{ij} = 2 \mu_\tau \hat{S}_{ij} \quad \text{Eqn. 3-12}$$

$$\hat{S}_{ij} = \frac{1}{2} \left(\frac{\partial \hat{u}_i}{\partial x_j} + \frac{\partial \hat{u}_j}{\partial x_i} \right) \quad \text{Eqn. 3-13}$$

In this current LES study the default subgrid-scale Smagorinsky-Lilly model in Fluent first proposed by Smagorinsky (1963) was used for all simulations performed. The subgrid-scale turbulence viscosity is given by:

$$\mu_t = \rho L_s^2 |\hat{S}| \quad \text{Eqn. 3-14}$$

where $|\hat{S}| = \sqrt{2\hat{S}_{ij}\hat{S}_{ij}}$ and the mixing length, L_s , is given by $L_s = \min(\kappa d, C_s V^{1/3})$ where κ is the von Karman constant, d is the distance to the closest wall, V is the computational cell volume and C_s is the Smagorinsky constant.

Various investigators have studied and debated the accuracy and validity of the Smagorinsky constant [Germano (1991), Lilly (1992), John and Layton (2002), Chen (2006), Leveque (2007)]. It is generally accepted that the value of the Smagorinsky constant, C_s , is non-universal and varies widely depending on flow conditions. Germano, et al. (1991) discussed the findings of a number of authors who found that the constant first proposed by Smagorinsky (1963) was not necessarily constant and for various reasons varied between 0.1 and 0.23. Germano, et al. (1991) suggested the incorporation of a variable C_s to allow for flexibility and a wider spread application of the Smagorinsky turbulent viscosity calculation. This modification by Germano, et al. (1991) also resolved some of the backscatter or energy transfer from small to large scale deficiencies of the original Smagorinsky model. Lilly (1992) went on to improve on the Germano, et al. (1991) model to account for numerical instabilities. Fluent offers the option of a constant or a dynamic coefficient for the Smagorinsky constant, C_s . The constant default option in Fluent of $C_s=0.1$, which as stated in the Fluent (2006) user manual is found to yield the best results for a wide range of flows, was used in this current investigation.

4 PIPE FLOW MESH SENSITIVITY TESTS

4.1 PIPE FLOW MESH AND SIMULATION PARAMETERS

When considering the computational mesh domain boundary conditions necessary to perform simulations of fully-developed turbulent pipe flow, periodic boundary conditions are applicable, since the flow pattern of fully-developed pipe flow is periodically repeating and the pipe has a cylindrical geometry that remains constant in the axial direction. Since transient effects are not considered, periodic boundary conditions are used to efficiently compute fully-developed turbulent pipe flow conditions. The total pipe length domain used was $L=5D$. The pipe diameter in this investigation of $D=0.06m$ was chosen to match the experimental investigation of Facciolo (2006).

Temporally developing pipe-flow simulations were performed to test the sensitivity of predictions to mesh distribution. All meshes used in this investigation were created using the meshing software Gambit. A total of six pipe meshes were tested at a Reynolds number of $Re=5 \times 10^3$. The six meshes are referred to as: M100L, M200L, M256L, M256L-SF, P130C, and P200C. Cross sections of these meshes are shown in Figure 2 and 3.

The M100L, M200L, M256L meshes shown in Figure 2 were created by splitting the cross section of the pipe into 5 sub-mappable regions (dash lines show sub-mappable regions). The inner circle sub-mappable region has a radius that is half that of the total pipe radius. These meshes all have 120 equally spaced circumferential nodes around the perimeter of the pipe. The difference between the M100L, M200L, M256L meshes is the total number of axial nodes along the axial distance. The M100L mesh has 100 axial nodes along the length of the pipe. The M200L mesh has 200, and the M256L mesh has 256 axial nodes. The M256L-SF mesh shown in Figure 2b also has 256 axial nodes but was created with a paved interior so as to avoid skewed elements observed at the four interior intersection nodes of the sub-mappable regions. The P130C and P200C meshes shown in Figure 3 were created using a paved scheme throughout the pipe. These two meshes were created by first meshing the edges of the pipe perimeter and the edges of four internal concentric surfaces at $r=(0.2R, 0.4R, 0.6R, \text{ and } 0.8R)$ such that equally spaced tangential distance, Δs , between nodes was maintained. The P130C and P200C

meshes have 130 and 200 perimeter nodes respectively, and both of these meshes have 256 axial nodes.

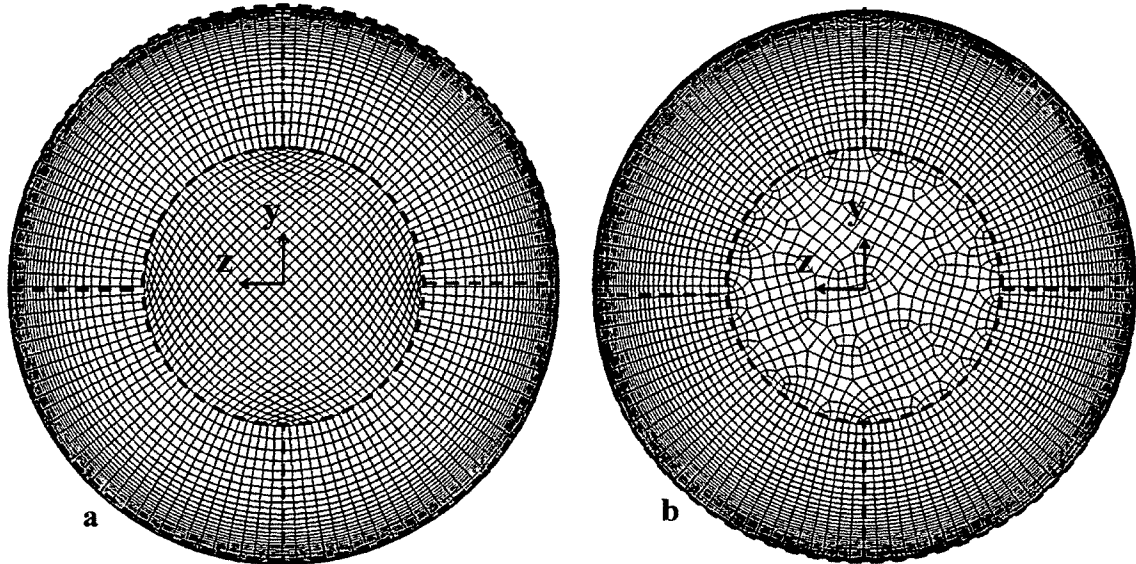


Figure 2: Pipe mesh cross sections: a. M100L, M200L, M256L b. M256L-SF.

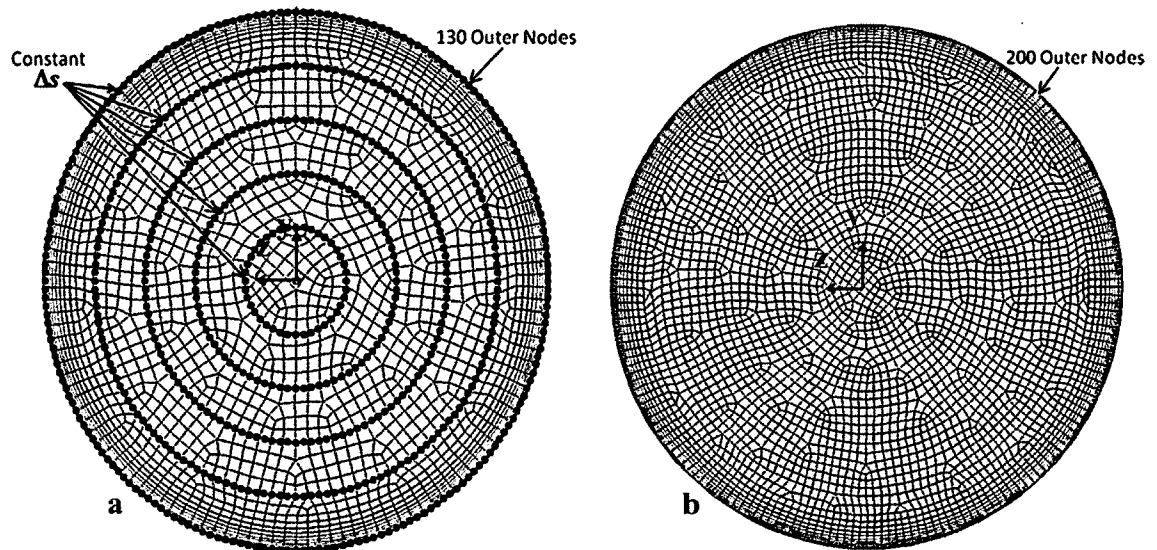


Figure 3: Pipe mesh cross sections: a. P130C b. P200C.

Table 1 summarizes the tested pipe mesh geometries and the total number of nodes in the tangential and axial direction, N_θ , and N_x respectively. The number of tangential nodes shown corresponds to the total number at the pipe wall perimeter, $r=R$ where $r=(y^2+z^2)^{1/2}$. The number of cells shown refers to the total number of calculation cells created from the nodes. All cells are hexahedral for all pipe meshes tested.

Table 1: Pipe meshes geometry and grid points summary.

	M100L	M200L	M256L	M256L-SF	P130C	P200C
L	5D	5D	5D	5D	5D	5D
$N_{\theta,(r=R)}$	120	120	120	120	130	200
N_x	100	200	256	256	256	256
Cells	4.50E+05	9.00E+05	1.31E+06	1.23E+06	6.18E+05	1.11E+06

The distance in wall units for the first 20 points measured across the center of the pipe from the pipe wall is shown in Table 2. Table 3 shows the pressure gradients prescribed across the periodic boundaries to produce flows with bulk Reynolds numbers of 5×10^3 , 12×10^3 , and 24×10^3 studied in this investigation. It should be noted that the same pressure gradient was applied when rotation was introduced. As is well known, maintaining the same pressure gradient and adding rotation to a pipe causes the bulk velocity to increase. The wall rotation rate to achieve a given desired swirl rate $S=V_w/U_b$ was thus initially set using an estimate of the non-rotating pipe bulk velocity but had to be re-adjusted a posteriori such that it accounted for the increase of bulk velocity due to the addition of rotation effects.

Table 2: Mesh comparison of distance in wall units ($Re=5 \times 10^3$, $S=0$) of the first 20 grid points from the pipe wall

Grid Point	M100L M200L M256L	M256L-SF	P130C	P200C
y_1^+	0.57	0.57	0.91	0.86
y_2^+	1.20	1.19	1.94	1.89
y_3^+	1.88	1.85	3.17	3.12
y_4^+	2.64	2.55	4.65	4.61
y_5^+	3.46	3.31	6.43	6.38
y_6^+	4.36	4.13	8.56	8.52
y_7^+	5.34	5.01	11.13	11.08
y_8^+	6.42	5.95	14.20	14.15
y_9^+	7.61	6.96	17.88	17.84
y_{10}^+	8.90	8.04	22.31	22.27
y_{11}^+	10.32	9.21	28.40	22.62
y_{12}^+	11.88	10.46	34.31	26.15
y_{13}^+	13.58	11.80	42.90	30.15
y_{14}^+	15.44	13.24	51.26	34.31
y_{15}^+	17.48	14.79	59.94	40.05
y_{16}^+	19.71	16.45	68.71	45.96
y_{17}^+	22.16	18.24	77.08	51.98
y_{18}^+	24.84	20.15	85.17	57.81
y_{19}^+	27.78	22.21	94.06	63.36
y_{20}^+	30.99	24.42	102.94	68.62

Table 3: Prescribed Pressure gradient and flow characteristics.

Re	Set Pressure Gradient (Pa/m)	U_b (m/s)	Flow Rate (m^3/s)	τ_w (Pa) Empirical	u_τ (m/s)	ε (m^2/s^3)	t^* (D/u_τ)	t_η
5.3E+03	0.661	1.290	3.65E-03	9.47E-03	8.79E-02	6.96E-01	6.83E-01	4.58E-03
1.2E+04	2.711	2.921	8.26E-03	3.96E-02	1.80E-01	6.47E+00	3.34E-01	1.50E-03
2.4E+04	9.120	5.843	1.65E-02	1.33E-01	3.30E-01	4.35E+01	1.82E-01	5.79E-04

The characteristic timescale, t^* , is defined as,

$$t^* = \frac{D}{U_\tau} \quad \text{Eqn. 4-1}$$

$$\text{where: } U_\tau = \left(\frac{\tau_w}{\rho} \right)^{1/2} \quad (\text{Friction velocity}) \quad \text{Eqn. 4-2}$$

$$\tau_w \approx 0.0396 \rho^{3/4} U_b^{7/4} \mu^{1/4} D^{-1/4} \quad (\text{Empirical wall shear stress}). \quad \text{Eqn. 4-3}$$

According to Eggels(1996), at a Reynolds number of 5.3×10^3 the Kolmogorov timescale t_η , is related to t^* , as $t_\eta = 0.0068 t^*$. This value of $4.64 \times 10^{-3} \text{ s}$ compares well with the current simulation value of 4.58×10^{-3} calculated based on the dissipation rate, ε , obtained from dimensional analysis. From Eqn. 4-4, ε is a function of the prescribed pressure gradient at the periodic boundaries, the bulk flow velocity, the volumetric flowrate and mass flowrate.

$$\varepsilon = P U_b \dot{Q} m^{-1} = \left(\frac{\text{kg}}{\text{m}^2 \text{s}^2} \right) \left(\frac{\text{m}}{\text{s}} \right) \left(\frac{\text{m}^3}{\text{s}} \right) \left(\frac{\text{s}}{\text{kg}} \right) = \left(\frac{\text{m}^2}{\text{s}^3} \right) \quad \text{Eqn. 4-4}$$

The Kolmogorov timescale, t_η , and length scale, η , are given as:

$$t_\eta = \left(\frac{\nu}{\varepsilon} \right)^{1/2} \quad \text{Eqn. 4-5}$$

$$\eta = \left(\frac{\nu^{3/4}}{\varepsilon^{1/4}} \right) \quad \text{Eqn. 4-6}$$

The characteristic timescale based on the friction velocity found at the Reynolds number tested is shown in Table 4.

Table 4: Friction velocity, characteristic timescale, and Kolmogorov timescale.

Re	U_τ (m/s)	t^* (s)	t_η (s)
5.3×10^3	0.083	0.723	0.0049
12×10^3	0.18	0.333	0.0023
24×10^3	0.33	0.182	0.0012

A conservative time step of $\Delta t = 0.0001s$, well below the Kolmogorov timescale at the highest Reynolds number of 24×10^3 , was chosen for all simulations performed. Standard procedures according to Fluent (2006) guidelines were followed in setting up and executing all simulations. The flow within the pipe domain was initialized with a laminar parabolic profile with the desired bulk velocity. The standard $k-\varepsilon$ model was then used to attain a turbulent profile solution. Once the $k-\varepsilon$ model converged, synthetic turbulence perturbations were added to the flow field and the standard LES model using the non-iterative time advancement scheme was started. All subsequent LES simulations were initialized using instantaneous LES flow fields of previous runs.

4.2 PIPE FLOW: $Re=5.3 \times 10^3$; $S=0$

Data sampling within FLUENT was enabled to collect statistical quantities throughout each simulation. Sampling for data averaging was reset every 5 second interval (50,000 time steps, $\Delta t = 0.0001sec$). One million time steps for a total of 100 seconds of flow data collection was performed for the non-rotating pipe trials for all meshes at $Re=5.3 \times 10^3$, $S=0$. As shown in Figure 4, statistics were collected at 5 axial distances, $x=(0, L/3, L/2, 2L/3 \text{ and } L)$, in both the y-axis and z-axis directions along the pipe's center cross section. For non rotating pipe flow simulations at $Re=5.3 \times 10^3$, statistics were gathered and plotted for the following quantities: Mean axial velocity, RMS axial, radial, and tangential velocity, Reynolds shear stress, RMS Pressure, and mean pressure. The average bulk velocity was calculated using the mean axial velocity profile integrated over the pipe's volume.

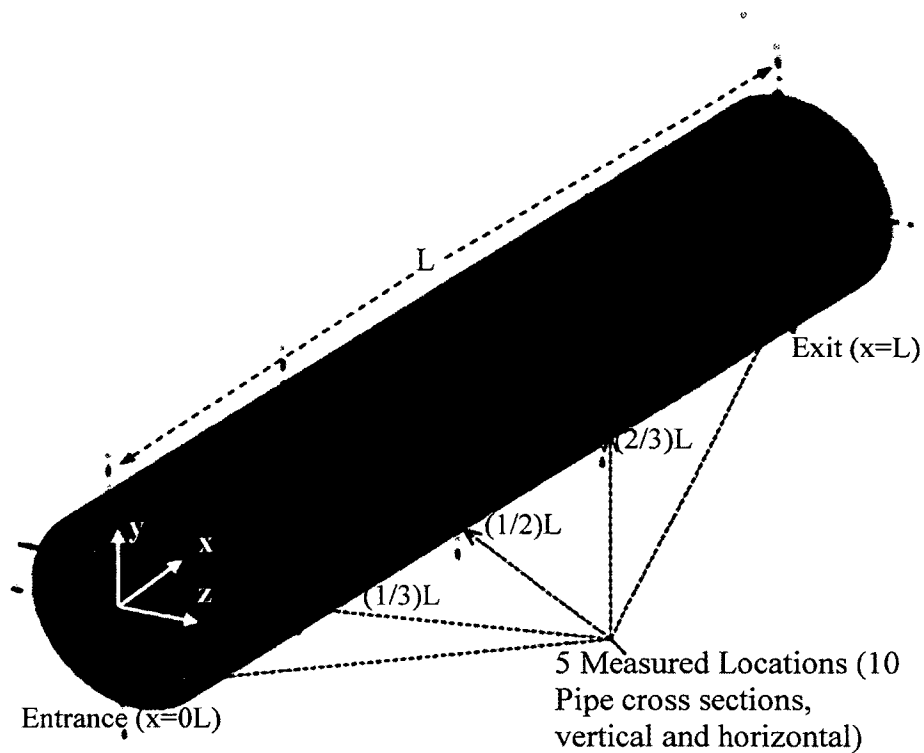


Figure 4: Pipe flow simulation data collection locations, 10 total. (5 axial distances in both Y and Z directions).

The first 10seconds (10^5 time steps) of data are omitted when computing the statistical averages. Figure 5 shows the temporal average at all measured locations as well as the overall temporal and spatial average for the mean axial velocity for mesh P130C. Note that the radial length notation r , where $r=(y^2+z^2)^{1/2}$, is used hereafter to denote the distance from the center-line of the pipe.

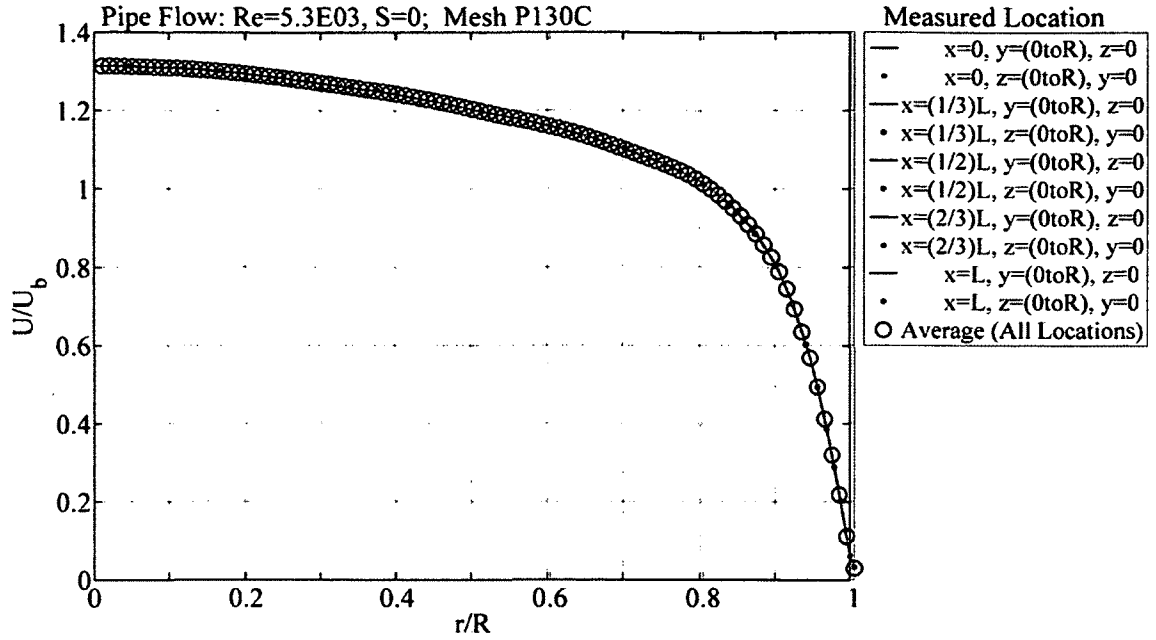


Figure 5: Mean axial velocity average at each measured location (temporal) and overall average for all locations (Mesh P130C).

The overall mesh average and standard deviation values of bulk velocity are shown in Figure 6. The average pipe wall shear stress, τ_w , is shown in Figure 7.

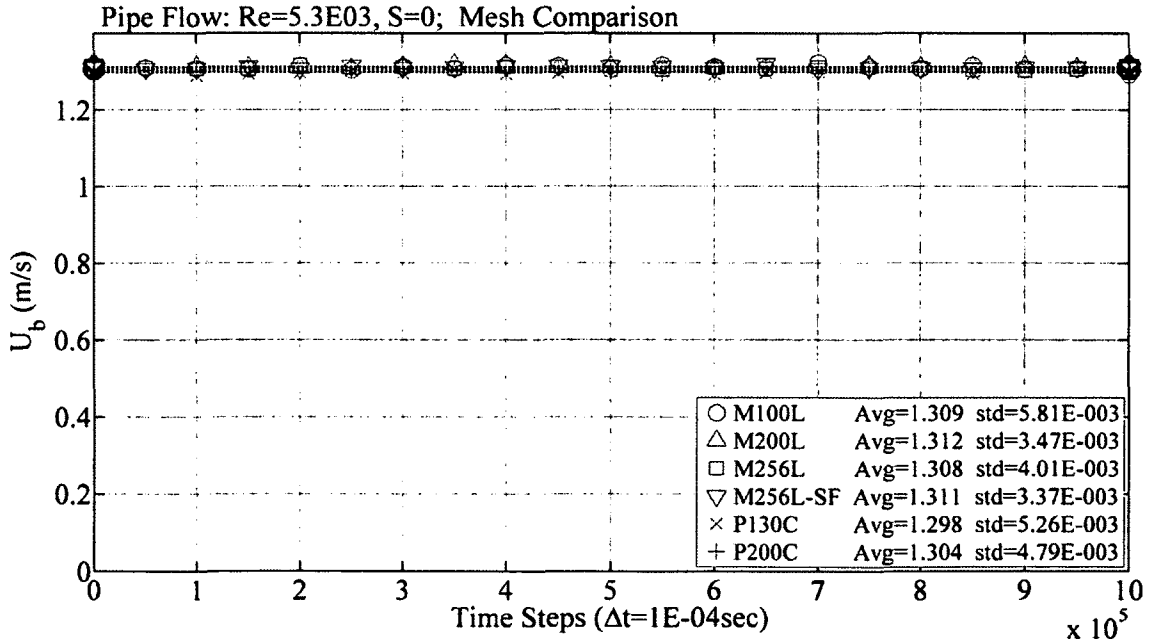


Figure 6: Average bulk velocity mesh comparison. $Re=5.3 \times 10^3$; $S=0$.

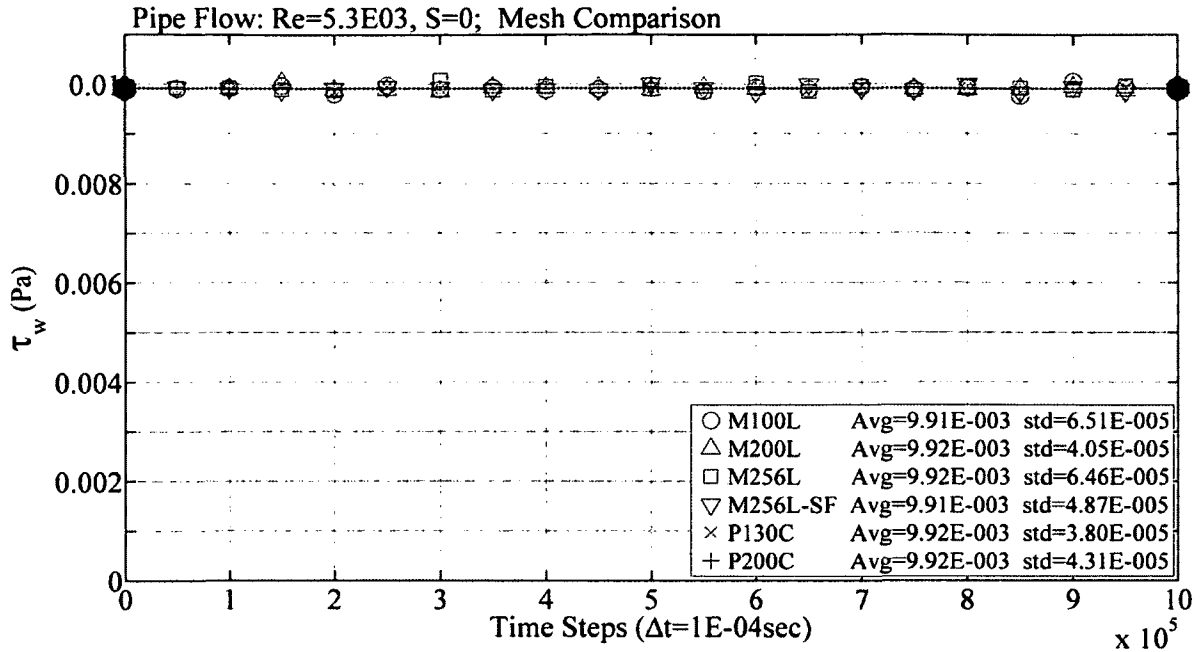


Figure 7: Average pipe wall shear stress. $Re=5.3 \times 10^3$; $S=0$.

Table 5 summarizes the overall bulk velocity and wall shear averages found for each mesh simulation tested at $Re=5.3 \times 10^3$, $S=0$. Shown along with the average simulation shear stress is the empirical shear stress calculated using the simulation average bulk velocity. With regards to the percent difference between the shear stress obtained from the simulations and that of the empirical formulation, Eqn. 4-3 shows that the latter is consistently slightly larger by approximately 1-3%. Therefore, all meshes give reasonable prediction of these averaged stress quantities.

Table 5: Pipe Flow: $Re=5.3 \times 10^3$, $S=0$. Average bulk velocity/wall shear grid comparison.

	M100L	M200L	M256L	M256L_SF	P130C	P200C
U_b (m/s)	1.309	1.312	1.308	1.311	1.298	1.304
Re	5377	5389	5373	5384	5333	5355
Simulation τ_{w1} (Pa)	9.91E-03	9.92E-03	9.92E-03	9.91E-03	9.91E-03	9.92E-03
Empirical τ_{w2} (Pa)	9.71E-03	9.75E-03	9.69E-03	9.73E-03	9.57E-03	9.64E-03
%Diff ($\tau_{w1}-\tau_{w2}$)	2.062	1.738	2.273	1.841	3.470	2.826

Figure 8 shows that for non-rotating pipe flow at $Re=5.3 \times 10^3$ there is negligible variation in the mean axial velocity profile found among all meshes tested.

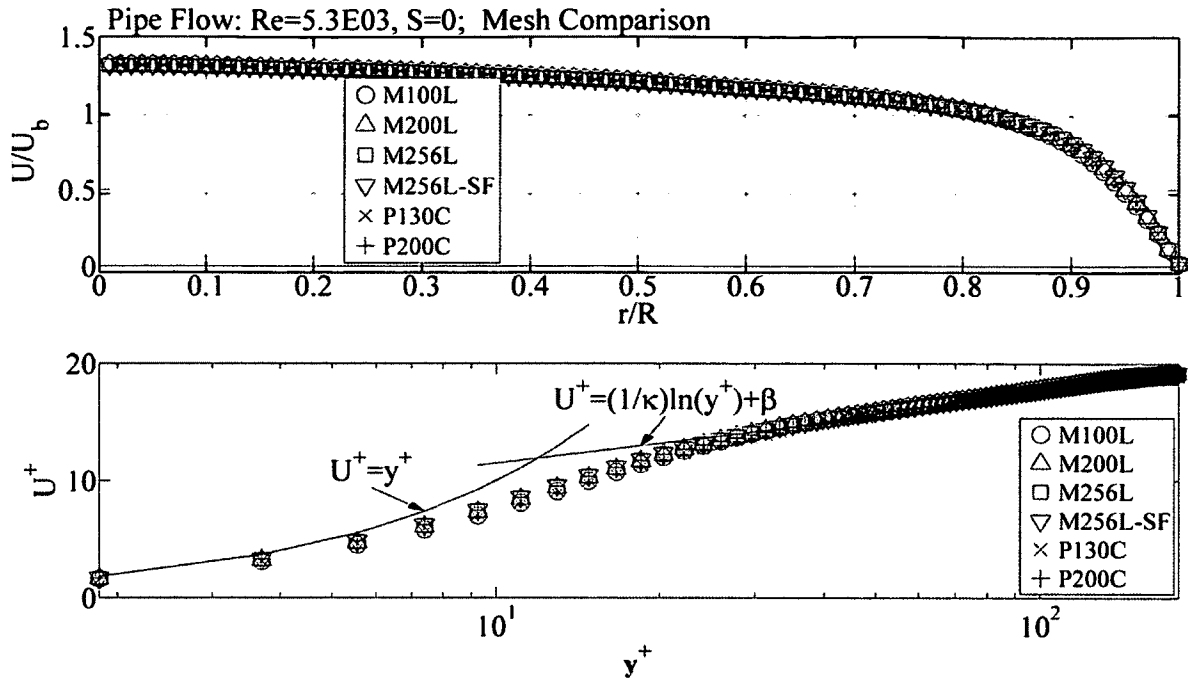


Figure 8: Average mean axial velocity normalized with bulk velocity U_b (top) and in wall units (bottom). $Re=5.3 \times 10^3$; $S=0$. ($\kappa = 0.41$, $\beta = 0.59$).

Figure 9 and 10 also show little variation in the turbulent intensity and axial-radial Reynolds shear stress profiles among the meshes tested with only the coarser mesh M100L showing slightly higher values for the axial turbulence intensity than the rest of the meshes from approximately $0.7 < r/R < 0.9$ with a slight shift in the peak magnitude further away from the wall. Conversely, the radial and tangential turbulent intensity appear to be lower for the M100L mesh. This seems to agree well with the observation made in Wu and Moin (2008): "in coarse DNS or LES calculations the streamwise component of turbulence intensity is amplified, whereas the other components are lower than those in resolved calculations." As pointed out in Wu and Moin (2008), this was the case in the coarser DNS simulation of Eggels, et al. (1994) although the effect for the radial turbulent intensity and axial-radial shear stress seems to be slightly more amplified for the current simulations.

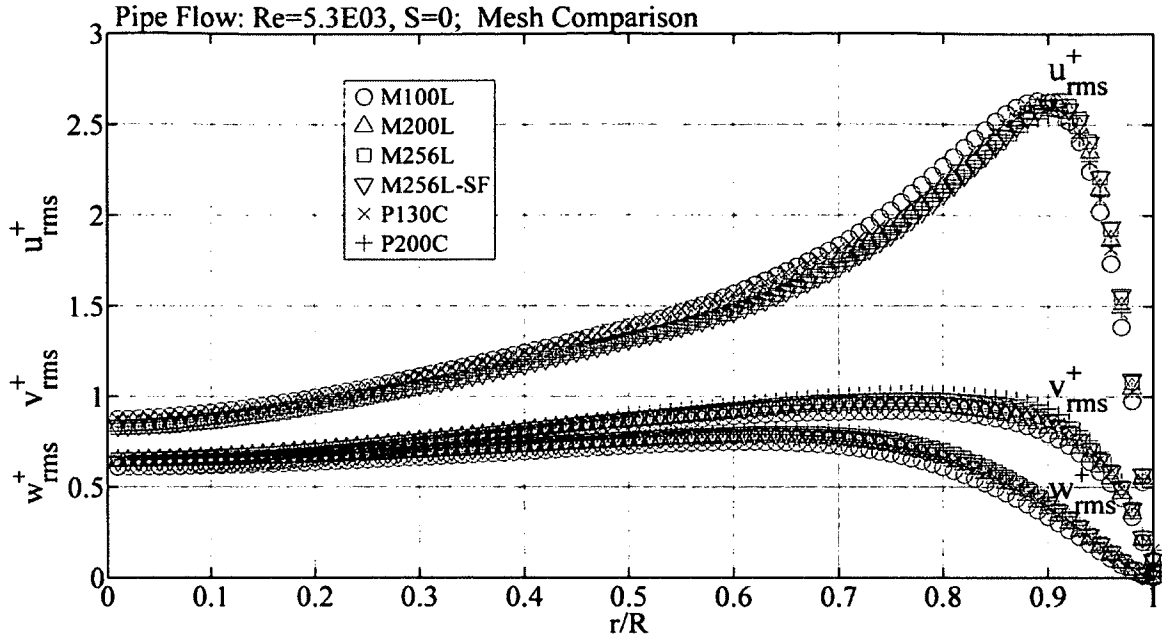


Figure 9: RMS turbulence intensities in wall units. $Re=5.3 \times 10^3$; $S=0$.

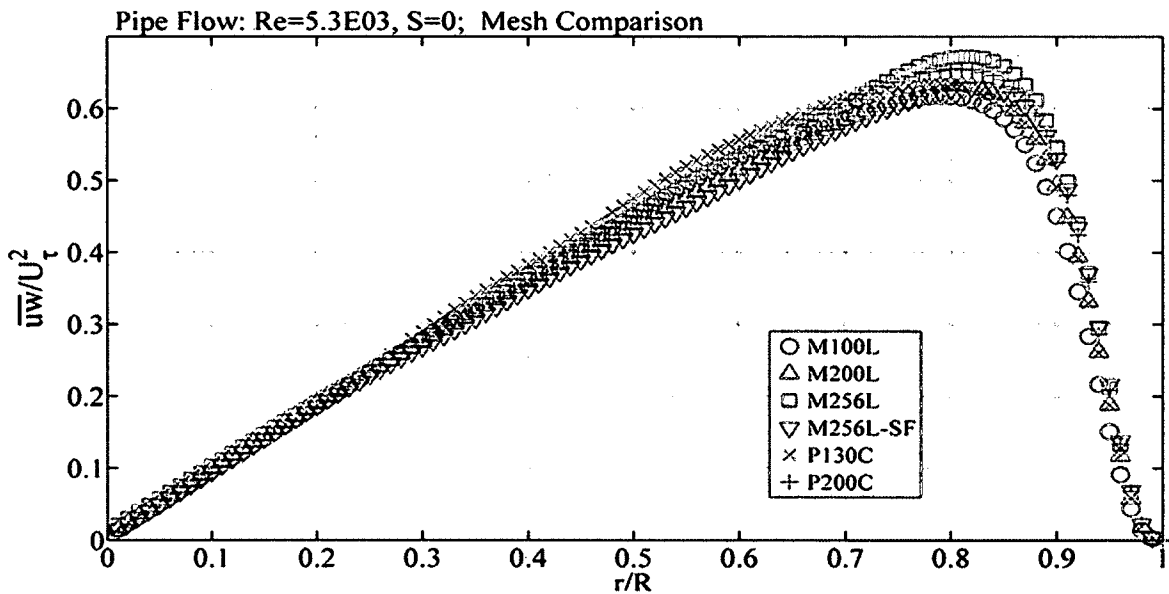


Figure 10: Reynolds shear stress (axial-radial) normalized with friction velocity. $Re=5.3 \times 10^3$; $S=0$.

Figure 11 shows only slight variation in the mean pressure profile for each mesh, except right near the wall for the M100L mesh and P200C mesh with the former under predicting and the latter over predicting. The rms-pressure values in Figure 12, on the other hand, do show a trend that appears to be dependent on the type of mesh. The two

un-mapped P130C and P200C meshes result in larger values, almost throughout the pipe cross-section than all other sub-mappable (M100L, M200L, M256L) meshes tested. Comparing the sub-mappable meshes, the coarser meshes (M100L, M200L) seem to give slightly lower values. These results suggest that the M100L mesh may not be sufficiently fine.

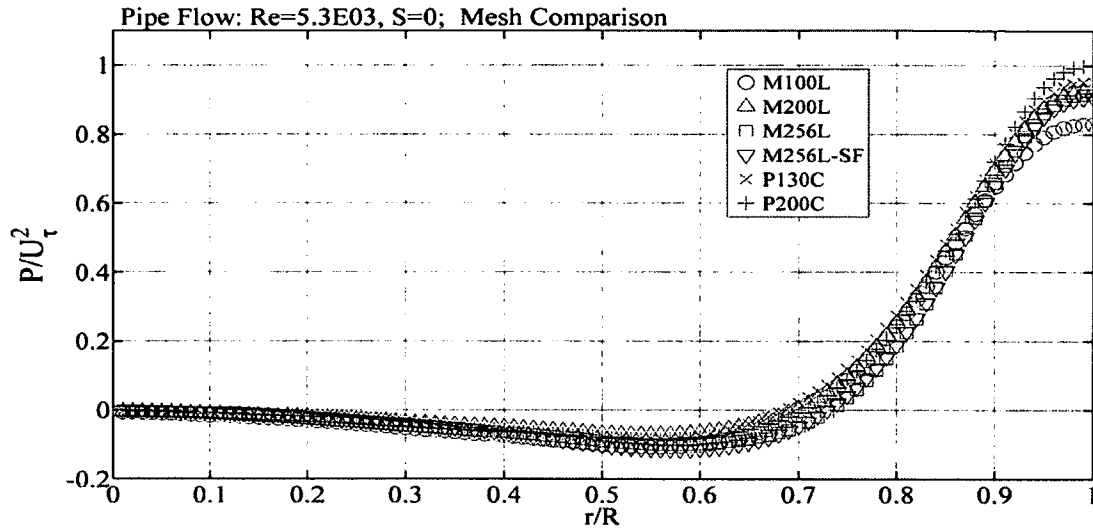


Figure 11: Mean Pressure normalized with friction velocity. $Re=5.3 \times 10^3$; $S=0$.

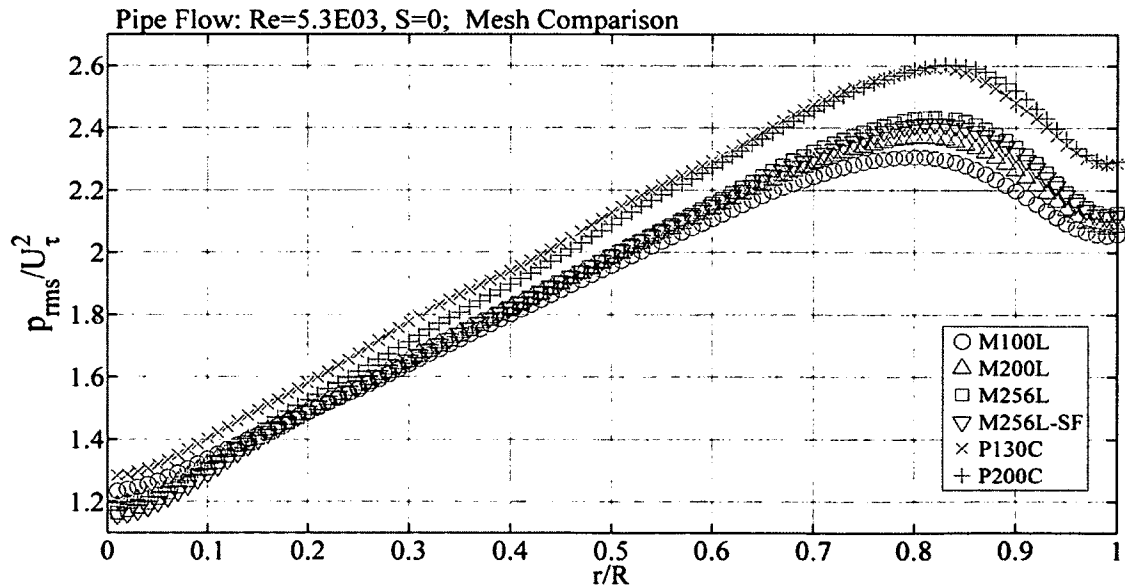


Figure 12: RMS Pressure normalized with friction velocity. $Re=5.3 \times 10^3$; $S=0$.

4.3 PIPE FLOW: $Re=5.3 \times 10^3$; $S=0.5, 1, 2$

For simulations of rotating pipe flow at $Re=5.3 \times 10^3$, meshes M100L, M200L, P130C, and P200C were used with rotation rates of $S=V_w/U_b=(0.5, 1, \text{ and } 2)$ chosen to match those investigated by the DNS study of Orlandi and Fatica (1997), which were performed at a Reynolds number of $Re=5.0 \times 10^3$. Not all meshes were tested for all rotation rates. Shown below in Table 6 is a comparison of the results of the centerline velocities, normalized with bulk velocity for the current simulations and for those of the DNS study of Orlandi and Fatica (1997) hereafter designated OF and experimental results of Reich and Beer (1989) hereafter designated as RB. Current results for all meshes tested show overall good agreement with both sets of data.

Table 6: Centerline Velocity normalized with bulk velocity ($Re=5.3 \times 10^3$). Orlandi and Fatica (1997, $Re=5.0^3$) (OF) and Reich and Beer (1989) (RB).

S	M100L U_{cl}/U_b	M200L U_{cl}/U_b	P130C U_{cl}/U_b	P200C U_{cl}/U_b	OF U_{cl}/U_b	RB U_{cl}/U_b
0	1.318	1.315	1.314	1.316	1.306	1.270
0.5	1.412	N/A	1.405	1.405	1.440	1.350
1	N/A	1.502	1.505	N/A	1.503	1.457
2	1.701	N/A	1.658	1.621	1.660	1.689

Following Orlandi and Fatica (1997), if we introduce $U = u/U_{CL}$, the shape factor H can be determined as $H = \int (1-U) dr / \int U(1-U) dr$. The shape factor represents the ratio of the displacement thickness and momentum thickness that can be used to determine the nature of the flow. A value of 1.3-1.4 is typical for turbulent flows. A value of 2.6 is typical for laminar flows. Table 7 shows that the shape factor calculated in the current simulations also match well with those of Orlandi and Fatica (1997) and Murakami and Kikuyama (1987) hereafter designated as MK. The increase in the shape factor indicates that with increasing rotation there is a tendency towards laminar flow.

Table 7: Pipe Flow: $Re=5.3 \times 10^3$, $S=(0.5,1,2)$ shape factor Coefficient in the present simulations and in Orlandi and Fatica (1997) (OF) and Murakami and Kikuyama (1987) (MK).

S	M100L <i>H</i>	M200L <i>H</i>	P130C <i>H</i>	P200C <i>H</i>	OF <i>H</i>	MK <i>H</i>
0	1.658	1.628	1.628	1.610	1.637	1.625
0.5	1.672	N/A	1.692	1.672	1.747	1.687
1	N/A	1.691	1.721	N/A	1.771	1.812
2	1.855	N/A	1.854	1.813	1.913	1.969

Figure 13 and 14 show the ratio of the mean axial velocity to the bulk velocity and centerline velocity, respectively, at all rotation rates. It can be seen that nearly perfect agreement among all meshes is found for the lower rotation rates of $S=0.5$ and $S=1$. At the higher rotation rate of $S=2$, however, there is a clear difference among the three meshes tested at this rotation rate. Mesh P200C gives a lower peak value than the coarser meshes, M100L and P130Cs. As expected, with increased rotation rate the velocity profile exhibits a more parabolic shape with the central region peak increasing and a decrease near the wall (suggesting laminarization).

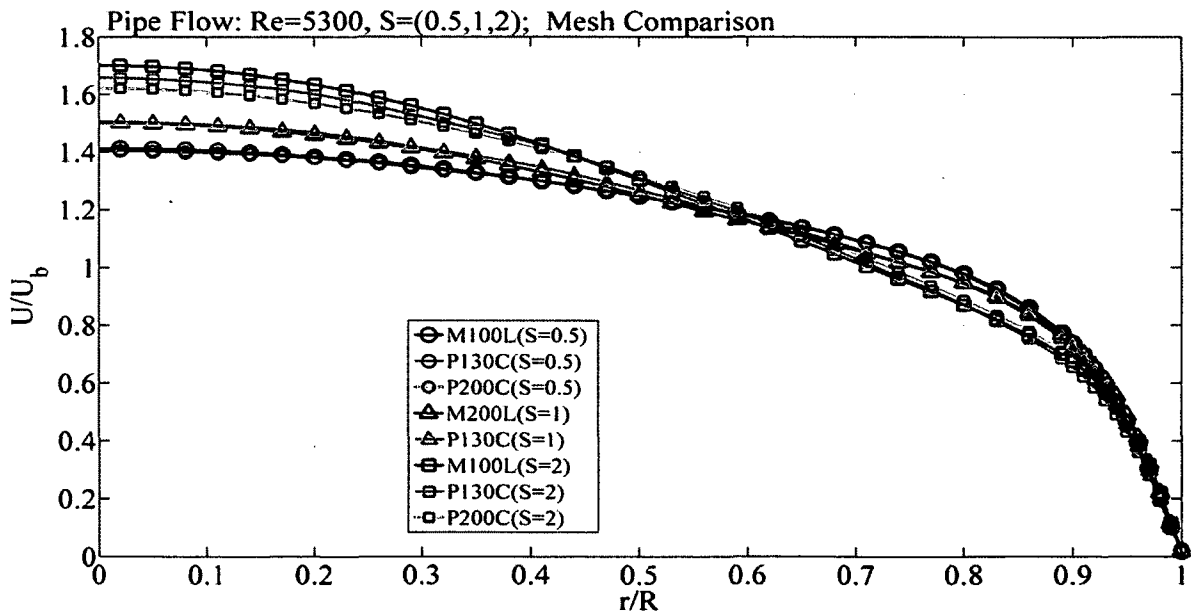


Figure 13: Mean axial velocity normalized with bulk velocity U_b . $Re=5.3 \times 10^3$; $S=0.5, 1, 2$.

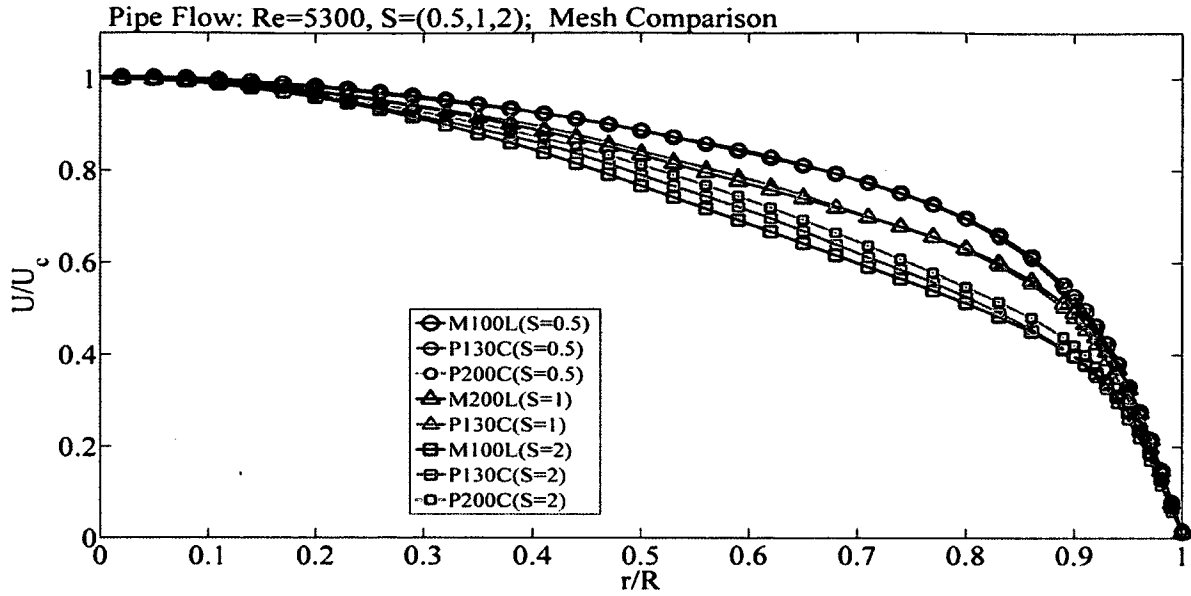


Figure 14: Mean axial velocity normalized with centerline velocity U_c . $Re=5.3 \times 10^3$; $S=0.5, 1, 2$.

The ratio of mean tangential to bulk velocity and wall velocity is shown in Figure 15 and 16, respectively. Little difference in mean tangential velocity is observed among the meshes tested except at the highest swirl rate of $S=2$.

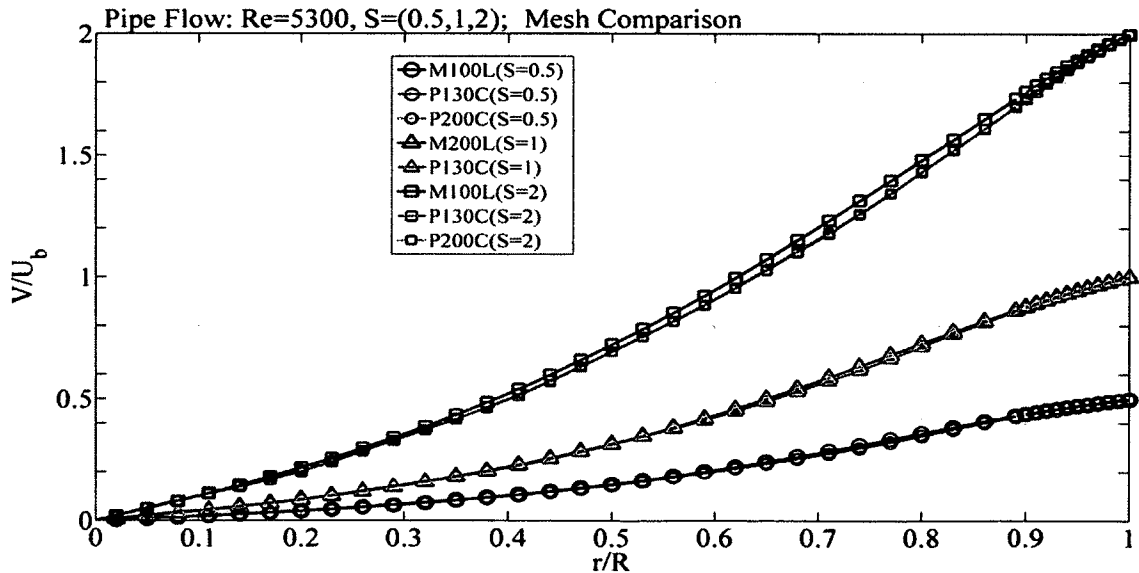


Figure 15: Mean tangential velocity normalized with bulk velocity U_b . $Re=5.3 \times 10^3$; $S=0.5, 1, 2$.

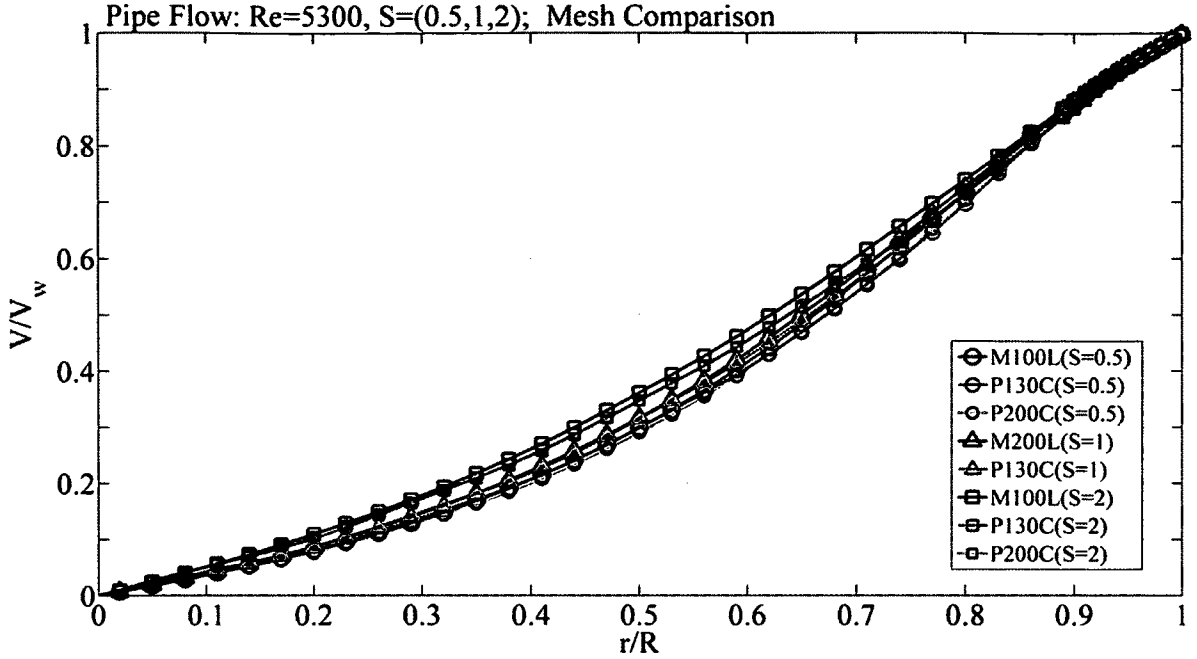


Figure 16: Mean tangential velocity ratio normalized with pipe wall velocity V_w , $Re=5.3 \times 10^3$; $S=0.5, 1, 2$.

4.4 PIPE FLOW: $Re=12 \times 10^3, 24 \times 10^3$; $S=0, 0.5$

For simulations at Reynolds numbers of $Re=2 \times 10^3, 24 \times 10^3$ only the M256L-SF, P130C, and P200C meshes were investigated. Simulations at these higher Reynolds numbers were performed for $S=0$ and $S=0.5$ rotation. The same time-step of $\Delta t = 1 \times 10^{-4}$ seconds, as the $Re=5.3 \times 10^3$ simulations is used, but this time unsteady statistics were reset every 1,000 iterations instead of every 5,000 previously.

For pipe flow without rotation, Figure 17 shows that the predicted bulk velocity for the M256L-SF mesh is only slightly higher (<3%) at both Reynolds numbers than those for the P130C and P200C meshes. With rotation, however, the predicted bulk velocity for the M256L-SF mesh is slightly lower (<2%) at both Reynolds numbers. With the addition of rotation it can be seen that the bulk velocity increases significantly by approximately 11% for all meshes tested at both Reynolds numbers when compared to non-rotating pipe flow cases.

Initially, the wall rotation rates, V_w , were chosen based on the lower non-rotating bulk velocity results found such that, $V_w = 0.5 U_{b,(S=0)}$. The significant increase in bulk velocity due to the prescribed wall rotation was such that the actual swirl rate observed

was well below the desired swirl rate, $S < 0.5$, with $S = V_w / U_{b,rotation}$ approximately equal to 0.4. The wall rotation rates were re-adjusted a posteriori to account for the increase in bulk velocity observed to achieve a true value of $S = V_w / U_{b,rotation} = 0.5$. The final wall rotation rates for all three meshes tested were set to $V_w = 55 \text{ Rad/sec}$ and 110 Rad/sec for $Re = 12 \times 10^3$ and $Re = 24 \times 10^3$ respectively to produce the desired rotation rate of $S = 0.5$ for all meshes tested.

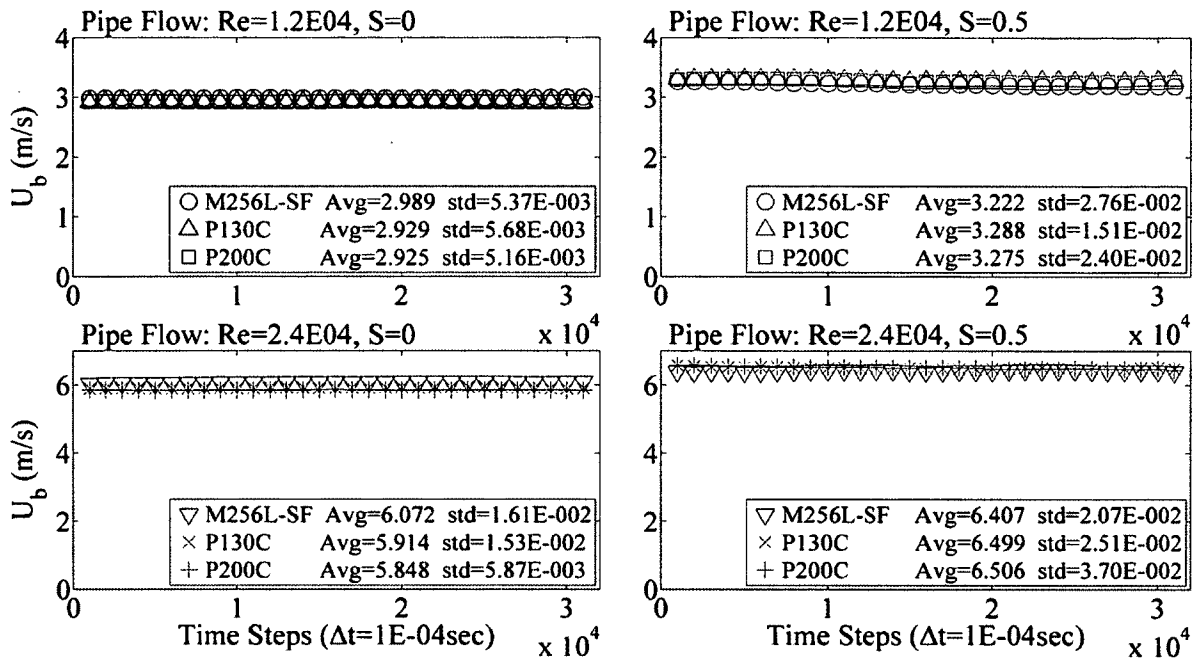


Figure 17: Average bulk velocity (1,000 time step samples). $Re = 12 \times 10^3, 24 \times 10^3$; $S = 0, 0.5$.

The pressure loss coefficient C_p is given by:

$$C_p = \frac{\Delta P}{\frac{1}{2} \rho U_b^2} \quad \text{Eqn. 4-7}$$

where ΔP is the pressure gradient as given in Table 3. The decrease in C_p at a constant pressure gradient associated to an increase in bulk velocity due to addition of rotation is shown in Figure 18. The decrease in pressure loss from $S = 0$ to $S = 0.5$ was approximately

9% at $Re=5.3 \times 10^3$ and approximately 20% for the two higher Reynolds number of $Re=12 \times 10^3$ and 24×10^3 .

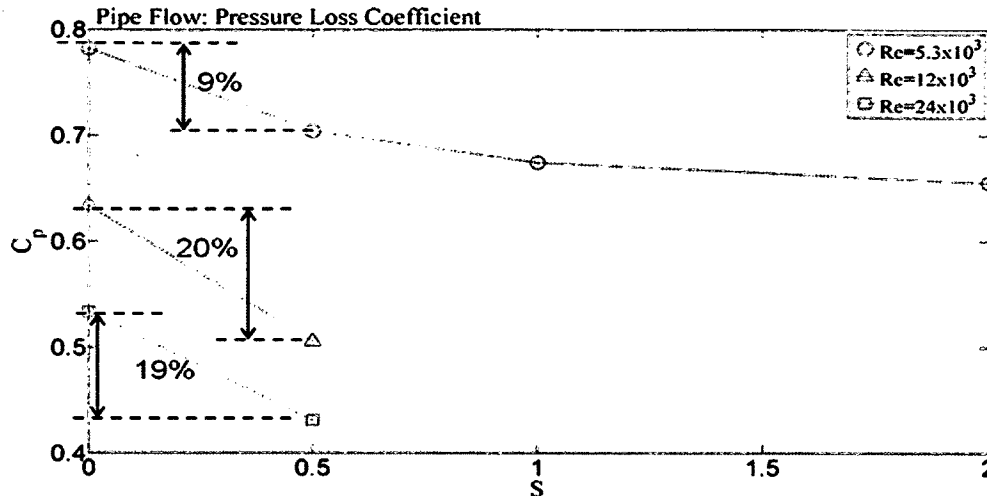


Figure 18: Pressure loss coefficient. $Re=5.3 \times 10^3$, 12×10^3 , 24×10^3 : Effect due to pipe rotation.

Figure 19, showing little variation, is observed in the computed wall shear stresses among the three meshes tested, which is to be expected since the same pressure gradients applied to the non-rotating cases (see Table 3) of 2.71 and 9.12 Pa/m respectively were maintained with addition of rotation.

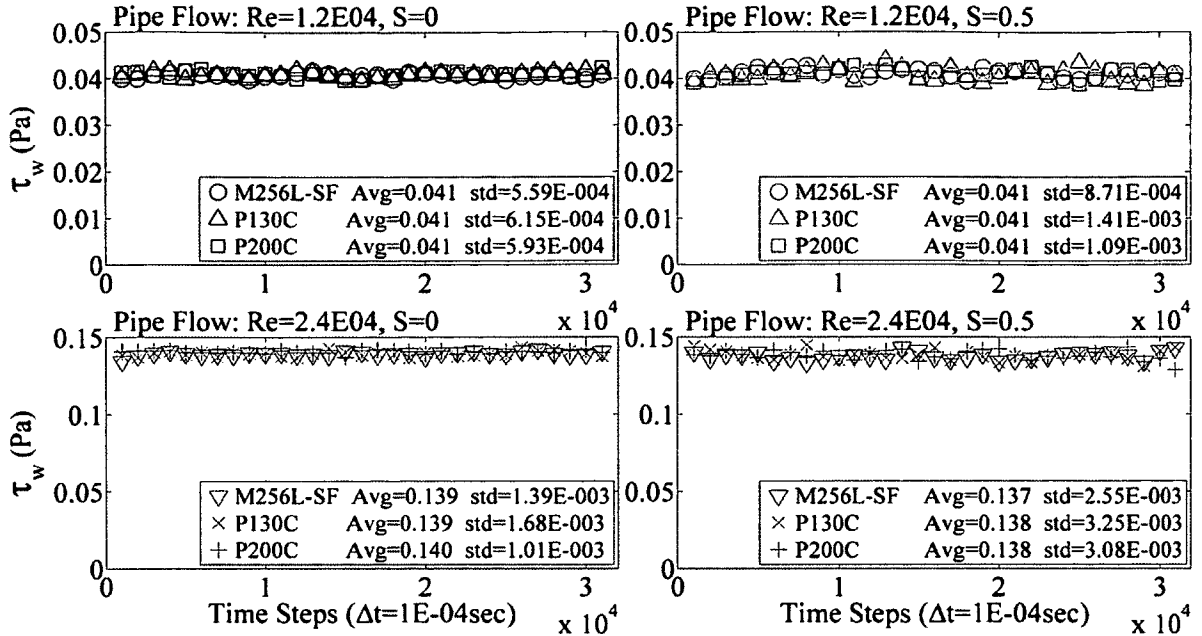


Figure 19: Average wall shear (1,000 time step samples). $Re=12 \times 10^3, 24 \times 10^3$; $S=0, 0.5$.

The mean axial velocity profiles normalized with the bulk velocity are shown in Figure 20. No significant difference in mean axial velocity is observed among the meshes tested. When normalized with bulk velocity it is seen that the velocity profile at the higher Reynolds number of $Re=24 \times 10^3$ shows a slightly flatter (more fully turbulent) profile at the pipe center for all meshes when compared to $Re=12 \times 10^3$. As expected, the addition of rotation tends to deform the velocity profile to a more parabolic profile with a higher central region velocity. When the mean axial velocities are normalized in wall units and compared to the theoretical law of the wall and log law, Figure 21 shows a significant under-prediction near the wall for all meshes tested at both Reynolds numbers. The meshes tested were initially created considering a lower Reynolds number of 5300 so as to have an approximate starting first point at $y^+=1$. At these higher Reynolds numbers of $Re=12 \times 10^3$ and $Re=24 \times 10^3$ the meshes do not appear to have the resolution necessary within the viscous layer ($y^+ < 5$) to accurately capture the log-layer velocity profile near the wall. When normalized with the bulk velocities Figure 22 shows little variation among the meshes tested for the mean tangential velocity.

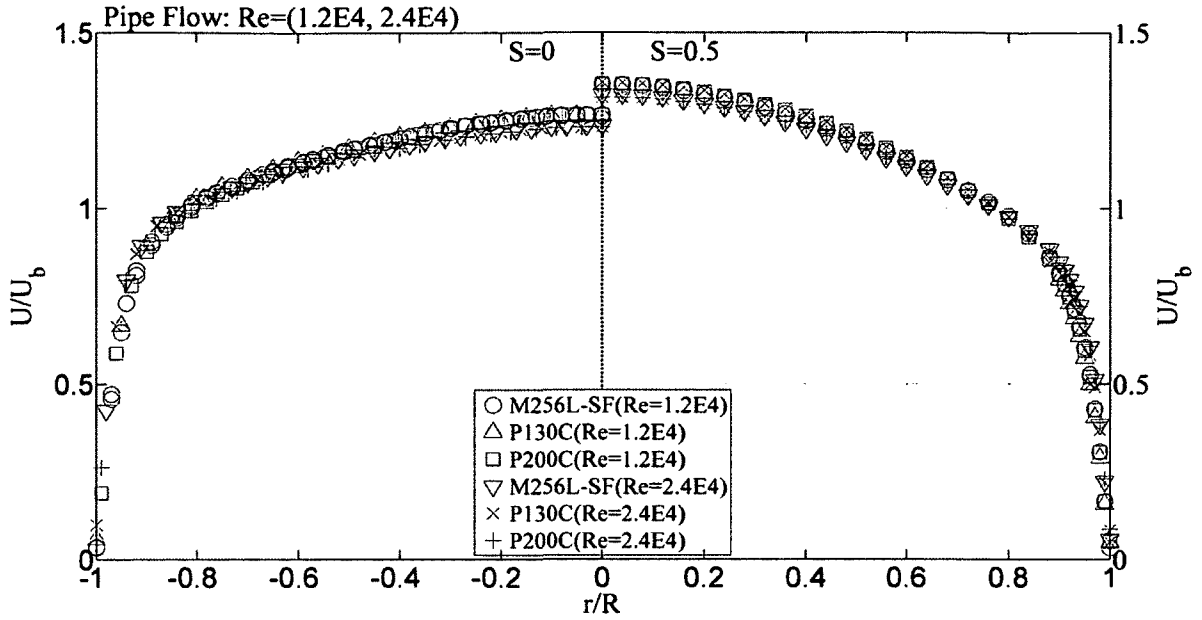


Figure 20: Mean axial velocity normalized with bulk velocity, $Re=12 \times 10^3, 24 \times 10^3$; $S=0, 0.5$.

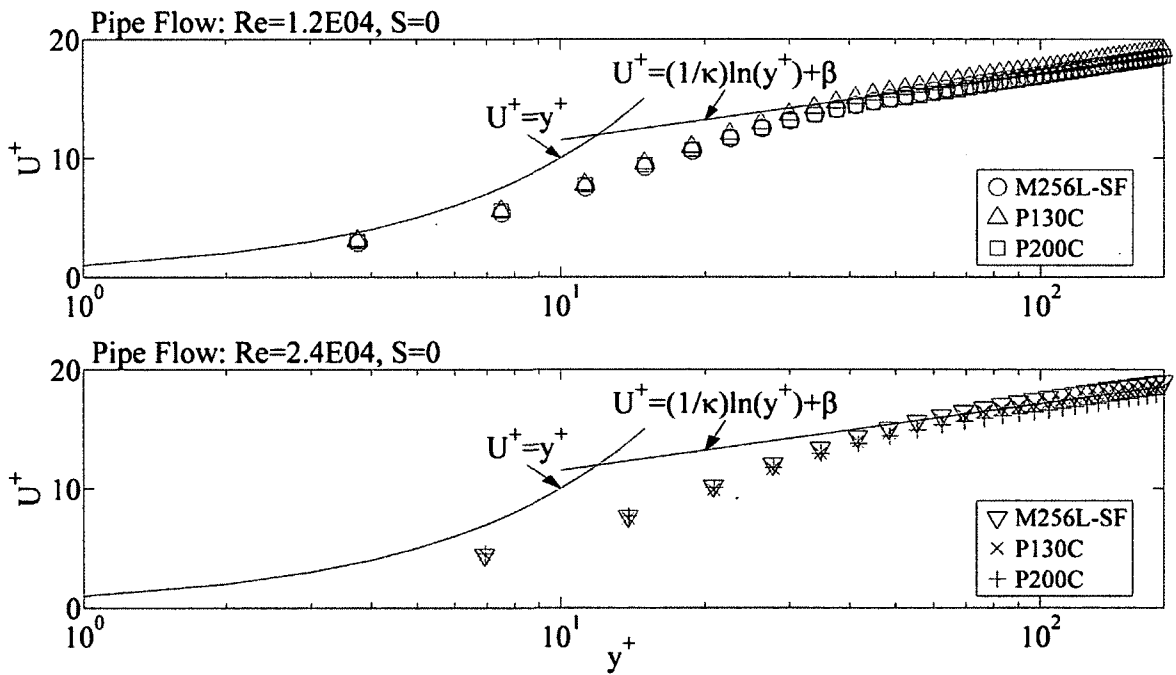


Figure 21: Mean axial velocity in wall units. $Re=12 \times 10^3, 24 \times 10^3$; $S=0$. $\kappa=0.41$ $\beta=5.9$.

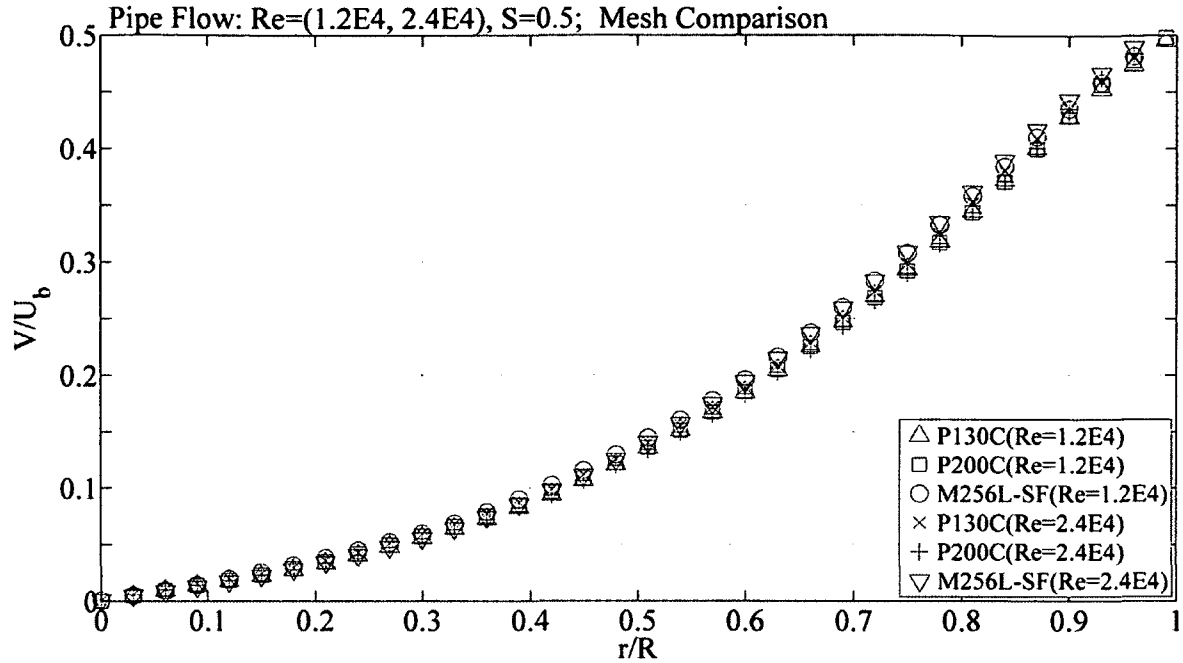


Figure 22: Mean tangential velocity normalized with bulk velocity. $Re=12 \times 10^3$, 24×10^3 ; $S=0.5$.

Figure 23 and 24 show the turbulent intensities normalized with bulk velocity for pipe flow at $Re=12 \times 10^3$ and $Re=24 \times 10^3$ respectively. There is little variation in the turbulent intensities found for all meshes tested at either Reynolds number. Addition of rotation appears to only give a slight increase in turbulent intensities near the central region of the pipe.

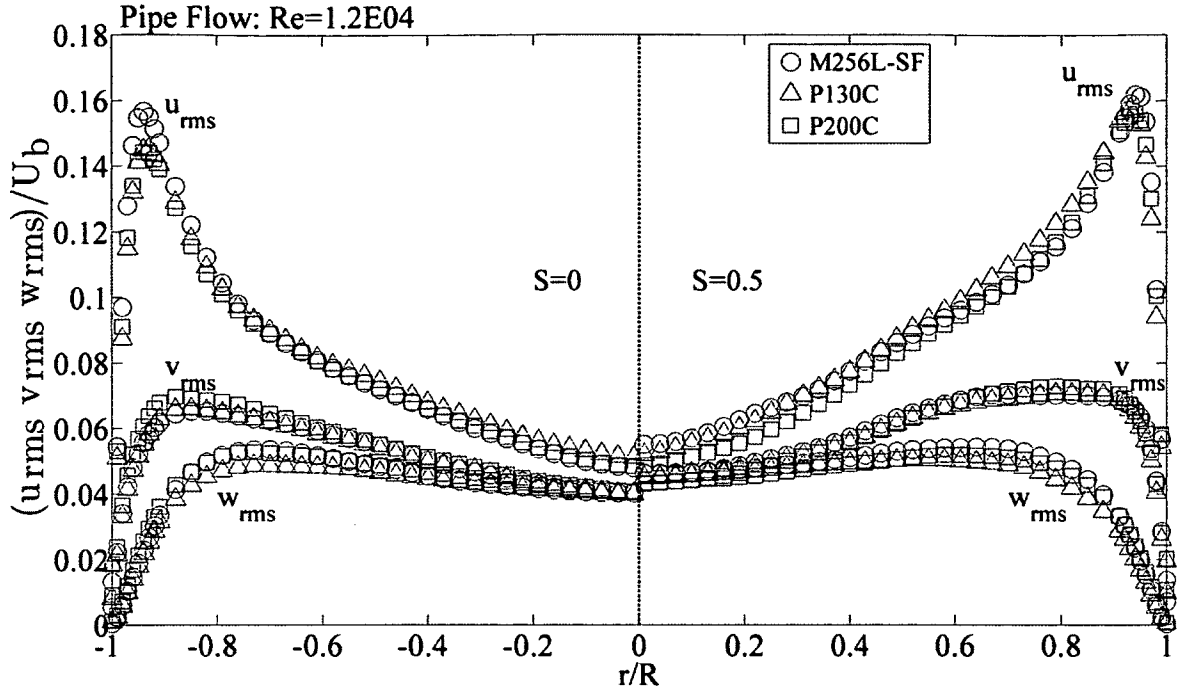


Figure 23: RMS velocities normalized with bulk velocity. $Re=12 \times 10^3$; $S=0, 0.5$.

The \overline{uw} Reynolds shear stress (axial-radial) for pipe flow at $Re=12 \times 10^3$ and $Re=24 \times 10^3$ is shown in Figure 25 and 26 respectively. It can be seen that in both cases the P130C mesh which is the coarser of the three meshes tested gives lower axial-radial stress values for both Reynolds numbers tested. Both the M256L-SF and P200C meshes give nearly identical results with only a slight deviation observed at $Re=12 \times 10^3$ from approximately $100 < y^+ < 180$ due to a drop in the axial-radial stress observed in the M256L-SF mesh simulation most likely due to insufficient data samples.

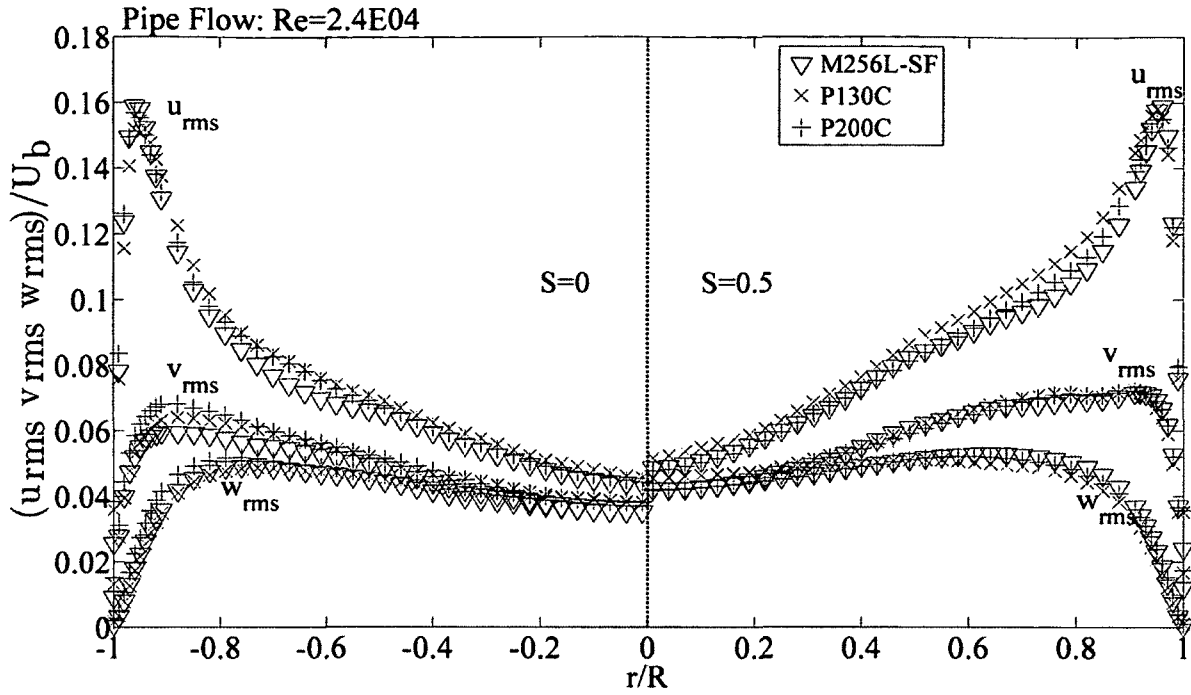


Figure 24: RMS velocities normalized with bulk velocity. $Re=24 \times 10^3$; $S=0, 0.5$.

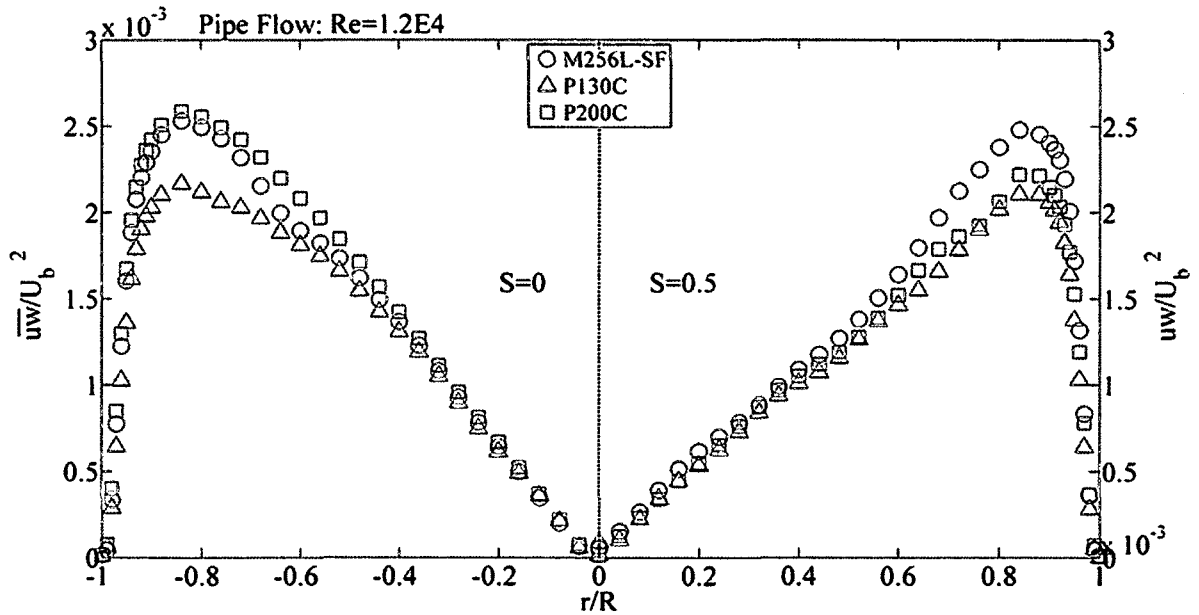


Figure 25: Reynolds shear stress (axial-radial) normalized with bulk velocity. $Re=12 \times 10^3$; $S=0, 0.5$.

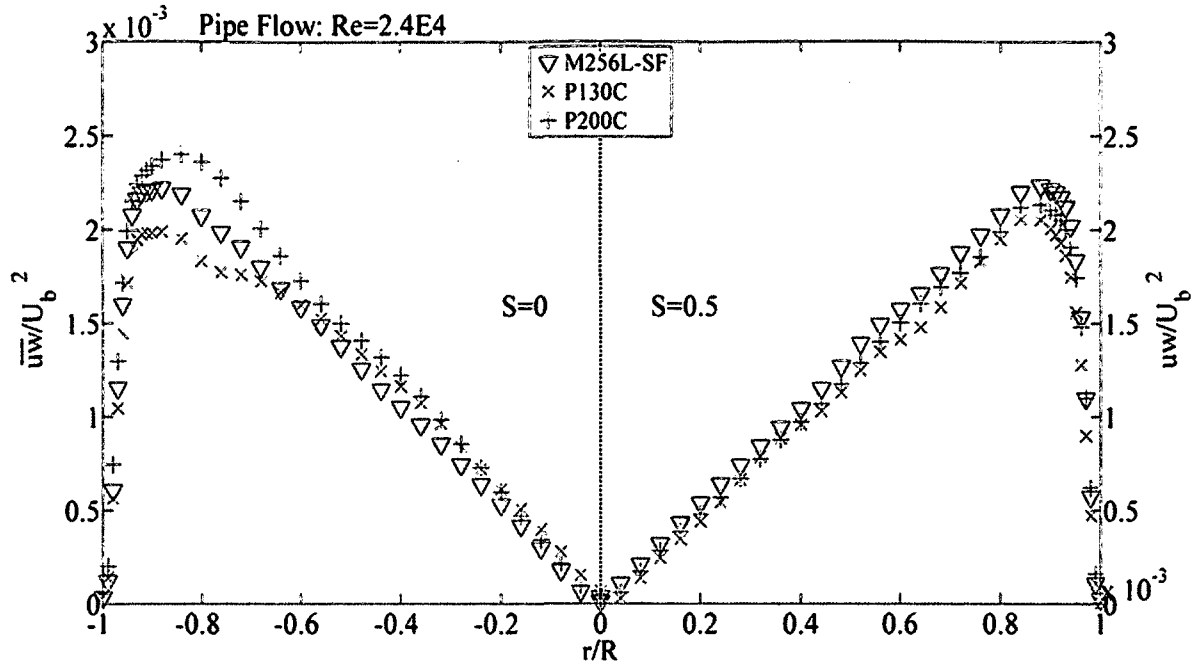


Figure 26: Reynolds shear stress (axial-radial) normalized with bulk velocity. $Re=24 \times 10^3$; $S=0, 0.5$.

Figure 27 shows the mean pressure results for non-rotating and rotating pipe flow for all meshes tested. It can be seen that all meshes give nearly identical results. The mean pressure results show little difference among the meshes tested with a slightly higher pressure near the wall observed for the higher Reynolds number of $Re=24 \times 10^3$ when rotation is included. When compared to the non-rotating case, the mean pressure observed is 30 times bigger near the wall. The rms-pressure results shown in Figure 28 show a similar trend as the mean pressure with a considerable increase when rotation is included. Based on the mesh results comparison of pipe flow at these higher Reynolds numbers of $Re=12 \times 10^3$ and $Re=24 \times 10^3$, there does not appear to be any significant difference among the three meshes tested. A noticeable deviation of the P130C RMS pressure at the higher Reynolds number of $Re=24 \times 10^3$ with rotation $S=0.5$ is the only indication that the coarser P130C may be the least adequate.

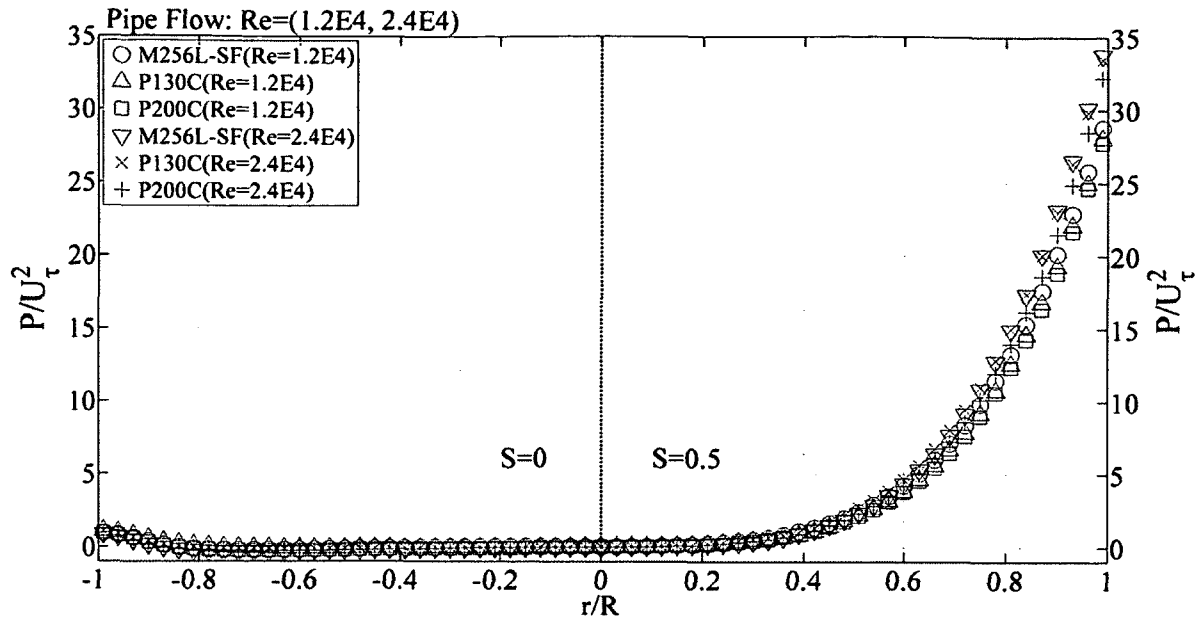


Figure 27: Mean Pressure. $Re=12 \times 10^3, 24 \times 10^3$; $S=0, 0.5$.

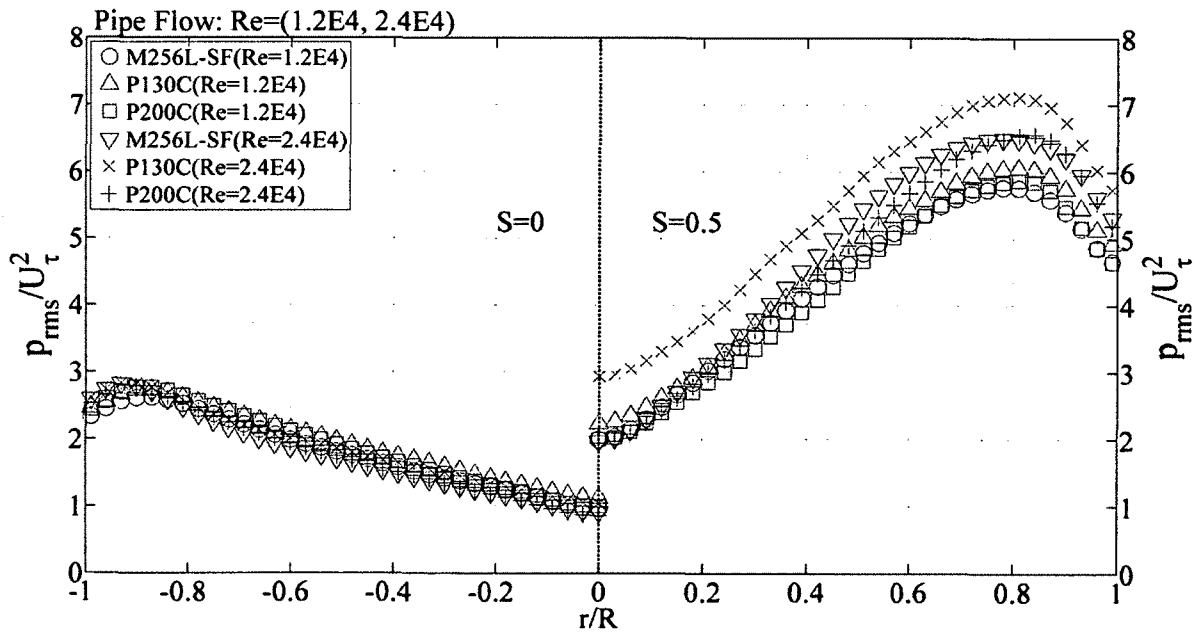


Figure 28: RMS Pressure. $Re=12 \times 10^3, 24 \times 10^3$; $S=0, 0.5$.

5 JET FLOW MESH SENSITIVITY TESTS

5.1 JET FLOW MESH AND SIMULATION PARAMETERS

The computational mesh and domain geometry for the jet simulations is shown in Figure 29. The domain consists of a rectangular box with dimensions of $10D \times 5D \times 5D$ ($D=0.06m$). Figure 29 also shows the boundary types used which include a jet velocity inlet (blue), a wall boundary (black) and five pressure outlets (red) (front side and upper not shown). The center mid plane (green) nodes of the jet computational grid is also shown.

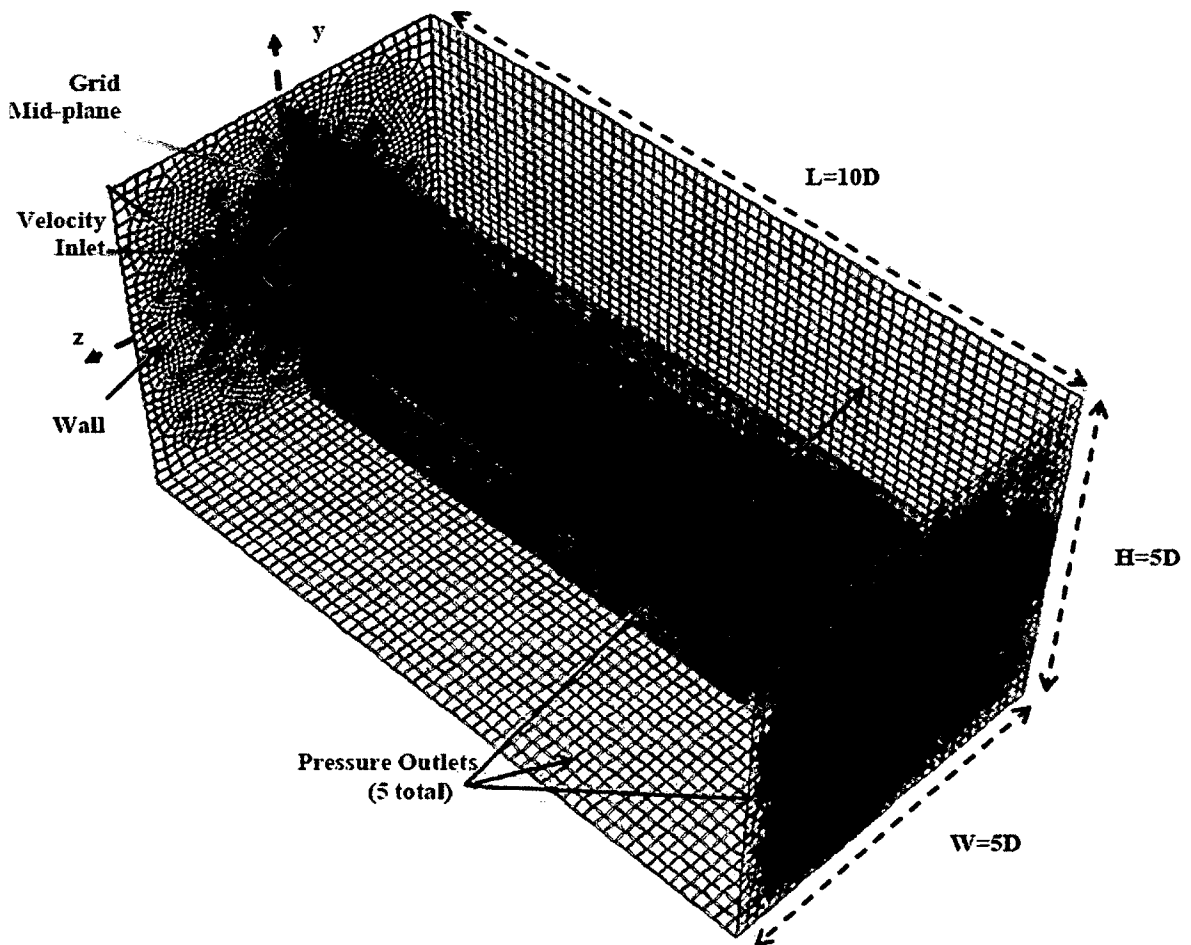


Figure 29: Jet mesh domain dimensions and boundary conditions.

Five jet meshes were created to test for grid independence. These meshes, shown in Figure 30 through 33, are referred to as Mesh1, Mesh2, Mesh3, Mesh4 and Mesh5. A brief description of each mesh is presented below.

- Mesh1: Has 6.65×10^3 hexahedral cells with a minimum cell volume of $1.75 \times 10^{-9} \text{ m}^3$ and maximum cell volume of $1.44 \times 10^{-6} \text{ m}^3$.
- Mesh2: Created by grid refinement of Mesh1 based on the mean axial velocity values calculated at a Reynolds number of 12×10^3 after 10,000 iterations. Grid refinement was performed on all cells in the Mesh1 domain having a mean x-velocity iso-value greater than 0.1 m/s . Refinement of cells meeting this criteria was accomplished by setting the maximum allowable cell volume within the mean x-velocity iso-value range to $5 \times 10^{-8} \text{ m}^3$. The refined mesh, Mesh2 has 1.33×10^6 cells.
- Mesh3: Created using a 'size function' which is a tool in the meshing software Gambit that allows for control of the mesh intervals for edges and mesh elements within the computational domain. Please see the Gambit user guide for a complete description of the types and detailed usage of meshing size functions. A 'fixed size' mesh sizing function was set at the jet inlet and attached to the entire computational domain with a starting size of 0.001 m , growth rate of 1.05 and maximum edge length of 0.005 m . The resulting mesh domain has 1.23×10^6 cells.
- Mesh4: Was created by refining Mesh3 using the same refinement method used for Mesh2 completed on the original Mesh1. Mesh 3 has 1.69×10^6 cells.
- Mesh5: Created with a sizing function as with Mesh3 but with a starting size of 0.001 m , growth rate of 1.05, and maximum edge length of 0.003 m . Mesh5 has 3.31×10^6 cells.

All jet meshes were created by first tracing the cells of the cross section of the P200C pipe (shown in Figure 3b) onto the jet inlet. Based on the pipe simulation results, it was decided that instantaneous velocity data collected from the P200C pipe simulations would be used as the initial condition for the jet simulations. Matching the cross section of the P200C pipe mesh cross section was thus done to avoid the need for spatial interpolation of the instantaneous velocity profiles set at the jet inlet. Figure 30 shows a side view of the mid plane grid along the axial direction of each mesh. Figure 31 through Figure 33 show cross sections of the jet meshes at $X=(0D, 5D, \text{ and } 10D)$. As stated

earlier, the inlet for all jet meshes correspond to the cross section of the P200C pipe mesh as shown in Figure 3b, and all jet mesh volume cells within the domain are hexahedral.

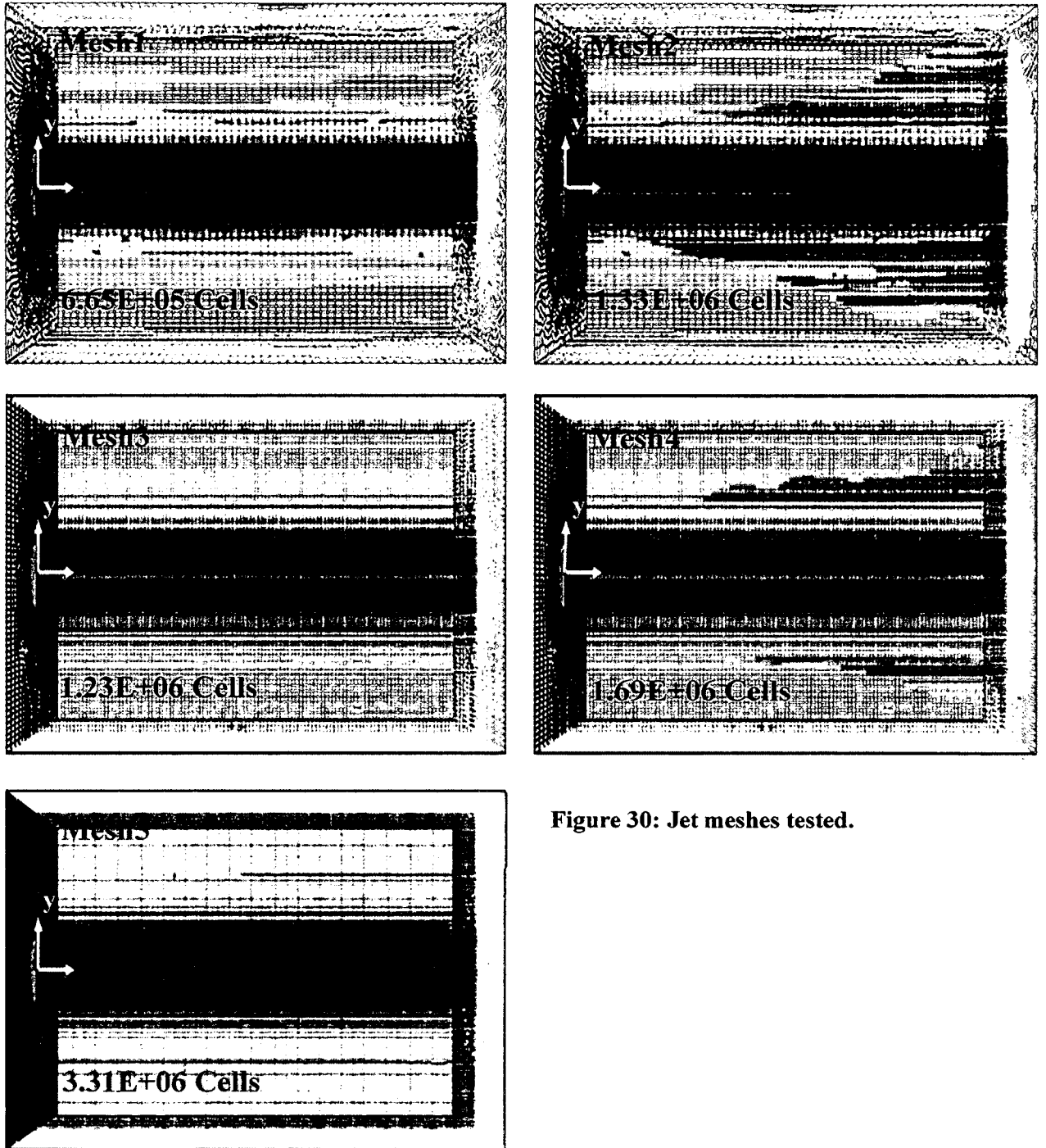


Figure 30: Jet meshes tested.

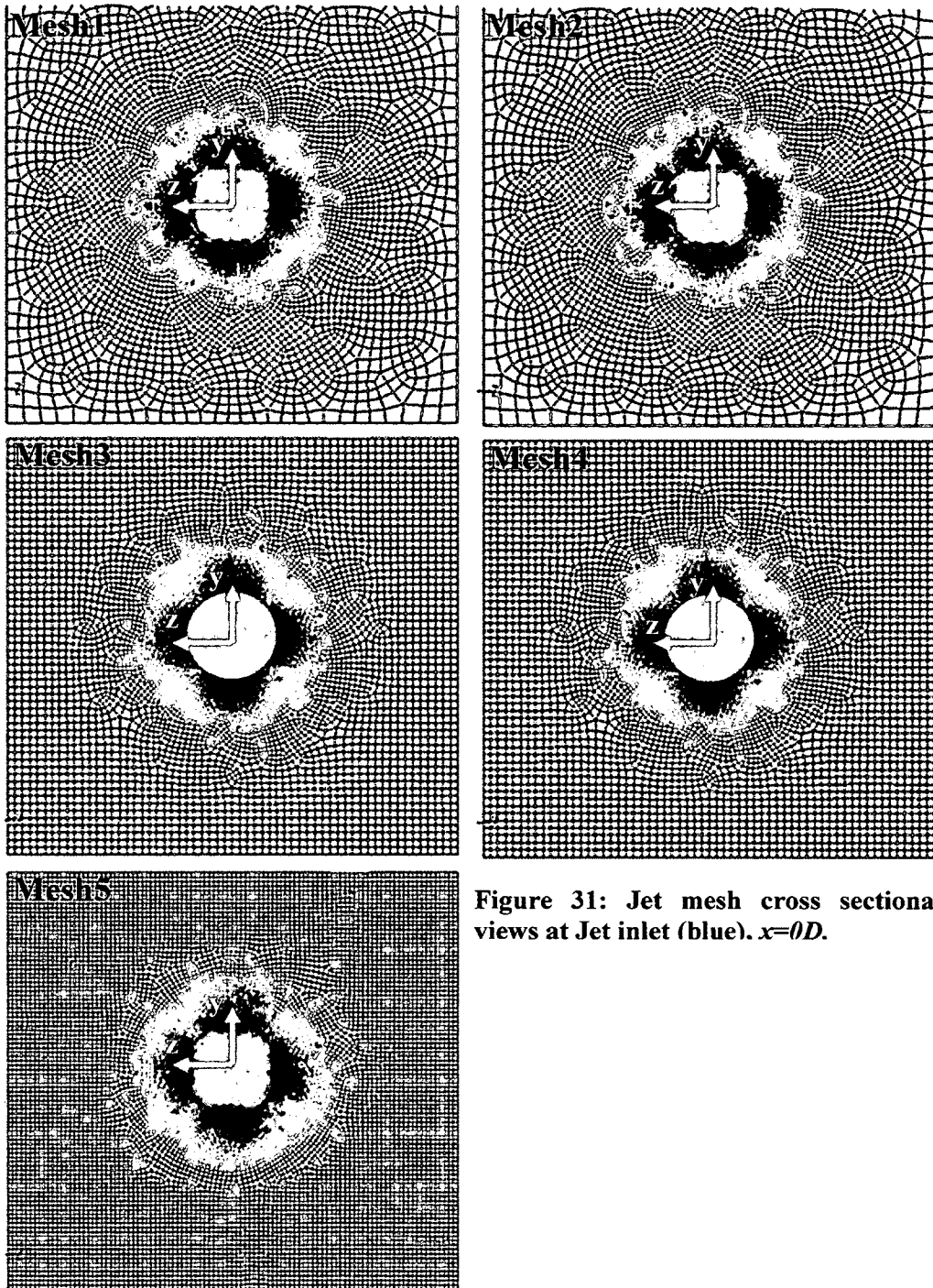


Figure 31: Jet mesh cross sectional views at Jet inlet (blue). $x=0D$.

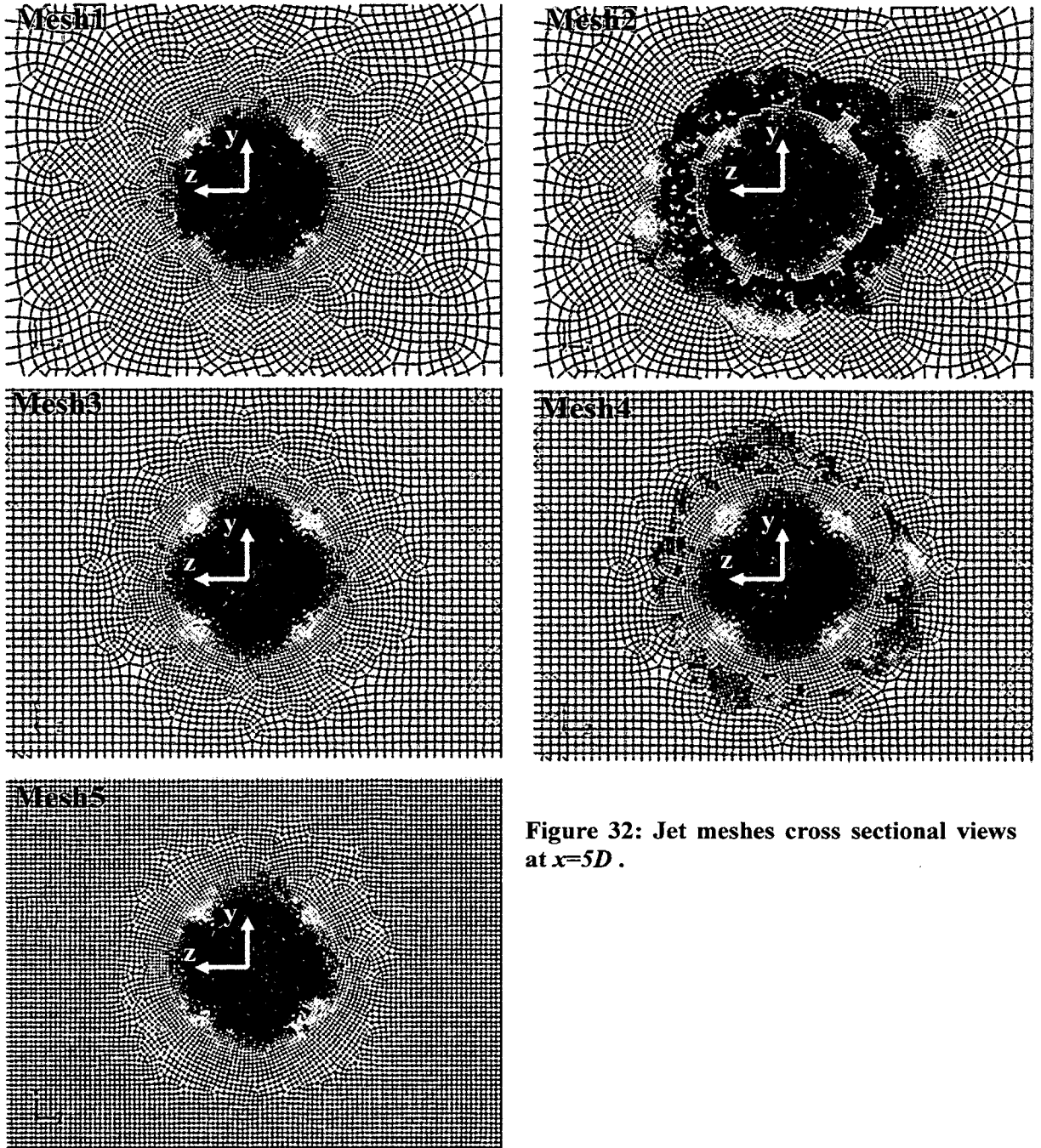


Figure 32: Jet meshes cross sectional views at $x=5D$.

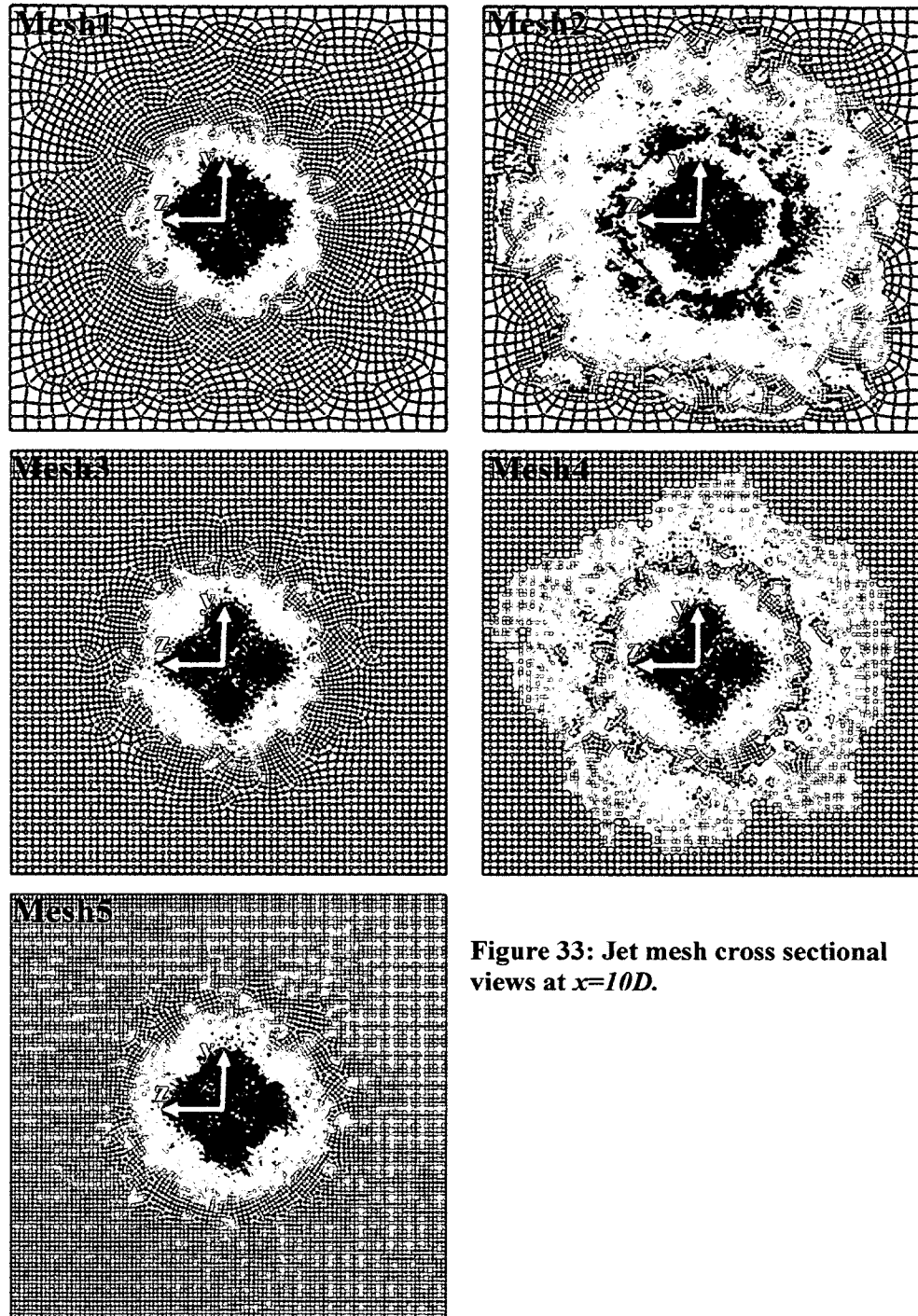


Figure 33: Jet mesh cross sectional views at $x=10D$.

5.2 JET FLOW: $Re=12 \times 10^3$, 24×10^3 ; $S=0, 0.5$

For non-swirling jet flow at $Re=12 \times 10^3$, the 5 jet meshes described in section 5.1 were tested. However, not all meshes were tested for all flow configurations. For non-swirling jet flow at $Re=24 \times 10^3$ all jet meshes were tested with the exception of jet mesh#4. For jet flow with rotation of $S=0.5$ at Reynolds numbers of $Re=12 \times 10^3$ and $Re=24 \times 10^3$ only jet mesh#3, which produced relatively similar results to the much finer but more computationally intensive mesh#5, was used. As described in the previous section, the instantaneous cross sectional area velocity profiles collected for the P200C pipe flow case were used as the input boundary conditions at the jet inlet for all 5 meshes. "P200C-Mesh1" and "P200C-Mesh2" and so on refers to using the P200C pipe flow simulation instantaneous velocity profiles with Jet Mesh#1 and Jet Mesh#2 respectively. In addition, the pipe instantaneous velocity profiles of both the P200C and M256L-SF mesh were tested with jet rotation to check for possible differences due to application of different input boundary conditions at the jet inlet.

As seen in Figure 34, for jet flow without rotation, the mean axial center-line velocity only seems to differ slightly for the coarser meshes #1 and #2, with the remainder of the meshes showing nearly identical results. The denser Mesh#5 does appear to give slightly larger centerline velocity values with a slower velocity decay starting from approximately $x/D > 4$ for both Reynolds numbers tested. As expected due to increased jet spreading, the beginning of the mean axial velocity decay appears to be further upstream for jet flow with rotation at approximately $x/D \sim 3$. Results for jet flow with rotation show that there is no significant difference between the two input conditions for the centerline mean axial velocity for either Reynolds number.

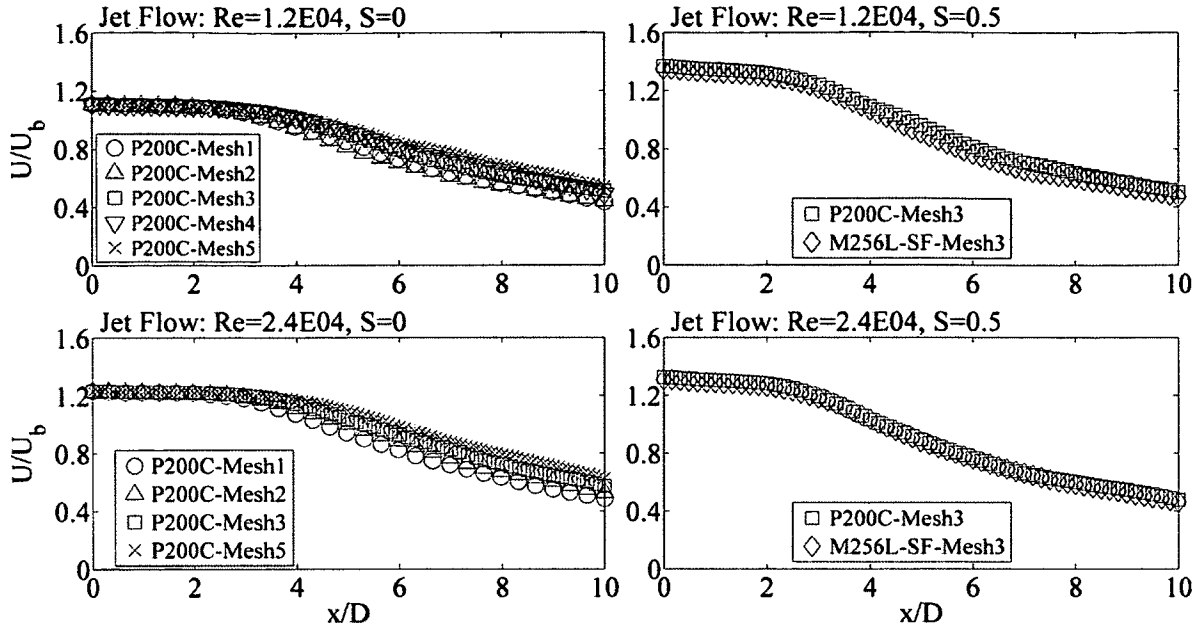


Figure 34: Jet Centerline Axial velocity normalized with bulk velocity. $Re=12 \times 10^3, 24 \times 10^3$; $S=0, 0.5$.

Figure 35 and 36 show 3-D views of the mean velocity profiles at several axial locations ($x/D=0, 2, 4, 6, 8, 10$) normalized with the bulk velocity for $Re=12 \times 10^3$ at $S=0$ and $S=0.5$, respectively. As expected, the axial velocity decreases more rapidly with rotation and spreads outward faster. For swirling jet flow, Figure 36 and 37 of the mean tangential velocity again confirm that there does not appear to be any significant difference between the two input conditions applied at the jet inlet for either Reynolds number.

Figure 39 through 41 show comparisons of the turbulent intensities. They confirm previous observations that the coarser mesh #1 and mesh #2 show slight deviations from the rest of the meshes. As was the case for pipe flow the coarser meshes appear to over-predict the axial turbulent intensity and under-predict both the radial and tangential turbulent intensities.

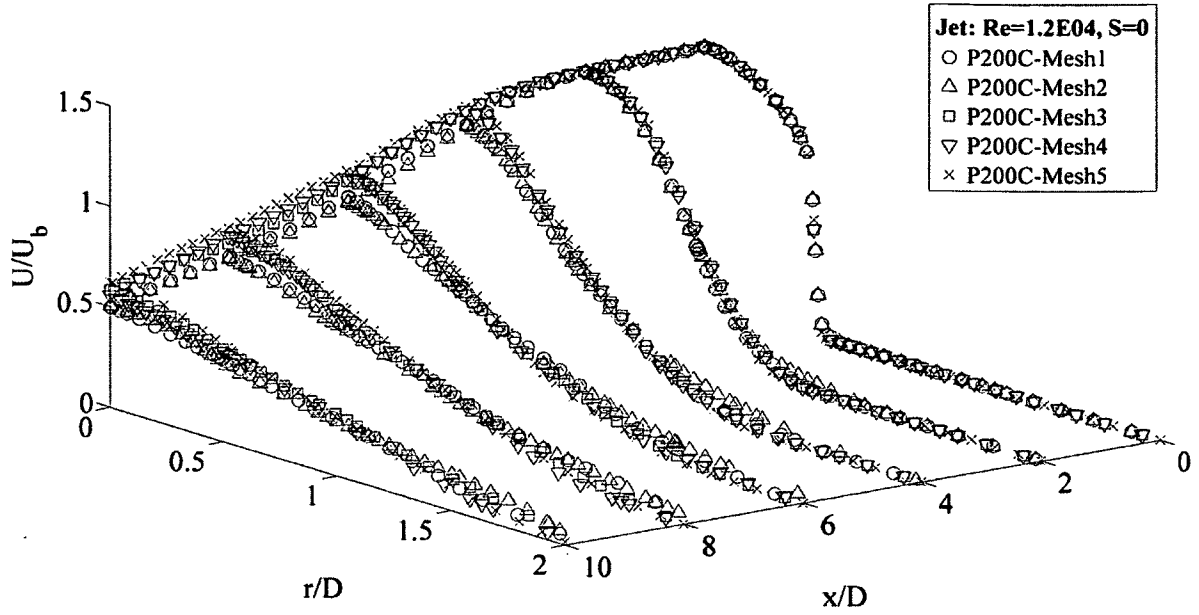


Figure 35: Jet mean axial velocity normalized with bulk velocity. $Re=12 \times 10^3$; $S=0$.

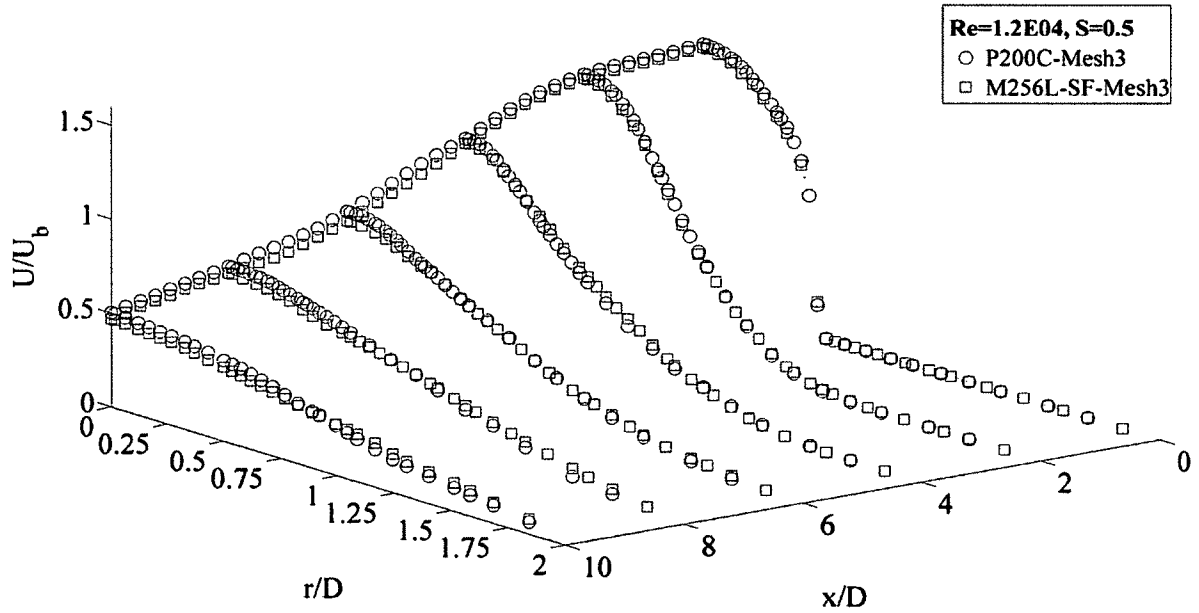


Figure 36: Jet mean axial velocity normalized with bulk velocity. $Re=12 \times 10^3$; $S=0.5$.

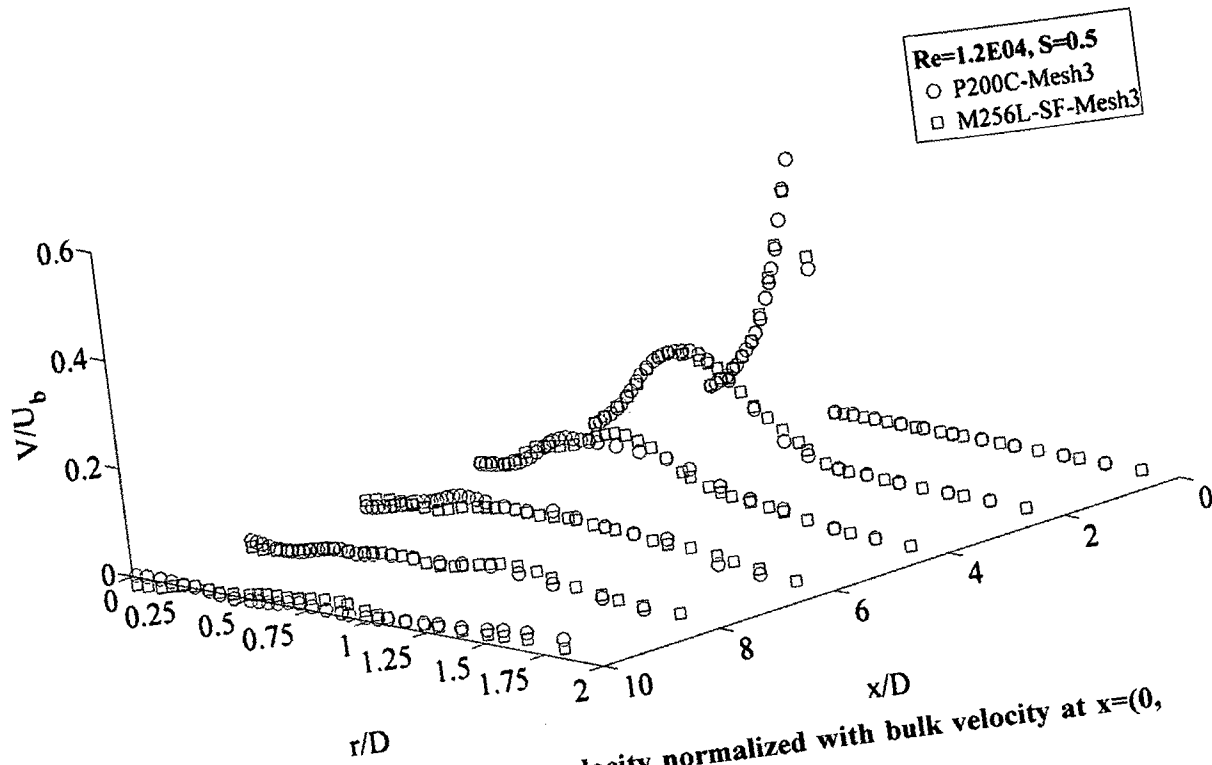


Figure 37: Jet mean tangential velocity normalized with bulk velocity at $x=(0, 2, 4, 6, 8, 10)D$. $Re=12 \times 10^3$; $S=0.5$

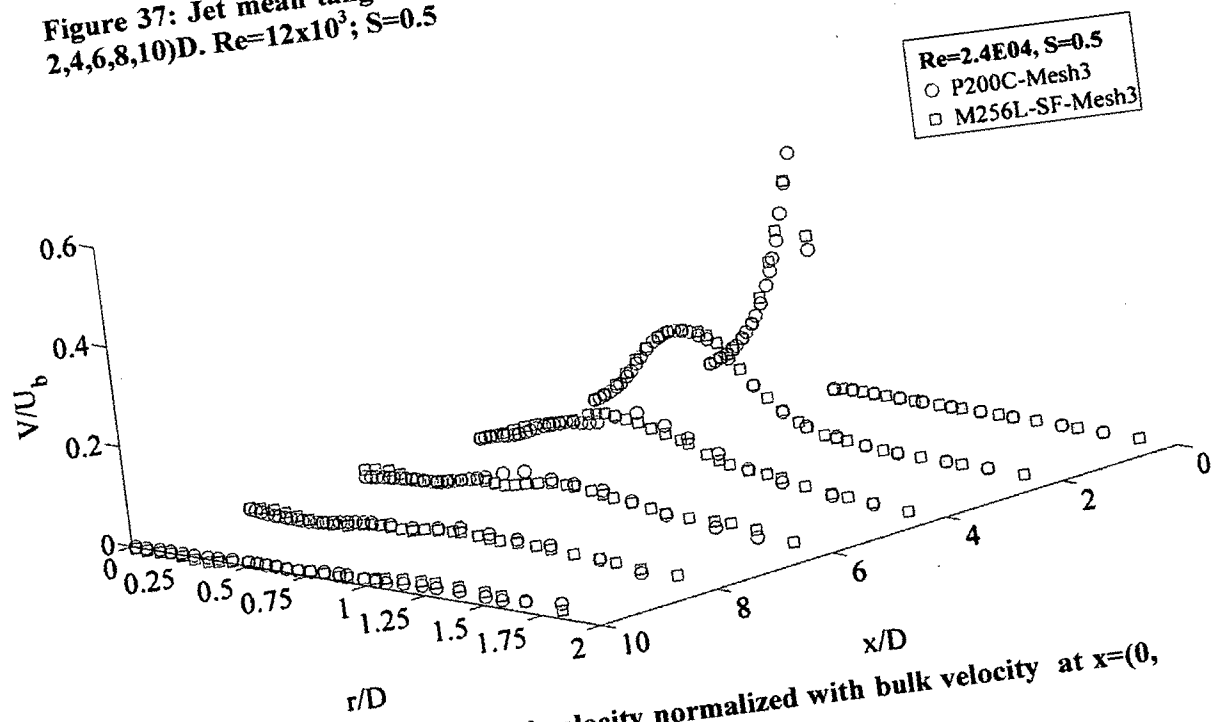


Figure 38: Jet mean tangential velocity normalized with bulk velocity at $x=(0, 2, 4, 6, 8, 10)D$. $Re=24 \times 10^3$; $S=0.5$

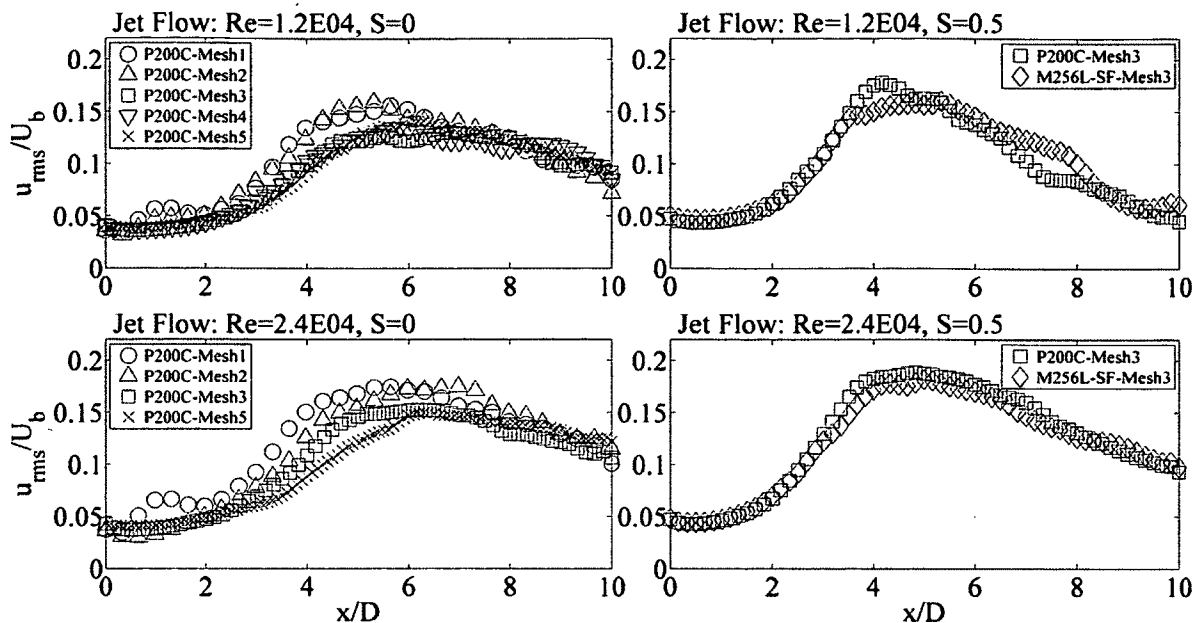


Figure 39: Jet Centerline RMS Axial velocity normalized with bulk velocity.
 $Re=12 \times 10^3, 24 \times 10^3$; $S=0, 0.5$.

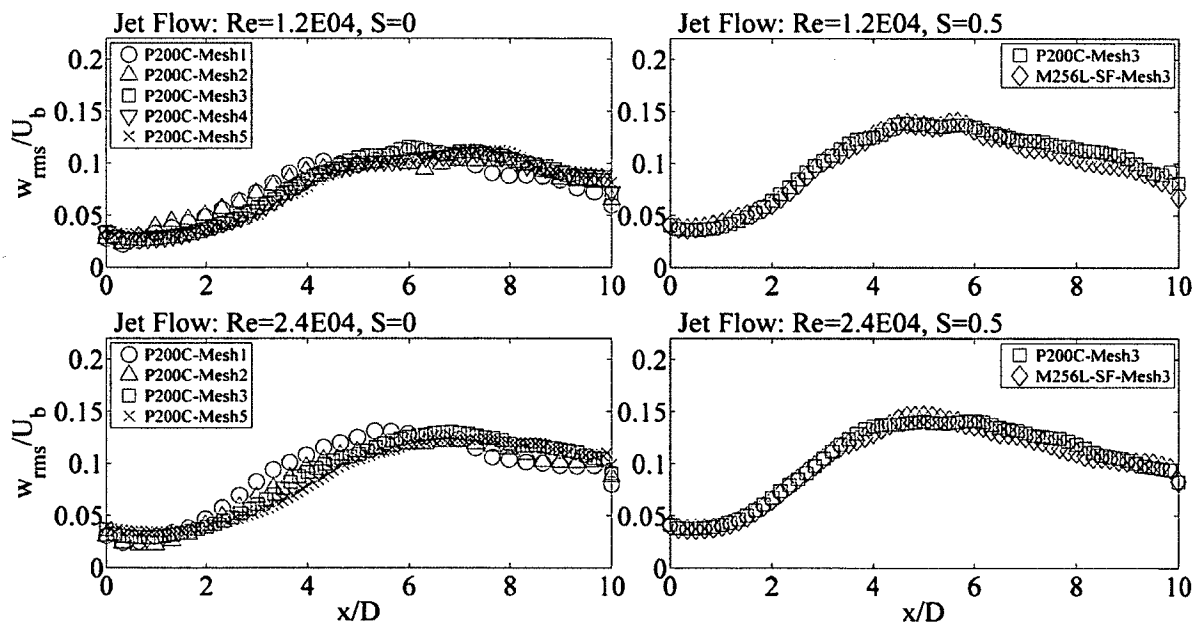


Figure 40: Jet Centerline RMS Radial velocity normalized with bulk velocity.
 $Re=12 \times 10^3, 24 \times 10^3$; $S=0, 0.5$.

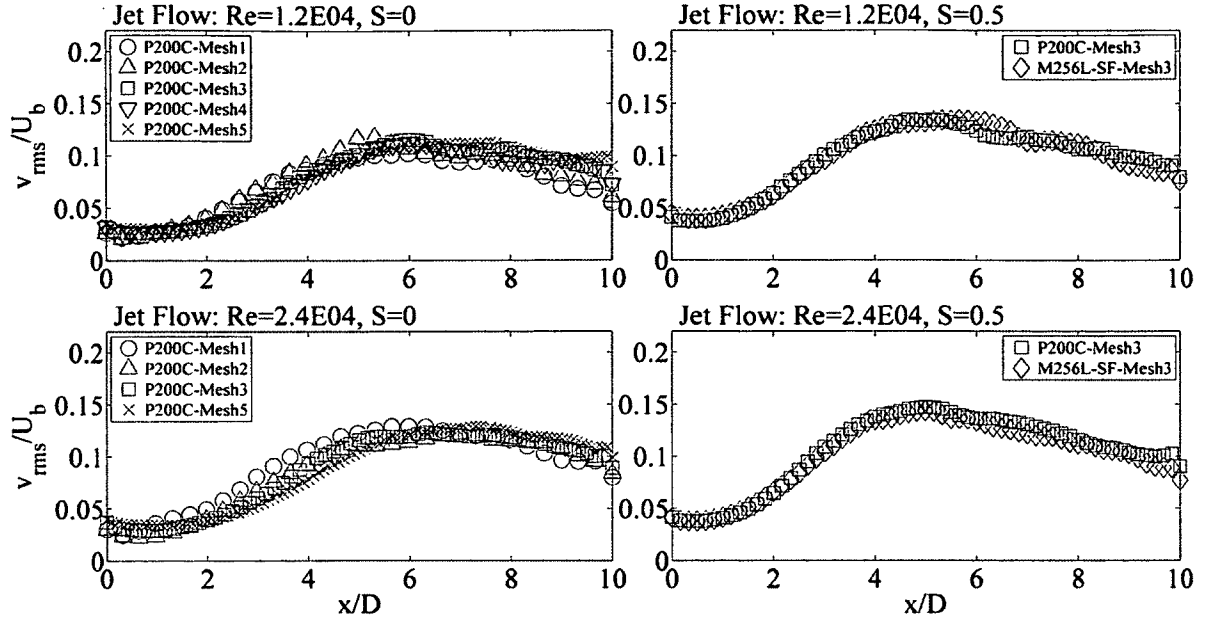


Figure 41: Jet Centerline RMS Tangential velocity normalized with bulk velocity. $Re=12 \times 10^3, 24 \times 10^3$; $S=0, 0.5$.

All three centerline Reynolds shear stress plots, \overline{uw} (axial-radial), \overline{uv} (axial-tangential) and \overline{vw} (radial-tangential), are shown in Figure 42 through Figure 44. For jet flow without rotation all Reynolds shear stress results show a similar trend with a nearly zero value up to about $x/D \sim 3.5$ at which point the values begin to oscillate with a greater magnitude. For jet flow with rotation the oscillations begin further upstream at around $x/D \sim 2.5$ and appear to be greater in magnitude especially for the axial-radial and axial-tangential stresses. The change in Reynolds stress magnitudes observed for all cases correspond to the point at which the centerline jet axial velocity begins to decay and the flow becomes fully turbulent.

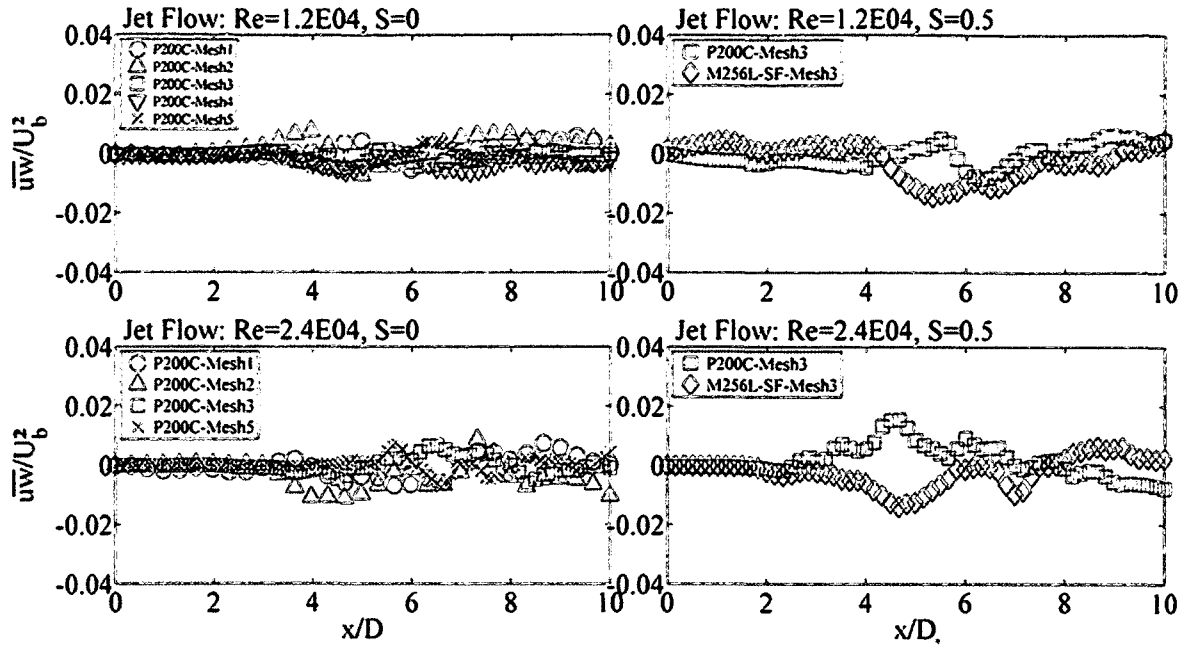


Figure 42: Jet centerline Reynolds shear stress (axial-radial) normalized with bulk velocity. $Re=12 \times 10^3, 24 \times 10^3$; $S=0, 0.5$.

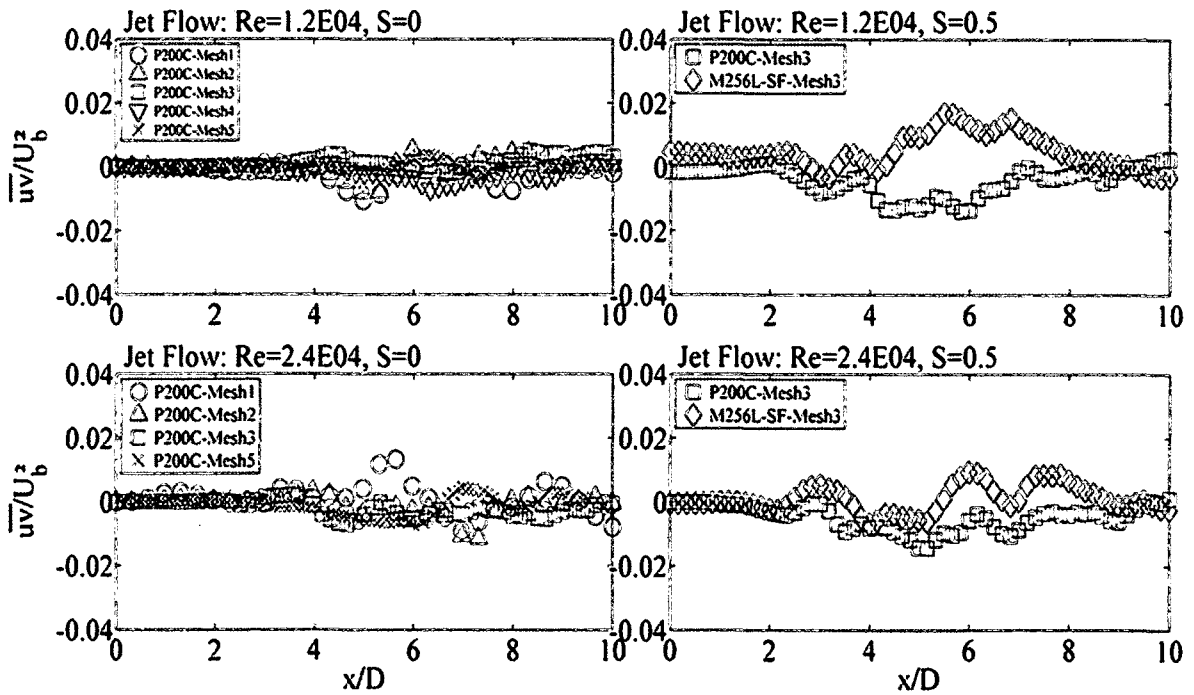


Figure 43: Jet centerline Reynolds shear stress (axial-tangential) normalized with bulk velocity. $Re=12 \times 10^3, 24 \times 10^3$; $S=0, 0.5$.

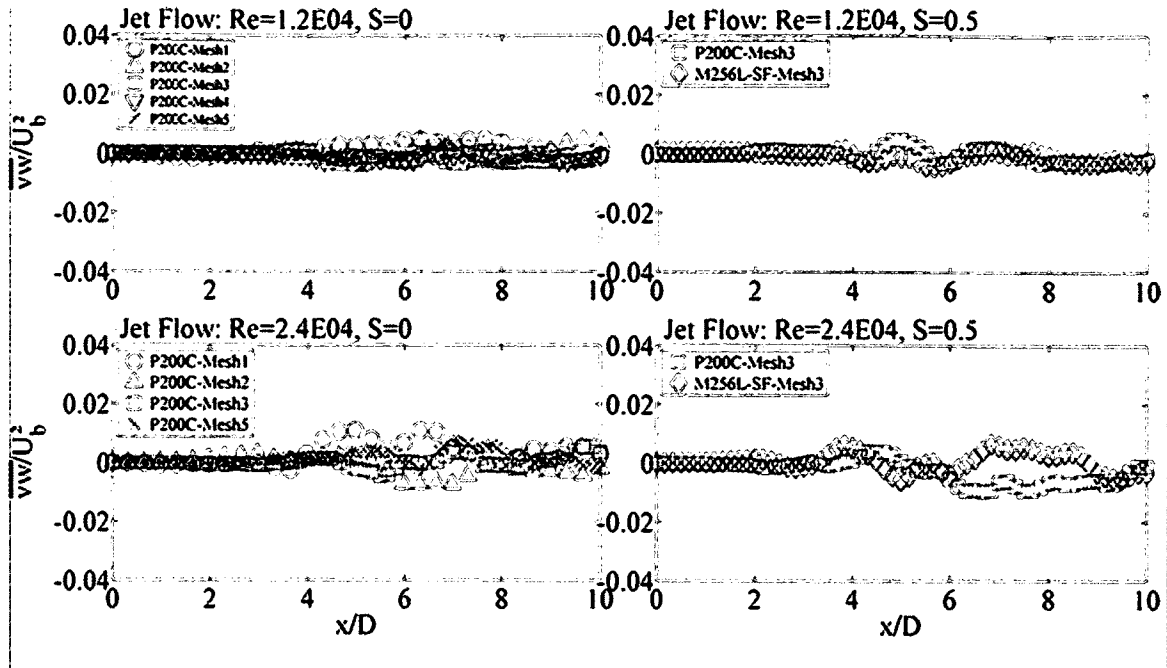


Figure 44: Jet centerline Reynolds shear stress (radial-tangential) normalized with bulk velocity. $Re=12 \times 10^3, 24 \times 10^3$; $S=0, 0.5$.

6 PIPE FLOW VALIDATION

Based on the results of grid sensitivity test in Section 4, mesh P200C was chosen for simulations to be compared to available data and to perform further analysis. All results presented hereafter are for the P200C pipe mesh only. Instantaneous axial velocities at various radial locations from non-rotating pipe flow simulations were recorded and are shown in Figure 45 at the various Reynolds numbers tested.

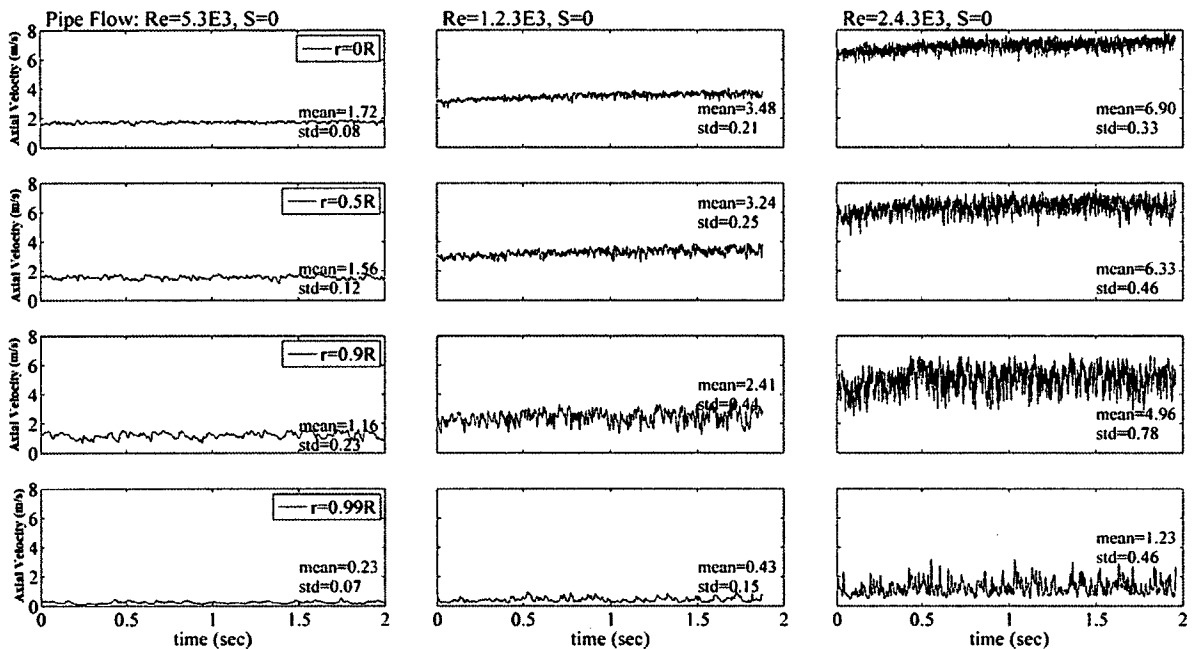


Figure 45: Instantaneous axial velocity. $Re=5.3 \times 10^3$, 12×10^3 , 24×10^3 ; $S=0$.

To determine proper turbulence decay of the LES solver in FLUENT, a spectral analysis using the discrete Fourier transform algorithm in MATLAB, `fft`, is implemented on the instantaneous velocity signals and compared with the Kolmogorov $-5/3$ energy spectrum power decay in the inertial subrange prediction. As shown in Figure 46 and 47 for Reynolds number of $Re=5.3 \times 10^3$ and $Re=24 \times 10^3$ respectively, current results show that sufficiently far from the wall $r < 0.9R$, there is a universal decay region which agrees with the $f^{5/3}$ law. Note that the four points shown correspond to the viscous sublayer ($r=0.99R$, $y^+=3$), the buffer layer ($r=0.9R$, $y^+=20$), intermediate layer ($r=0.5R$, $y^+=80$) and the outer layer ($r=0$, $y^+=170$) for flow at the lowest Reynolds number of

$Re=5.3 \times 10^3$. As expected, very near the wall ($r=0.99$), within the viscous layer where there is less turbulence, especially at the lower Reynolds number, the area of turbulence decay is minimal. At $Re=5.3 \times 10^3$ the location of $r=0.9R$ corresponding to the buffer layer as seen in Figure 46 shows an extension of the turbulence decay region occurs. Even further from the wall in the intermediate($r=0.5R$) and outer layer($r=0$) region where turbulence is fully-developed the area of turbulence decay is even larger. As seen in the significant fluctuations in velocity in Figure 45, at the higher Reynolds number $Re=24 \times 10^3$ the point of $r/R=0.99$ appears to already be within the buffer layer. As seen in Figure 47 a slight extension of the turbulent decay region is still noticeable going away from the wall up to $r/R=0.9$ which appears to lie within the intermediate/fully-developed region since no further increase in the turbulent decay region is noticeable beyond that. As expected, the turbulent decay region is more prevalent at the larger Reynolds numbers which are more turbulent.

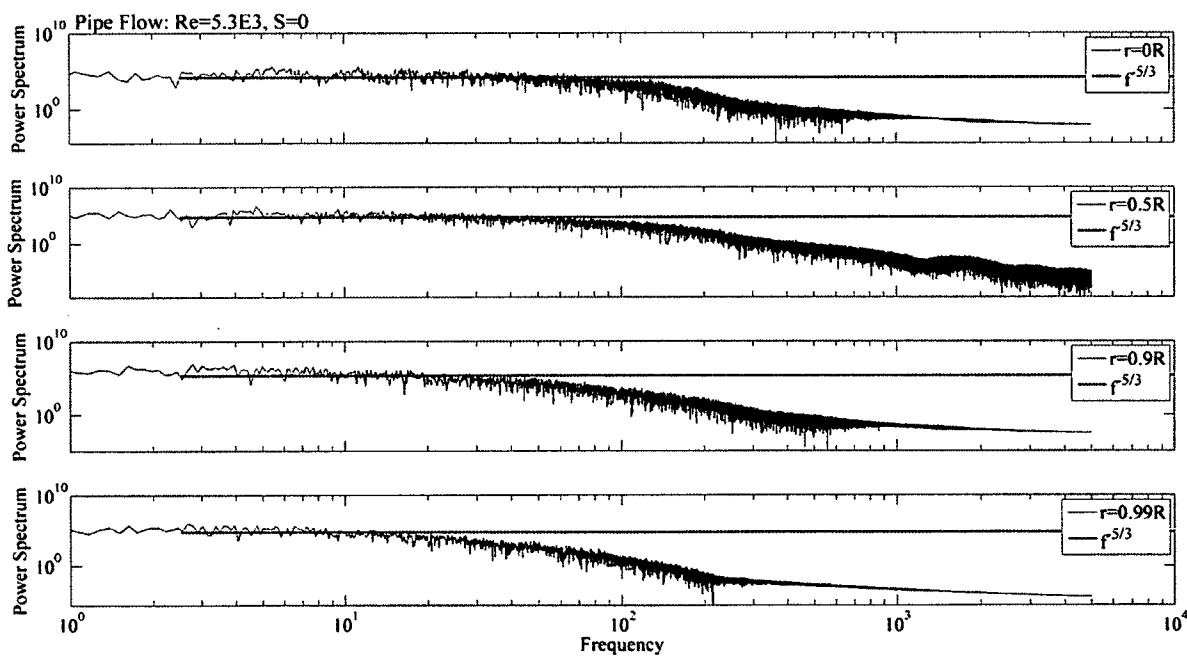


Figure 46: FFT power decay. Pipe flow $Re=5.3 \times 10^3$ $S=0$.

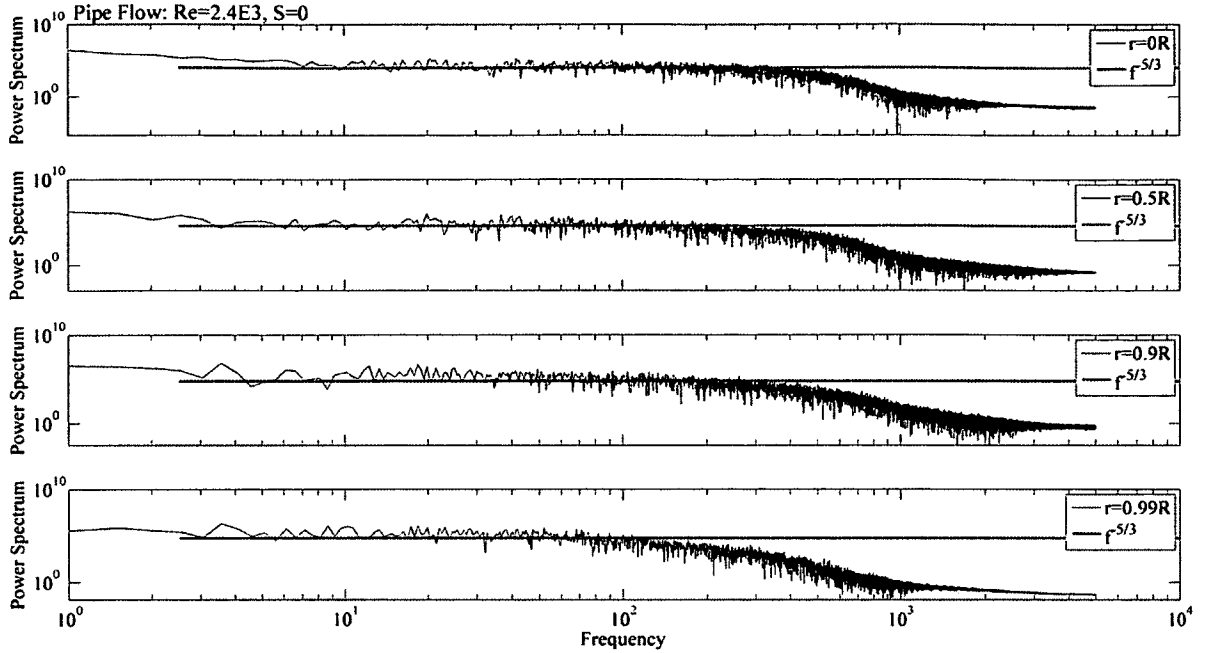


Figure 47: FFT power decay. Pipe flow $Re=24 \times 10^3$ $S=0$.

6.1 PIPE FLOW: $Re=5.3 \times 10^3$; $S=0$

Current LES simulation parameters for the P200C pipe mesh are shown in Table 8 along with the DNS simulation studies by Loulou-1997 (NASA), Orlandi and Fatica-1997 (Stanford), Eggels-1994 (Delft University) and Wu and Moin-2008 at the center for turbulence research (CTR). Data for three of the four DNS studies ('NASA', 'Stanford', 'Delft') used to validate the current simulations can be found in the AGARD(1997) database compiled on October 1997 by the Working Group 21 of the Fluid dynamics panel. CTR data of Wu and Moin (2008) can be found on the Center for Turbulence Research website.

The axial spacing in wall units, Δx^+ , and the tangential spacing at the outer perimeter in wall units, $\Delta \theta^+$, shown in Table 8 are found according to the following expressions.

$$\Delta x^+ = \frac{U_r \Delta x}{\nu} \quad \text{Eqn. 6-1}$$

$$\Delta \theta^+ = \frac{U_r \Delta s}{\nu} \quad \text{Eqn. 6-2}$$

where: $\Delta x = \frac{L}{N_x} = \frac{5D}{N_x}$ $N_x = (\# \text{ of axial Nodes})$

$\Delta s = \frac{\pi R \alpha}{180}$ $\alpha = \frac{360}{N_\theta}$ $N_\theta = (\# \text{ of Perimeter Nodes})$ Eqn. 6-3

Table 8: Pipe flow results and grid comparison with available validation data.
($Re=5.3 \times 10^3$, $S=0$, * $Re=5.6 \times 10^3$, ** $Re=4.9 \times 10^3$)

Mesh	Current	Previous DNS Studies			
	LES Study	NASA*	Stanford**	Delft	CTR
L	5D	5D	7.5D	5D	7.5D
U_b	1.304	1.000	0.500	0.039	1.000
U_c	1.715	1.294	0.648	0.051	1.290
Re_b	5355	5600	4900	5300	5300
ν (m ² /s)	1.46E-05	3.57E-04	2.04E-04	1.46E-05	3.77E-04
u_τ	9.00E-02	6.77E-02	3.47E-02	2.63E-03	6.84E-02
U_b/u_τ	14.489	14.770	14.397	14.730	14.610
U_c/u_τ	19.063	19.110	18.669	19.310	18.850
U_c/U_b	1.316	1.294	1.297	1.311	1.290
$C_f(x10^{-3})$	9.53	9.16		9.22	
$C_{f \text{ blas}}(x10^{-3})$	9.23	9.13	9.44	9.26	9.26
N_r	40	72	96	96	256
N_θ	200	160	128	128	512
N_x	256	192	256	256	512
r_w^+	0.86	0.39	0.37	0.94	0.17
Δr_{max}^+	7.37	5.71	2.35	1.85	1.65
Δr_{avg}^+	4.27	2.79	1.34	1.85	0.71
Δx	1.17E-03	0.0521	0.0586	0.0391	0.0293
$\Delta(R\theta)_w$	9.42E-04	0.0393	0.0491	0.0491	0.0123
x^+	7.22	9.87	9.97	7.03	5.31
$(R\theta)^+$	5.81	7.44	8.35	8.8	2.2

For grid wall boundary layer resolution comparison purposes, the distance in wall units, $y^+ = \frac{u_\tau y}{\nu}$, is shown in Table 9 for the first 20 points from the wall for the P200C

pipe mesh in this current investigation at $Re=5.3 \times 10^3$, as well as the meshes of the aforementioned DNS studies of turbulent pipe flow found in the literature.

Table 9: Distance in wall units, for first 20 points from pipe wall at $Re=5.3 \times 10^3$, $S=0$. *NASA ($Re=5.6 \times 10^3$), **Stanford ($Re=4.9 \times 10^3$).

Grid Point	Current LES Study	Previous DNS Studies			
	P200C	NASA*	Stanford**	Delft	CTR
y_1^+	0.00	0.00	0.18	0.93	0.00
y_2^+	0.86	0.39	0.54	2.78	0.17
y_3^+	1.89	0.91	0.95	4.63	0.34
y_4^+	3.12	1.48	1.39	6.49	0.51
y_5^+	4.61	2.09	1.88	8.34	0.68
y_6^+	6.38	2.75	2.41	10.20	0.86
y_7^+	8.52	3.45	2.99	12.05	1.04
y_8^+	11.08	4.20	3.62	13.90	1.22
y_9^+	14.15	5.01	4.31	15.76	1.40
y_{10}^+	17.84	5.87	5.06	17.61	1.59
y_{11}^+	22.27	6.79	5.88	19.47	1.78
y_{12}^+	22.62	7.78	6.76	21.32	1.97
y_{13}^+	26.15	8.83	7.72	23.17	2.16
y_{14}^+	30.15	9.95	8.75	25.03	2.36
y_{15}^+	34.31	11.15	9.87	26.88	2.56
y_{16}^+	40.05	12.43	11.07	28.74	2.76
y_{17}^+	45.96	13.79	12.35	30.59	2.97
y_{18}^+	51.98	15.23	13.72	32.45	3.17
y_{19}^+	57.81	16.76	15.18	34.30	3.38
y_{20}^+	63.36	18.39	16.73	36.15	3.60

Figure 48 shows excellent agreement for the mean axial velocity for non-rotating pipe flow at $Re=5.3 \times 10^3$ between current LES simulation and DNS data.

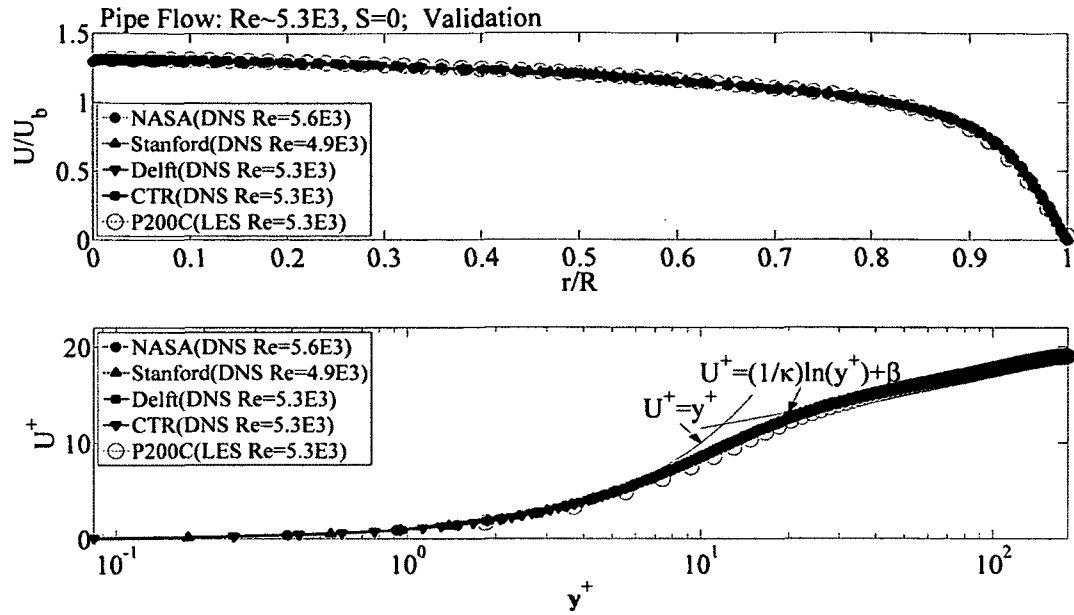


Figure 48: Mean axial velocity, normalized with bulk velocity (top), in wall units (bottom) $Re=5.3 \times 10^3$; $S=0$.

The turbulent intensity profiles in the axial, radial and tangential directions shown in Figure 49 also agree well with the validation data. The axial turbulence intensity profile found for the peak magnitude of the axial velocity turbulent intensity, however, seems to be shifted slightly further away from the wall and seems to slightly under predict the turbulent axial intensity near the wall from $0.9 < r/R < 1$. The turbulent radial intensity also shows slight under-prediction from $0.6 < r/R < 0.9$ when compared to the validation data. Similar under-prediction behavior is observed for the axial-radial shear stress as shown in Figure 50. Overall, the results appear to be reasonable and compare well with the DNS data.

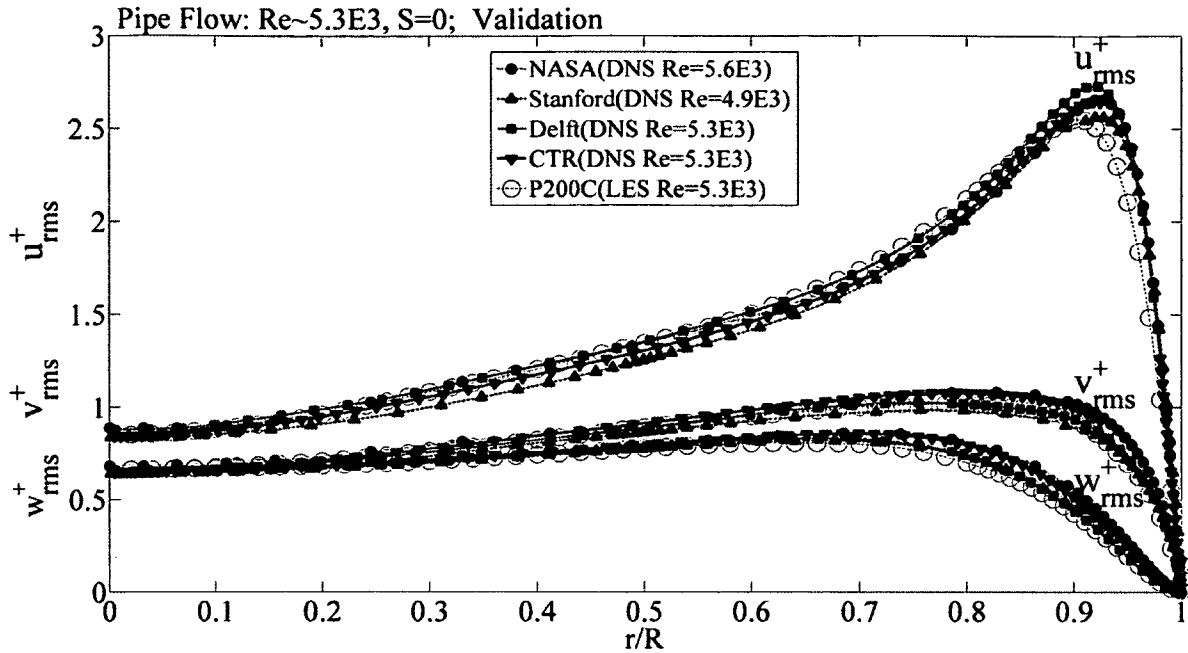


Figure 49: Turbulence intensities in wall units. $Re=5.3 \times 10^3$; $S=0$.

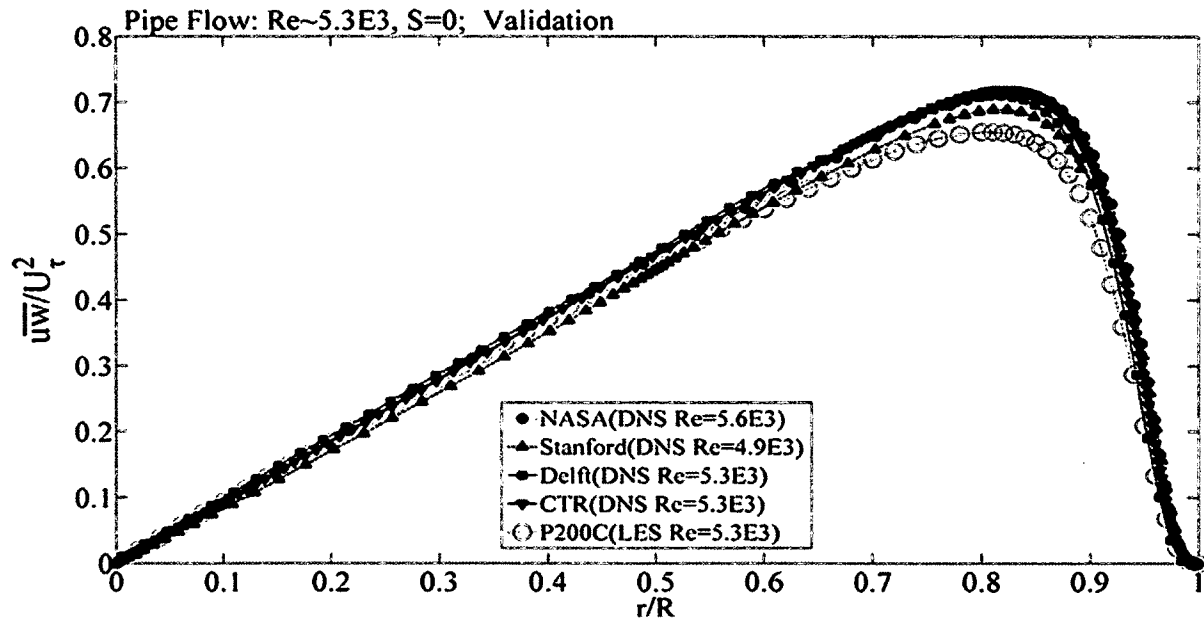


Figure 50: Reynolds shear stress (axial-radial) normalized with friction velocity. $Re=5.3 \times 10^3$; $S=0$.

6.2 NON-ROTATING PIPE FLOW: $Re=12 \times 10^3, 24 \times 10^3$; $S=0$

For pipe flow at a Reynolds number of $Re=12 \times 10^3$ and 24×10^3 without rotation, results were compared to the experimental results of Durst (1995), Facciolo (2006), Itoh, et al. (1996), and Eggels (1994-Delft) as well as the DNS results of Wu and Moin (2008-CTR). All plotted figures include the Reynolds number used in each study. Figure 51 shows good agreement in the mean axial velocity with all available data found in the literature with a slight under prediction near the wall. This under prediction as explained earlier is likely due to insufficient grid resolution near the wall within the viscous layer ($y^+ < 5$) as was shown to be the case in Figure 21.

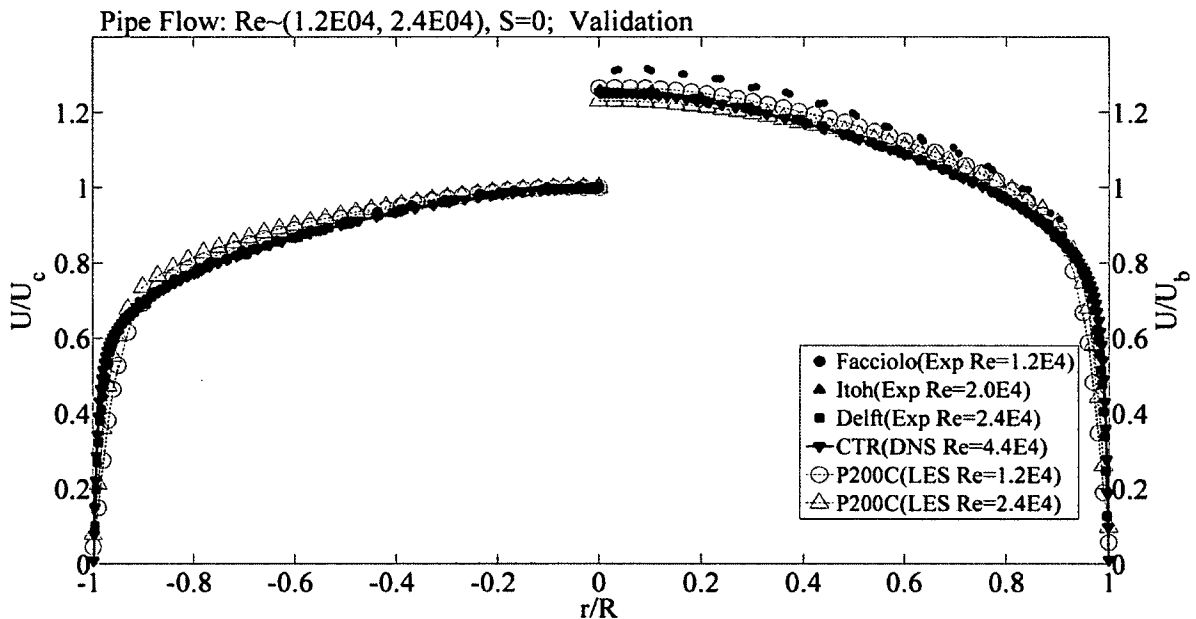


Figure 51: Mean axial velocity, normalized with centerline velocity (left) and with bulk velocity (right). $Re=12 \times 10^3, 24 \times 10^3$; $S=0$.

Figure 52 shows that when normalized by the bulk velocity the axial turbulence intensity appears to significantly under predict the experimental results of Facciolo (2006) throughout the central region of the pipe from $0 < r/R < 0.8$ but appears to agree well for this same region with both the experimental results of Itoh, et al. (1996) and DNS results of Wu and Moin (2008-CTR). For the same region of $0 < r/R < 0.8$ both the radial and tangential turbulent intensities agree quite well with the DNS data of Wu and Moin

(2008-CTR) but significantly under predict the experimental results of Itoh, et al.(1996), especially for the radial turbulent intensity component. Very near the wall, experimental results are not available; when compared to the DNS results of Wu and Moin (2008-CTR) performed at a higher Reynolds number of $Re=44 \times 10^3$, the axial turbulence intensity maximum peak appears to be shifted further away from the wall.

Current simulations results suggest this discrepancy could be in part due to a Reynolds number dependence since the simulations results at the higher Reynolds number of $Re=24 \times 10^3$ do appear to show an axial turbulence intensity maximum peak that is shifted closer to the wall than at the lower $Re=12 \times 10^3$. Very near the wall at $0.9 < r/R < 1$ the axial turbulence peak also shows a slight over prediction at the highest Reynolds number of $Re=24 \times 10^3$ when compared to Wu and Moin (2008-CTR) while both the radial and tangential turbulent intensities seem to be well under predicted. This behavior observed could again be in part due to the difference in Reynolds number used but is more likely due to the lack of grid resolution near the wall of the current LES simulations which would seem to agree well with the observation made in Wu and Moin (2008) that "in coarse DNS or LES calculations the streamwise component of turbulence intensity is amplified, whereas the other components are lower than those in resolved calculations." When normalized in wall units the axial turbulent intensity results of the P200C mesh shown in Figure 53 still show a significant shift in the maximum peak away from the wall, but the peak magnitude is actually lower than that of Wu and Moin (2008) which again suggests a Reynolds number dependence that affects the friction velocity used to scale the turbulence component. Further away from the wall the axial turbulent intensity results agree reasonably well with the experimental results of Durst (1994) appearing to follow the trend of increasing turbulent intensity accordingly as the Reynolds number increases.

Discrepancies in rms values could also be due to inadequate near-wall mesh resolution, previously shown in Figure 21. Another possibility is the use of the sub-grid scale model with a constant value of C_s as the Smagorinsky model. The Germano, et al. (1991) model might have produced better results but at increased computational cost.

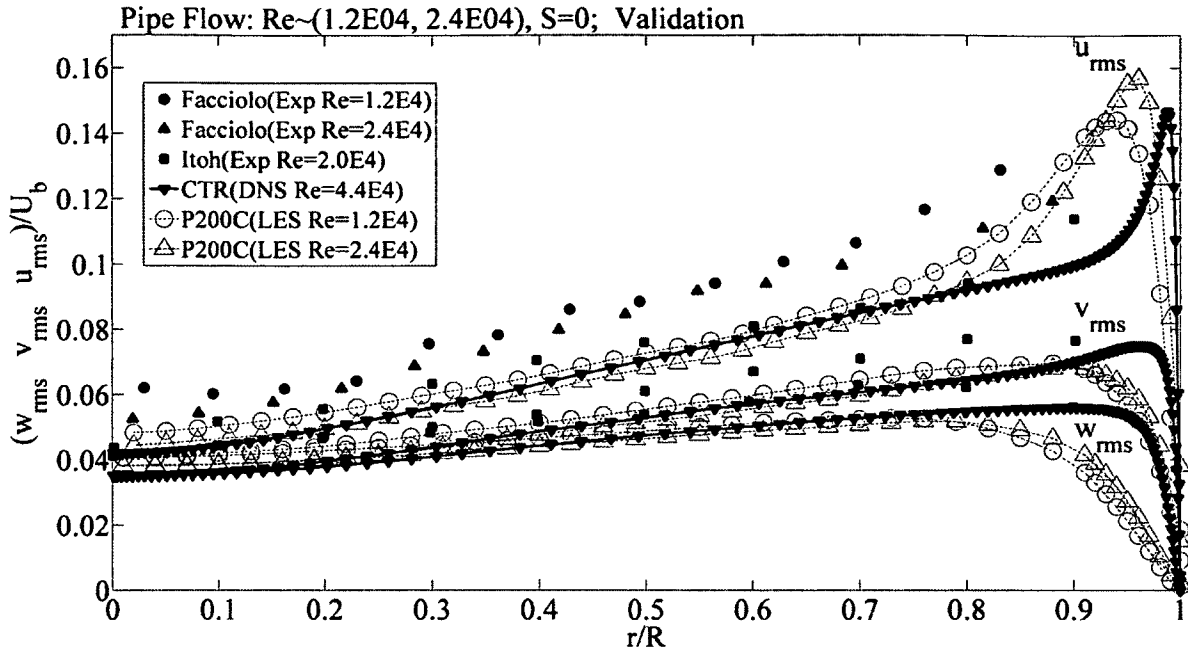


Figure 52: RMS velocities normalized with bulk velocity. $Re=12 \times 10^3, 24 \times 10^3$; $S=0$.

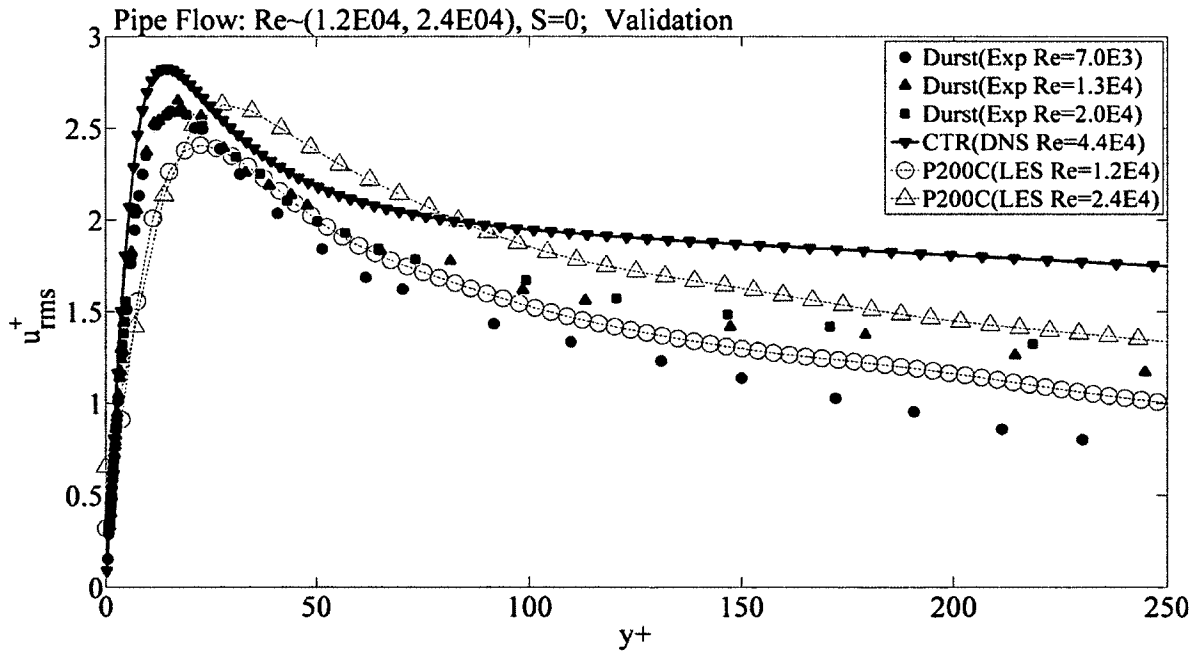


Figure 53: RMS axial velocity in wall units. $Re=12 \times 10^3, 24 \times 10^3$; $S=0$.

Figure 54 and 55 show under-prediction of both the radial and tangential turbulent intensities near the wall but also seem to give acceptable results further away from the wall. A clear under prediction is also noted for the \overline{uw} Reynolds shear stress in Figure 56

for the results at $Re=24 \times 10^3$ when compared to the results of Eggels(1994-Delft) performed at the same Reynolds number.

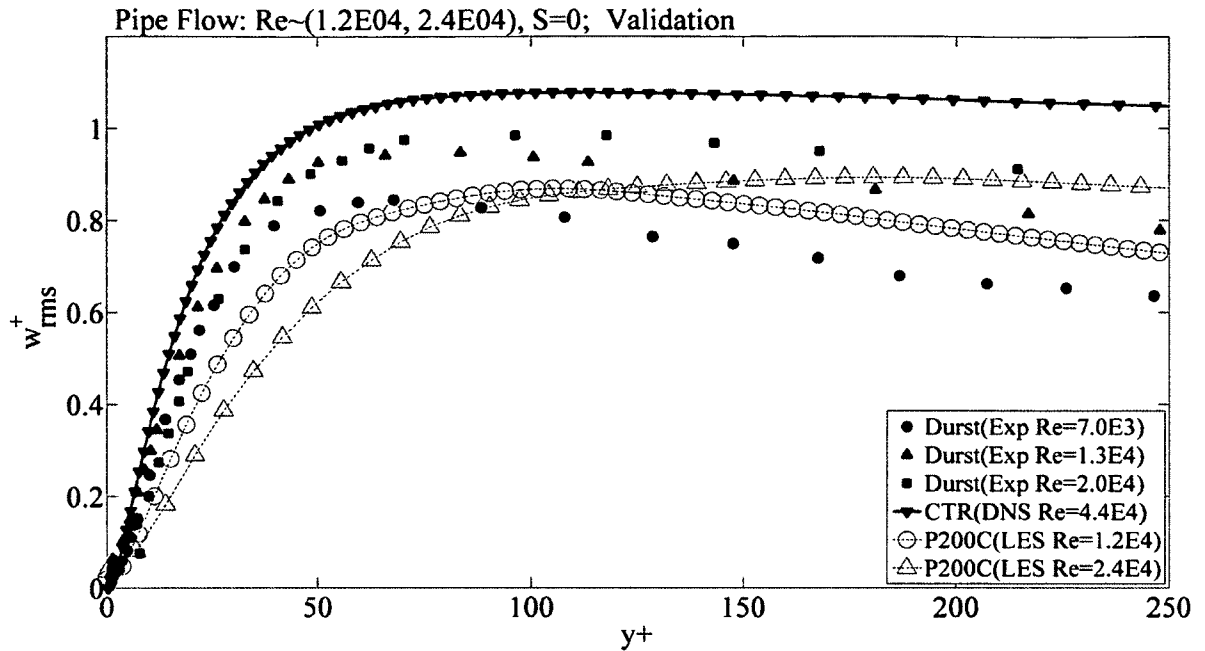


Figure 54: RMS radial velocity in wall units. $Re=12 \times 10^3, 24 \times 10^3$; $S=0$.

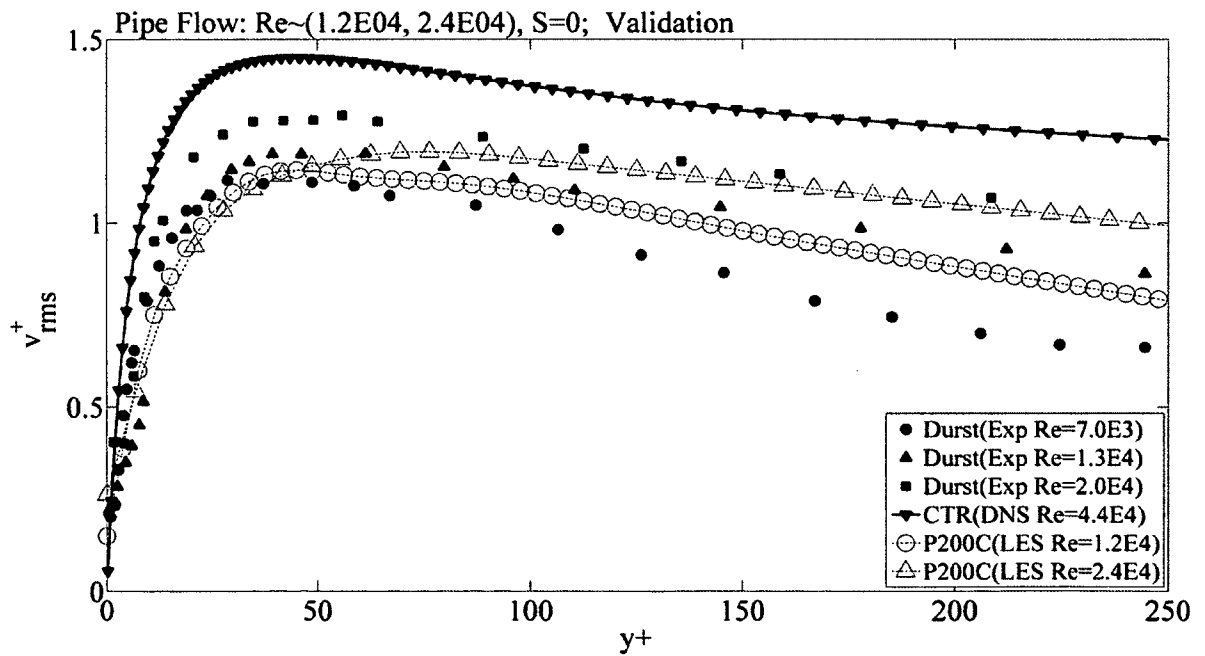


Figure 55: RMS tangential velocity in wall units. $Re=12 \times 10^3, 24 \times 10^3$; $S=0$

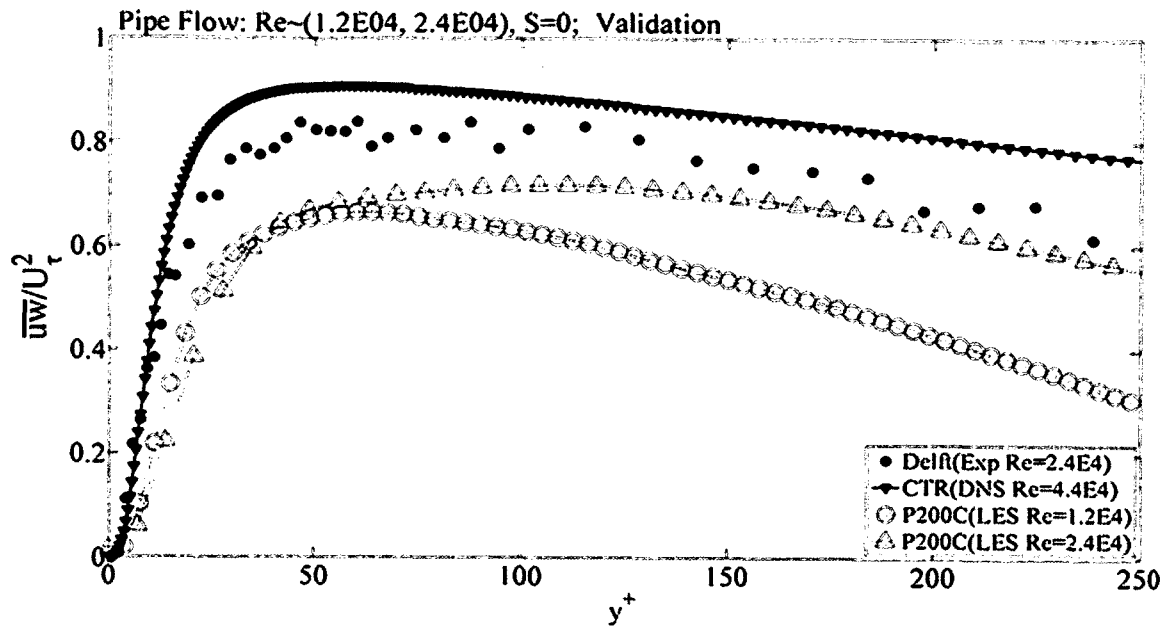


Figure 56: Reynolds shear stress (axial-radial) velocity normalized with friction velocity $Re=12 \times 10^3, 24 \times 10^3$; $S=0$.

6.3 ROTATING PIPE FLOW: $Re=5.3 \times 10^3$; $S=0.5, 1, 2$

For pipe flow at a Reynolds number of $Re=5.3 \times 10^3$ with rotation ($S=0.5, 1, 2$), current LES results were compared to the DNS results of Facciolo (2006) and Orlandi and Fatica (1997-Stanford) as well as the LES results of Feiz(2003) which were performed at comparable Reynolds numbers and swirl rates. All plotted results include the Reynolds number and rotation rates used in each study.

Figure 57 and 58 show excellent agreement with all validation data for the mean axial results normalized with the bulk velocity and centerline velocity respectively. Figure 57 shows how the velocity profile of rotating pipe flow becomes more peaked with an increase in centerline velocity as the rotation rate increases, clearly demonstrating previous findings of the mean axial velocity profile tending toward a parabolic shape with increased rotation (i.e. laminarization). Figure 59 shows the velocity profile normalized in wall units. It is seen that addition of rotation to the pipe shows a slight decrease in velocity in the buffer with increasing rotation. Rotation causes a disruption in the log-layer such that it does not follow the log-layer law as it does for pipe flow without rotation. This is the main reason why, as pointed out in Hirai, et al. (1988), traditional 2-equation models that rely on the log-layer wall are incapable of predicting rotating pipe flow.

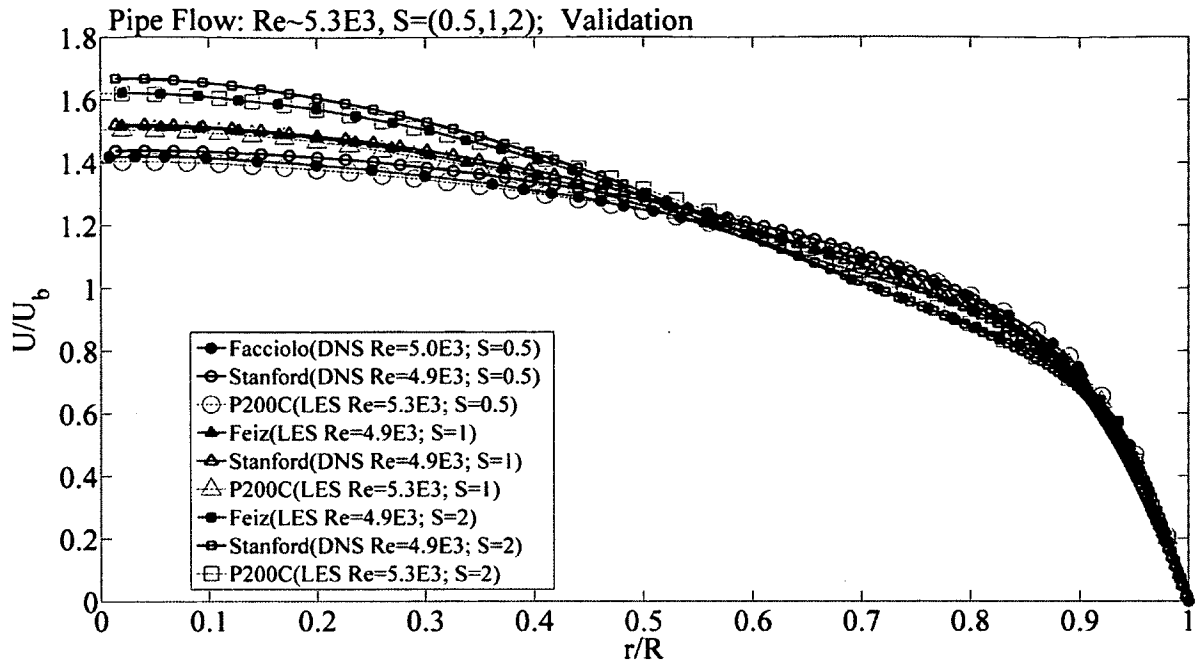


Figure 57: Mean axial velocity normalized with bulk velocity. $Re=5.3 \times 10^3$; $S=0.5, 1, 2$.

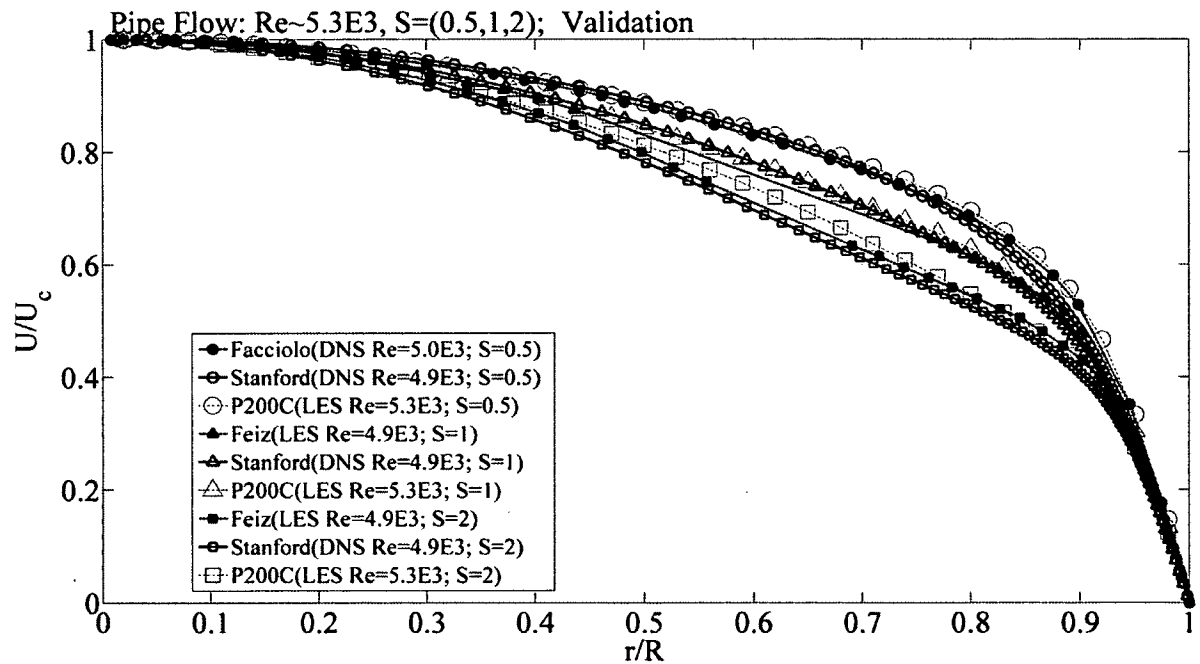


Figure 58: Mean axial velocity normalized with centerline velocity. $Re=5.3 \times 10^3$; $S=0.5, 1, 2$.

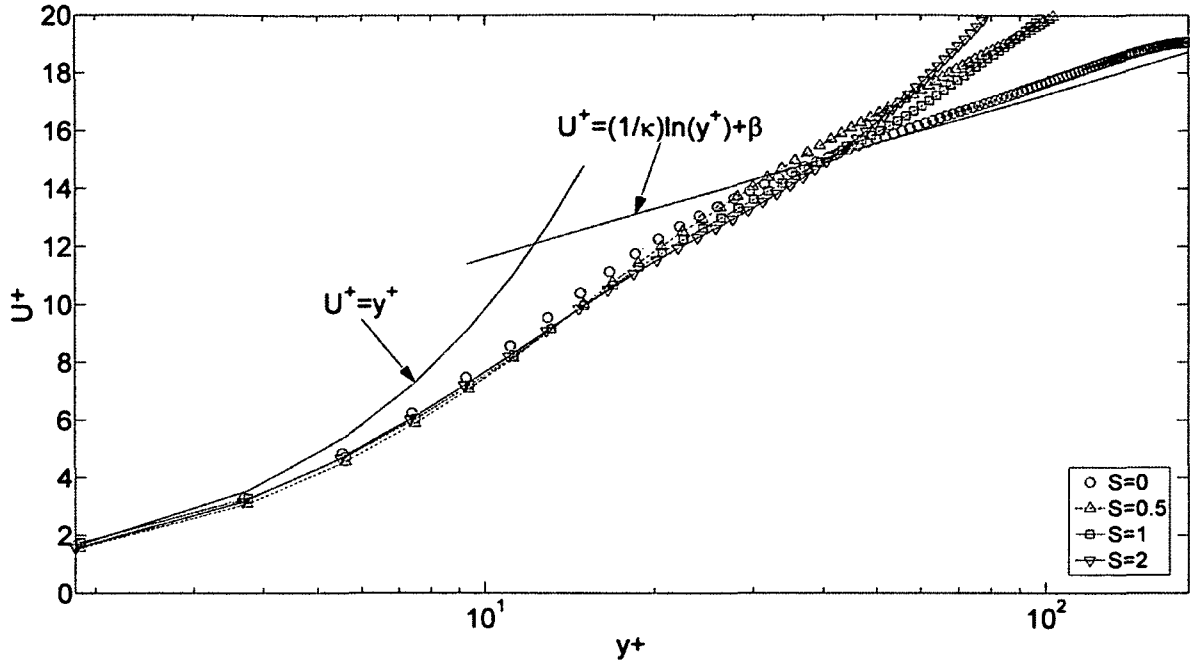


Figure 59: Mean axial velocity in wall units. $Re=5.3 \times 10^3$; $S=0.5, 1, 2$; $\kappa=0.41$; $\beta=5.9$. Rotation effects on log-layer.

Figure 60 shows the mean tangential velocity normalized with the bulk velocity. There is excellent agreement with both the DNS results of Facciolo (2006) and LES results of Feiz (2003). However, they all appear to differ significantly in the central region of the pipe from the results of Orlandi and Fatica (1997-Stanford) which do not seem to follow the expected parabolic curve and instead appear to give a more solid body rotation profile. As rotation increases Figure 61 shows that when normalized with the pipe wall velocity V_w the current LES simulations capture the same profile trend in the central region observed by DNS results of Facciolo (2006) and LES results of Feiz (2003) but show discrepancy with the Orlandi and Fatica (1997-Stanford) data.

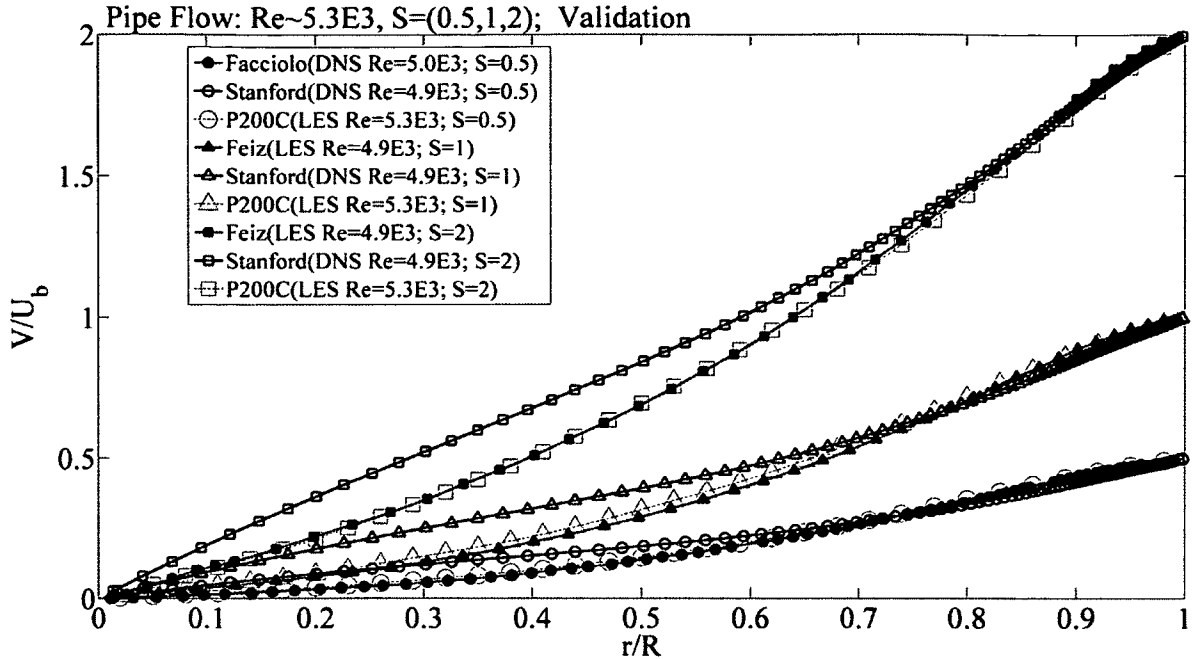


Figure 60: Mean tangential velocity normalized with bulk velocity. $Re=5.3 \times 10^3$; $S=0.5, 1, 2$.

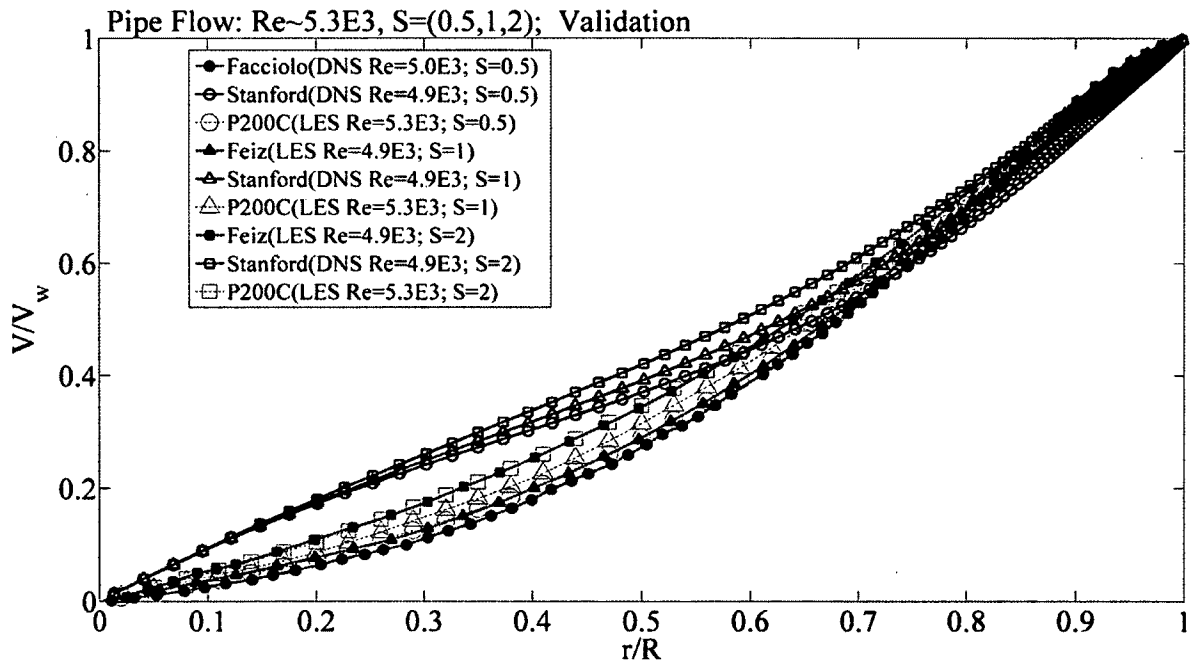


Figure 61: Mean tangential velocity normalized with V_w . $Re=5.3 \times 10^3$ $S=0.5, 1, 2$.

Figure 62 through 64 of the turbulent intensities show generally good agreement with the other data available. For swirl rates of $S=0.5$ to $S=1$ the addition of rotation causes the axial turbulent intensity to decrease near the wall and increase near the central

region. At the highest swirl rate of $S=2$ the axial RMS velocity peak becomes a flat region from approximately $0.65 < r/R < 0.9$. This flattening is considered by Orlandi and Fatica (1997) to be a low-Reynolds number effect since this flattening behavior was not observed in the higher Reynolds number ($Re=3E4$) experiments undertaken by Nishibori, et al.(1987). All results show that the central region axial turbulent intensity near the central region decreases going from a swirl number of $S=1$ to $S=2$ although it is much more subtle in the current LES simulations than validation data of Feiz, et al.(2003) and Orlandi and Fatica (1997-Stanford). Figure 63 and Figure 64 show increases in both the radial and tangential turbulent intensities throughout the pipe with increase in swirl rate from $S=0.5$ to $S=1$, especially in the central region of the pipe. The increase in radial and tangential RMS velocities, however, seems to be minimal for the current LES simulation going from a rotation rate of $S=1$ to $S=2$.

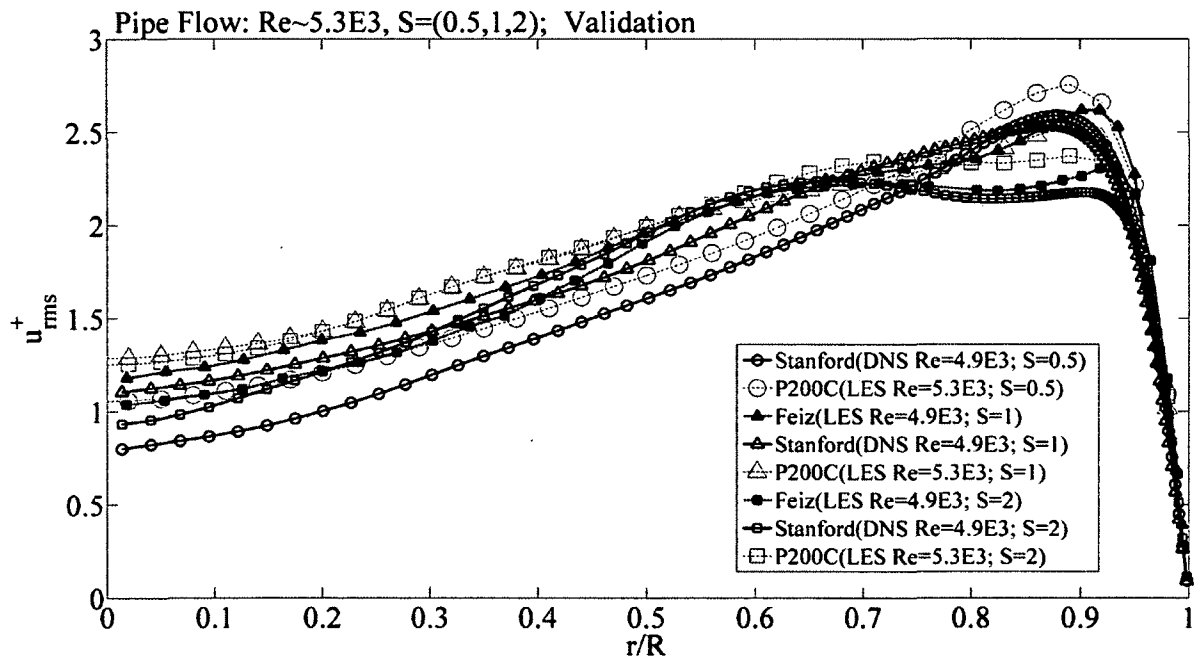


Figure 62: RMS Axial velocity in wall units. $Re=5.3 \times 10^3$; $S=0.5, 1, 2$.

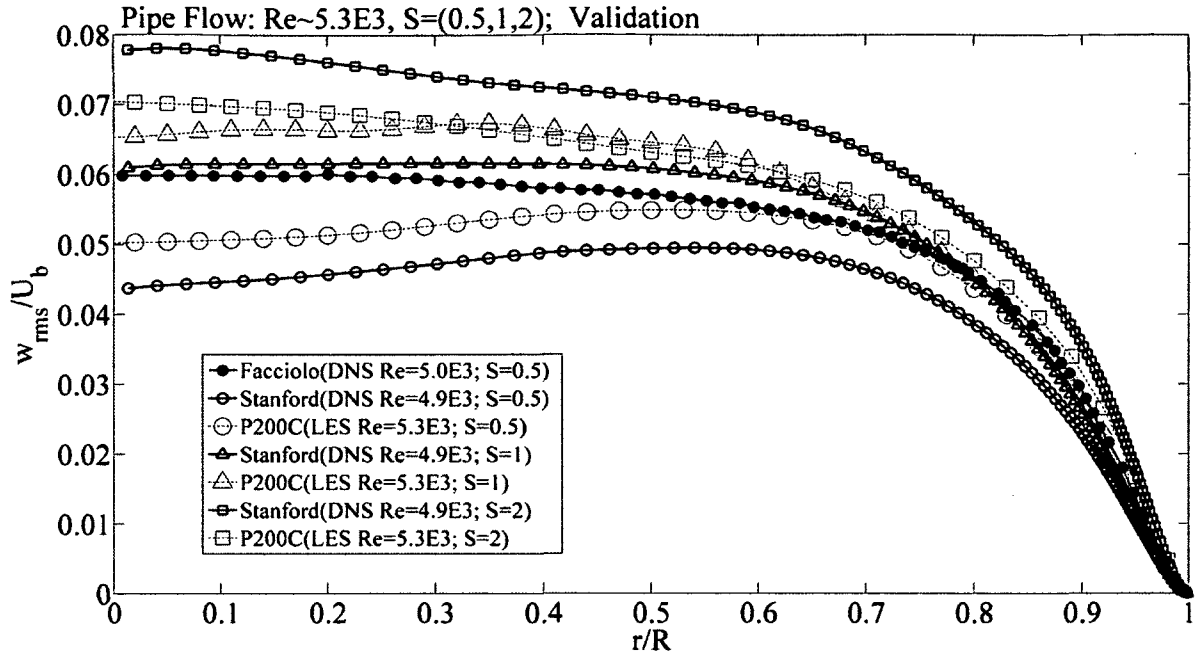


Figure 63: RMS radial velocity normalized with bulk velocity. $Re=5.3 \times 10^3$; $S=0.5, 1, 2$.

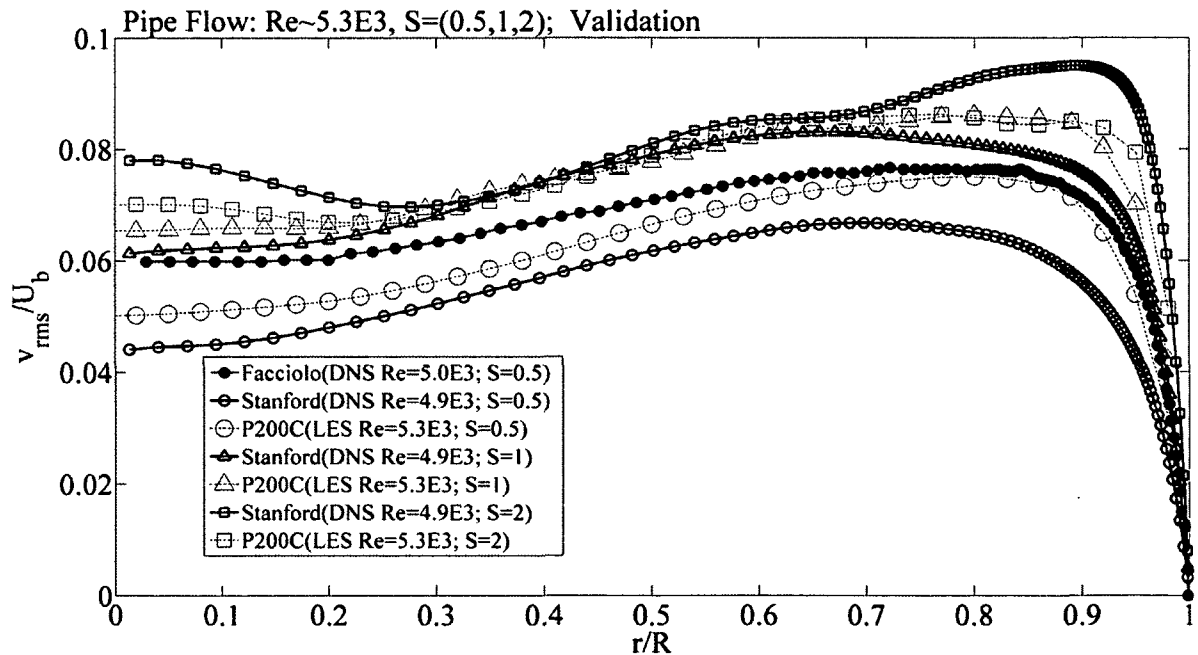


Figure 64: RMS tangential velocity normalized with bulk velocity. $Re=5.3 \times 10^3$; $S=0.5, 1, 2$.

The influence of rotation has been found to reduce the axial-radial shear stress, \overline{uw} , while increasing the other two Reynolds stresses, axial-tangential (\overline{uv}) and radial-tangential \overline{vw} , as can be seen in Figure 65 thru 67. Axial-radial (\overline{uw}) Reynolds shear

stress results shown in Figure 65 are in good agreement between current LES simulations and available validation data. Figure 66 shows the axial-tangential (\overline{uv}) Reynolds shear stress which is zero in non-rotating pipe flow. As rotation is increased beyond $S=0.5$ oscillatory behavior in the axial-tangential Reynolds stress is observed. As explained by Orlandi (2000), these oscillations occur due to long spiral structures that form in the central region of the pipe with their effect being more pronounced as rotation increases. The high values of axial-tangential stress are related to the tilting of the near wall vortical structures (Orlandi, 1997). The radial-tangential \overline{vw} shear stress in Figure 67 does not show such oscillatory behavior and has the smallest magnitude of all Reynolds shear stresses. The current LES results for Reynolds stresses show satisfactory trends and values that match validation data.

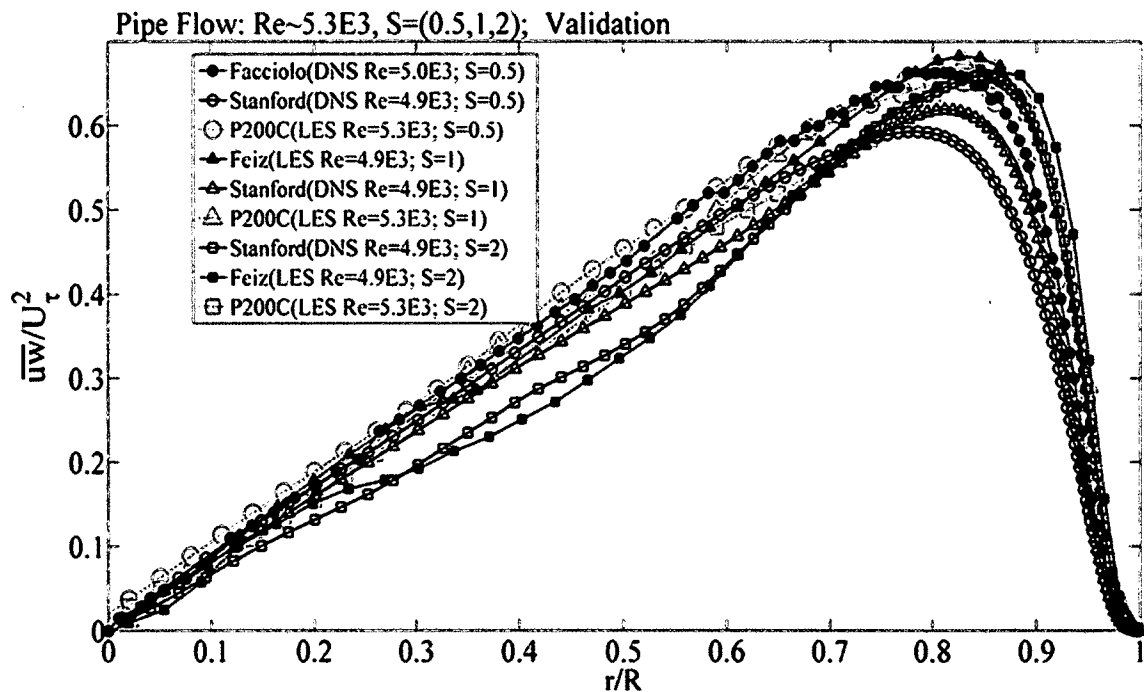


Figure 65: Reynolds shear stress (axial-radial) normalized with friction velocity. $Re=5.3 \times 10^3$; $S=0.5, 1, 2$.

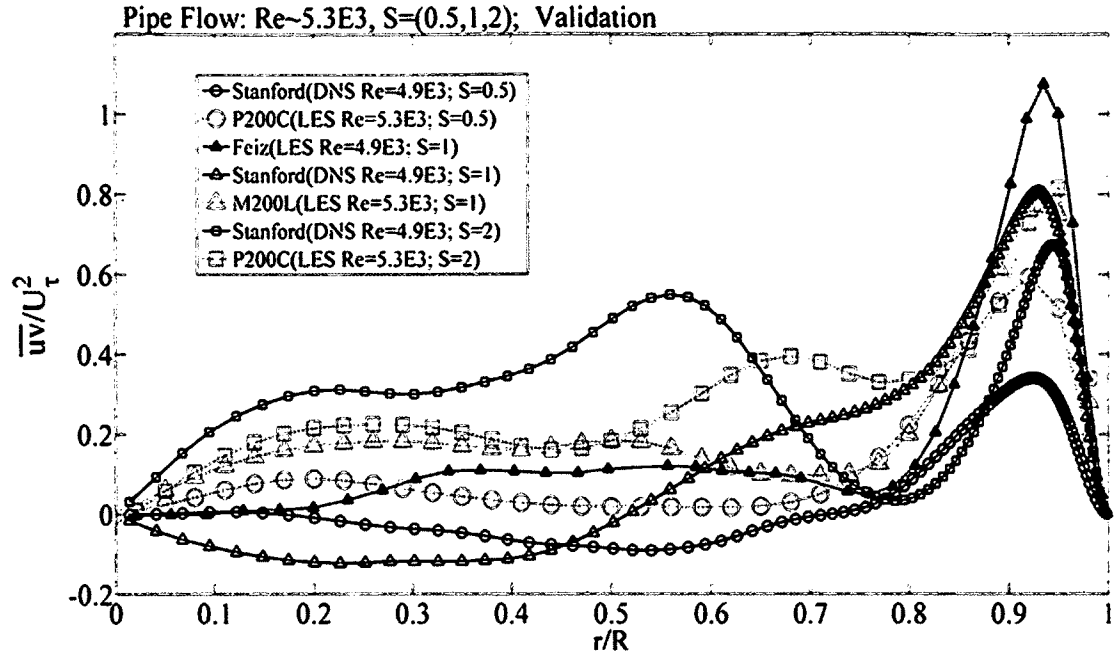


Figure 66: Reynolds shear stress (axial-tangential) normalized with friction velocity. $Re=5.3 \times 10^3$; $S=0.5, 1, 2$.

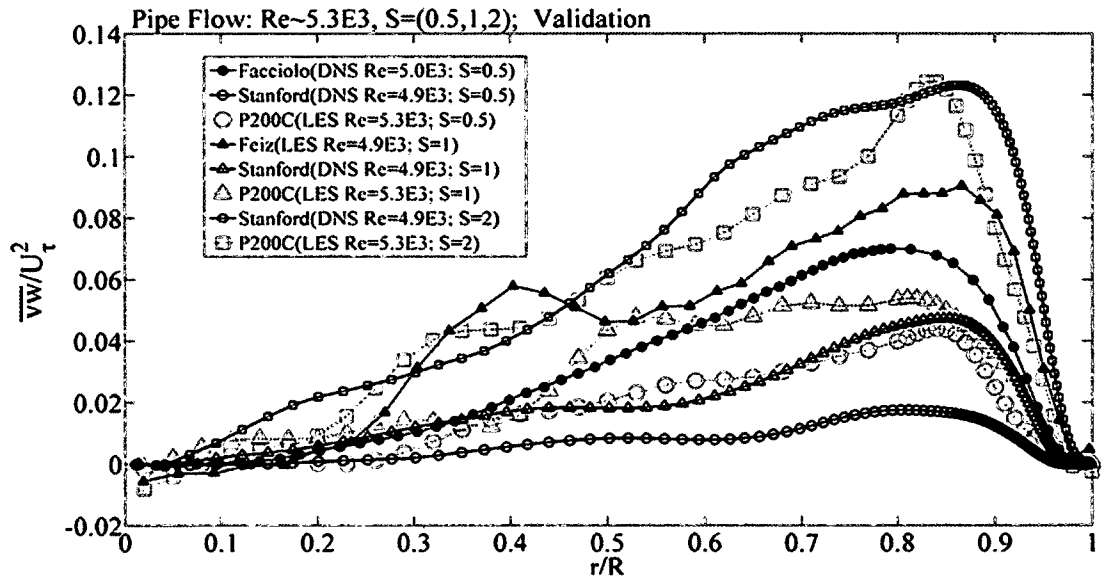


Figure 67: Reynolds shear stress (radial-tangential) normalized with friction velocity. $Re=5.3 \times 10^3$; $S=0.5, 1, 2$.

6.4 ROTATING PIPE FLOW: $Re=12 \times 10^3, 24 \times 10^3$; $S=0.5$

For pipe flow with $S=0.5$ rotation at Reynolds numbers of $Re=12 \times 10^3$ and $Re=24 \times 10^3$ results of the LES on the P200C mesh are compared to the DNS and experimental results of Facciolo (2006), Itoh, et al. (1996) and the LES simulations of Yang (2000). As seen in Figure 68, the current mean axial velocity agrees well with all available validation data. When normalized with the bulk velocity it appears that the experimental data results for mean axial velocity of Facciolo(2006) are significantly higher than all other data. It should be noted that this data of Facciolo(2006) is what will be used to validate the jet flow results in the following sections.

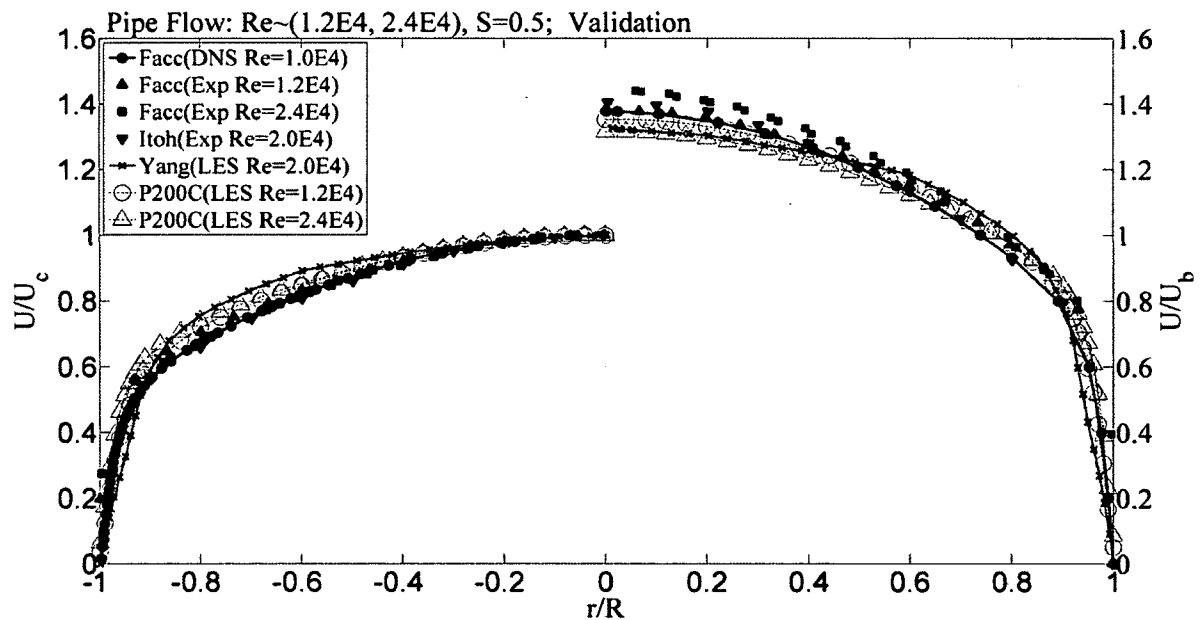


Figure 68: Mean axial velocity, normalized with centerline velocity (left) and bulk velocity (right) $Re=12 \times 10^3, 24 \times 10^3$; $S=0.5$.

Figure 69 shows that current LES results of the mean tangential velocity are nearly a perfect match when compared to both the DNS and experimental data of Facciolo (2006) but appear to deviate significantly from the LES results of Yang (2000) and experimental results of Itoh, et al. (1996).

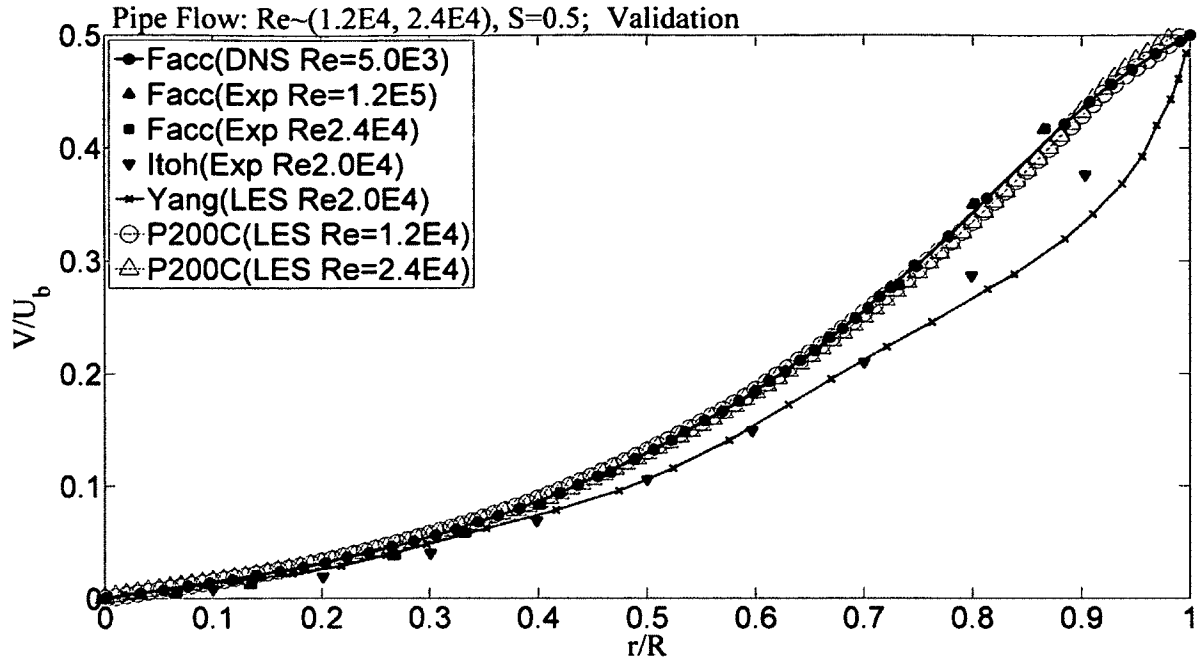


Figure 69: Mean tangential velocity normalized with U_b . $Re=12 \times 10^3, 24 \times 10^3$; $S=0.5$.

Figure 70 shows that the current LES results for the RMS axial velocity appear to be in very good agreement with the experimental data of both Facciolo (2006) and Itoh, et al. (1996). The LES results of Yang(2000) seem to significantly under predict the RMS axial velocity and their maximum peak also seems to be shifted further away from the wall when compared to available experimental data and the current LES simulations. The current results for the RMS radial velocity shown in Figure 71, however, seem to over-predict near the central region while under predicting the peak value near the wall displaying an overall flatter shape than all the other data. A possible reason for this discrepancy could be the highly dissipative nature of the Smagorinsky subgrid scale model used. The results for the RMS tangential velocity shown in Figure 72 are in better agreement than the radial rms results, especially with the Facciolo (2006) experimental results.

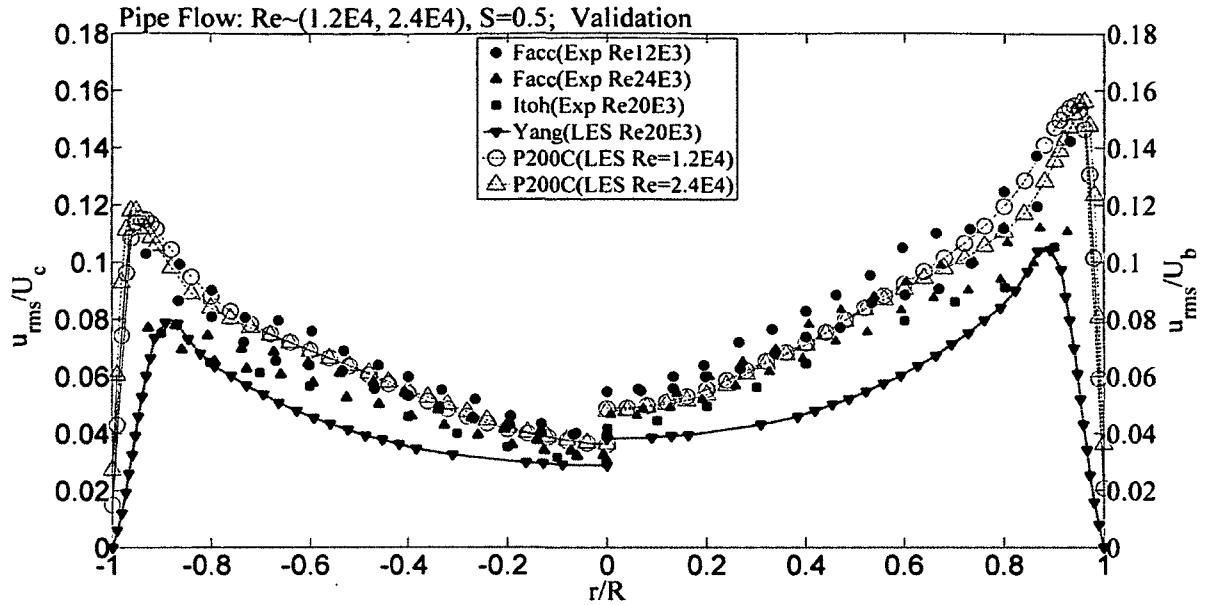


Figure 70: RMS axial velocity normalized with centerline velocity (left) and bulk velocity (right). $Re=12 \times 10^3, 24 \times 10^3$; $S=0.5$

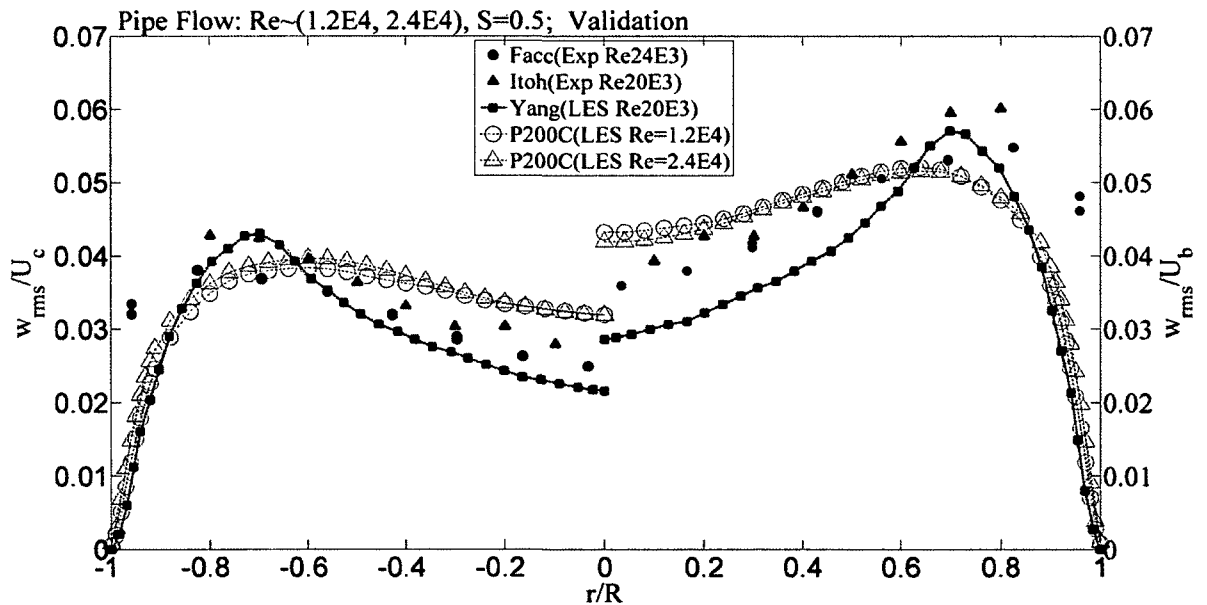


Figure 71: RMS radial velocity normalized with centerline velocity (left) and bulk velocity (right). $Re=12 \times 10^3, 24 \times 10^3$; $S=0.5$

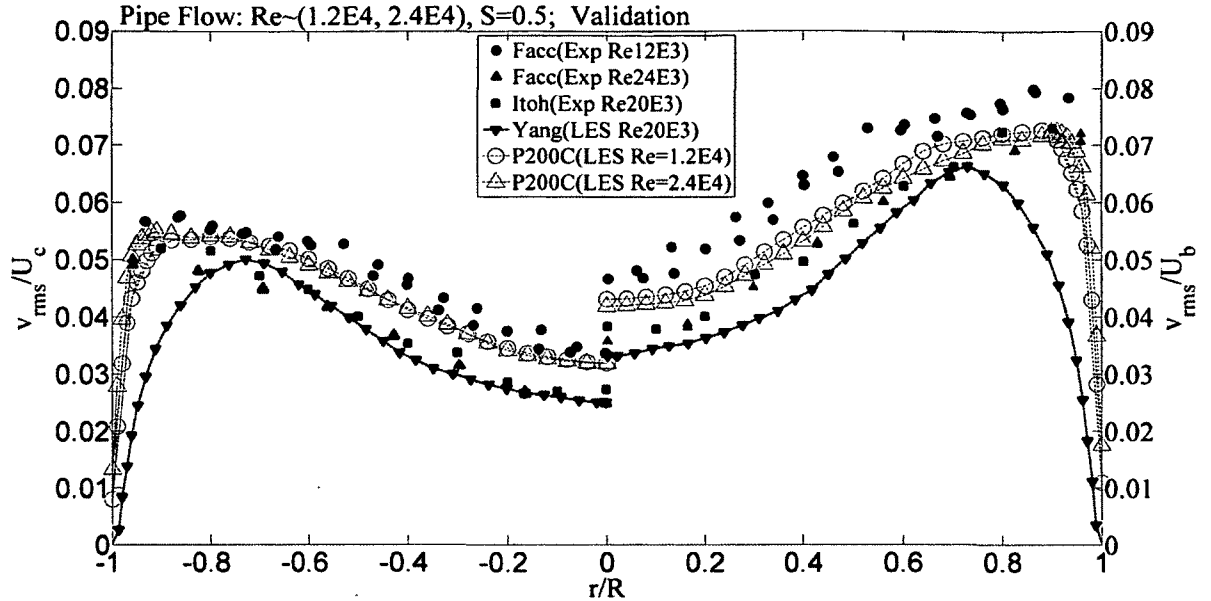


Figure 72: RMS tangential velocity normalized with centerline velocity (left) and bulk velocity (right). $Re=12 \times 10^3, 24 \times 10^3$; $S=0.5$.

6.5 PIPE FLOW: REYNOLDS STRESS ANISOTROPY

The invariant representation of Reynolds stresses is a useful tool to quantify the departure from isotropy, axisymmetry and two-component turbulence. A brief review of the invariant analysis developed by Lumley and Newman(1977) is presented. The Reynolds stress tensor ($\tau_{ij} = \overline{\rho u_i u_j}$), may be written in terms of an anisotropic (τ'_{ij}) and an isotropic tensor (τ^o_{ij}). The isotropic part may be written as $\tau^o_{ij} = (1/3)\tau^o_{kk}\delta_{ij}$ and the anisotropic part as $\tau'_{ij} = \tau_{ij} - (\tau_{kk}/3)\delta_{ij}$. In order to define the limiting states of turbulence Lumley and Newman(1977) defined the anisotropic tensor

$$b_{ij} = \frac{\overline{u_i u_j}}{q^2} - \frac{1}{3}\delta_{ij} \quad \text{Eqn. 6-4}$$

where $q^2 = \overline{u_k u_k}$ is twice the turbulent kinetic energy, and the coordinate indices i, j, k range over the set $\{1, 2, 3\}$ corresponding to 1-u (Axial), 2-v (Tangential) and 3-w (Radial). The first invariant of the anisotropic tensor b_{ij} is zero. The second and third invariants can be written as:

$$II_b = b_{ij} b_{ji} \quad \text{Eqn. 6-5}$$

$$III_b = b_{ij} b_{jk} b_{ki} \quad \text{Eqn. 6-6}$$

For realizable turbulence, the diagonal elements of b_{ij} are restricted to $(-1/3 \leq b_{ij} \leq 2/3)$. Based on these restrictions, in the simplest case of axisymmetric turbulence Lumley(1978) concluded that all realizable turbulence must lie inside the region bounded by the joint variations of II_b and III_b as follows:

$$II_b = \frac{3}{2} \left(\frac{4}{3} |III_b| \right)^{2/3} \quad \text{Eqn. 6-7}$$

In the case of isotropic two-component turbulence all off diagonal components of $\overline{u_i u_j}$ vanish such that the relation between the invariants for the two-component turbulence may be expressed as:

$$II_b = \frac{2}{9} + 2III_b \quad \text{Eqn. 6-8}$$

Figure 73 shows the anisotropy-invariant map defined by Eqn. 6-5 and Eqn. 6-6 which bounds all realistic turbulence. The two curves shown in the figure correspond to axisymmetric turbulence and the straight line corresponds to two-component turbulence. The limiting points in the right and left corner points correspond to one-component and isotropic two-component turbulence, respectively. At the origin, turbulence is isotropic with all diagonal components equal, and off diagonal values are zero.

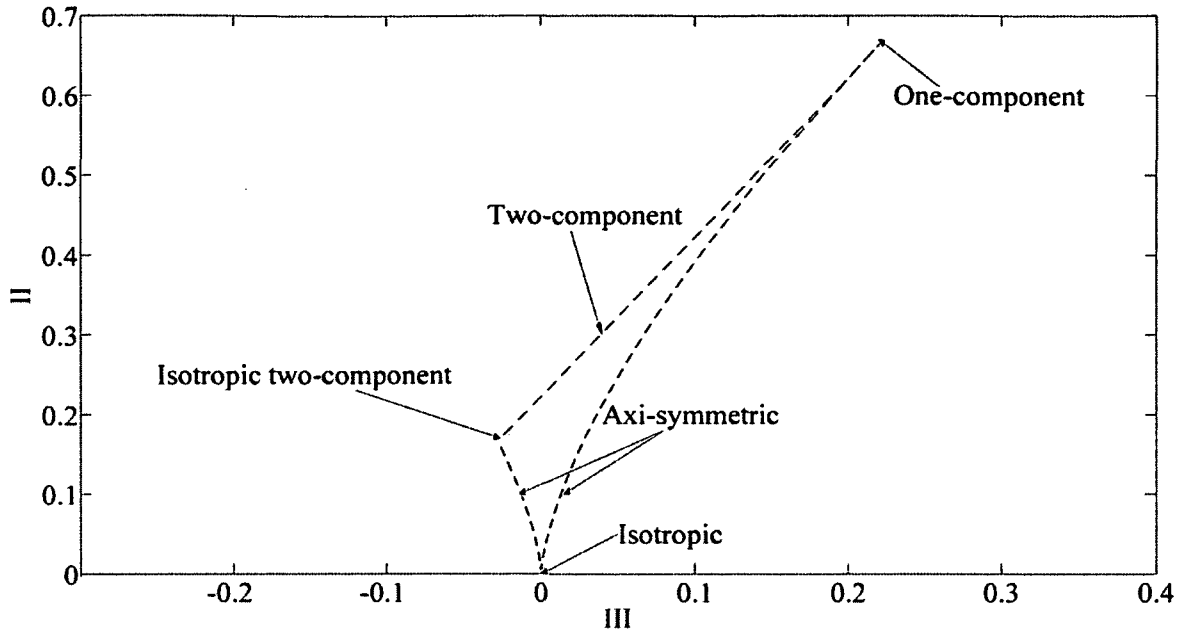


Figure 73: Reynolds stress anisotropy invariant map showing limiting boundaries.

The Reynolds stress anisotropic tensor components and the scalar invariants map for pipe flow at $Re=5.3 \times 10^3$ and $S=(0,0.5,1,2)$ are shown in Figure 74 and 75, respectively. Figure 74 shows that the b_{11} component is dominant in the near wall region, $0.8 < r/R < 1$. In the absence of rotation it approaches the one-component value of 0.67. With the introduction of rotation, there is a transfer of turbulent energy from the component to the b_{22} component, whereas b_{33} is unchanged. The b_{22} component is in the tangential direction; hence, pipe rotation imparts additional turbulent energy in the direction of rotation. On the other hand, near the center of the pipe, with increased rotation, energy is transferred from the b_{11} to both the b_{22} and b_{33} component, resulting in near isotropy. With respect to the shear stress components, increased rotation led to reduction of the b_{12} component and increases in the b_{13} component. In the absence of rotation, the pipe flow is axi-symmetric and the b_{13} component is zero. With the addition of pipe rotation, the moving wall imparts strong shear at the wall; hence, the b_{13} component is increased significantly.

Figure 75 shows the Reynolds stress anisotropy invariant map, between the wall and the center of the pipe, for various swirl rates. Each map starts on the 2-component limit in the viscous sublayer, because of the blocking effect. They move rightwards,

towards the 1-component limit, in the buffer layer. They then turn and move towards isotropy in main turbulent inner and outer layers. At the pipe center, $r=0$, the Reynolds stress is essentially isotropic. The effect of rotation is to move the maps leftwards away from the one-component limit, thereby reducing near-wall anisotropy and increasing the rate of return to isotropy as the pipe center is approached.

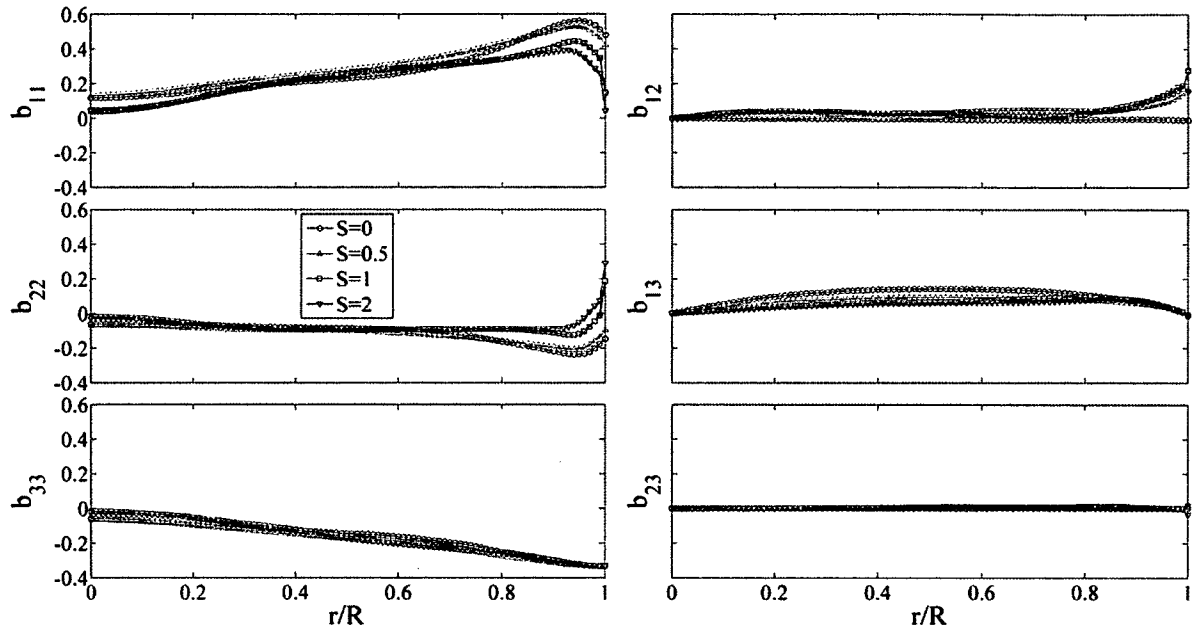


Figure 74: Reynolds stress anisotropy tensor components for pipe flow at $Re=5.3 \times 10^3$ and $S=0, 0.5, 1, 2$: Effect of rotation rate.

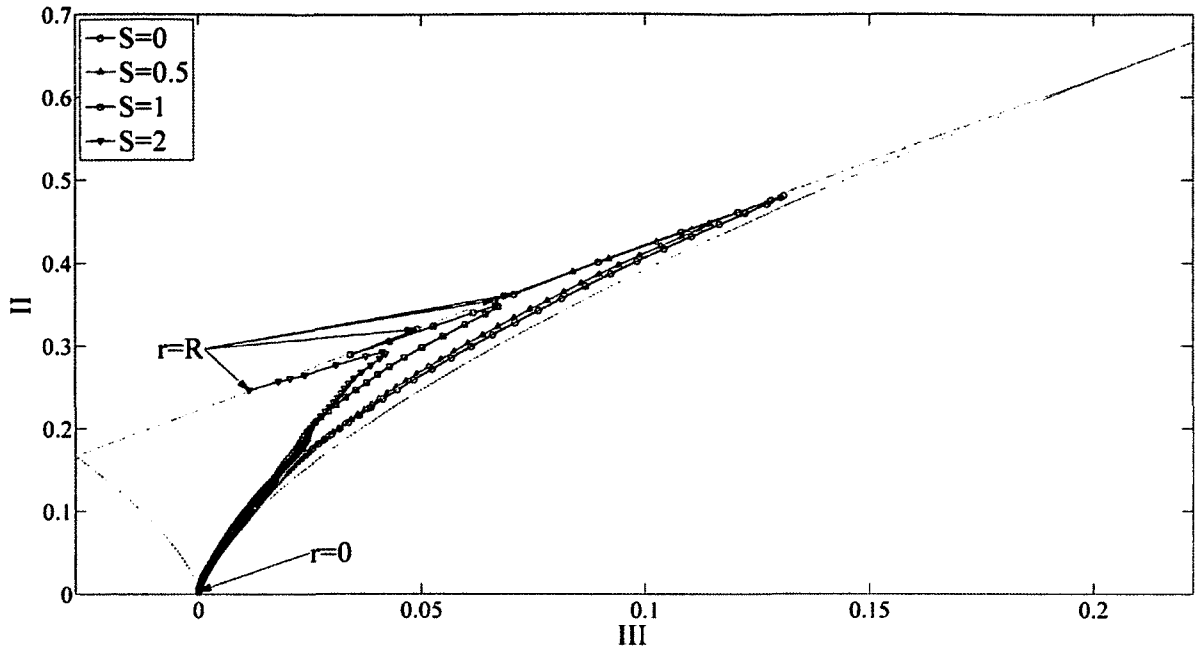


Figure 75: Reynolds stress anisotropy invariant map of pipe flow $Re=5.3 \times 10^3$ and $S=0,0.5,1,2$: Effect of rotation rate.

Figure 76 shows the anisotropy tensor components at the three Reynolds numbers tested. All components collapse at the higher Reynolds numbers of $Re=12 \times 10^3$ and 24×10^3 . All nonzero components (b_{11} , b_{22} , b_{33} , b_{12}) differ for the lower Reynolds number $Re=5.3 \times 10^3$ suggesting there is a Reynolds number effect present. The anisotropy invariant map also shows a collapse of the higher Reynolds number and shows a return towards isotropy moving towards the center of the pipe ($r=0$) that is further from the axisymmetric limit than the lower Reynolds number of $Re=5.3 \times 10^3$.

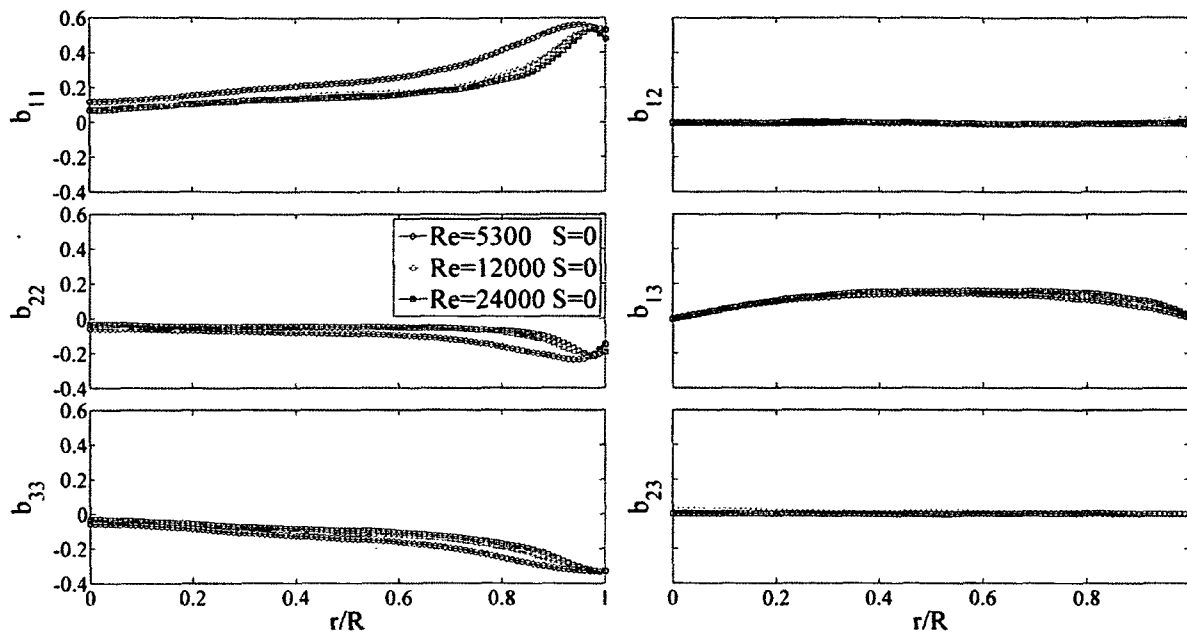


Figure 76: Reynolds stress anisotropy tensor components for pipe flow at $Re=5.3 \times 10^3$, 12×10^3 , 24×10^3 ; $S=0$: Effect of Reynolds number.

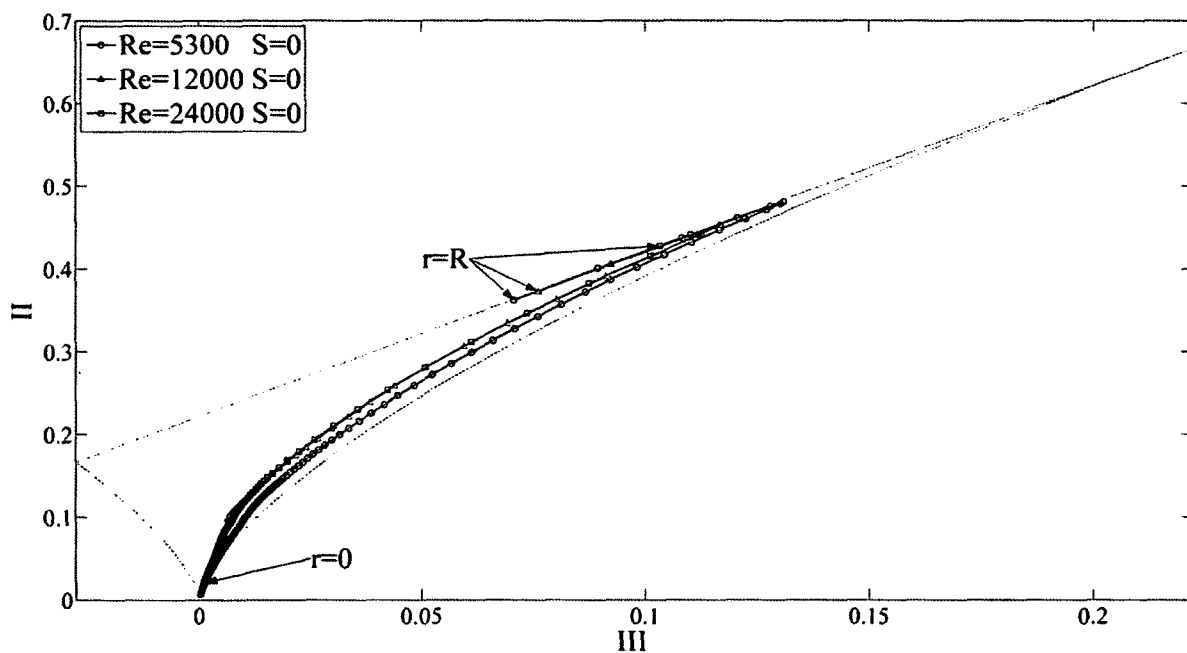


Figure 77: Reynolds stress anisotropy invariant map for pipe flow at $Re=5.3 \times 10^3$, 12×10^3 , 24×10^3 ; $S=0$: Effect of Reynolds number.

7 JET FLOW VALIDATION

7.1 JET FLOW: $Re=12 \times 10^3, 24 \times 10^3$; $S=0, 0.5$

Axisymmetric jet flow studies have typically used one of two boundary conditions: either jet flow exiting a smooth contraction nozzle or jet flow exiting a long pipe, with the vast majority using the former. Only a limited number of studies of round turbulent jet flow emitted from a fully-developed pipe were found in the literature, [Rose(1962), Boguslawski and Popiel(1979), Lai(1991), Papadopoulos and Pitts(1998), Ferdman, et al.(2000), Facciolo(2006)]. The parameters for fully-developed turbulent jet flow exiting a pipe were chosen in this investigation to match the experimental data of Facciolo (2006) since this was the only study found to include and report data for rotating pipe flow as well as swirling jet flow emitted from a fully-developed rotating pipe.

For jet flow with no rotation the two current cases used for validation comparison purposes are the "P200C-Mesh3" and "P200C-Mesh5" simulations which refer to the cases where the instantaneous cross sectional area velocity profiles collected for the P200C pipe flow simulation were used as the jet inlet boundary condition using jet mesh#3 and jet mesh#5 respectively. Non-swirling jet flow results were compared to the experimental results of Facciolo(2006), Lai(1991) and Ferdman, et al.(2000). For jet flow with rotation, only mesh#3 was tested and current results were once again compared to the experimental results of Facciolo(2006) as well as their DNS results performed at a Reynolds number of $Re=10^4$, and the experimental results of Rose(1962) were performed at a Reynolds number of 9.6×10^3 and slightly higher rotating rate of $S=0.6$.

As shown in Figure 78, the mean centerline axial velocity when normalized with the bulk velocity of the current simulations seems to be significantly lower than all the experimental data of Facciolo(2006) throughout the domain, including immediately near the jet inlet, for both Reynolds numbers of $Re=12 \times 10^3$ and $Re=24 \times 10^3$, with and without rotation. When compared to the experimental data of Ferdman, et al. (2000) at a Reynolds number of $Re=24 \times 10^3$ and $S=0$, however, Figure 79 shows that the current results agree more closely and are actually slightly higher near the jet inlet.

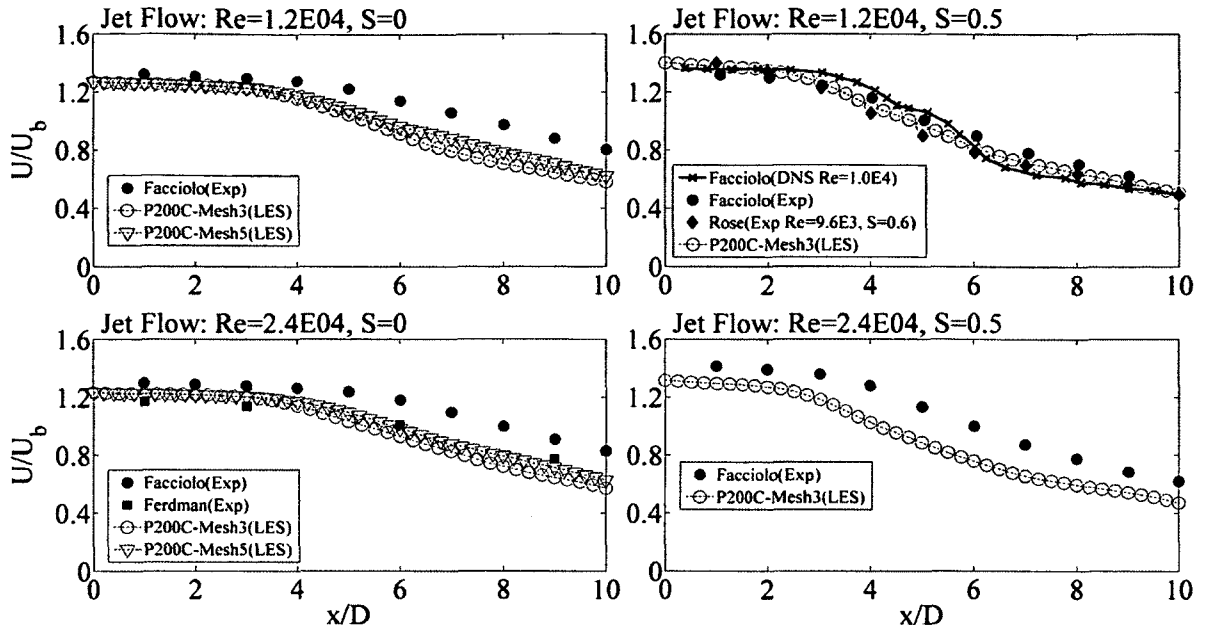


Figure 78: Jet centerline axial velocity normalized with U_b .

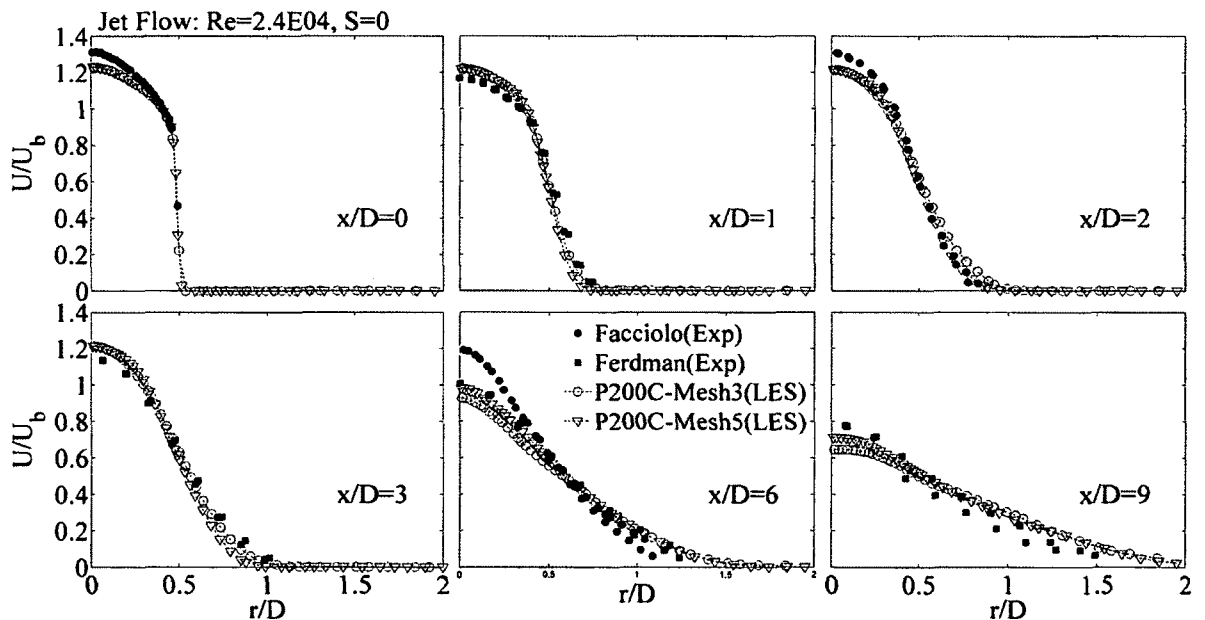


Figure 79: Jet profiles of axial velocity normalized with U_b . $Re=24 \times 10^3$; $S=0$.

For jet flow with rotation of $S=0.5$, Figure 78 shows that current results again seem to under predict the experimental results of Facciolo(2006) at both Reynolds numbers tested. At a Reynolds number of $Re=12 \times 10^3$ with rotation current results agree better with the DNS data of Facciolo(2006) performed at a slightly lower Reynolds

number of $Re=10^4$ especially near the inlet from $0 < x/D < 2$ and further downstream from $6 < x/D < 10$ but still exhibits a slightly faster decay in the intermediate region from $2 < x/D < 6$. As seen in Figure 78, the current simulations also display the influence of jet rotation to change the velocity decay curve as observed by Facciolo(2006). Without rotation the velocity decay is nearly linear, but with addition of rotation the velocity decay is slightly curved, with an initially larger decay slope from approximately $2 < x/D < 7$, followed by a lower decay slope thereafter from $7 < x/D < 10$.

It should be pointed out that the discrepancy (lower velocity) observed between the current LES simulations jet mean axial velocity normalized with the bulk velocity and the experimental data of Facciolo(2006) was also observed in the validation of the mean axial velocity of the non-rotating pipe flow, as was shown in Figure 51. Compared to other validation data (both experimental and DNS) of non-rotating pipe flow, it was shown in Figure 51 that they agreed better with current results and appear to collapse to the same profile regardless of Reynolds number when normalized with the bulk velocity, suggesting that the experimental data of Facciolo (2006) may be slightly higher, perhaps due to experimental error in accurately determining a bulk velocity value used to scale the mean axial velocity.

The centerline velocity, normalized with value at the jet inlet ($x/D=0$), is shown in Figure 80 to decay faster for the current simulations than in other data with the exception of the experimental data of Rose(1962), which was performed at a Reynolds number of 9.6×10^3 and rotation rate of $S=0.6$, which appears to closely match current results of jet flow at a higher Reynolds number of $Re=12 \times 10^3$ and $S=0.5$. When normalized with the centerline velocity, both non-swirling experimental data sets of Lai(1991) and Ferdman, et al.(2000) closely match that of Facciolo(2006) and seems to suggest that the mean centerline velocity decay of the current LES simulation is indeed over predicted, with the end of the potential core region occurring about half a diameter further upstream than both sets of experimental data. The faster decay rate is likely due to a combination of insufficient grid resolution as well as the known highly dissipative nature of the Smagorinsky subgrid scale model used in the current LES simulations. As expected, the over prediction in decay seems to be slightly larger for the coarser jet mesh#3 than the finer jet mesh#5.

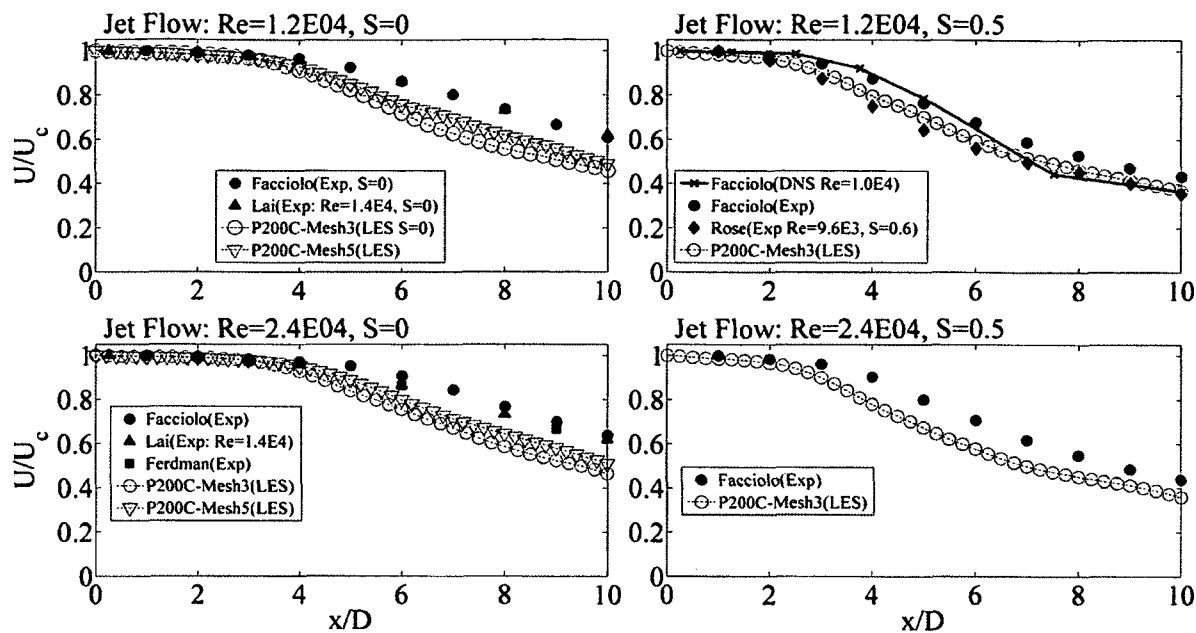


Figure 80: Jet Centerline Axial velocity normalized with U_c .

Figure 81 shows the axial velocity profiles normalized with the local centerline velocity, at various axial locations. The agreement with the experimental data of Lai(1994) is excellent throughout the domain, with perhaps a slight over prediction after $x/D > 8$ for the coarser jet mesh#3. Figure 82 shows similar agreement between the current LES and the experimental results of Facciolo(2006) and Ferdman, et al.(2000) for non-swirling jet flow at a Reynolds number of $Re=24 \times 10^3$.

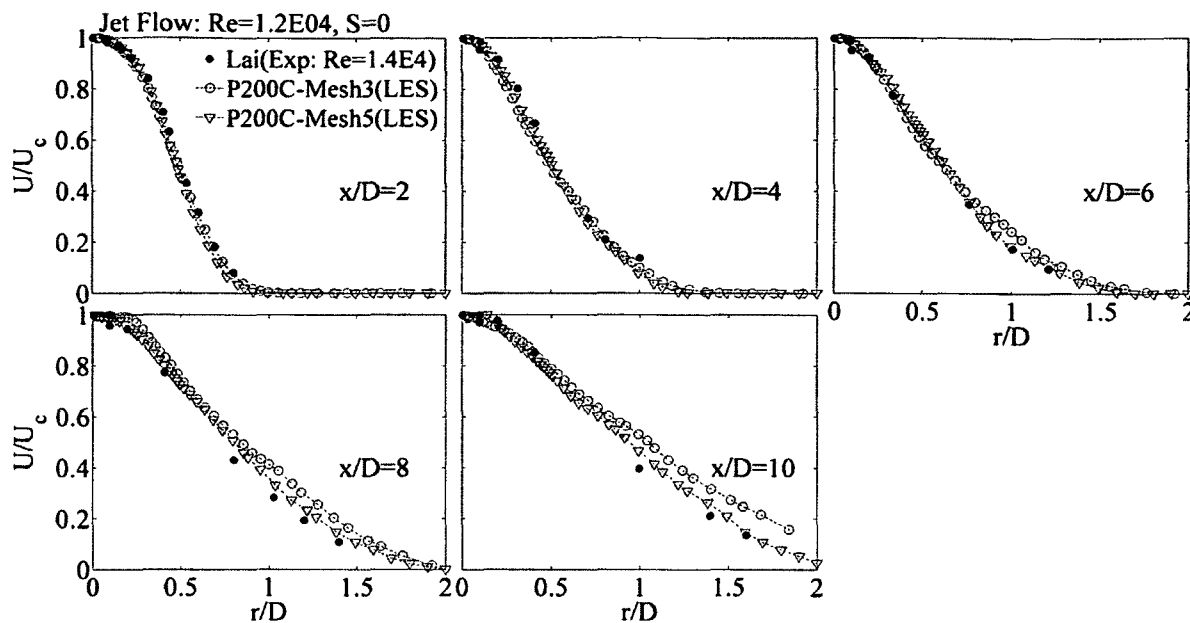


Figure 81: Jet profiles of axial velocity normalized with U_c . $Re=12 \times 10^3$; $S=0$.

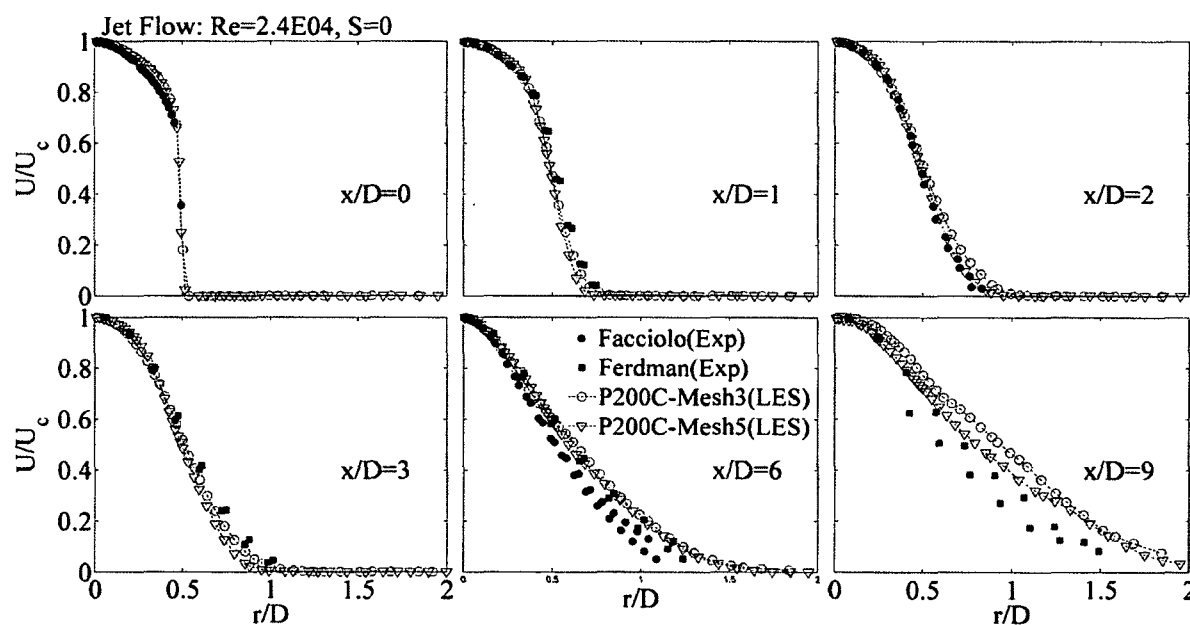


Figure 82: Jet profiles of axial velocity normalized with U_c . $Re=24 \times 10^3$; $S=0$.

Axial velocity profiles for jet flow with rotation of $S=0.5$ are shown in Figure 83 and 84 for Reynolds number of $Re=12 \times 10^3$ and $Re=24 \times 10^3$ respectively. At $Re=12 \times 10^3$, the current results are normalized with the bulk velocity U_b and compared to the DNS ($Re=10^4$) results of Facciolo(2006) at six axial locations. As was seen in Figure 80, the

centerline decay in the current simulations is faster which is consistent with a wider jet spread at all measured locations. It is interesting to note that the DNS results of Facciolo(2006) show an increase in velocity decay rate after $x/D=5$, which is higher than the current simulations such that by $x/D=7$ the mean centerline is actually lower than in the current simulations. From $x/D=7$ till $x/D=10$, the centerline velocity decreases significantly for the DNS data of Facciolo(2006) such that it is equal in magnitude to the jet centerline velocity predicted by the current LES simulations at $x/D=10$ although the jet spread of the current simulations is still considerably larger. The larger spread rate observed is in part explained due to the fact that no entrainment was allowed for the DNS simulations of Facciolo(2006) which used a code that required that the mass be conserved such that jet expansion is given only by diffusivity. Facciolo(2006) stated that since rotation greatly influences entrainment, the axial decay in their DNS simulation is not able to follow the correct trend of the jet. Furthermore, although their experimental and DNS start from very similar values, as seen in Figure 78, the axial decay in the latter is much slower compared to their experimental data such that the potential core is much longer. No explanation is offered, but after $x/D>3$ Facciolo(2006) point out that the trend changes and the axial velocity decay of their DNS simulation changes with the axial velocity decay of their DNS simulations being much higher such that the experimental and DNS simulation curves cross each other around $x/D\sim 5$ with the DNS simulation showing lower axial velocities than the LDV experimental data thereafter downstream.

For jet flow with $S=0.5$ and $Re=24\times 10^3$, Figure 84 compares the mean axial velocity profiles. Results are plotted at three axial distances and are normalized with both the bulk velocity U_b and local centerline velocity U_c . Those normalized with U_c agree better with the experimental data of Facciolo(2006) than those normalized with U_b , which suggests that the correct jet spread rate is predicted.

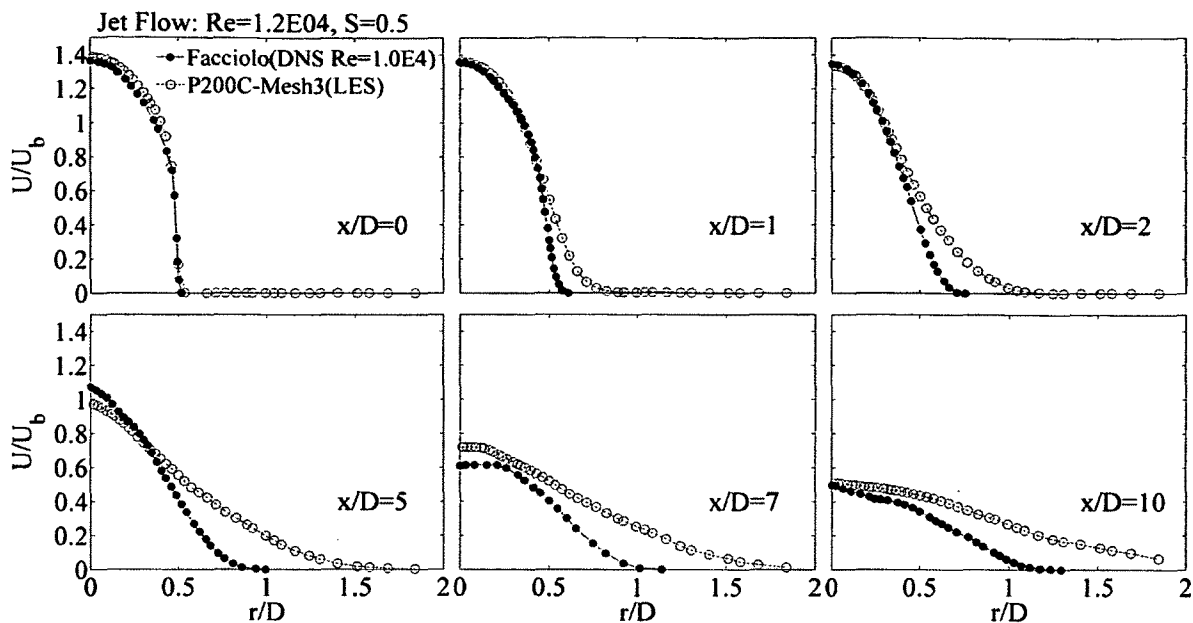


Figure 83: Jet profiles of axial velocity normalized with U_b . $Re=12 \times 10^3$; $S=0.5$.

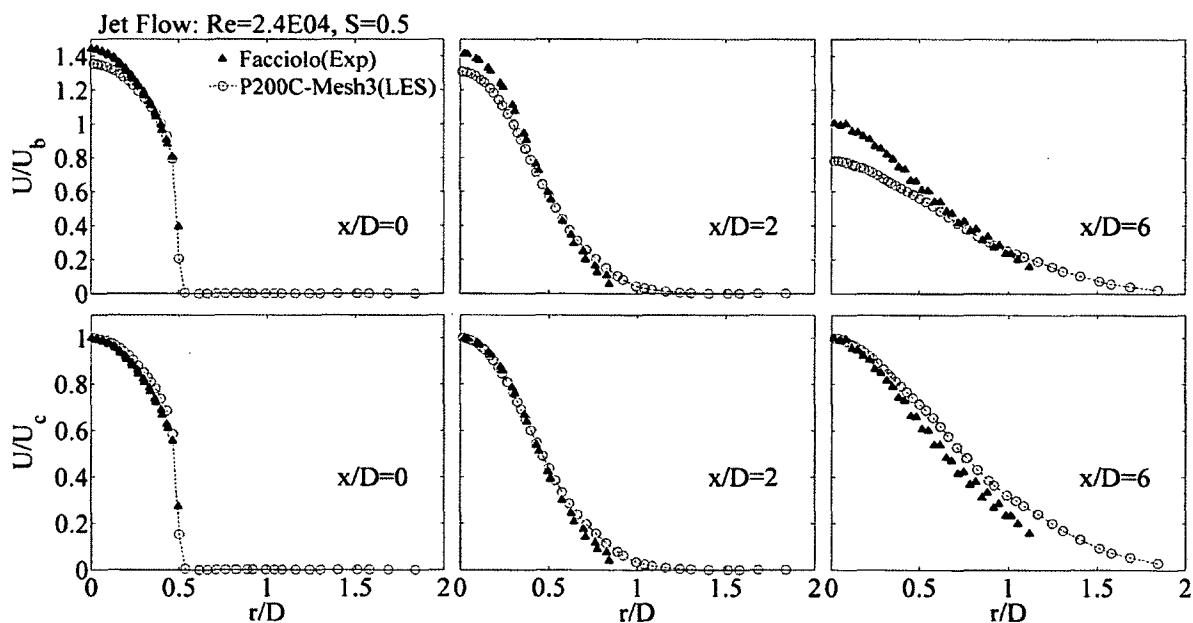


Figure 84: Jet profiles of axial velocity normalized with U_b (top) and U_c (bottom). $Re=24 \times 10^3$; $S=0.5$.

Figure 85 shows the jet half width, $r_{1/2}$, the radial distance where the jet axial velocity is half the centerline velocity, ($U=0.5U_c$). It is seen that within the potential core, $x < 3D$, the jet spread rate is nearly unaffected by the addition of swirl at either

Reynolds number. Beyond the jet core, however, the jet spread increases with swirl, more so at the higher Reynolds number of $Re=24 \times 10^3$.

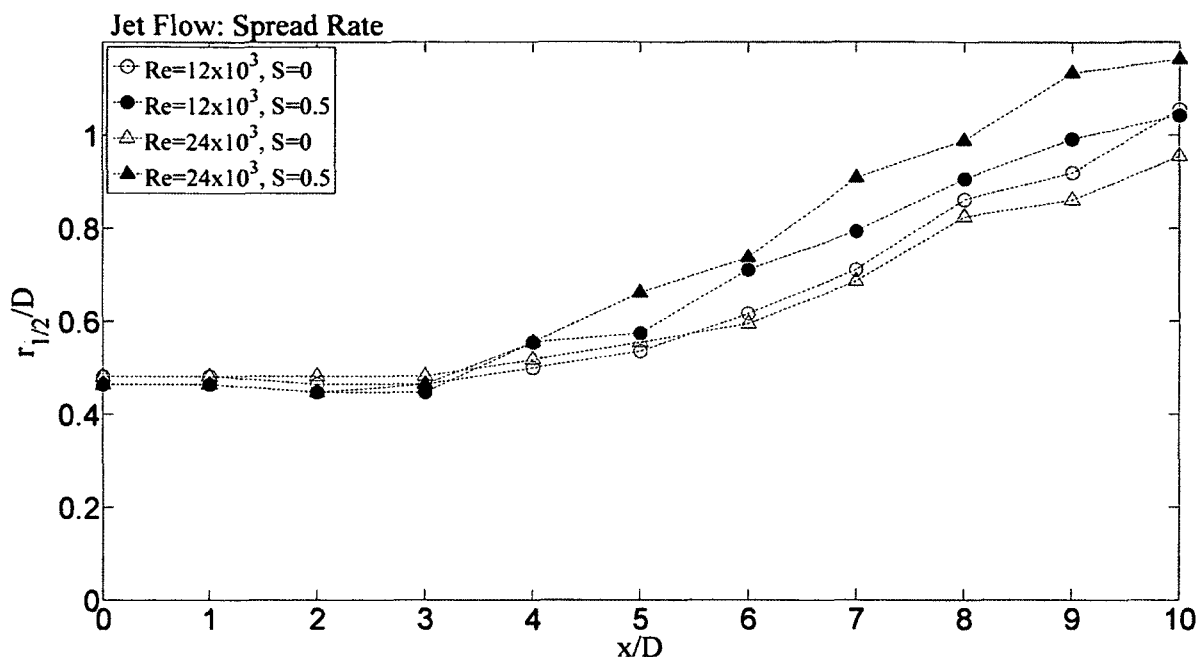


Figure 85: Jet half width. $Re=12 \times 10^3, 24 \times 10^3$; $S=0, 0.5$.

Mean tangential velocity results for the jet flow with $S=0.5$ are compared in Figure 86 and 87 for $Re=12 \times 10^3$ and $Re=24 \times 10^3$, respectively. The current LES results of the mean tangential velocity normalized with the pipe wall tangential velocity, V_w , for $Re=12 \times 10^3$, $S=0.5$ are compared to the DNS results of Facciolo(2006) at six axial locations. Within the potential core region $0 < x/D < 2$ the results compare reasonably well, but similar to the mean axial velocity, there are significant deviations further downstream. The difference in spread rate is again likely due to the lack of jet entrainment of the DNS simulations of Facciolo(2006). Figure 87 shows much better agreement between the current LES simulations and the experimental data of Facciolo(2006) for $Re=24 \times 10^3$ at $S=0.5$, matching magnitude and velocity profiles nearly perfectly throughout the domain.

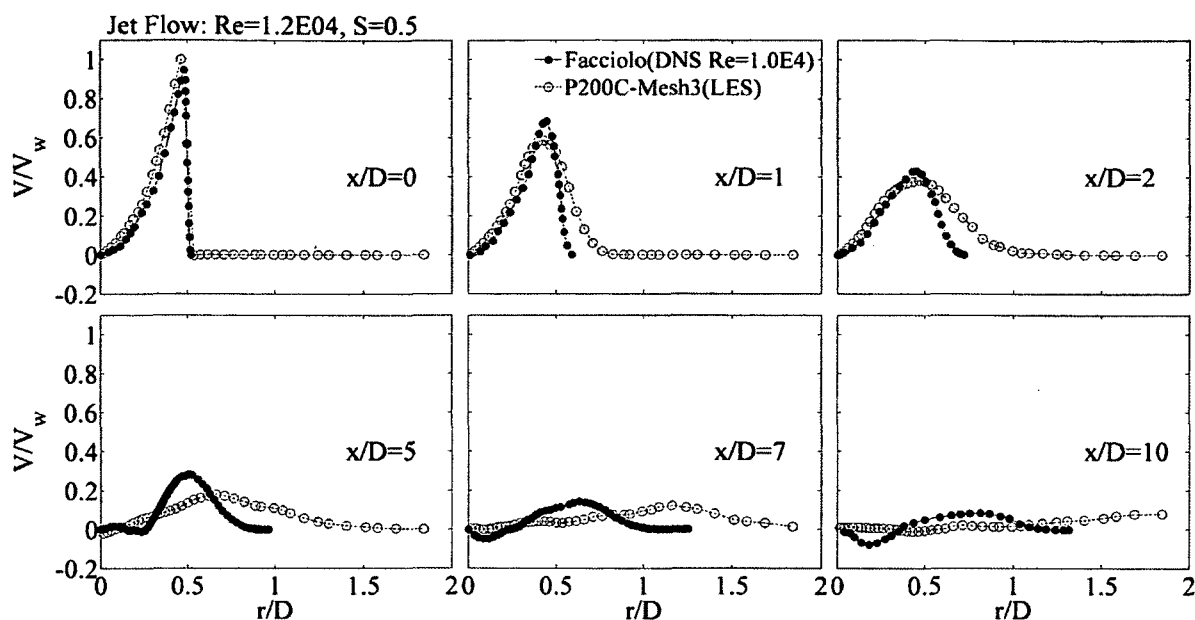


Figure 86: Jet profiles of mean tangential velocity normalized with V_w . $Re=12 \times 10^3$; $S=0.5$

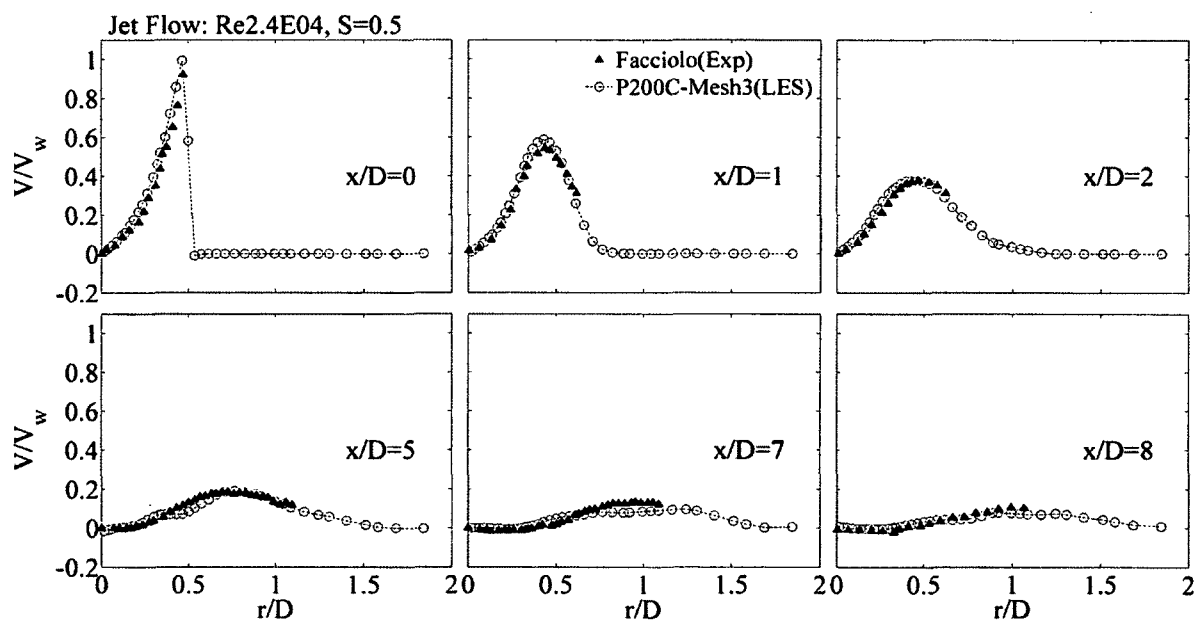


Figure 87: Jet profiles of mean tangential velocity normalized with V_w . $Re=24 \times 10^3$; $S=0.5$

For jet flow without rotation, the centerline variation of the turbulence intensity of the axial component is shown in Figure 88 to closely match the experimental results of Facciolo(2006) and Ferdman, et al.(2000). Both mesh#3 and mesh#5 give similar results, but the finer Mesh5 does show somewhat better agreement with experimental data from

$3 < x/D < 6$ at the higher Reynolds number of $Re = 24 \times 10^3$. Results for jet flow without rotation show an initial region of weak increase in the turbulence level from about $1 < x/D < 3$, characteristic of the jet's potential core region. Downstream of the core region the axial turbulence intensity grows significantly for approximately 3 diameter lengths, over-predicting the experimental data from $4 < x/D < 6$, prior to reaching a maximum at around $x/D = 6$. The decrease after reaching a maximum is more pronounced for the current LES simulations than the experimental data of Facciolo(2006), which appears to simply level off beyond $x/D > 7$.

For jet flow with $S = 0.5$, Figure 88 shows that the increase in axial turbulence intensity is greater, and the rise occurs about a diameter length further upstream than the jet flow without rotation. The maximum also moves upstream by approximately one diameter length to around $x/D = 5$. The shift and increase in axial turbulence intensity is due to a decrease in the jet's potential core length and enhanced mixing due to jet rotation. At a Reynolds number of $Re = 12 \times 10^3$ and $S = 0.5$, current results agree with the experimental results of Facciolo(2006). The magnitude is a close match as well from the jet inlet all the way to near the maximum peak, that is from $0 < x/D < 5$. The observed decrease in magnitude after reaching the maximum, however, is significantly more for the current simulations and considerably under predicts the experimental data of Facciolo(2006) beyond $x/D > 5$. At a Reynolds number of $Re = 24 \times 10^3$ and $S = 0.5$, the initial increase and maximum axial turbulence peak seem to be about a diameter further upstream than the experimental data of Facciolo(2006). It is also seen that the decrease in axial turbulence is also greater for the current simulations beyond reaching a maximum. Although the current results of axial turbulent intensities seem to under predict the experimental results of Facciolo(2006) downstream, it is interesting to note that regardless of Reynolds number or rotation rate, all current LES simulations seem to give the same axial turbulent intensity value of $u_{rms}/U_b \approx 0.1$ at $x/D = 10$. This is interesting since it is consistent with the observation made by Facciolo(2006) who pointed out that all their axial turbulent intensity data tested for $Re = 12 \times 10^3$, 24×10^3 and $S = 0, 0.2, 0.5$ also collapsed at the same location, albeit at a higher value of $u_{rms}/U_b \approx 0.16$.

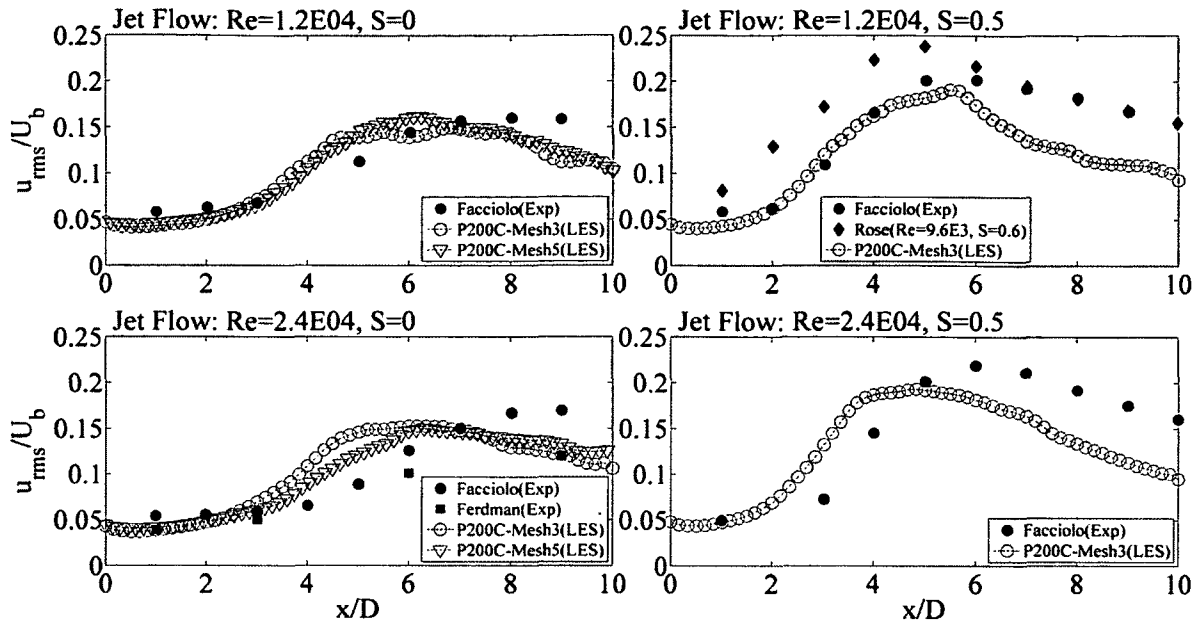


Figure 88: Axial component of turbulent intensity along the centerline.

Figure 89 and 90 show the axial turbulence profiles at various axial distances for current LES simulations as well as the experimental results of Facciolo(2006) and Ferdman, et al. (2000) at a Reynolds number of $Re=24 \times 10^3$ and $S=0$. Unfortunately, the experimental data of Facciolo(2006) and Ferdman, et al.(2000) have only one common location; $x/D=6$. From the available profiles, however, the current results match the axial turbulent intensity profiles of both sets of data reasonably well at all compared locations. When compared to the experimental data of Ferdman, et al. (2000), Figure 91 shows that the current LES simulations show a significantly larger magnitude near the jet center ($r/D < 0.5$) at $x/D=(1,3,6)$ but appear to match in magnitude further from the center. At $x/D=9$ current results match Ferdman, et al. (2000) in both magnitude and profile shape. At $x/D=2$ the current LES simulations coincide quite well with the results of Facciolo(2006), especially for the finer mesh#5. At $x/D=6$, it is seen that near the center of the jet the current results begin closer in magnitude to the experimental results of Facciolo(2006) but appear to fall right in between their data and that of Ferdman, et al. (2000) from approximately $0.25 < x/D < 0.75$. Beyond $x/D > 0.75$, the current LES simulations and both sets of experimental data agree well.

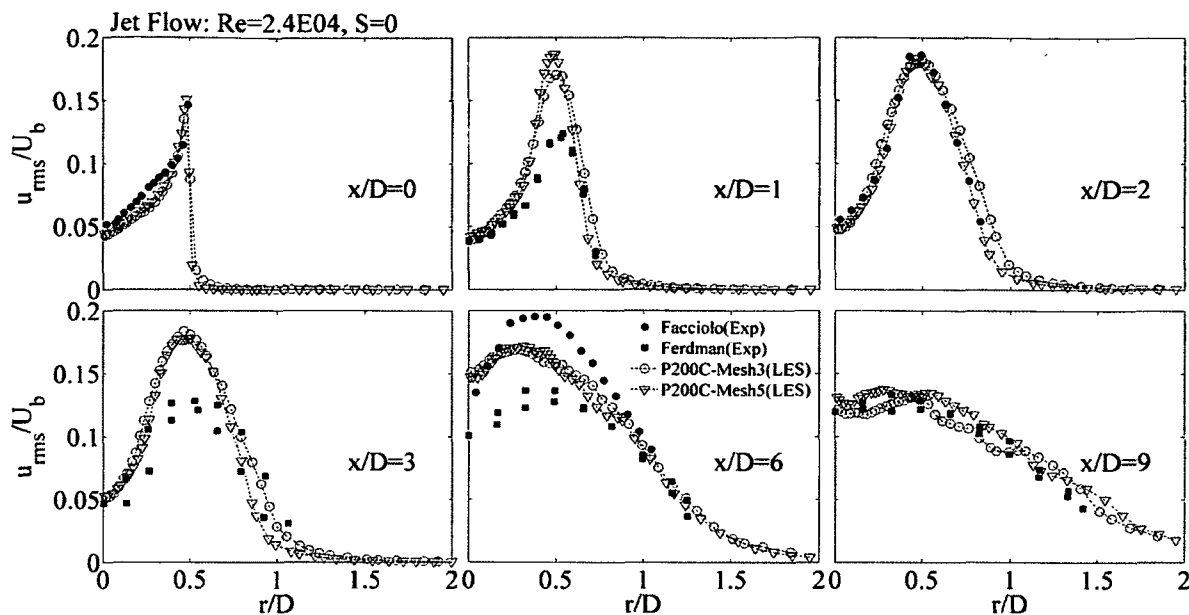


Figure 89: Profiles of axial component of turbulent intensity normalized with U_b . $Re=24 \times 10^3$; $S=0$.

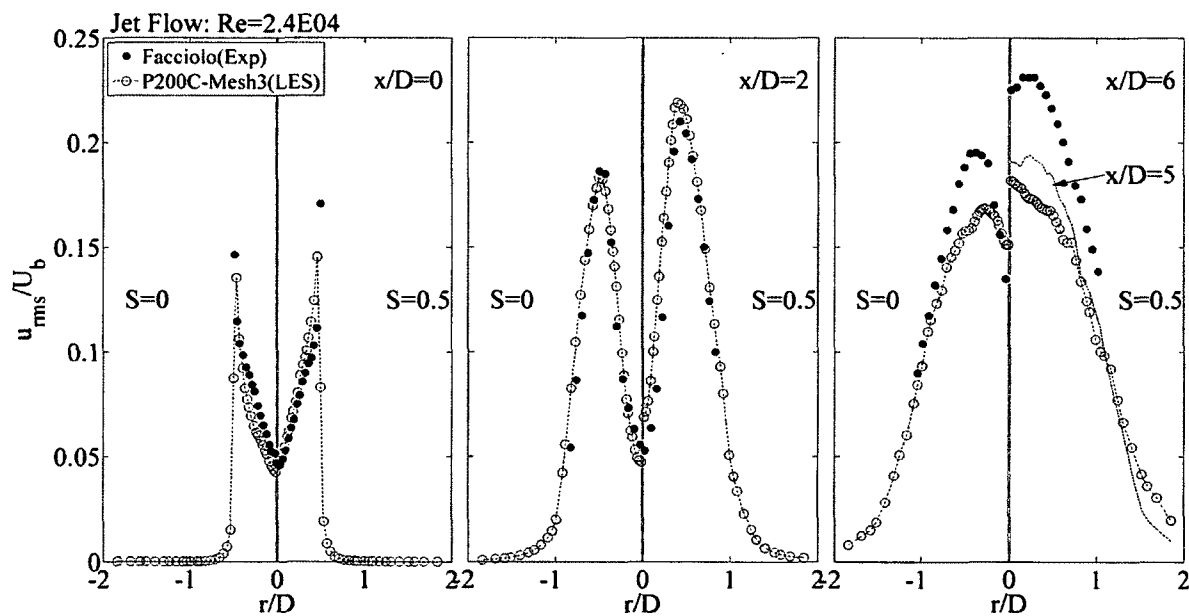


Figure 90: Profiles of axial component of turbulent intensity normalized with U_b . $Re=24 \times 10^3$; $S=0, 0.5$.

Figure 91 shows the centerline variation of the turbulence intensity component, v_{rms}/U_b . At a Reynolds number of $Re=24 \times 10^5$ and $S=0.5$ the radial component, w_{rms}/U_b , made available in Facciolo(2006) is also plotted in Figure 91. Similar to the axial

turbulence intensity component for jet flow without rotation, the current simulations display an initial region of weak increase in the turbulence level of v_{rms}/U_b within the core region ($1 < x/D < 3$) followed by a large increase in magnitude that reaches a maximum at approximately $x/D=6$. Beyond the maximum there is also a decrease in the v_{rms}/U_b turbulence intensity component not noticeable in either the experimental data of Facciolo(2006) or Ferdman, et al. (2000). Unlike the axial component, however, at a Reynolds number of $Re=12 \times 10^3$ and $S=0$ the current results seem to match the experimental data of Facciolo(2006) in the intermediate region ($3 < x/D < 7$) more closely, although the offset near the jet inlet of the current magnitude seems to be considerably lower. At the higher Reynolds number of $Re=24 \times 10^3$, the offset is much less. These offsets were also present in the non-rotating pipe flow data as was seen in Figure 52. Similar to the higher values of the mean axial velocity data of the experimental data of Facciolo(2006), Figure 52 seems to suggest that their pipe flow values are significantly higher at $r=0$ for all turbulent intensities when compared to other validation data made available.

At $Re=24 \times 10^3$ and $S=0$, current results of v_{rms}/U_b again seem to over predict the data of Facciolo(2006) in the intermediate region ($3 < x/D < 7$) but appear to match the magnitude of the few available experimental data points of Ferdman, et al. (2000) much closer. Again little difference is observed between the two meshes tested with perhaps a slightly better agreement of mesh#5 with the experimental data in the intermediate region ($3 < x/D < 7$).

For rotating jet flow at $Re=12 \times 10^3$ and $S=0.5$ Figure 91 shows that when compared to the experimental data of Facciolo(2006), there is a notable under prediction in v_{rms}/U_b throughout the jet domain although the profile shape seems to accurately match and the under prediction appears to be due to an offset that is likely due to a difference in bulk velocities used for scaling. For rotating jet flow at the higher Reynolds number of $Re=24 \times 10^3$ and $S=0.5$, both current results and experimental results of Facciolo(2006) shows that there is little difference between the two turbulence intensity components v_{rms}/U_b and w_{rms}/U_b . As was the case in the axial component of turbulence intensity, the same shift is observed in the current simulation for both the radial and tangential component with a shift of approximately 1 diameter length upstream.

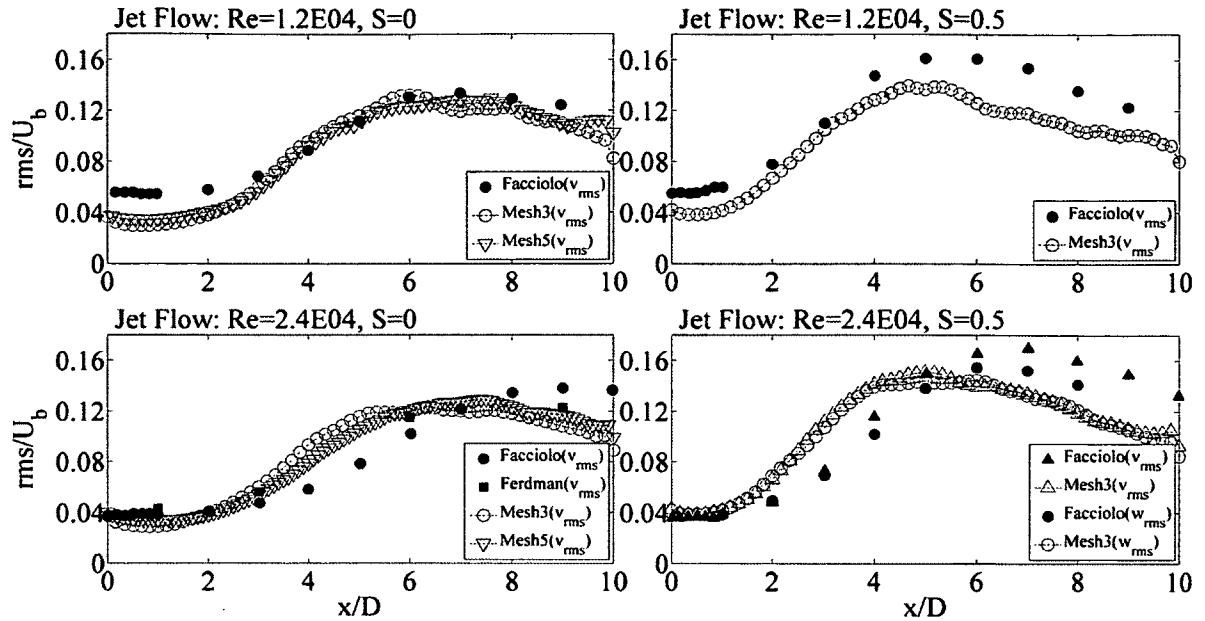
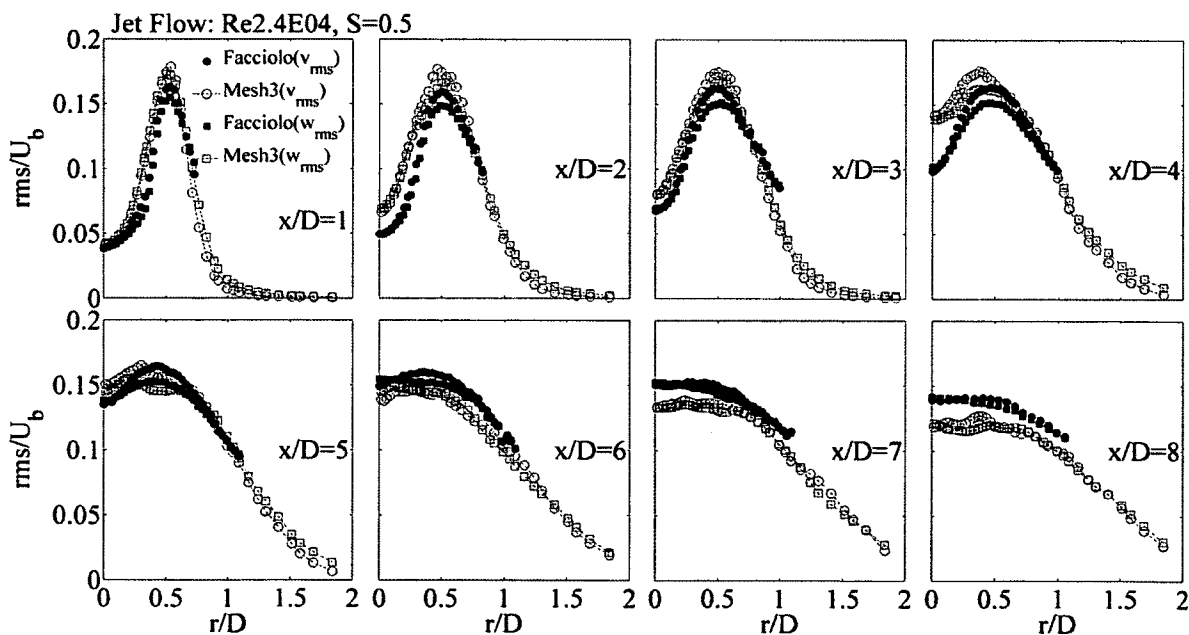
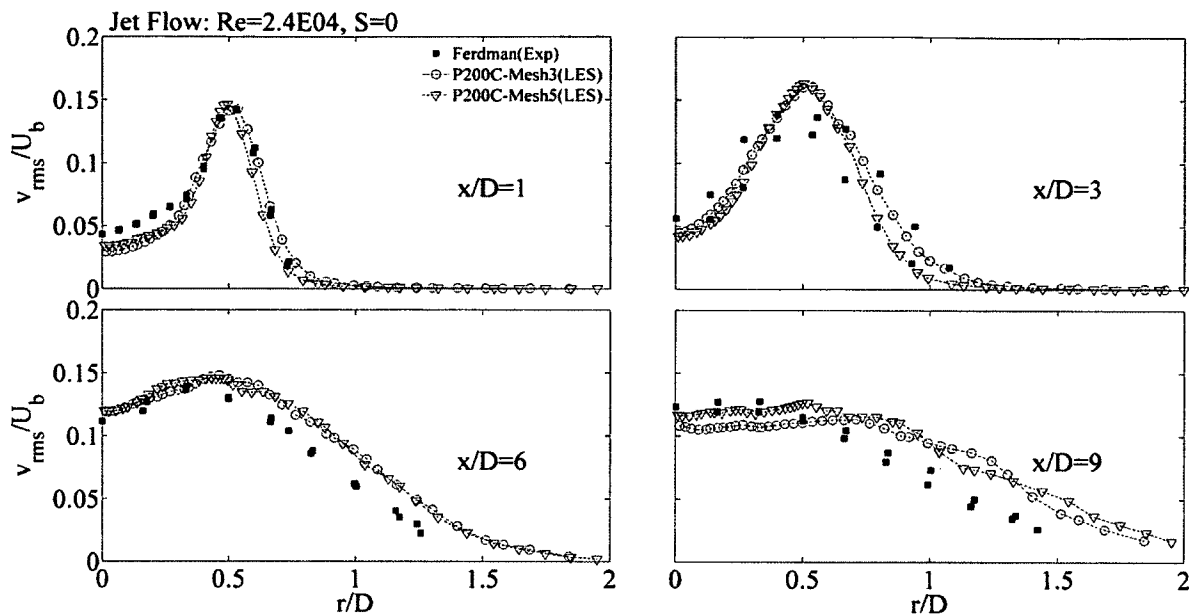


Figure 91: Radial (w_{rms}) and tangential (v_{rms}) components of turbulent intensity along the centerline normalized with U_b .

Experimental validation data of the transverse turbulence intensity profiles at various axial locations were only available for Ferdman, et al. (2000) at $Re=24 \times 10^3$, $S=0$. As seen in Figure 92, current v_{rms}/U_b turbulence intensity profile results at $Re=24 \times 10^3$, $S=0$ match reasonably well with the available results of Ferdman, et al. (2000) at all axial locations [$x/D=(1,3,6,9)$]. The shape and maximums predicted in the current simulations seem to coincide well with Ferdman, et al. (2000) with only a slight over prediction in the turbulent intensity beyond $x/D=6$ in the outer edge of the jet ($r/D>0.5$).

At $Re=24 \times 10^3$, $S=0.5$, both the azimuthal and radial velocity components were made available for Facciolo(2006) and are plotted against current results in Figure 93. Besides the offsets discussed previously for the centerline turbulent intensities as observed in Figure 91, current LES profiles seem to match reasonably well at all locations. As noted in Facciolo(2006) there is little difference between the development of both components and lay almost entirely on the same curve in both the central and outer part of the jet. The maximum peak occurs at approximately $r/D=0.5$ at an axial distance of $x/D=1$. As the jet moves downstream, the jet maximum proceeds to gradually decrease and move toward the centerline due to the shear layer penetrating into the jet. At

around $x/D=7$ both radial and tangential turbulent intensity profiles become almost flat the center of the jet.



The Reynolds shear stress results for jet flow at $Re=24 \times 10^3$, $S=0$, are presented in Figure 94. Current simulation results show fair agreement with experimental results of Ferdman, et al. (2000) and Facciolo(2006) at all axial locations. As expected due to symmetry, the value of the Reynolds shear stress is zero along the jet axis throughout. The maximum is observed at an axial distance of $x/D=1$ and radial distance of approximately $r/D=0.5$. The current LES maximum observed seems to be significantly higher than Ferdman, et al. (2000). This over prediction also observed at $x/D=3$ is possibly due to lack of resolution in the experimental results. Despite the over-prediction the location of the maximum peaks and general profile shapes of the Reynolds shear stress seem to be a good match. Further downstream as the maximum gradually decreases, the Reynolds shear stress magnitude at $x/D=(6,9)$ of the current simulations seems to be much closer in agreement to the experimental results of Ferdman, et al. (2000) and both show a slight shift in the maximum towards the jet's center axis.

For jet flow with $S=0.5$ rotation at a Reynolds number of $Re=24 \times 10^3$, Figure 95 shows the shear Reynolds stress results for both \overline{uv}/U_c^2 and \overline{vw}/U_c^2 compared to those of Facciolo(2006) at an axial distance of $x/D=6$. The increase in \overline{uv}/U_c^2 of the current results seems to initially match both the experimental and LES data of Facciolo(2006) but under predicts $1 < r/D < 0.5$ due to a slight oscillation observed in the slope. As seen in Figure 95 oscillations in the current data are even more apparent for the low magnitude \overline{vw}/U_c^2 Reynolds shear stress and seem to suggest either an error in the data collected or insufficient samples.

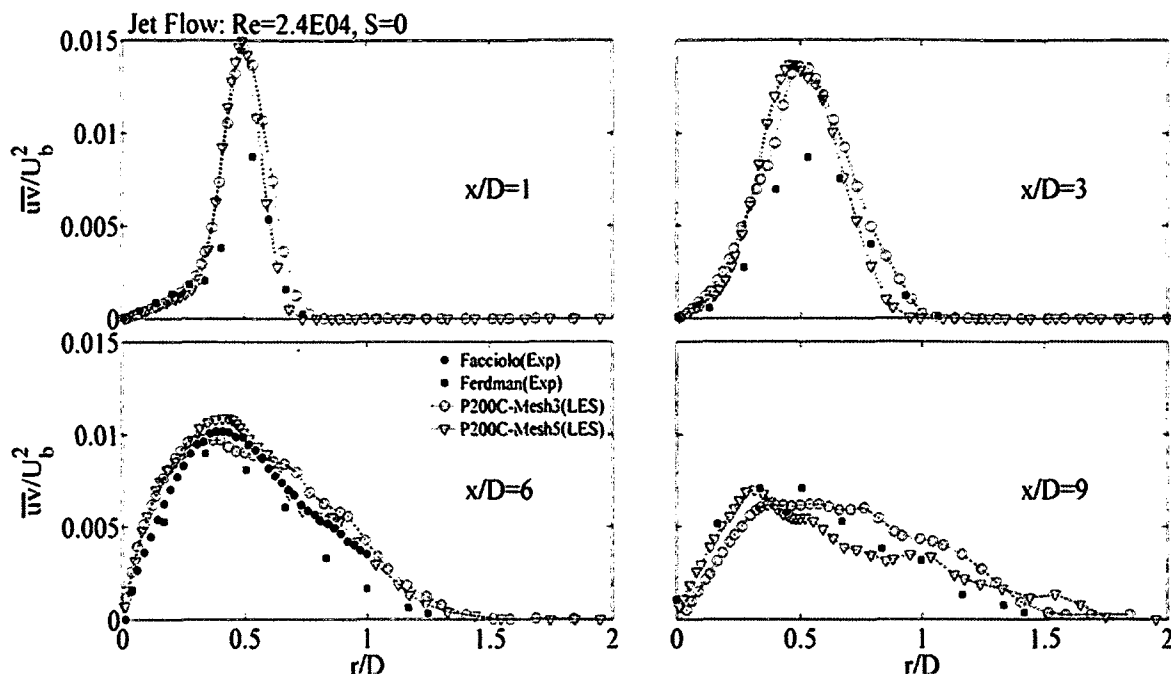


Figure 94: Jet Reynolds shear stress profiles (axial-tangential) normalized with U_b . $Re=24 \times 10^3$; $S=0$.

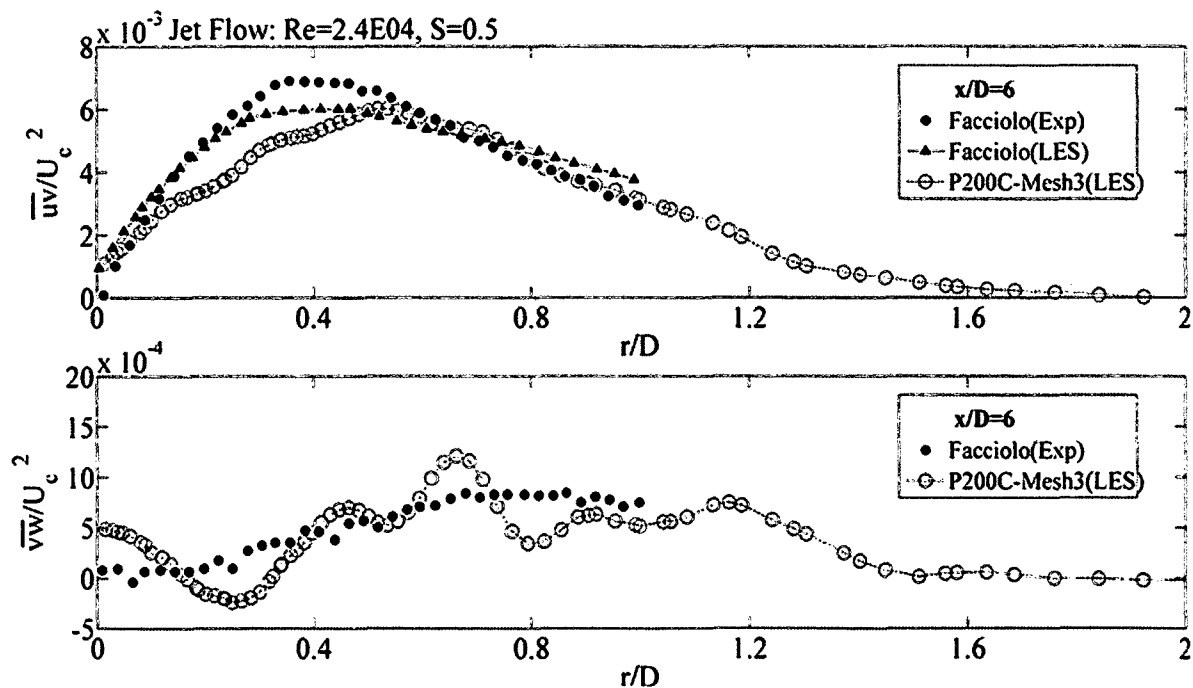


Figure 95: Jet Reynolds shear stress profiles top-(axial-tangential), bottom-(radial-tangential) normalized with U_c . $Re=24 \times 10^3$ $S=0.5$.

7.2 JET FLOW: REYNOLDS STRESS ANISOTROPY

The anisotropic tensor b_{ij} components of Eqn. 6-4 are shown in Figure 96 for all jet configurations simulated at an axial distance of $x/D=6$. The values are calculated and plotted up to a radial distance of $r/R=2$. There does not appear to be any notable differences in the anisotropic tensor component due to the Reynolds numbers or rotation rates tested. The b_{11} component decreases toward zero moving away from the jet center. The b_{22} component shows an opposite trend, increasing towards zero from $0 < r/R < 2$. In the same range that the b_{22} component begins to oscillate and decrease, the b_{33} component which was relatively constant from $0 < r/R < 2$ begins to increase. The b_{12} shear stress anisotropy tensor component is zero at the jet center and increases up to approximately $r/R=0.8$ reaching a maximum and remaining constant all the way up to approximately $r/R=2$ at which point oscillations are present. The b_{12} and b_{13} components which remain at zero except in the outer region beyond $r/R > 2$ (not shown) of the jet where oscillations are observed. The oscillating behavior beyond $r/R > 2$ observed in the anisotropic component is due to the intermittency of turbulence approaching the jet's edge where incursion of irrotational ambient fluid due to entrainment is present.

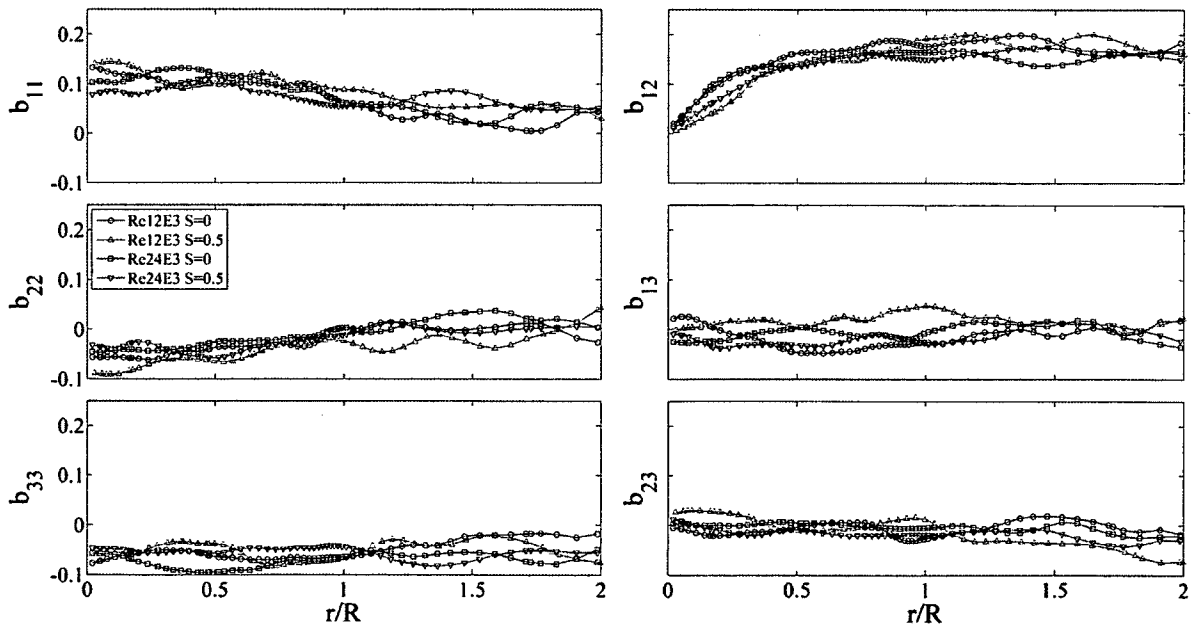


Figure 96: Anisotropy tensor components for Jet flow at $Re=12 \times 10^3$, 24×10^3 ; $S=0, 0.5$ at $x/D=6$.

Figure 97 thru 99 show, side by side, the global view and a zoomed in view of the anisotropy invariant map. For all jet flow configurations tested it is seen that the anisotropy invariants lie near the isotropic limit, between the axis-symmetric boundaries. Figure 97 compares the effect of Reynolds numbers, $Re=12 \times 10^3$, 24×10^3 . The close up view of the invariant map in Figure 97 shows that for both Reynolds number the anisotropy invariants begins near the isotropic the center of the jet ($r=0$) and follow the axisymmetric turbulent line moving from the center of the jet ($r=0$) towards the jet's edge. The proximity of the invariant values to both the isotropic and axisymmetric limit is closer for the higher Reynolds number of $Re= 24 \times 10^3$. The departure from axis-symmetry that occur faster at the lower Reynolds number and the smaller magnitude values of the II invariant for the higher Reynolds number show a higher level of isotropy suggesting there may be a Reynolds number effect present.

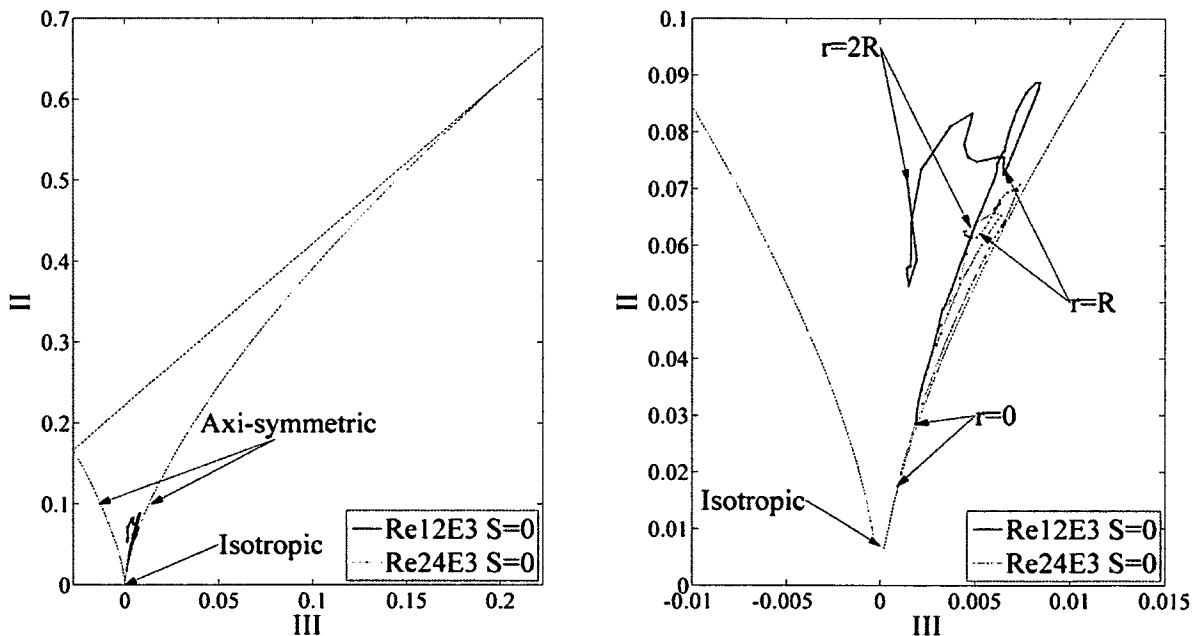


Figure 97: Jet flow anisotropy invariant map at $x/D=6$ for $Re=12 \times 10^3$, 24×10^3 ; $S=0$.

The effect on anisotropy due to rotation is shown in Figure 98 and 99 for $Re=12 \times 10^3$ and 24×10^3 respectively. Figure 98 shows that at a Reynolds number of $Re=12 \times 10^3$ rotation of $S=0.5$ results in a shift of the anisotropy invariants away from the axisymmetry boundary near the jet center ($r=0$). Somewhere in the radial range of

$R < r < 2R$ it is seen that for both $S=0$ and $S=0.5$ there is an irregular departure from the axi-symmetry boundary on the right hand side of the invariant map. Figure 99 shows that at the higher Reynolds number of $Re=24 \times 10^3$ the anisotropy invariants in the range of $R < r < 2R$ are more closely compacted and remain closer to the axi-symmetric boundary than the lower Reynolds number. A comparison between Figure 98 and 99 clearly shows that at both $S=0$ and $S=0.5$ the magnitudes of the II invariant are lower and remain closer to the isotropic limit with a closer proximity to the axi-symmetric line at the higher Reynolds number further suggesting there is a Reynolds number effect present.

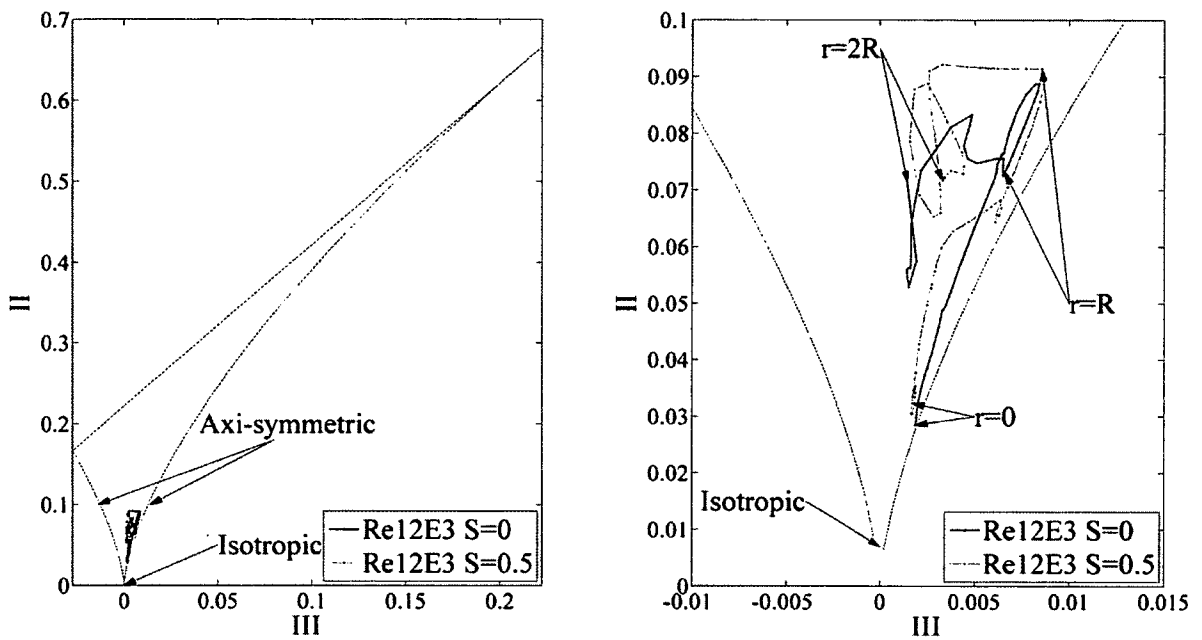


Figure 98: Jet flow anisotropy invariant map at $Re= 12 \times 10^3$; $S=0, 0.5$.

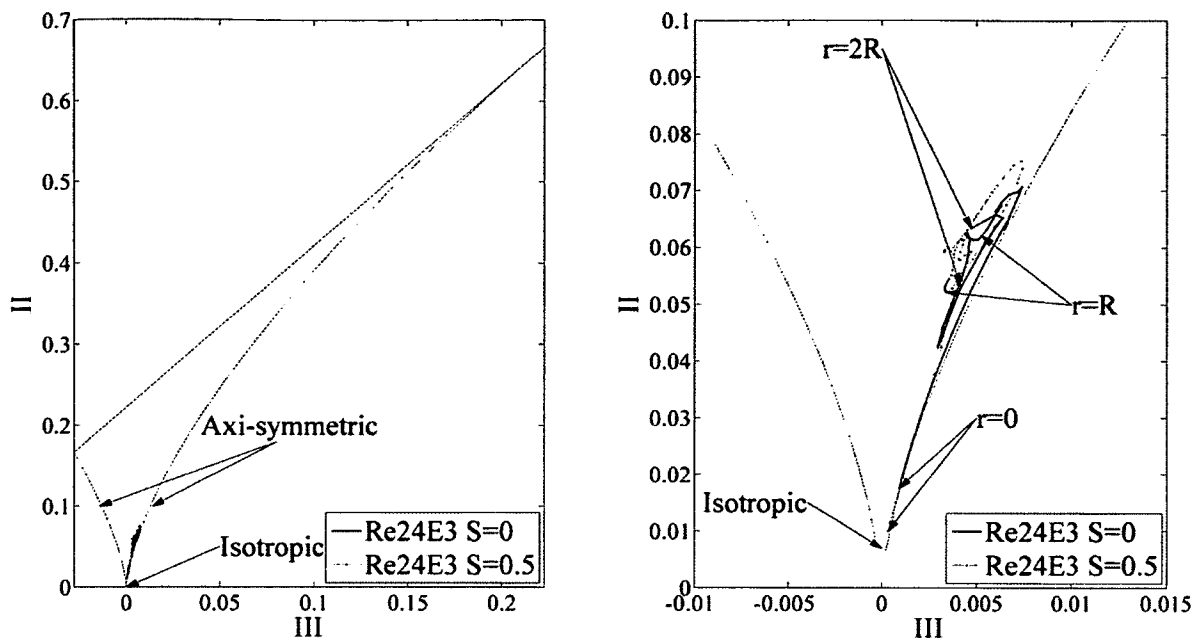


Figure 99: Jet flow anisotropy invariant map at $Re = 24 \times 10^3$, $S = 0, 0.5$.

8 PARTICLE-LADEN JET

8.1 PARTICLE-LADEN JET SETUP AND PARAMETERS

To simulate particle laden jet flow, spherical particles were injected at the interface between the pipe outlet and the jet inlet. Particle injection was initialized after initial jet flow development of 1000 time steps at $t=0.1\text{sec}$. Subsequent injections occurred every 100th time step ($\Delta t = 0.0001\text{sec}$) or every 0.01sec thereafter. Particles were introduced at the jet inlet plane, $x=0$, with an initial velocity equal to the local instantaneous fluid velocity. As shown in Figure 100, one particle was injected at every jet inlet cell (2796Total, ID: 0-2795). Location of the particles is initially at the center of each injection cell.

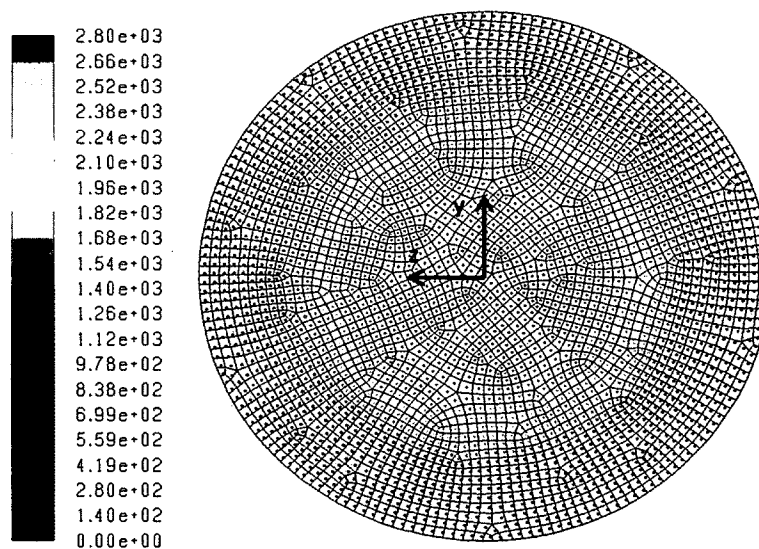


Figure 100: Jet inlet depicting particle injection locations. (Particles colored by particle ID).

Injected particles are considered to be rigid spheres with uniform diameter and constant density, $\rho_p = 1000\text{kg/m}^3$. Particles injected into the jet flow had diameters of 10, 100 or 500 μm . These particles are considered to be large such that sub-grid scales would have a negligible effect on their trajectories. Table 10 summarizes parameters of the particle injection.

Table 10: Particle response time and Stokes number. Bulk velocity estimate of $U_b=5.8\text{m/s}$, correspond to non-rotating ($S=0$) jet flow at $Re=24 \times 10^3$.

Diameter D_p (μm)	Re ($S=0$)	U_b (m/s)	Volume Vol_p (m^3)	Mass m_p (kg)	Response time (sec) t_p	Stokes $St = (t_p U_b/R)$
10	24×10^3	5.8	5.2×10^{-16}	5.2×10^{-13}	3.1×10^{-4}	0.06
100	24×10^3	5.8	5.2×10^{-13}	5.2×10^{-10}	3.1×10^{-2}	6
500	24×10^3	5.8	6.5×10^{-11}	6.5×10^{-8}	7.8×10^{-1}	150

$$\text{Where particle response time: } t_p = \frac{\rho_p D_p^2}{18 \rho v} \quad \text{Eqn. 8-1}$$

$$\text{Stokes: } St = \frac{t_p U_b}{R} \quad \text{Eqn. 8-2}$$

Simulations were performed using jet mesh#3, which has 1.23×10^6 cells. Grid dependency tests in Section 5 showed that it produced results that were almost as good as the finer jet mesh#5 which has 3.31×10^6 cells. Because the discrete phase model in the FLUENT code did not allow for the use of the fractional time step method, an iterative time step method had to be utilized. A maximum of 20 iterations could be used at each time step to allow for convergence. The discrete phase model requires a particle mass or volume flow rate below 10% of the fluid flow rate.

Table 11 shows that the mass flow ratio is <1% in this study.

Table 11: Particle Volume/Mass fraction.

Re ($S=0$)	U_b (m/s)	Air Mass Flow Rate (kg/s)	10% Mass Flow Rate (kg/s)	# Particles to achieve 10% Mass Flow	Actual # of Particles (2796) mass%
24×10^3	5.84	0.02	0.002	30921	0.9

Time integration of particle trajectory equations can be set in FLUENT by specifying either the "length scale" or "length step factor". Integration time step is equivalent to the approximate distance a particle will travel before its motion equations are solved again and its trajectory is updated. Length scale, L , controls integration time step size used to integrate equations of motion for the particle for iteration within each control volume. A smaller length scale gives more accuracy. It is recommended that

$L \sim X/100$ where the domain boundary in this case is $X=10D=0.6m$ so that $L \sim X/100 \sim 0.006$. The option for the specification of the step length factor, on the other hand allows Fluent to compute the time step in terms of the number of time steps required for a particle to traverse a computational cell. The estimated transit time, Δt^* , is the time for a particle to traverse the current continuous phase control volume, $\Delta t = \frac{\Delta t^*}{\lambda}$. Where λ is the step length factor and is roughly equivalent to the number of time steps required to traverse the current continuous phase control volume. One simple rule of thumb given in the FLUENT user guide is to allow the setting of the parameters above; if you want the particles to advance through a domain consisting of N grid cells into the main flow direction, then the step length factor, λ times N should be approximately equal to the maximum number of time steps $\lambda N_x \sim \text{Max Number Steps}$. The step length factor for all simulations was changed from the default value of 5 to 10. To prevent the possibility of stagnant particles staying in the computational domain indefinitely the max number of steps is set to 10,000, such that particles do not reside in the jet domain for longer than 1second.

Two-way turbulence coupling or the effect of particle on turbulent quantities was not explored. Experiments by Kulick, et al. (1994) and Kaftori, et al. (1995) showed that for low volume fractions, as is the case in the current simulations, the turbulence modifications are negligible. Inter-collision forces of particles was also neglected due to low volume fraction of the particles. The spherical drag law with unsteady particle tracking was implemented. As recommended by the Fluent(2006) user manual for unsteady simulations, DPM sources were updated every flow iteration. The number of continuous phase iterations per DPM iteration were set to the default of 10. If the number of continuous phase iterations per DPM iteration is less than the number of iterations required to converge the continuous phase between time steps, then sub-iterations are done. Here, particles are tracked to their new positions during a time step and DPM sources are updated; particles are then returned to their original state at the beginning of the time step. At the end of the time step, particles are advanced to their new positions based on the continuous-phase solution. If the number of continuous phase

iterations per DPM iteration is larger than the number of iterations specified to converge the continuous phase between time steps, however, the particles are advanced at the beginning of the time step to compute the particle source terms.

The stochastic (discrete random walk model-DRW) model for turbulent dispersion of particles was enabled. In this model the dispersion of particles due to turbulence includes the instantaneous value of the fluctuating fluid velocity. Random effects of turbulence accounted for by a “number of tries” or computing of trajectories of representative particles. The integral time scale or time spent in turbulent motion along the particle path is proportional to particle dispersion rate. The larger its value, the more turbulent motion in the flow. The integral time-scale constant was left at the default value of 0.15.

8.2 PARTICLE-LADEN JET RESULTS

Particles data within the jet domain collected included particle location, particle velocity components, particle id and particle residence time. Figure 101 shows the total global particle count in the domain collected every 1000th time step (every 0.1sec). Figure 101 shows that for both non-rotating ($S=0$) and rotating ($S=0.5$) jet flow, it takes approximately 1 second or 10,000 time steps for both 10 μm ($St=0.06$) and 100 μm ($St=6$) particles to saturate the domain and reach a total particle count equilibrium, whereas it only takes 2-3 thousand time steps (0.2-0.3Sec) for the heavier particle of 500 μm ($St=150$) to do so.

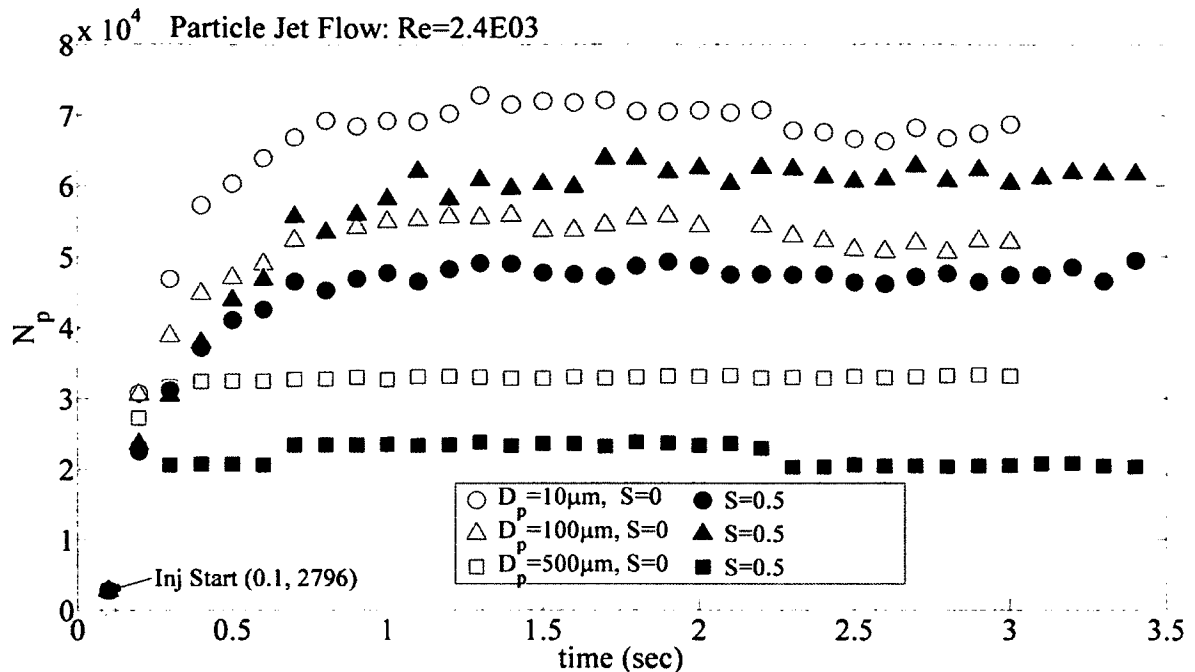


Figure 101: Global particle count within domain.

For non-rotating, $S=0$ jet flow, the count for lighter particles in the domain is greater than heavier particles with the total count of the lighter $10\ \mu m$ particles approximately 28% and 57% more than the $100\ \mu m$ and $500\ \mu m$ particles respectively. For the non-rotating jet the initial instantaneous velocity of the particles is nearly entirely in the axial direction, heavier particles which have more axial momentum, move axially through and out of the domain at a faster rate than the lighter particles and thus have a lower total particle count. With the addition of rotation, however, Figure 101 shows that the particle count is actually greater for medium sized particles with a diameter of $100\ \mu m$ than the smaller $10\ \mu m$ particles by approximately 15%.

Figure 102 shows the instantaneous particle distribution for particles found within a plane of thickness $\Delta z = 0.1D$ (with $z = \pm 0.1R$) from the center midplane ($z=0$) at $t=2\text{sec}$. Without rotation, the spread of smaller $10\ \mu m$ ($St=0.06$) and $100\ \mu m$ ($St=6$) particles is greater than the larger $500\ \mu m$ ($St=150$) particles which remain more concentrated towards the center of the jet. Addition of rotation produces a significant effect on particle distribution for both the $100\ \mu m$ and $500\ \mu m$ particles but does not seem to considerably change the particle distribution of the smaller $10\ \mu m$ particles. It

appears that the radial velocity component causes the largest ($500 \mu\text{m}$) particles to maintain their initial trajectory and continue to move outwards and eventually exit the jet, whereas the lighter particles of $10 \mu\text{m}$, with less radial momentum, simply diffuse and tend to remain closer to the jet core with little noticeable change in spread in comparison to the non-rotating jet flow. Figure 103 superimposes instantaneous axial velocity contours onto the particle distribution at $t=2\text{sec}$. Figure 104 and 105 show similar pictures at cross-sections $x/D=1$ and 5 , respectively. Without swirl, the particles remain, mostly, within the core of the jet, at both cross-sections. The addition of swirl has a profound effect on the particle radial location, which increased with particle size. In fact, for the largest size, most of the particles have exited into the free stream and are no longer within the jet. Whereas for the smallest size, they are still within the jet core. Therefore, if a cyclone separator was used to separate discrete phase particles from a carrier fluid phase, the larger-sized particles would be more easily removed whereas small-size particles may remain dispersed within the fluid phase.

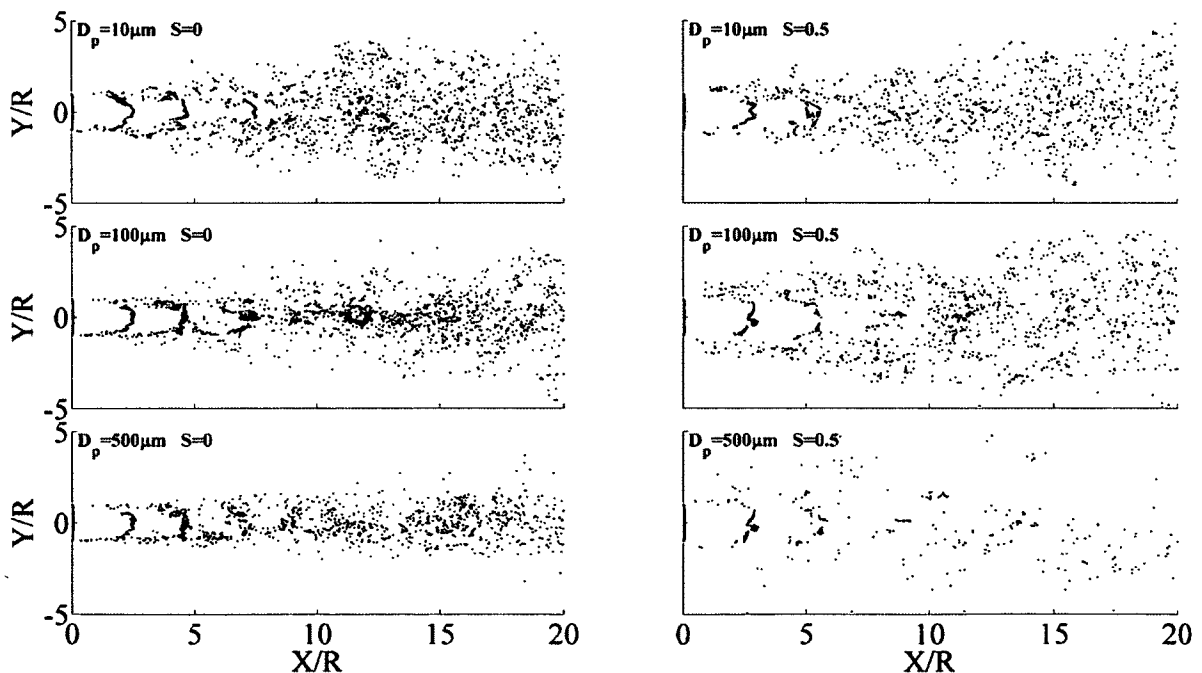


Figure 102: Midplane ($z=0$) view of particles distribution at $t=2\text{sec}$. $Re= 24 \times 10^3$; $S=0, 0.5$.

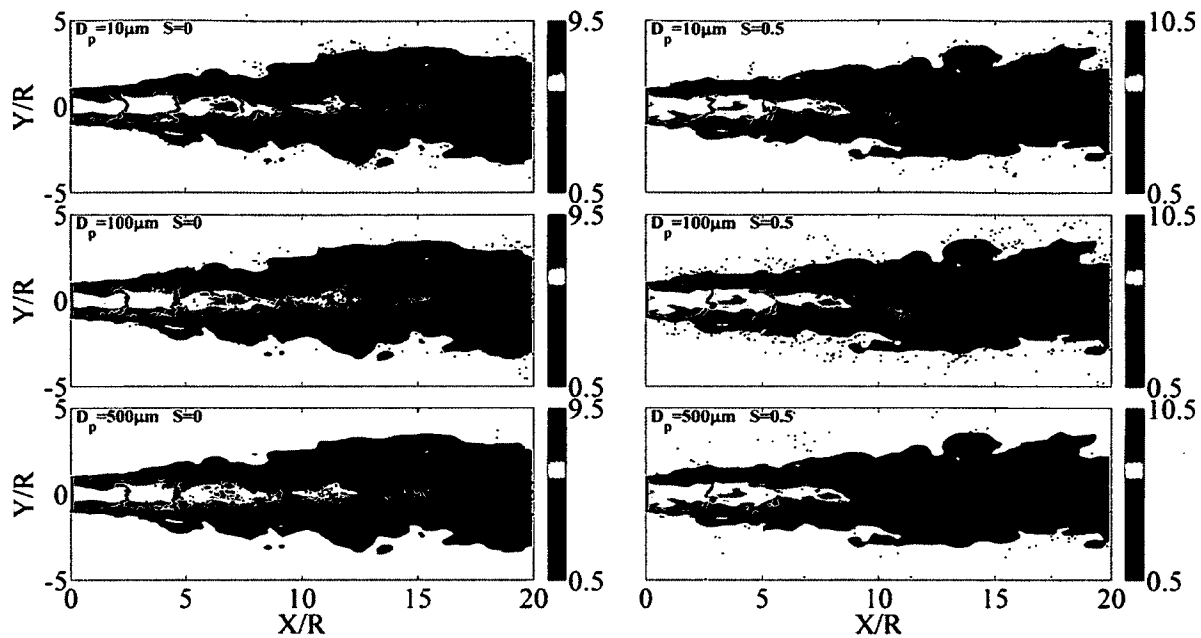


Figure 103: Midplane ($z=0$) contours of instantaneous axial velocity (m/s) and particles distribution at $t=2$ sec. $Re= 24 \times 10^3$; $S=0, 0.5$.

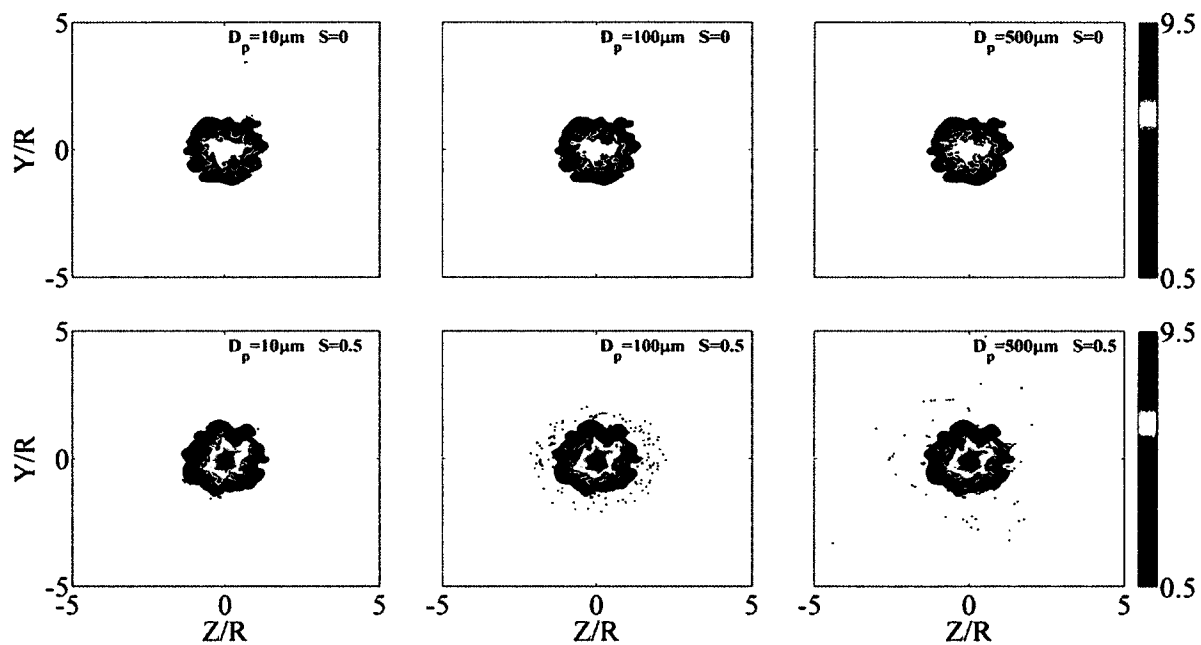


Figure 104: Contours of instantaneous axial velocity (m/s) and particle distribution at $x/D=1$, $t=2$ sec. $Re= 24 \times 10^3$; $S=0, 0.5$.

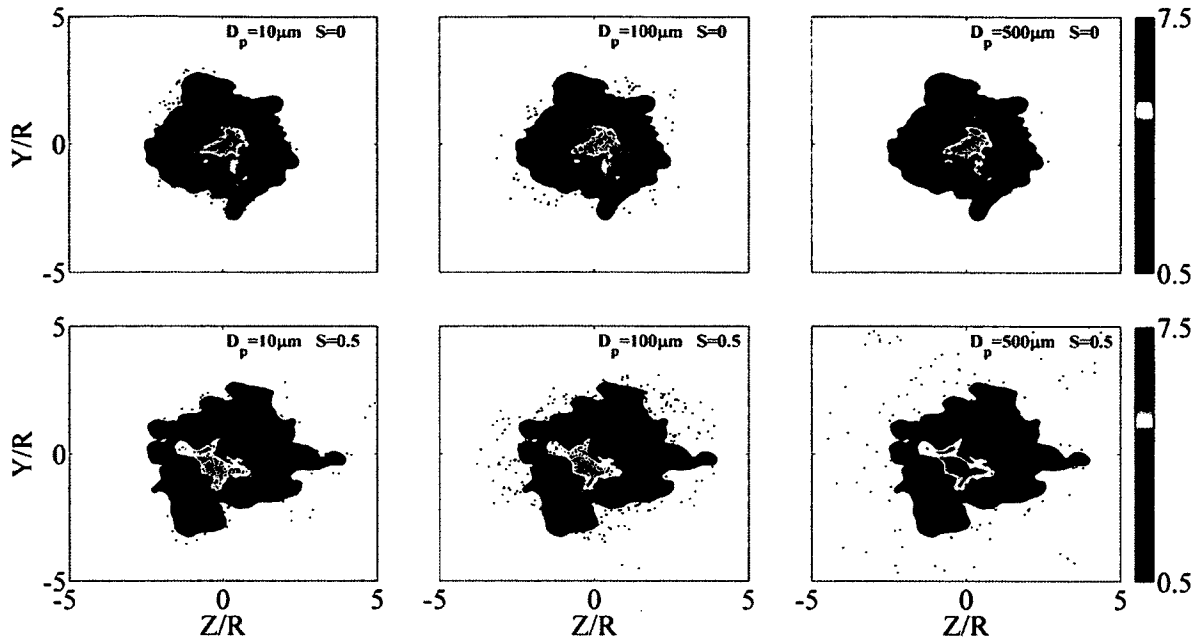


Figure 105: Contours of instantaneous axial velocity (m/s) and particle distribution at $x/D=5$, $t=2$ sec. $Re= 24 \times 10^3$; $S=0, 0.5$.

To examine the effect of the vorticity field in possibly promoting preferential particle agglomeration, instantaneous spanwise vorticity contours are superimposed onto the particle distribution at the midplane ($z=0$) in Figure 106. Similarly, instantaneous axial vorticity contours are superimposed on particle distribution at cross-sections $x/D=1$ and 5 , in Figure 107 and 108, respectively. There is strong evidence of agglomeration at regions with high axial vorticity shown in Figure 107. This is not apparent further downstream at $x/D=5$, shown in Figure 108. For jet flow without rotation, Figure 106 does appear to suggest there might be areas of preferential accumulation towards the center of the jet for $100 \mu m$ particles at around $x/R=10$. Preferential accumulation of $100 \mu m$ particles corresponding to a Stokes number of $St=6$ would agree with previous findings [Longmire and Eaton(1992), Uthupan, et al.(1994), Luo, et al.(2006)] that have shown that particles with a Stokes number in the order of $St \sim O(1)$ tend to show preferential accumulation behavior in areas of low vorticity.

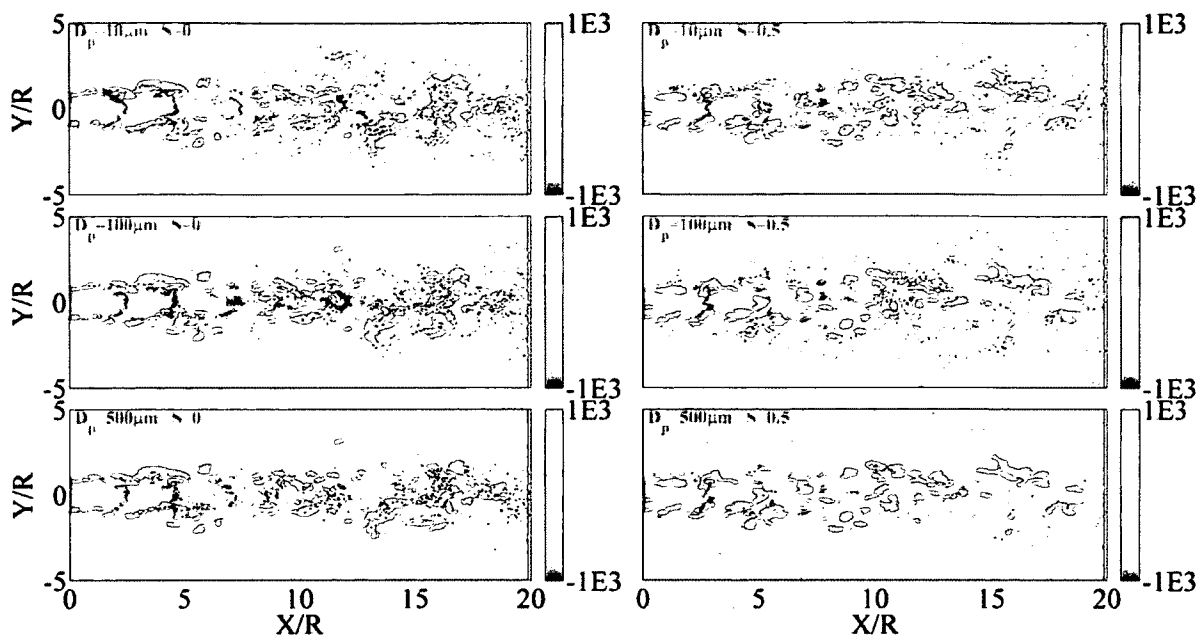


Figure 106: Midplane ($z=0$) contours of instantaneous spanwise vorticity (1/s) and particle distribution. $Re= 24 \times 10^3$; $S=0, 0.5$.

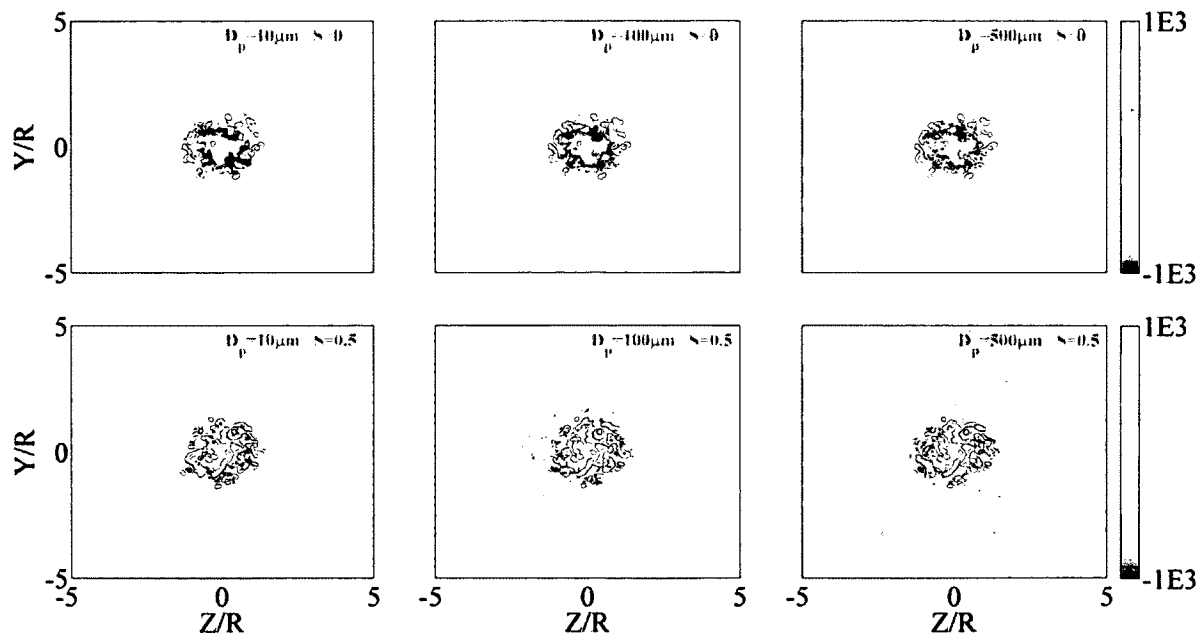


Figure 107: Contours of instantaneous axial vorticity (1/s) and particle distribution at $x/D=1$, $t=2$ sec. $Re= 24 \times 10^3$; $S=0, 0.5$.

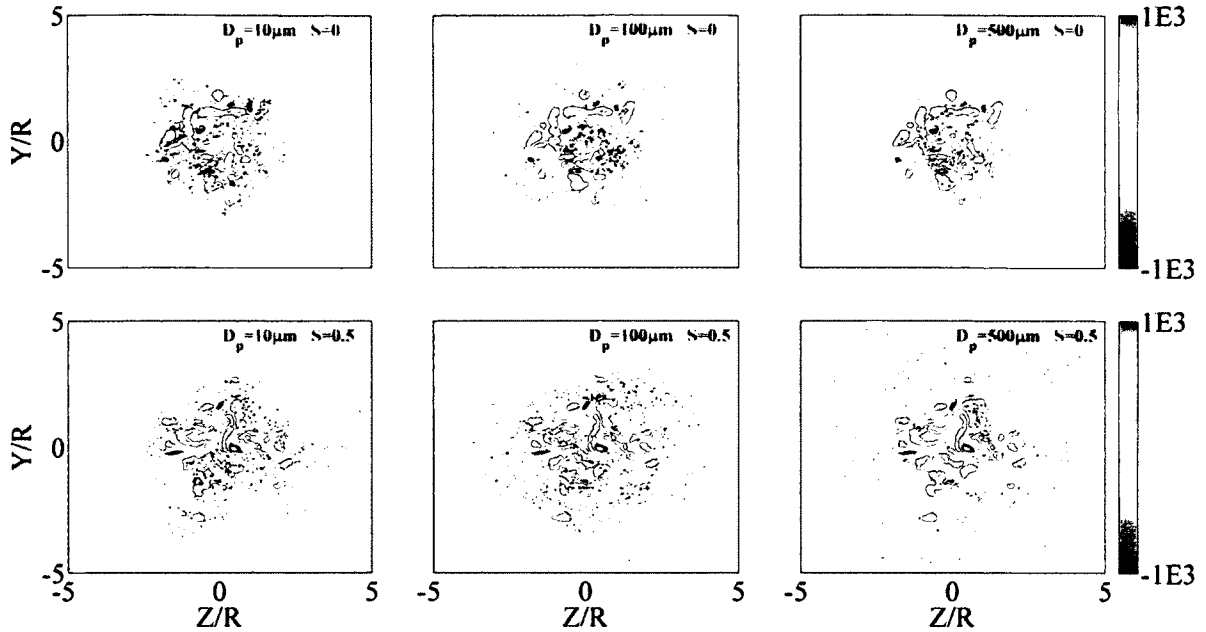


Figure 108: Contours of instantaneous axial vorticity (1/s) and particle distribution at $x/D=5$, $t=2\text{sec}$. $Re= 24 \times 10^3$; $S=0, 0.5$.

Particle behavior, observed and described qualitatively in Figure 103 through 108 thus far, is now quantitatively examined by considering averaged particle quantities at various axial locations. The average particle axial (U_p), tangential (V_p) and radial (W_p) velocities are presented in Figure 109. The averages presented were calculated by sampling all particles passing through an axial plane of width $\Delta x = 0.1D$ (where $x = x_i \pm 0.1R$) at ten axial locations, $x=(1,2,3\dots 10)D$. Sampling was done every time step with a total of 200 and 400 samples for jet flow at $S=0$ and $S=0.5$ respectively.

As expected, Figure 109 shows that the average downstream particle axial velocity, U_p , for jet flow without rotation increases with increasing particle size due to corresponding increase in initial particle axial momentum. For the largest $500 \mu m$ particles the axial velocity remains nearly constant throughout the domain length. With added rotation the average axial velocity appears to be only slightly larger for both $500 \mu m$ particles and $10 \mu m$ particles. For the midsize $100 \mu m$ particles however the overall average particle axial velocity with $S=0.5$ rotation is considerably lower than without rotation. The tangential velocity, \bar{V}_p , also shows that it is significantly lower for

the 100 μm particles upstream from $x/D=1$ to 4 than both 10 μm and 500 μm particles which have nearly equal tangential velocity throughout. Both of these significant drops in average axial and tangential velocity observed for the 100 μm particles is due to their initial migration outside the jet core into a low-speed stagnant zone where the particles quickly lose their initial momentum. A significant particle average radial velocity \overline{W}_p is only observed for the largest (500 μm) particles throughout the jet, which decreases linearly till the domain exit.

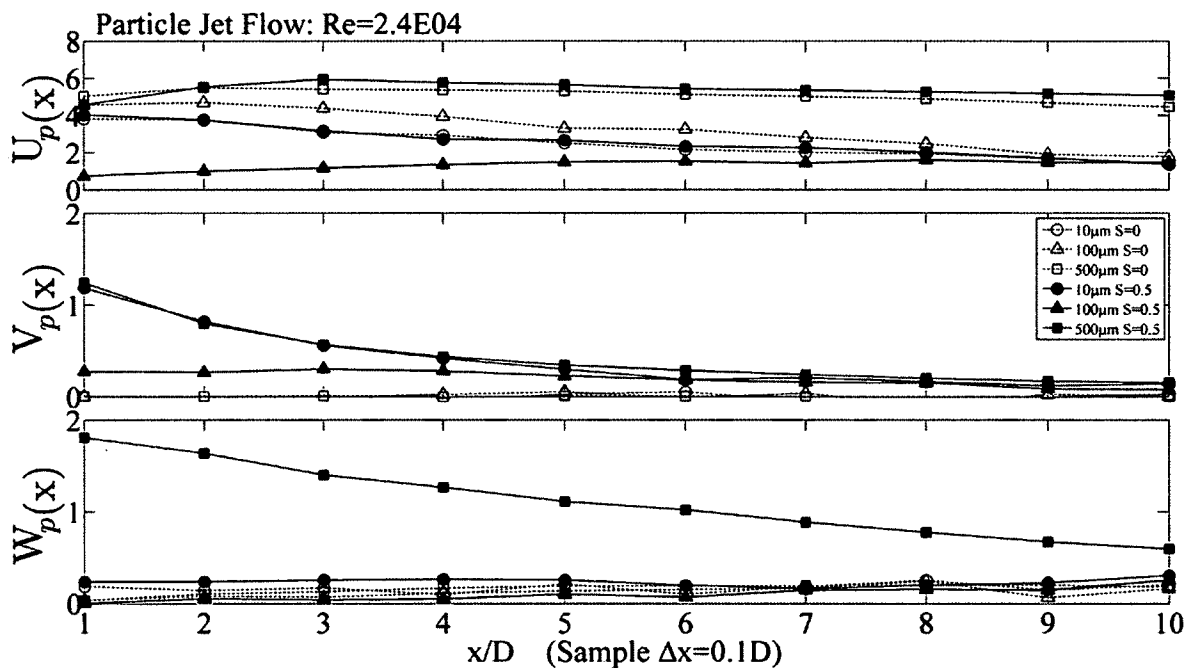


Figure 109: Average particle axial (U_p), tangential (V_p) and radial (W_p) velocities (m/s) at various downstream axial locations. $\text{Re}=24 \times 10^3$; $S=0, 0.5$.

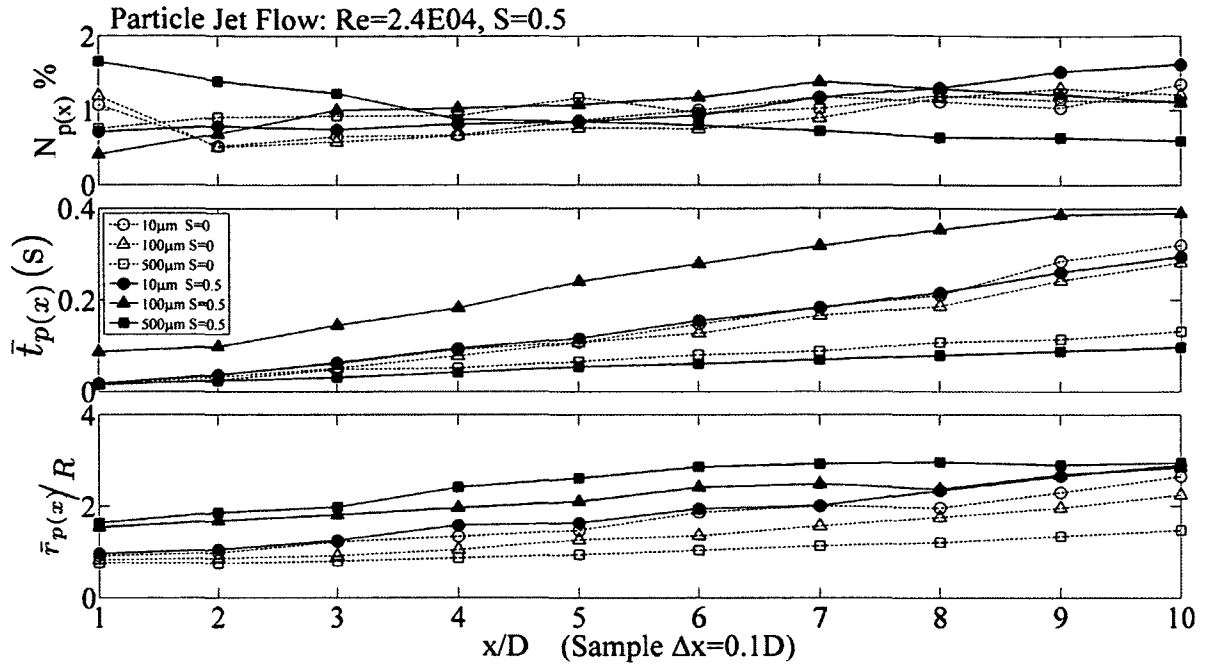


Figure 110: Particle count fraction, average residence time and average radial distance at various downstream axial locations. $Re = 24 \times 10^3$; $S = 0, 0.5$.

Figure 110 shows the particle fraction number, $N_{p(x)\%}$, average particle residence time, \bar{t}_p , and average radial distance, \bar{r}_p , of all particles found at each sampled axial location. The particle fraction number, $N_{p(x)\%}$, is the percentage of total number of particles found at each sampled axial plane, $N_{p(x)}$ divided by the total number of particles in the entire domain N_p .

$$N_{p(x)\%} = \frac{N_{p(x)}}{N_p} \times 100 \quad \text{Eqn. 8-3}$$

The particle fraction percent varies only slightly with axial location with and without rotation. In general, it appears to increase gradually downstream for all particle sizes, with the exception of 500 μm with rotation, for which it decreases throughout the domain. The decrease in this case is attributed to the particles' radial velocity component that causes them to continually move out of the domain. In Figure 110, \bar{r}_p , is the average radial distance for all particles sampled at each axial plane. Without rotation, it is larger for smaller particles, whereas the trend is opposite with rotation.

In Figure 110, \bar{t}_p , is the total time, on average, that particles have remained within the domain for all the particles present within the sampled axial location. It appears to be unaffected by rotation for the $10 \mu m$ particles. It decreases slightly for the larger $500 \mu m$ particles. For the mid-sized $100 \mu m$ particles, however, the change in particle residence time is markedly different with and without rotation, increasing by about 25%, in the former. The increase is again attributed to the particles initially migrating outside the jet core into a low velocity stagnant zone where their average axial velocity decreases significantly thereby causing the particles to move slower downstream.

To quantify the observed particle concentration shift away from the jet core of the $100 \mu m$ particles, a particle concentration in the radial direction at each axial location, is calculated as follows,

$$C_{p(x,r)} = \frac{N_{p(x,\Delta r_i)}}{V_{(\Delta r_i)}} \quad \text{Eqn. 8-4}$$

where $N_{p(x,\Delta r_i)}$ is the total number of particles found at each sampled axial location within a given radial interval Δr_i as shown in Figure 111. $V_{(r)} = \pi(\Delta r_i^2)\Delta x$ is the total sample volume. The sampled radial interval is set to $\Delta r = R/15$, where r goes from $(0 \rightarrow 5R)$ and axial sample plane width of $\Delta x = 0.1D$.

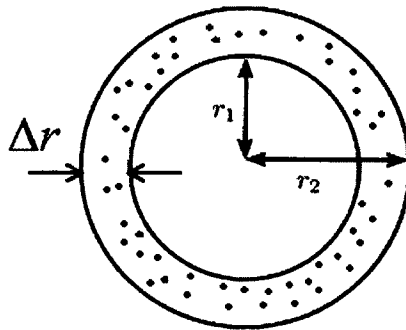


Figure 111: Depiction of particle concentration radial count sampling interval.

Figure 112 and 113 show the particle concentration profiles normalized with the particle concentration at the inlet, C_0 , at $x/D=(1,2,3)$ and $x/D=(5,7,10)$, respectively. With rotation the shift in the peak of the profiles to higher values of r/R is greatest for the mid-sized ($100\ \mu\text{m}$) particles. In general, the peak is lower and the profiles are broader.

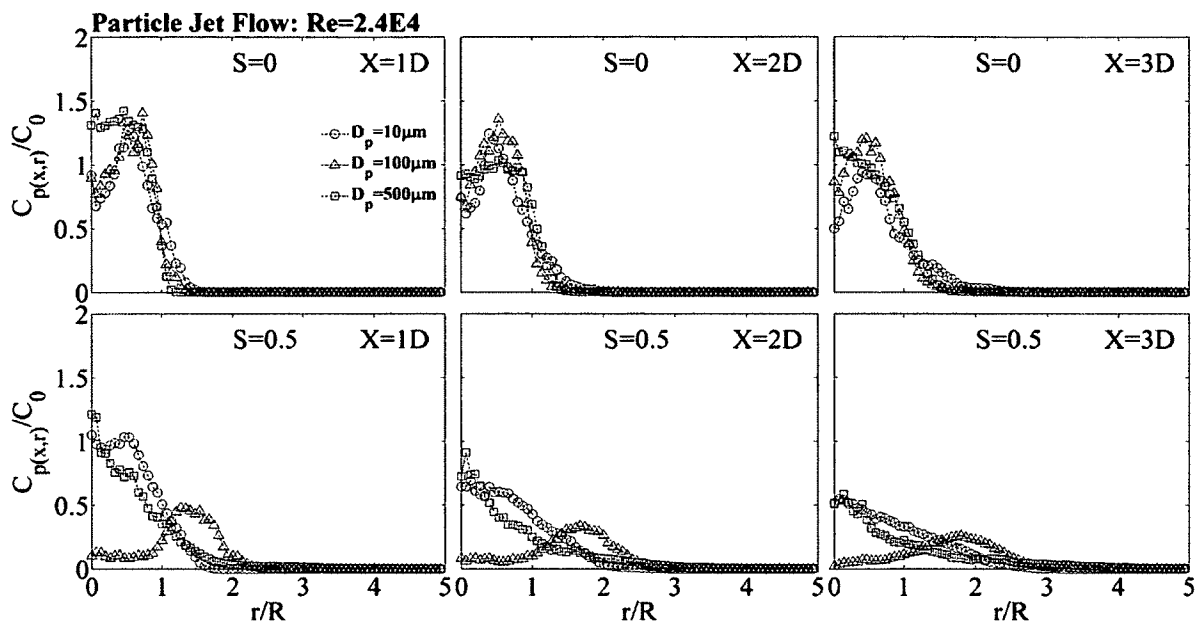


Figure 112: Particle concentration at $x/D=(1,2,3)$.

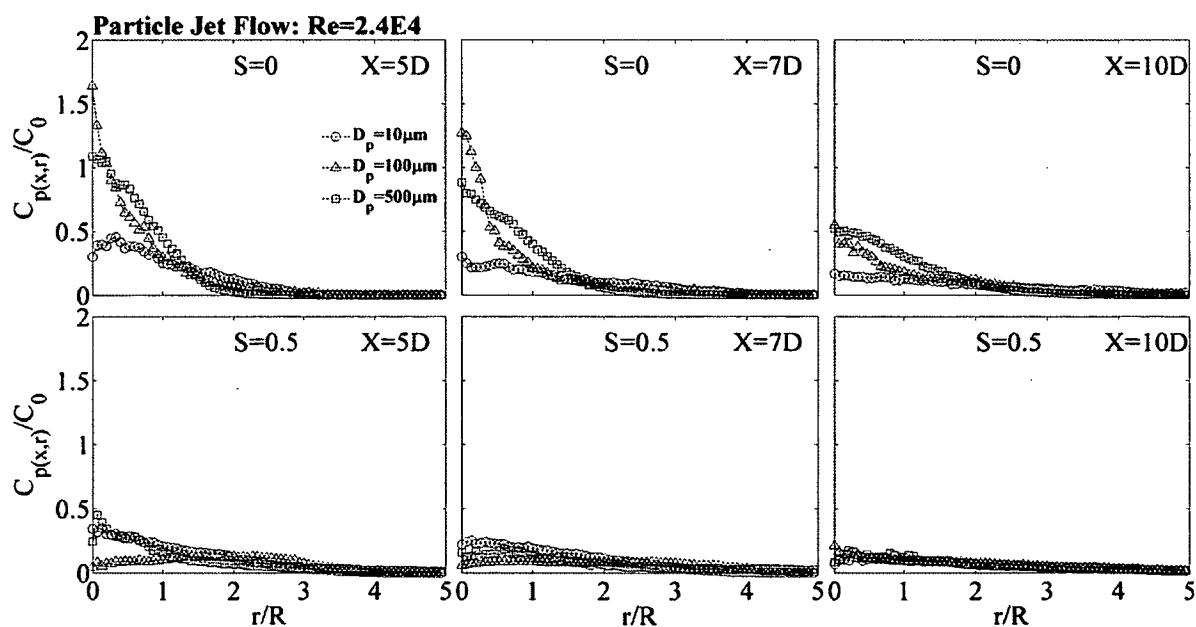


Figure 113: Particle concentration at $x/D=(5,7,10)$.

Figure 114 and 115 compare time-averaged velocity profiles of the particles and the fluid phase. The particle velocity averages were calculated by summing the instantaneous particle axial velocities of all particles sampled and found to pass through a given axial location and radial interval and dividing by the total number of particles within that interval as follows:

$$U_{p(x,r)} = \frac{1}{N_{p(x,r)}} \sum_{i=1}^{N_{p(x,r)}} u_{p,i(x,r)} \quad \cdot \quad \text{Eqn. 8-5}$$

Figure 114 shows that for $S=0$, particle and fluid velocities have the same centerline peak up to $x/D=4$. Beyond that, the particles move faster because they retain more of their initial momentum, whereas the flow velocity is reduced by entrainment of ambient fluid and mixing. The scatter observed in the particle axial velocity for $r/R>1$ at $x=1D-4D$ occurs because the particles are in the free-stream, outside the jet. Starting at a downstream distance of $x=4D$ the mean axial velocity for the larger $500 \mu m$ particle is noticeably larger away from the jet center. The maximum centerline axial velocity between the particles and the fluid flow seems to start diverging starting at around $x=5D$. By the downstream distance of $x=7D$, the mean axial velocity for the larger $500 \mu m$ particle is noticeably larger than that of the fluid flow across the entire jet width.

Figure 115 shows that, with the addition of rotation, the largest particles move much faster than the fluid at nearly all cross-sections, but the smaller-sized particles have velocity profiles which are virtually the same as for the fluid phase.

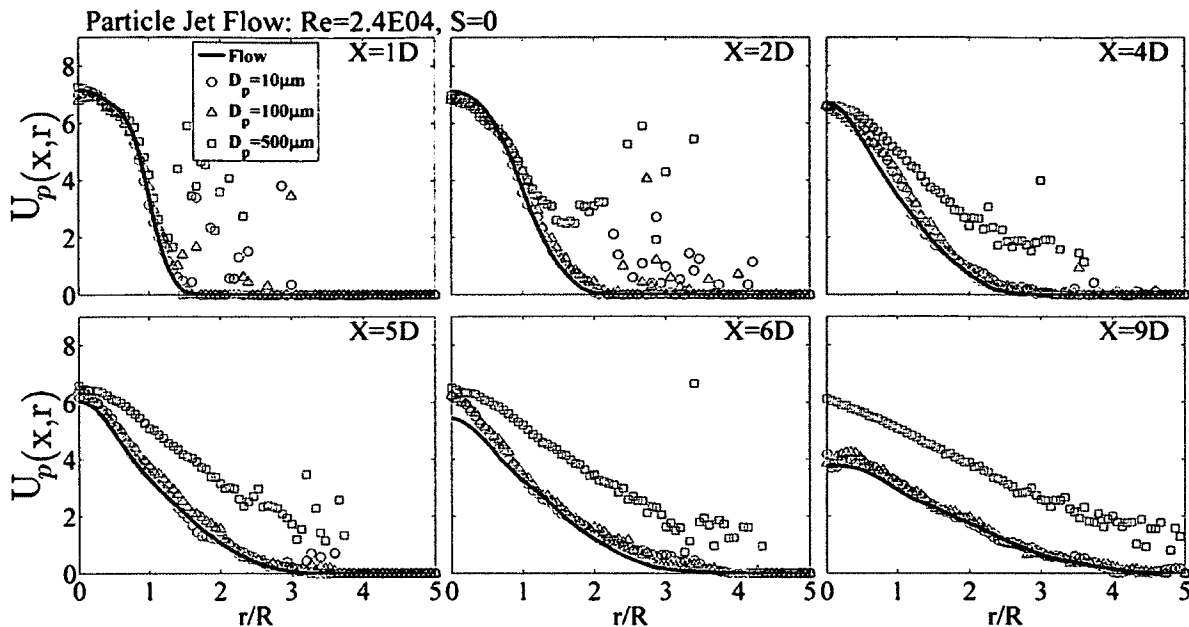


Figure 114: Average axial particle velocity (m/s), $Re=24 \times 10^3$; $S=0.5$.

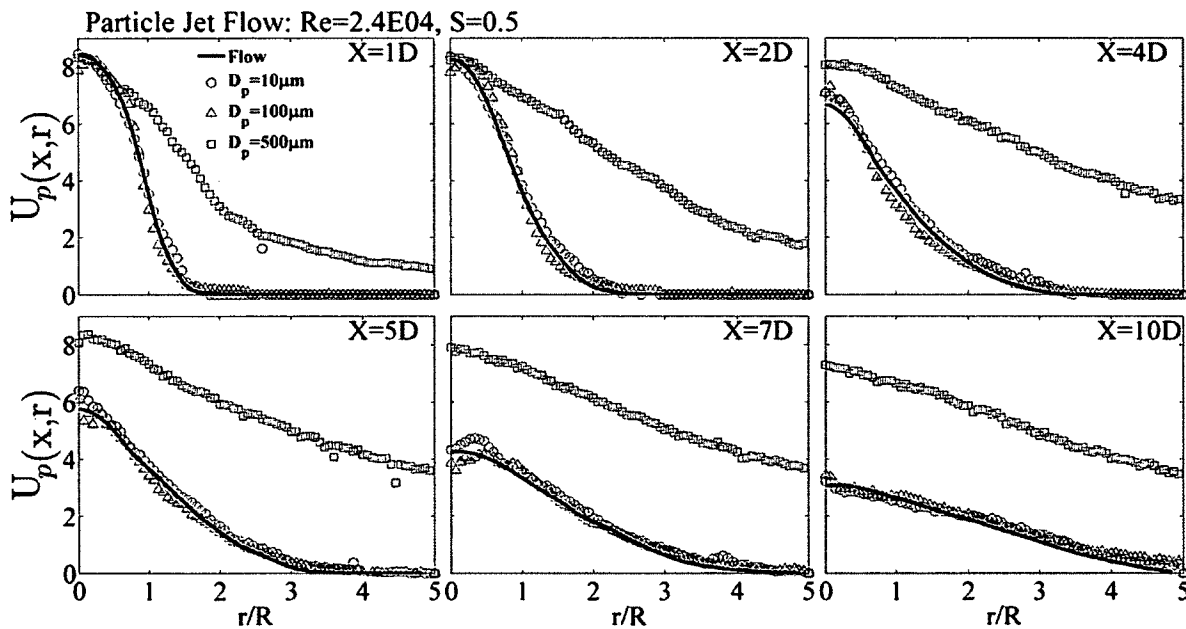


Figure 115: Average axial particle velocity (m/s), $Re=24 \times 10^3$; $S=0.5$.

In Figure 116, the tangential component of the average velocity for the jet and the various particles are compared. The smaller particles ($10\mu m$ and $100\mu m$) have similar profiles to the jet fluid phase, except for downstream ($x>5D$) where the smallest particles

show some drift. On the other hand, the largest particles ($500\ \mu\text{m}$) have tangential velocities which are much higher than jet fluid phase ones. For the most part, most of this particle motion is outside the jet core.

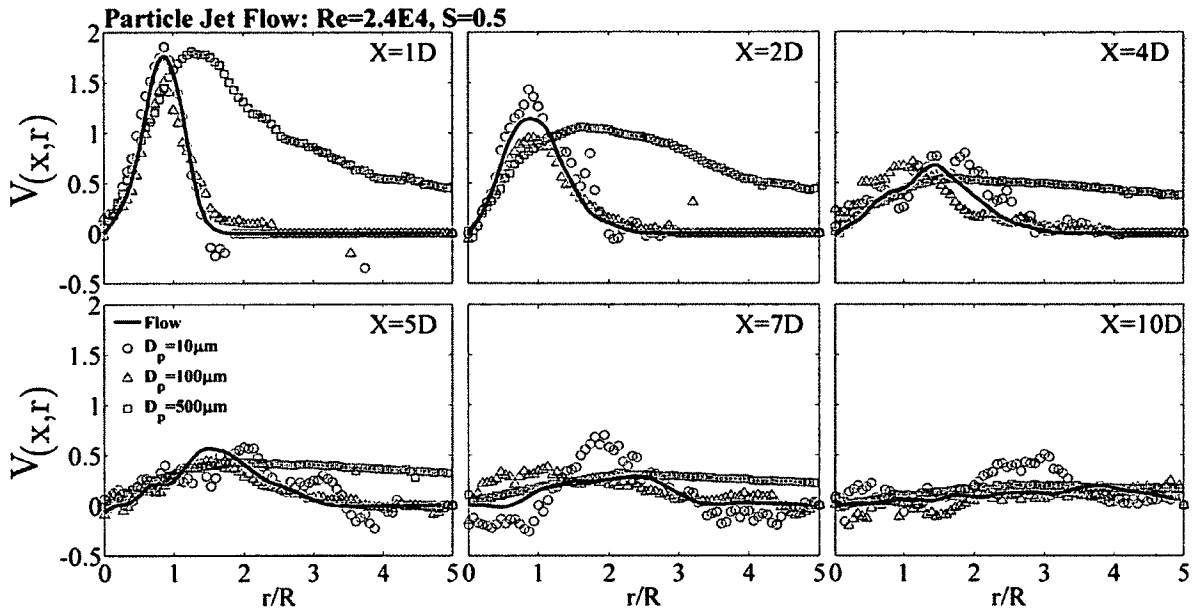


Figure 116: Average tangential velocity, $\text{Re}=24 \times 10^3$; $S=0.5$

The global rate of particle dispersion in the streamwise direction $D_r^T(x)$, is defined as

$$D_r^T(x) = \frac{\sqrt{\sum_{i=1}^N (r_i(x) - r_{i0})^2}}{N_{p(x)}} \quad \text{Eqn. 8-6}$$

where $N_{p(x)}$ is the total number of particles passing through a cross-sectional plane x during the entire sampling time, $r_i(x)$ is the radial displacement of the i^{th} particle that is passing through the plane, and r_{i0} is the initial radial displacement of the i^{th} particle when it was first injected into the jet domain. Figure 117 shows the total dispersion function along the streamwise position calculated for each case. It is seen that, without rotation, the values for $D_r^T(x)$ are inversely related to particle size, with larger particles showing lower dispersion. With particle rotation, the dispersion for the largest particle increases considerably. Mid-sized particles showed significant increase in dispersion, relative to

non-rotating jet, only in the near field $x/D < 3$. The smallest particles were largely unaffected by rotation.

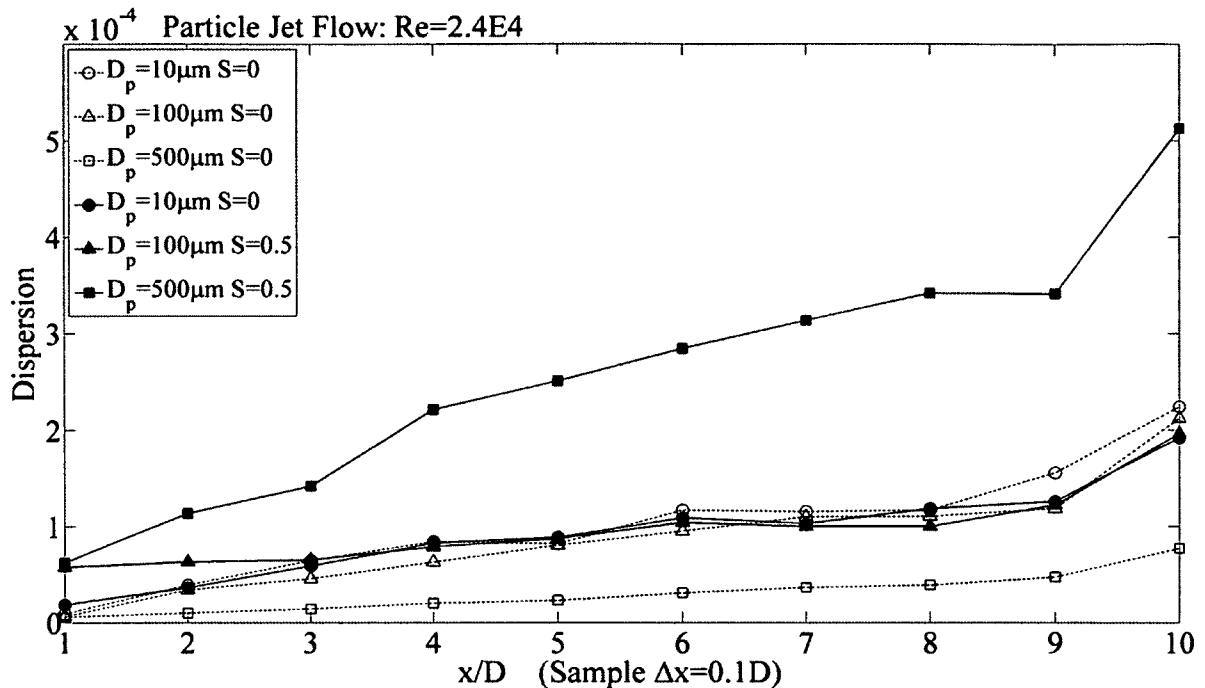


Figure 117: Particle Dispersion

Figure 118 shows trajectories of particles injected at six different radial locations for the jet flow at $Re=24 \times 10^3$ and $S=0.5$. The jet edge, where the jet axial velocity is equal to $U=0.98U_c$ is also shown as a reference. A total of 1000 time steps are shown for the $10 \mu m$ and $100 \mu m$ particles and 500 time steps for $500 \mu m$ particles. The travel path of smaller particles is more dependent on flow structures while the largest ($500 \mu m$) particles appear to be unaffected. All particles injected close to the center of the jet at $r_{inj}=0$ appear to show an initial trajectory that moves them gradually away from the jet center. This is probably due to centrifugal forces. For particles injected near the edge of the jet, the largest ones continue to move outward while the smallest ones return towards the center of the jet. The trajectory of the midsize $100 \mu m$ particles injected near the edge of the jet inlet shows that they initially moved out of the jet into the ambient surroundings, before they are re-entrained into the jet further downstream.

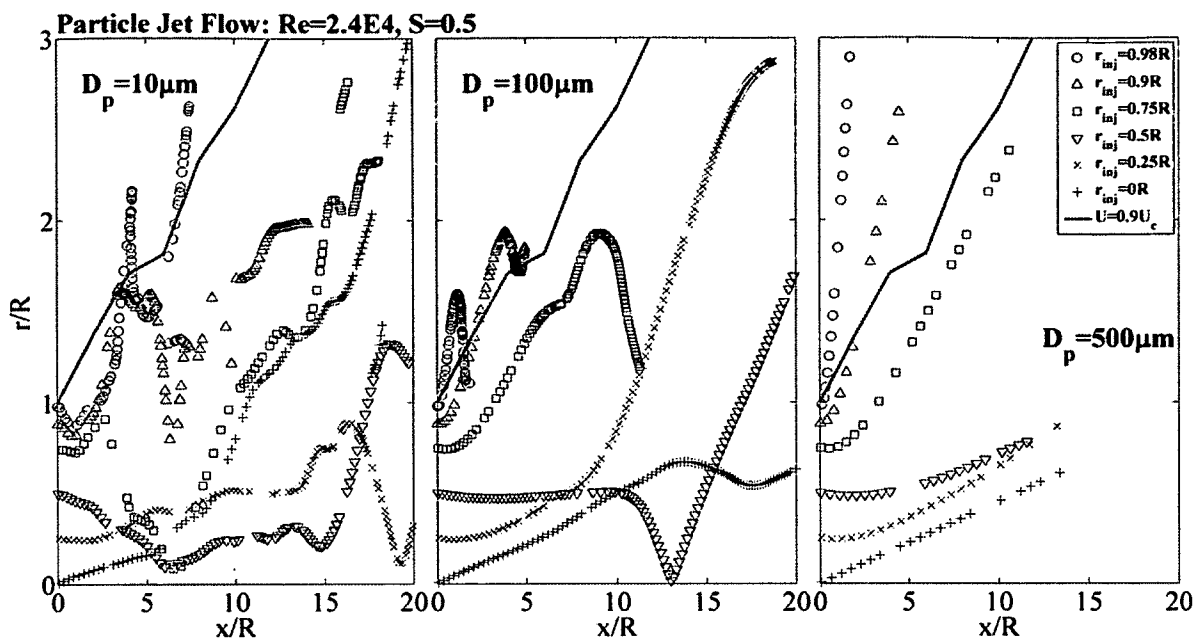


Figure 118: Particle trajectories

9 SUMMARY AND CONCLUSIONS

Large-Eddy Simulations have been carried out to study the near-field flow of particle-laden swirling turbulent round jet generated from a fully-developed axially rotating pipe. The standard subgrid-scale Smagorinsky-Lilly model with a constant Smagorinsky constant was used for all simulations performed. Lagrangian tracking with one way coupling was used to analyze fluid-particle dispersion in the near field.

Various pipe and jet meshes were tested for grid sensitivity. For pipe flow simulations it appears that all meshes tested had acceptable grid refinement, and there was minimal difference among the meshes tested at all Reynolds numbers. At the lowest Reynolds number of $Re=5.3 \times 10^3$, turbulent intensity profiles near the wall results of the coarser pipe mesh (M100L) did, however, verify the trend observed by Wu and Moin (2008) that for a coarse mesh, the streamwise component of turbulence intensity is amplified while the radial and tangential components decrease. The grid sensitivity test for the five meshes tested for jet flow also showed this trend. With the addition of rotation there was no significant difference among the pipe meshes tested except at the highest rotation rate of $S=2$. For the jet meshes tested, the mean axial center-line velocity was the only other indicator of the jet meshes grid refinement quality. With increased mesh refinement, results showed a trend of increasing centerline velocity and slower velocity decay.

Overall, both pipe and jet flow results agreed well with available data at all Reynolds numbers and rotation rates tested. Rotating pipe flow results confirm some previous findings, such as the deformation of the mean axial velocity profile towards the laminar Poiseuille-profile, a reduction in the turbulence near the wall region and an increase in the outer region of the pipe with increased pipe swirl. At a constant pressure gradient, an increase in bulk velocity was observed with addition of pipe rotation. The decrease in pressure loss from $S=0$ to $S=0.5$ was approximately 9% at $Re=5.3 \times 10^3$ and approximately 20% for the two higher Reynolds number of $Re=12 \times 10^3$ and 24×10^3 . Calculation of the anisotropy tensor components of the Reynolds stresses shows a redistribution of anisotropy due to pipe rotation. Suppression of the axial component of Reynolds stress near the wall and amplification of the tangential component of Reynolds

stress occurred as rotation is increased. Anisotropy invariant mapping showed that increasing pipe rotation results in movement away from the one-component limit in the buffer layer.

The instantaneous velocity profiles at the exit of the pipe flow simulation were utilized as inlet conditions for the jet flow simulation. Turbulent jet flow was analyzed at the Reynolds numbers of $Re=12 \times 10^3$ and 24×10^3 and swirl rates of $S=0$ and $S=0.5$. Jet swirl is observed to change the characteristics of the jet flow field with an increase in jet spread, velocity decay and a decrease in the jet potential core. The axial turbulent intensity component was shown to increase with the addition of swirl. Invariant mapping analysis of the Reynolds stress anisotropy tensor, performed downstream of the jet potential core showed that there is a slight Reynolds number effect between $Re=12 \times 10^3$ and 24×10^3 , with and without rotation. Across the jet, the invariants map closely to the axi-symmetric limit. Differences are seen mainly for large values of r/D , which are probably at the edge of the jet in the intermittent turbulent region.

Validated jet flow results at $Re=24 \times 10^3$ were used to study particle dispersion of 10, 100, and 500 μm diameter corresponding to a Stokes number of 0.06, 6, and 150, respectively. Lagrangian tracking with one way coupling was used to analyze particle statistics and dispersion in the near field. Particles were introduced intermittently with a low mass loading ($<1\%$) at the jet inlet with an initial velocity equal to the local instantaneous fluid velocity. Without jet rotation particle dispersion is inversely related to particle size with larger particles showing lower dispersion. Addition of jet swirl was found to cause the heavier particles to continuously travel outward and escape out the side of the domain. Particle dispersion was unaffected by jet rotation, for the smallest 10 μm particles. However, for mid-sized ones (100 μm), particle concentration was observed to be shifted outward, relative to the non-rotating case. The migration of particles near the inlet towards outside the jet core results in these particles residing in a stagnant zone where their velocity decreases prior to being entrained back into the jet flow and traveling downfield.

This research has shown the viability of LES for the analysis of rotating pipe and swirling jet flows. This work could be beneficial to several applications such as cyclone separators that are used to separate discrete phase particles of various sizes from a carrier

fluid phase. The current work has shown particle dispersion of three different size particles with the addition of rotation that could be used to design cyclone separators. This work can also be beneficial to the oil and gas industry, where rotational phase separators are important for separation of oil/water or liquid/gas mixtures. This research could also be applied to combustion. A crucial parameter in combustion/fuel injection is the degree of inter-phase mixing. Particle concentration analysis performed in this study could be applied to optimizing fuel droplets and air mixture to improve combustion efficiency. Analysis of particle dispersion behavior of known contaminants that can arise from chemical and biological warfare attacks can be vital to saving lives. Results of particle dispersion of various diameters investigated in this work can be used to aid to develop devices and strategies that can effectively contain and remove these contaminants. This work has established a methodology to aid in future analysis of these and other practical applications and has provided an initial set of data for the effect of jet swirl on dispersion of particles at three Stokes numbers.

Recommendations for advancing the understanding of rotating pipe/jet flow would include performing simulation of higher pipe/jet swirl rates at various Reynolds numbers to further aid in characterizing Reynolds shear stress anisotropic effects due to rotation and Reynolds number. Increased particle mass loading to determine instantaneous particle preferential accumulation and interaction and two-way coupling to characterize turbulence modulation due to particle-fluid interaction should also be considered.

REFERENCES

1. AGARD. 1998. "A Selection of Test Cases for the Validation of Large-Eddy Simulations of Turbulent Flows." *Advisor Group for Aerospace Research & Development*, Advisor Report 345, ISBN 92-836-1072-5.
2. Balachandar, S. and Eaton, K. 2010. "Turbulent Dispersed Multiphase Flow", *Annual Review of Fluid Mechanics*. 42:111-133.
3. Ball, C. G. and Pollard, A. 2008. "A Review of Experimental and Computational Studies of Flow from the Round Jet." Internal Report: Department of Mechanical and Materials Engineering, Queen's University.
4. Billant, P., Chomaz, J.M. and Huerre, P. 1998. "Experimental study of vortex breakdown in swirling jets." *Journal of Fluid Mechanics* 376:183-219.
5. Bradshaw, P. 1969. "The analogy between streamline curvature and buoyancy in turbulent shear flow." *Journal of Fluid Mechanics* 36:177-191.
6. Boguslawski, L., and Popiel, C. O. 1979. "Flow structure of the Free Round Turbulent Jet in the Initial Region." *Journal of Fluid Mechanics* 90:531-539.
7. Chen, Q. 2006. "Investigation of the Effects of Subgrid-Scale Turbulence on Resolvable-Scale Statistics." Dissertation, Clemson University.
8. Chigier, N. A., and Chervinsky, A. 1967. "Experimental Investigation of Swirling Vortex Motion in Jets." *Journal of Applied Mechanics* 34(2):443-451.
9. Crow, S.C. and Champagne, F.H. 1971. "Orderly structure in jet turbulence." *Journal of Fluid Mechanics* 48:547-591.
10. Crowe, C.T., Chung, J.N. and Troutt, T.R. 1989. "Particle Mixing in Free Shear Flows." *Progress in Energy and Combustion Science* 14:171-194.
11. Dimotakis, P. E., Miake-Lye, R. C., and Papantoniou, D. A. 1983. "Structure and Dynamics of Round Turbulent Jets." *Physics of Fluids* 26:3185-3192.
12. Durst, F., Jovanovic, J. and Sender, J. 1995. "LDA measurements in the near-wall region of a turbulent pipe flow." *Journal of Fluid Mechanics* 295:305-335.
13. Durst, F., Passtrapanska, M., Jovanovic, J. and Lienhart., H. 2006. "Turbulence measurements in a swirling pipe flow." *Experiments in Fluids* 41:813-827
14. Eggels, J.G.M., Unger, F., Weiss, M.H., Westerweel, J., Adrian, R.J., Friedrich, R., and Nieuwstadt, F.T.M. 1994. "Fully developed turbulent pipe flow: a comparison between direct numerical simulation and experiment." *Journal of Fluid Mechanics* 268:175-209.
15. Eggels, J., 1994 " Direct and large eddy simulation of turbulent flow in a cylindrical pipe geometry." Dissertation, Delft University of Technology, The Netherlands.
16. Elghobashi S. 1991. "Particle-laden turbulent flows: direct simulation and closure models." *Applied Scientific Research* 48:301-14.
17. Elghobashi S. 1994. "On predicting particle-laden turbulent flows." *Applied Scientific Research* 52:309-29.
18. Facciolo, L. 2006. "A study of axially rotating pipe and swirling jet flows." Technical Reports from Royal Institute of Technology, Department of Mechanics.
19. Facciolo, L., Maciel, Y., Duwig, C., Fuchs, L. and Alfredsson, P.H. 2008. "Near-field dynamics of a turbulent round jet with moderate swirl." *International Journal of Heat and Fluid Flow* 29(3):675-686.

20. Farokhi, S., Taghavi, R. and Rice E.J. 1989. "Effect of initial swirl distribution on the evolution of a turbulent jet." *AIAA Journal* 27(6):700-706.
21. Feiz, A.A., Ould-Rouis, M. and Lauriat, G. 2002. "Large eddy simulation of turbulent flow in a rotating pipe." *Journal of Heat and Fluid Flow* 24:412-420.
22. Fellouah, H., Ball, C. G., and Pollard, A. 2009. "Reynolds Number Effects Within the Development Region of a Turbulent Round Free Jet." *International Journal of Heat and Mass Transfer* 52:3943-3954.
23. Ferdman, E., Otugen M.V. and Kim, S. 2000. "Effect of initial velocity profile on the development of round jets." *Journal of Propulsion and Power* 16:676-686
24. FLUENT User Manual. 2006. FLUENT Vol 6.3, FLUENT, Inc., Lebanon, NH
25. Ganapathisubramani, B., Longmire, E. K. and Marusic, I. 2002. "Investigation of Three Dimensionality in the Near Field of a Round Jet Using Stereo PIV." *Journal of Turbulence* 3(16)1-12.
26. Germano, M., Piomelli, U., Moin, P. and W. Cabot. 1991. "A Dynamic Subgrid-scale Eddy Viscosity Model." *Physics of Fluids* 3(7):1760-1765.
27. Gilchrist, R. and Naughton, J. 2005. "Experimental Study of Incompressible Jets with Different Initial Swirl Distributions: Mean Results." *AIAA Journal* 43(4):741-751.
28. Gore, R. A. and Crowe, C. T. 1989. "Effect of particle size on modulating turbulent intensity." *International Journal of Multiphase Flow* 15:279-285.
29. Gupta, A. K., Lilley, D. G. and Syred, N. 1984. *Swirl flows*. Kent England: Turnbridge Wells Abacus Press.
30. Hetsroni, G. 1989. "Particle-turbulence interaction." *International Journal of Multiphase Flow* 15:735-746.
31. Hirai S, Takagi T and Matsumoto M. 1988. "Prediction of the laminarization phenomena in an axially rotating pipe flow." *Journal of Fluids in Engineering* 110:424-43.
32. Hussain, A. K. M. F. and Zaman, K. B. M. Q. 1981. "The 'preferred mode' of the axisymmetric jet." *Journal of Fluid Mechanics* 110:39-71.
33. Itoh, M., Imao, S. and Harada, T. 1996. "Turbulent characteristics of the flow in an axially rotating pipe." *International Journal of Heat and Fluid Flow* 17:444-451.
34. Itoh, M., Imao, S., Yamada, Y. and Zhang, Q. 1992. "The characteristics of spiral waves in an axially rotating pipe." *Experiments in Fluids* 12:277-285.
35. Ivanic, T., Foucault, E. and Pecheux, J. 2003. "Dynamics of swirling jet flows." *Experiments in fluids*, 35(4):317-324.
36. John, V., and Layton, J. 2002. "Analysis of Numerical Errors in Large Eddy Simulations." *Journal of Numerical Analysis* 40(3):995-1020.
37. Jung, D., Gamard, S. and George, W. K. 2004. "Downstream Evolution of the Most Energetic Modes in a Turbulent Axisymmetric Jet at High Reynolds Number. Part 1. The Near-Field Region." *Journal of Fluid Mechanics* 514:172-204.
38. Kaftori D, Hetsroni G. and Banerjee, S. 1995. "Particle behavior in the turbulent boundary layer. I. Motion, deposition and entrainment." *Physics of Fluids* 7:1095-1106.
39. Kikuyama, K. and Murakami, M. 1980. "Turbulent flow in axially rotating pipes." *Journal of Fluids Engineering* 102:97-103.
40. Kikuyama, K., Murakami, M., Nishibori, K. and Maeda, K. 1983. "Flow in an axially rotating pipe." *JSME International Journal* 26(214):506-513.

41. Kikuyama, K., Murakami, M., Nishibori, K. and Maeda, K. 1987. "Laminarization of turbulent flow in the inlet region of an axially rotating pipe." *JSME International Journal* 30(260):255-262.
42. Kulick, J.D., Fessler, J.R., and Eaton, J.K. 1994. "Particle response and turbulence modifications in fully developed channel flow." *Journal of Fluid Mechanics* 277:109-134.
43. Lai, J.C.S. 1991. "The preferred mode of a tube jet." *Journal of Heat and Fluid Flow* 2(3):284-286.
44. Leveque, E., Toschi, F., Shao, L. and Bertoglio, J.P. 2007. "Shear-improved Smagorinsky model for large-eddy simulation of wall-bounded turbulent flows." *Journal of Fluid Mechanics* 570:491-502.
45. Liang, H. and Maxworthy, T. J. 2005. "Vortex breakdown and mode selection of swirling jets in stationary or rotating surroundings." *Journal of Fluid Mechanics* 525: 115-159.
46. Lilley, D.G. 1977. "Swirling flows in combustion: A review." *AIAA Journal* 15:1063-1078.
47. Lilly, D. K. 1992. " A proposed modification of the Germano Subgrid-scale Closure Method." *Physics of Fluids* 4(3):633-635.
48. Loiseleux, T. and Chomaz, J. M. 2003. "Breaking of rotational symmetry in a swirling jet experiment." *Physics of Fluids* 15:511-523.
49. Longmire, E., and Eaton, J. 1992. " Structure of Particle-laden Round Jet." *Journal of Fluid Mechanics* 236:217-257.
50. Loulou, P., Moser, R. D., Mansour, N. N. and Cantwell, B. J. 1997. "Direct numerical simulation of incompressible pipe flow using a B-spline spectral method." NASA Technical Memorandum, 110436.
51. Lumley, J.L. 1978. "Computational modeling of turbulent flows." *Advances in Applied Mechanics* (18)123-176.
52. Lumley, J.L. and Newman, G. 1977. "The return to isotropy of homogeneous turbulence." *Journal of Fluid Mechanics* 82:161-178.
53. Lucca-Negro, O. and O'doherty, T. 2001. "Vortex breakdown: a review." *Progress in Energy and Combustion Science* 27:431-481.
54. Luo, k., Klein, M., Fan, J. and Cen, K. 2006. "Effects on particle dispersion by turbulent transition in a jet." *Physics Letters A* 357:345-350.
55. Mi, J., Nobes, D. and Nathan, G. J. 2001. "Influence of Jet Exit Conditions on the Passive Scalar Field of an Axisymmetric Free Jet." *Journal of Fluid Mechanics* 432:91-125.
56. Michioka, T. and Kurose, R. 2008. "Large-Eddy Simulation of Particle Diffusion in a Particle-laden Swirling Jet." *Journal of Fluid Science and Technology* 73(725):30-37.
57. Nallasamy, M. 1987. "Turbulence models and their applications to the predictions of internal flows: a review." *Computers and Fluids*; 15(2):151-194.
58. Nishibori, K., Kikuyama K. and Murakami M. 1987. "Laminarization of turbulent flow in the inlet region of an axially rotating pipe." *JSME International Journal* 30:255-262.
59. Orlandi, P. and Ebstein, D. 2000. "Turbulent budgets in rotating pipes by DNS." *International Journal of Heat and Fluid Flow* 21:499-505.

60. Orlandi, P. and Fatica, M. 1997. "Direct simulations of turbulent flow in a pipe rotating about its axis." *Journal of Fluid Mechanics* 343:43-72.
61. Panda, J. and McLaughlin, D. K. 1994. "Experiments on the instabilities of a swirling jet." *Physics of Fluids* 6:263-276.
62. Papadopoulos, G. and Pitts, W. M. 1998. "Scaling the Near-Field Centerline Mixing Behavior of Axisymmetric Turbulent Jets." *AIAA Journal* 36(9):1635-1642.
63. Papadopoulos, G., and Pitts, W. M. 1999. "A Generic Centerline Velocity Decay Curve for Initially Turbulent Axisymmetric Jets." *Journal of Fluids Engineering* 121: 80-85.
64. Park, S. H. and Shin, H. D. 1993. "Measurement of entrainment characteristics of swirling jets." *International Journal of Heat and Mass Transfer* 136:4009-4018.
65. Pratte, B. D. and Keffer, J. F. 1972. "The swirling turbulent jet." *Journal of Basic Engineering* 93:739-748.
66. Reich, G. and Beer, H. 1989. "Fluid flow and heat transfer in an axially rotating pipe-I. Effect of rotation on turbulent pipe flow." *International Journal of Heat and Mass Transfer* 32(3):551-562.
67. Richards, C.D. and Pitts, W.M. 1993. "Global density effects on the self-preservation behavior of turbulent free jets." *Journal of Fluid Mechanics* 245:417-435
68. Rose, W. G. 1962. "A swirling round turbulent jet." *Journal of Applied Mechanics* 29:615-625.
69. Satake, S. and Kunugi, T. 2002. "Direct numerical simulation of turbulent heat transfer in an axially rotating pipe flow: Reynolds shear stress and scalar flux budgets." *International Journal of Numerical Methods for Heat and Fluid Flow* 12(8):958-1008.
70. Shinneeb, A. M., Bugg, J. D. and Balachandar, R. 2008. "Quantitative investigation of Vortical Structures in the Near-Exit Region of an Axisymmetric Turbulent Jet," *Journal of Turbulence*, 9(19)1-20.
71. Smagorinsky, J. 1963. "General Circulation Experiments with the Primitive Equations, I. the Basic Experiment." *Monthly Weather Review* 91(3)99-164.
72. Uthupan, J., Aggarwal, S. K., Grinstein, FF. and Kailasanath, K. 1994. "Particle Dispersion in a Transitional Axisymmetric Jet: A Numerical Simulation." *AIAA Journal* 32(10):2004-2014.
73. Weisgraber, T. H. and Liepman, D. 1998. "Turbulent Structure During Transition to Self-Similarity in a Round Jet." *Experiments in Fluids* 24:210-224.
74. White, A. 1964. "Flow of a fluid in an axially rotating pipe." *Journal of Mechanical Engineering Science* 6(1):47-52.
75. Wu, X. and Moin, P. 2008. "A direct numerical simulation study on the mean velocity characteristics in turbulent pipe flow." *Journal of Fluid Mechanics* 608:81-112.
76. Xu, G. and Antonia, R. A. 2002. "Effect of different initial conditions on a turbulent round free jet." *Experiments in Fluids* 33:677-683.
77. Yang, Z. 2000. "Large Eddy Simulation of fully developed turbulent flow in a rotating pipe." *Journal for Numerical Methods in Fluids* 33:681-694.

VITA

Name

Nicolas Castro

Department

Department of Mechanical Engineering
238 Kaufman Hall
Old Dominion University
Norfolk, VA 23529

Education

Ph.D. Mechanical Engineering Old Dominion University	December 2012 Norfolk, VA
M.S. Mechanical Engineering	August 2005
B.S. Mechanical Engineering Virginia Commonwealth University	December 2002 Richmond, VA

Publications

- Mossi, K., Bryant, R., Castro, N., Mane, P. 2005. "Boundary Condition Effects on Piezoelectric Synthetic Jets." *Integrated Ferroelectrics* 71: 257–266.
- Mossi, K., Bryant, R., Castro, N., Mane, P. 2007. "Piezoelectric actuators as synthetic jets: Cavity dimension effects." *Journal of Intelligent Materials Systems and Structures*. 18(11):1175-1190
- Demuren, A.O., Sexton, W., Castro, N. 2008. "Experimental Study of Dust Pick-Up and Suspension Process from Large Mining Truck Traveling in Unpaved Dirt Road." Report, Caterpillar Inc.
- Demuren, A.O., Sexton, W., Castro, N. 2008. "Analytical Simulations of the Effects of Dust Mitigation Devices on Dust Clouds Trailing the Caterpillar 797." Report, Caterpillar Inc.
- Demuren, A.O., Gyuricsko, E., Diawara, N., Castro, N., Carter, J., Bhaskara, R. 2009. "Impaired Insulin Delivery During Continuous Subcutaneous Insulin Infusion." Report, ODU, Children's Hospital of the King's Daughters.
- Demuren, A.O., Gyuricsko, N., Castro, N. 2010. "Impaired Insulin Delivery During Continuous Subcutaneous Insulin Infusion II." Report, ODU, Children's Hospital of the King's Daughters.